Lu Wang

Ultradeep Carbonate Gas Reservoirs

Reservoir Characteristics and Percolation Mechanism

Springer

Ultradeep Carbonate Gas Reservoirs

Lu Wang

Ultradeep Carbonate Gas Reservoirs

Reservoir Characteristics and Percolation Mechanism

Springer

Lu Wang
Department of Petroleum Engineering
College of Energy
Chengdu University of Technology
Chengdu, Sichuan, China

ISBN 978-981-19-9707-5 ISBN 978-981-19-9708-2 (eBook)
https://doi.org/10.1007/978-981-19-9708-2

© The Editor(s) (if applicable) and The Author(s), under exclusive license to Springer Nature Singapore Pte Ltd. 2023
This work is subject to copyright. All rights are solely and exclusively licensed by the Publisher, whether the whole or part of the material is concerned, specifically the rights of translation, reprinting, reuse of illustrations, recitation, broadcasting, reproduction on microfilms or in any other physical way, and transmission or information storage and retrieval, electronic adaptation, computer software, or by similar or dissimilar methodology now known or hereafter developed.
The use of general descriptive names, registered names, trademarks, service marks, etc. in this publication does not imply, even in the absence of a specific statement, that such names are exempt from the relevant protective laws and regulations and therefore free for general use.
The publisher, the authors, and the editors are safe to assume that the advice and information in this book are believed to be true and accurate at the date of publication. Neither the publisher nor the authors or the editors give a warranty, expressed or implied, with respect to the material contained herein or for any errors or omissions that may have been made. The publisher remains neutral with regard to jurisdictional claims in published maps and institutional affiliations.

This Springer imprint is published by the registered company Springer Nature Singapore Pte Ltd.
The registered company address is: 152 Beach Road, #21-01/04 Gateway East, Singapore 189721, Singapore

Preface

Carbonate gas reservoirs play an important role in the world energy pattern, accounting for 26% of the total 370 large natural gas fields discovered in the world. In addition, the recoverable reserves of carbonate gas reservoirs are 72.4×10^{12} m^3, accounting for 46% of the recoverable reserves of all gas reservoirs. With the development and progress of hydrocarbon theory and technology, ultradeep carbonate gas reservoirs have become the key areas of fossil fuel exploration and development. The annual gas production of conventional natural gas in Sichuan Basin, the cradle of China's modern natural gas industry, is 350×10^8 m^3, of which the annual production of natural gas in the ultradeep carbonate gas reservoir accounts for more than 83%, indicating that the ultradeep carbonate gas reservoir is the most potential hydrocarbon resource field in China and even in the world.

The ultradeep carbonate gas reservoir has experienced a geological history of more than 100 million years, as well as multistage tectonic movement and diagenetic transformation, thereby forming a coexistence pattern of multiple media, including microscopic pores, macroscopic pores, dissolution cavities and fractures. Therefore, this type of gas reservoir is characterized by extremely strong reservoir heterogeneity, extremely high temperature and pressure, special percolation mechanism, complex gas–water relationship, difficult reserve evaluation, and large difference in gas well productivity. A systematic and comprehensive investigation of the reservoir characteristics and percolation mechanism of ultradeep carbonate gas reservoirs is a prerequisite for scientific and efficient development and is also the main content of this monograph. At present, there is a lack of theoretical research on ultradeep carbonate gas reservoirs because of the limitations of experimental techniques and analytical methods. Our team has preliminarily formed a variety of research techniques through 6 years of technical breakthrough and practice accumulation on the ultradeep carbonate gas reservoirs of Sinian Dengying Formation and Cambrian Longwangmiao Formation in Sichuan Basin, namely comprehensive evaluation technique of reservoir characteristics and storage-percolation capacity, ultra-high temperature and pressure physical simulation experiment technique, microscopic visualization technique based on CT scanning and microelectronics lithography, and heterogeneous reservoir development physical simulation technique. The key

techniques and methods introduced in this monograph can meet the needs of efficient development of ultradeep carbonate gas reservoirs at this stage and are expected to provide theoretical basis and technical reference for readers to conduct relevant research on similar gas reservoirs.

The monograph is comprised of five chapters. Chapter 1 gives a detailed introduction to the reservoir characteristics and fluid properties of the ultradeep carbonate gas reservoir based on a variety of testing techniques, and a analysis of the storage and percolation capacity of various types reservoirs according to the established reservoir-type classification standards. The ultra-high temperature and pressure physical simulation experiment technique and equipment are introduced in Chap. 2, and the gas-phase and gas–water two-phase percolation mechanism and percolation capacity of different types of reservoirs in ultradeep carbonate gas reservoirs under actual formation conditions are revealed. In Chap. 3, the microscopic visualization technique of fluid percolation based on CT scanning and microelectronic lithography is presented. Then, the complex gas–water relationship and the formation mechanism of residual water and trapped gas of different types of reservoirs during the hydrocarbon accumulation and water encroachment processes are qualitatively and quantitatively studied. Chapter 4 focuses on the sensitivity characteristics and formation damage mechanisms of water, salinity, velocity, acid, and alkali of different types of reservoirs in ultradeep carbonate gas reservoirs. Furthermore, both the permeability and porosity stress sensitivity degree and characteristics of different types of reservoirs are determined. The monograph ends with Chap. 5 which reveals the gas production characteristics and gas supply capacity of differential types of reservoirs in ultradeep carbonate gas reservoirs with interlayer heterogeneity and horizontal heterogeneity, and analyzes the effects of reservoir heterogeneity, permeability difference, depletion pressure differential, initial water saturation, and water encroachment on the gas production capacity of the two types of heterogeneous gas reservoirs. In addition, the suggestions for efficient development of gas reservoirs are put forward according to the reservoir characteristics and percolation mechanism of ultradeep carbonate gas reservoirs. I hope this systematic monograph will be valuable to academics and engineers working in the related area.

I would like to sincerely thank my former Ph.D. advisor, Prof. Shenglai Yang at the China University of Petroleum (Beijing), who introduced me to the interesting field of ultradeep carbonate gas reservoirs in 2015. I would also like to thank the leaders and engineers of PetroChina Southwest Oil and Gas Field Company for their technical support to my monograph. Furthermore, I would like to thank my wife, Dr. Xingli Xu, for her consideration in my life during my monograph edition. Last but not least, I am grateful for the financial support provided by the National Science and Technology Major Projects of China (2016ZX05015-003), the National Natural Science Foundation of China (51774300), the Natural Science Foundation of Sichuan Province (2022NSFSC0205), and the Open Fund of State Key Laboratory of Oil and Gas Reservoir Geology and Exploitation (PLC2020007).

Many research contents introduced in this monograph are still in the exploratory stage, because the exploration and development of ultradeep carbonate gas reservoirs is a new research field. Owing to my limited knowledge, there might be some mistakes and flaws in this monograph. Please don't hesitate to correct me.

Chengdu, China Dr. Lu Wang

Contents

About the Author

Lu Wang works as Associate Professor and Master's Supervisor in the Department of Petroleum Engineering, College of Energy at Chengdu University of Technology. He holds a B.Eng. degree in Petroleum Engineering form the Xi'an Shiyou University, an M.Eng. degree and a Ph.D. degree in Oil & Gas Field Development Engineering from the China University of Petroleum (Beijing). The Petroleum Engineering courses that he teaches include Reservoir Engineering, Natural Gas Engineering, Petrophysics, and Shale Reservoir Development Technology. His main research interests are Oil & Gas Reservoir Evaluation, Complex Percolation Mechanism, and CO_2 Capture, Utilization and Storage. He has co-authored more than 50 peer-reviewed journal papers and conference papers. He is a Young Member of the National Academic Committee of Percolation Mechanics and a Member of Society of Petroleum Engineers (SPE). He serves as Advisor, Editor and Reviewer for many academic journals in energy and geology fields, e.g., Chemical Engineering Journal, Applied Energy, Energy, Fuel, Marine and Petroleum Geology, Energy & Fuels, Petroleum Science, Petroleum Exploitation & Development, Journal of Petroleum Science & Engineering, Journal of Natural Gas Science & Engineering, Energy Science & Engineering, International Journal of Hydrogen Energy, Natural Resources Research, Capillarity, Geofluids, Frontiers in Energy Research, Energies.

Chapter 1
Reservoir Characteristics of the Ultradeep Carbonate Gas Reservoir

A significant proportion of global fossil fuel reserves and production are contributed by carbonate reservoirs. The huge exploration and exploitation potential of carbonate reservoirs has always been the focus of scholars and engineers all over the world (Garing et al., 2014; Luo et al., 2017; Wang et al., 2020; Zhang et al., 2018). At present, ultradeep carbonate gas reservoirs have become the significant areas of global exploration and exploitation with the continuous development of oil and gas theory and technology. In recent years, the ultradeep carbonate gas reservoirs (depth > 4500 m) in the Sichuan Basin have made significant progress in the Cambrian Longwangmiao Formation and the Sinian Dengying Formation successively. The annual production capacity of the Longwangmiao Formation gas reservoir has reached more than 100×10^8 m^3. The proven reserves of Sinian gas reservoirs, which are difficult to develop, are approximately 6000×10^8 m^3, with an annual gas production capacity of more than 63×10^8 m^3. Both ultradeep carbonate gas reservoirs in the Sichuan Basin show optimistic prospects for exploration and exploitation (Zou et al., 2014). However, ultradeep carbonate gas reservoirs have experienced a geological history of more than 100 million years, as well as multistage tectonic movements and paleokarstification. Ultimately, the ultradeep carbonate gas reservoir formed a coexistence pattern of multiple media, including microscopic pores, macroscopic pores, dissolution cavities and fractures. The complexity and variability of the distribution of various types of media in both horizontal and vertical directions result in extremely heterogeneous reservoirs. Strong reservoir heterogeneity is a macroscopic performance of complex pore throat structures, which increases the difficulty of evaluating the storage and percolation capacities of ultradeep carbonate gas reservoirs (Corbett et al., 2017; Hulea & Nicholls, 2012; Makhloufi et al., 2013; Matonti et al., 2015; Norbisrath et al., 2015; Ronchi & Cruciani, 2015; Wang et al., 2020; Zhang et al., 2022). Therefore, it is of theoretical and practical significance to systematically and comprehensively study the multiscale reservoir characteristics of ultradeep carbonate gas reservoirs (Gao & Li, 2016; Garing et al., 2014; Gundogar et al., 2016). However, ultradeep carbonate gas reservoirs have the typical characteristics of extremely strong heterogeneity, various types of reservoir spaces and percolation

© The Author(s), under exclusive license to Springer Nature Singapore Pte Ltd. 2023

L. Wang, *Ultradeep Carbonate Gas Reservoirs*,
https://doi.org/10.1007/978-981-19-9708-2_1

channels. The existing research methods and procedures of reservoir characteristics are not completely applicable to ultradeep carbonate gas reservoirs. The purpose of this chapter is to introduce the reservoir characteristics of the Deng IV Member ultradeep carbonate gas reservoir in the Gaoshiti-Moxi area, Sichuan Basin. Furthermore, a systematic reservoir classification standard for ultradeep carbonate gas reservoirs was formulated for the first time based on the typical reservoir characteristics, and the storage and percolation capacities of different types of carbonate reservoirs were also evaluated.

1.1 Geological Setting of the Ultradeep Carbonate Gas Reservoir

1.1.1 Tectonic Setting

The Dengying Formation gas reservoir in Sinian System, one of the typical ultradeep carbonate gas reservoirs introduced in this book, are located in the Sichuan Basin. The Sichuan Basin is located in the south central Asian continent and is one of the largest natural gas-bearing basins in China. The Sichuan Basin is divided into five tectonic units according to the fault-fold structure zone, namely the Central Sichuan Flat-Gentle Paleouplift Mesozoic-Slope Belt, North Sichuan Low-Gentle Fault Belt, West Sichuan Low-Steep Fault Belt, East Sichuan High-Steep Fault-Fold Belt and South Sichuan Low-Steep Dome Belt (Fig. 1.1) (Li et al., 2013; Xu et al., 2012). From the plane, the studied ultradeep carbonate gas reservoir is distributed in the Gaoshiti-Moxi area. The Gaoshiti-Moxi area is situated in the central part of the Flat-Gentle Paleouplift Mesozoic-Slope Belt in the Central Sichuan Basin, with an area of 5288 km^2 and a total closure of 429 m (Fig. 1.1) (Jin et al., 2017). The Flat-Gentle Paleouplift Mesozoic-Slope Belt in the Central Sichuan Basin is the earliest, longest and largest giant uplift of the Sichuan Basin. The axis starts from Leshan in the west and reaches Longnüsi in the east. Taking the entire denudation zone of the Silurian system as a benchmark, the paleouplift area is 6.25×10^4 km^2 (Fig. 1.1) (Yang et al., 2016). This paleouplift has an important influence and prominent control effect on the natural gas accumulation of the Dengying Formation (Du et al., 2014). At present, there are many large natural gas reservoirs developed along the horizontal direction of this paleouplift, including the Weiyuan gas field at the core and the Ziyang gas trap on the western slope of the paleouplift, as well as the Gaoshiti, Moxi and Longnüsi gas reservoirs at the core and the Hebaochang gas reservoir on the eastern slope of the paleouplift (Fig. 1.2). The target formation has undergone four periods of tectonic evolution since the formation of this paleouplift (Luo et al., 2015). The prototype of its structure was formed in the Sinian Dengying period, and then greatly expanded under the influence of the Tongwan Movement in the later Dengying period. Subsequently, it developed rapidly in the late Lower Cambrian because of the most active basement faults. Owing to the Caledonian movement in the late Silurian, the basic range of

the Central Sichuan Paleouplift was established. Eventually, the basic scope of the Central Sichuan Paleouplift was established after the Caledonian movement in the late Silurian. The Deng IV Member experienced various constructive and destructive diagenesis processes after deposition, including compaction, cementation, metasomatism, dissolution, filling. Among them, compaction, cementation and filling are destructive diagenesis that lead to the reduction of storage space, the deterioration of petrophysical properties, and the enhancement of heterogeneity. The multistage karstification experienced by the Deng IV Member is the most favorable diagenesis for reservoir development. Based on the investigation of the fault characteristics in the target formation, it was found that it has experienced many tectonic movements, mainly the crustal ascending and descending movement. The folds are not strong and the structure is gentle. There are 22 faults with an extension of more than 10 km in the study area, which have a certain control effect on the tectonic pattern of the Gaoshiti-Moxi area. There are three groups of normal faults in the study area, including east–west direction, north-west direction and north-east direction, which are distributed in rows and belts. The faults are mainly north-west trending normal faults, with dip angles generally ranging from 60° to 80°.

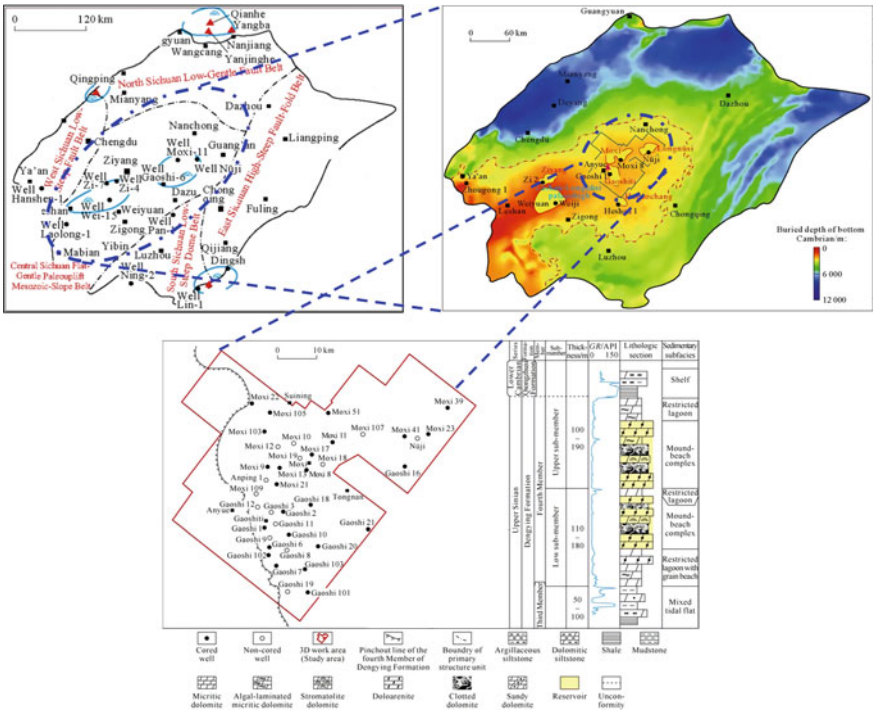

Fig. 1.1 Location of the Gaoshiti-Moxi area, shape of the Leshan-Longnüsi paleouplift, and stratigraphic characteristics of the Deng IV formation (modified after Jin et al., 2017; Li et al., 2013; Yang et al., 2016)

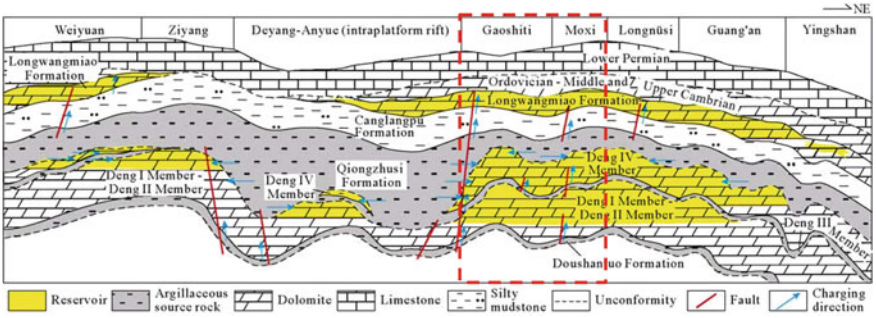

Fig. 1.2 Distribution of reservoir rocks and source rocks of the Sinian-Lower Cambrian in the Central Sichuan Paleouplift (modified after Yang et al., 2016)

1.1.2 Sedimentary Setting

In vertical, the Sinian system is composed of the Dengying Formation and the Doushantuo Formation, and the Dengying Formation can be subdivided into Deng I, Deng II, Deng III and Deng IV Members from bottom to top (Fig. 1.2). The main lithologic of the Deng I Member is algae poor dolomite that cannot store natural gas with industrial value. The Deng III Member is a temporarily developed shore-land facies clastic mudstone, which plays the role of a hydrocarbon source bed (Du et al., 2014). Compared with the Deng I and Deng III Members, the cyanobacteria of the Deng II and Deng IV Members are relatively enriched, thereby forming regional algae enrichment intervals. Consequently, the main lithology of the dominant reservoir rocks in ultradeep carbonate gas reservoirs include algae doloarenite and algae clotted dolomite (Fig. 1.2) (Li et al., 2013). The Deng IV Member of Sinian System in the Gaoshiti-Moxi area is the main carbonate gas reservoir under exploration and development at this stage. The Deng IV Member and the Deng III Member are in successive sedimentation and conformable contact. In contrast, the Deng IV Member is in unconformable contact with the overlying Maidiping Formation and Qiongzhusi Formation dominnated by limestone and mudstone. The Deng IV Member was eroded and pinched out in the western stratum because of the influence of the taphrogenic trough. The Deng IV Member was uplifted by the Tongwan Movement, and the residual thickness of the eroded stratum ranges from 280 to 380 m. The stratum tends to thin from north to south and from east to west. The Deng IV Member experienced two transgressive–regressive cycles, and it can be subdivided into two four-level sequences, namely the Deng IV upper submember and the Deng IV lower submember, based on lithology, electrical properties, sedimentary cycles and seismic sequence characteristics. The gas reservoirs are mainly distributed in the algal dolomite and grain dolomite in the middle-lower part of the upper submember and middle-upper part of the lower submember (Fig. 1.1) (Jin et al., 2017). In the sedimentary cycle, both the upper submember and lower submember of Deng IV Member show the basic characteristics of a gradual transition from algal mounds or

lagoons to moud caps from bottom to top. It could be seen from the section diagrams of connected wells that there is an obvious complementary relationship between the thickness of the upper and lower submembers in the Gaoshiti and Moxi areas (Fig. 1.3). The thickness of the upper submember is obviously thinner in the Gaoshiti area than in the Moxi area, whereas the lower submember is thicker in the Gaoshiti area and becomes thinner towards Moxi area. The thickness of the lower submember is generally stable because it has not been eroded, ranging from 130 to 200 m, while the residual thickness of the upper submember ranges from 90 to 220 m after being eroded.

The Deng IV Member is a platform margin facies, which can be sudivided into five microfacies, namely mound base, mound core, mound flat, mound cap and mound flank (Fig. 1.4). The dominant sedimentary microfacies of the upper and lower submembers are algae mud mound and grain beach, respectively. Therefore, the favorable combination of sedimentary facies of the Deng IV Member is a mound-beach complex: the mound cores are dominated by algal clotted dolomite and are rich in layered crystal cavities and fenestral structures, and the mound cap comprises algal stromatolite dolomite, and the mound wing comprises algal doloarenite.

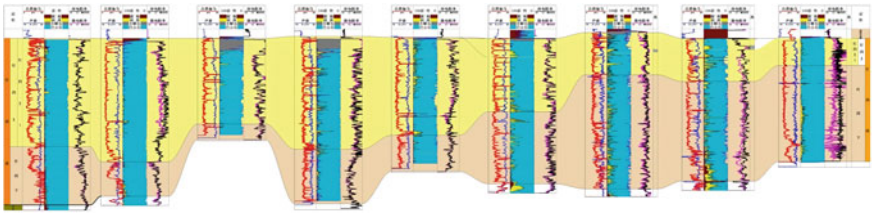

Fig. 1.3 Sectional diagram of connected wells in Deng IV Member gas reservoir

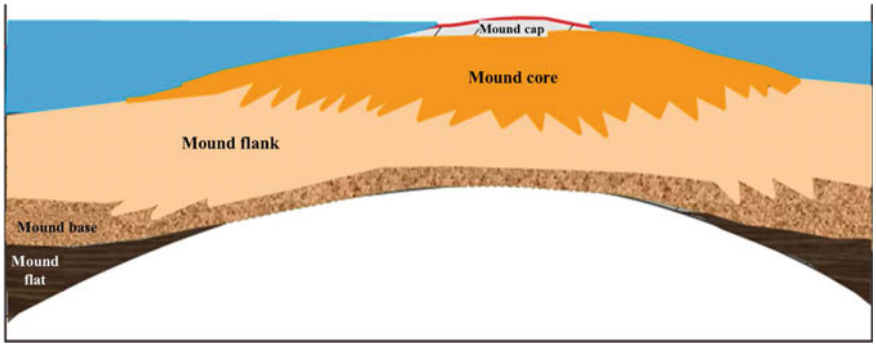

Fig. 1.4 Sedimentary model of mound-beach complex in Deng IV Member of Gaoshiti-Moxi area

1.2 Comprehensive Evaluation Method for Ultradeep Carbonate Gas Reservoirs

1.2.1 Samples and Testing Process

The development of multiscale pores, cavities and fractures in the Deng IV Member in the Gaoshiti-Moxi area leads to strong horizontal and interlayer heterogeneity of the gas reservoir. If only a small number of samples in some local areas are selected for investigation and analysis, the conclusion drawn cannot accurately describe the reservoir characteristics of the entire Deng IV Member. Therefore, it is necessary to select a certain number of carbonate cores from different depths of different gas wells to provide a large number of samples support for the investigation of pore structure characteristics. More than 600 plunger carbonate core samples with a diameter of 25 mm were used to study the reservoir characteristics, storage and percolation capacities of ultradeep carbonate gas reservoirs of the Deng IV Member. These core samples were taken from more than 30 wells in the Deng IV Member, and the coring depth ranges from 4950 to 5500 m. Although these core samples were taken from the upper submember and lower submember of Deng IV Member, the two submembers were not analyzed separately. This is because the sedimentary facies, rock types and pore characteristics of the upper and lower submembers are similar and can be studied as a whole. Logging data and producing tests show that there is no external water body in the Deng IV Member, and the water production of gas wells is relatively small. Therefore, most of the samples were taken from gas layers, and a small part of the samples were taken from water-bearing gas layers.

These samples were used for a variety of measurements, namely, conventional petrophysical measurements (649 samples), casts thin section analyses (48 samples), scanning electron microscopy tests (36 samples), high pressure mercy injection tests (24 samples) and multiscale CT scanning experiments (4 samples). It should be noted that the selection of samples in different types of tests is logical. Firstly, all samples were subjected to conventional petrophysical measurements to obtain basic data such as length, diameter, weight, porosity and permeability. In addition, all samples were photographed for morphological observation. Subsequently, samples with different porosity ranges and different permeability ranges were selected for casting thin section (CTE) and scanning electron microscopy (SEM) tests to ensure the representativeness of the research results. The information about the lithology type, reservoir space characteristics and filled mineral composition could be obtained by analyzing the CTE images. The information about the type, size, distribution, coordination number, and filling mineral of pores and throats could be obtained by analyzing the SEM images. Then, 24 samples with different combinations of pores, cavities and fractures were selected for high pressure mercury injection (HPMI) testing based on the pore throat characteristics obtained from the CTE and SEM tests. Different capillary pressure curves and pore throat characteristic parameters obtained by HPMI test can assist in the reservoir type classification of ultradeep carbonate gas reservoirs with strong heterogeneity. Finally, four types of typical

samples were selected for multiscale computed tomography (CT) scanning based on the classification results of the CTE, SEM and HPMI tests. CT scanning can provide a large number of high-resolution two-dimensional (2D) images of pore throat structure. The reconstructed three-dimensional (3D) topology network model can provide many valuable quantitative parameters of pore throat structure, including pore throat radius, pore throat volume, pore throat distribution, throat length, coordination numbers, fracture number and fracture aperture. In addition, the temperature and pressure data of the Deng IV Member reservoir were analyzed based on the field tests of some gas wells. The properties and components of natural gas and formation water were obtained through laboratory tests. Furthermore, the distribution characteristics of reservoir thickness were studied based on the logging interpretation results.

1.2.2 Conventional Petrophysical Measurements

A total of 649 carbonate samples were first selected for conventional petrophysical measurements. However, the traditional gas measurement method cannot accurately measure porosity and permeability data for ultradeep carbonate core samples. Therefore, helium porosimeter (UltraPore-300, Core Lab, USA) and overburden pulse permeability meter (PDP-200, Core Lab, USA) were used to determine the porosity and permeability of the samples, respectively (Fig. 1.5). The advantage of using helium to measure sample porosity is that it avoids personal error caused by the weighing process and the insufficient saturation after vacuuming. In addition, tiny and inert helium molecules can enter microscopic pores that nitrogen molecules cannot, without corroding or trapping in the pores. The advantage of using overburden pulse method to measure sample permeability is that the measurement accuracy can reach 1×10^{-5} mD. Besides, when the Klinkenberg permeability is greater than 1×10^{-4} mD, the pulse permeability at a test pressure of 1000 psi is the real Klinkenberg permeability, and therefore no correction is required. The conventional petrophysical measurement process was conducted according to the National Standard GB/T 29172-2012 of the P.R. of China.

1.2.3 Casting Thin Sections

The lithologies, mineral compositions and reservoir spaces of 48 polished thin sections of carbonate cores were observed and analyzed through an polarizing microscope (Axioskop 40 Pol, Zeiss, Jena Germany). Firstly, casting thin sections with dimensions of 20 mm × 20 mm × 5 mm were fabricated and impregnated with blue epoxy resin for distinction of pores and matrix. Then, these thin section were ground to a thickness of 0.03 mm before being observed under a polarizing microscope. Furthermore, GSA Image Analyse software was used to analyze microscopic images

(a) Helium porosimeter (b) Overburden pulse permeability meter

Fig. 1.5 Equipments for measuring the porosities and permeabilities of carbonate core samples

of these thin sections, including the size and shape of pore throats, surface porosity, mineral composition and filling conditions. The fabrication process of casting thin sections refer to the Industry Standard SY/T 5913-2004 of the P.R. of China. The test and analysis procedure of casting thin sections is based on the Industry Standard SY/T 6103-2019 of the P.R. of China. The ambient temperature and humidity were maintained at 23 °C and 35%, respectively. The classification basis of carbonate pore types is referred to the research of Choquette and Pray (1970).

1.2.4 SEM Testing

36 core samples were used for SEM testing to observe and analyze the pore throat types and structural characteristics of ultradeep carbonate gas reservoirs. Firstly, all core samples were cut into slices with dimensions 10 mm × 10 mm × 5 mm, and a thin gold layer was plated on the polished surface using an ion-sputtering apparatus (EM SCD500, Leica, Wetzlar Germany). Then, a scanning electron microscope (SU8010, Hitachi, Tokyo Japan) was used to conduct SEM tests according to the National Standard GB/T 17361-2013 of the P.R. of China. The working distance and acceleration voltage were set to 9–11 mm and 0.1–30 kV, respectively. The ambient temperature and humidity were maintained at 23 °C and 35%, respectively.

1.2.5 HPMI Testing

The HPMI testing is usually used to quantitatively study the pore throat size and its distribution (Jiao et al., 2020). However, the mercury conformance and the ink-bottle effect could cause errors in HPMI test results, which has been verified by several studies (Okolo et al., 2015; Peng et al., 2017; Schmitt et al., 2013; Zhang

et al., 2018). Mercury conformance is a phenomenon in which mercury fills the surface irregularly during the initial stage of mercury intrusion, resulting in inaccurate mercury saturation values. Therefore, the original data obtained by HPMI test must be corrected before analysis according to the Industry Standard SY/T 5346-2019 of the P.R. of China. Mercury requires external injection pressure to overcome capillary forces to enter the pore throat system. The ink-bottle effect means that the mercury actually overcomes the capillary resistance generated by the neck entrance size rather than the actual pore size. This is the reason why the pore size distribution measured by HPMI test is lower than the actual situation. It is widely known that the mercury withdraw efficiency cannot reach 100%, and the greater the difference between the pore size and the throat size, the lower the mercury withdraw efficiency. It reflects that a large amount of mercury is trapped in the pore throat system (Zhang et al., 2018). Therefore, the size of some large pores is underestimated because they are mistaken for small pores or throats. Although there are certain errors in the investigation of pore throat size, the HPMI method provide valuable evaluations of porosity, permeability, displacement pressure, median pressure, skewness coefficient, variable coefficient, homogeneity coefficient, and maximum mercury saturation. These parameters could directly or indirectly reflect the storage and percolation capacities of carbonate core samples (Lai et al., 2018; Li et al., 2018).

24 typical core samples were used for HPMI testing on a mercury porosimeter (AutoPore IV 9500, Micromeritics, USA). These samples need to be pretreated before HPMI testing, including washing with ethanol and then vacuum drying at 150 °C for at least 12 h. The purpose of this HPMI test, unlike previous studies, is to classify carbonate core samples rather than determine the size and distribution of pore throats. Core classification based on HPMI test results can provide a basis for selecting representative samples for multiscale CT scanning. More importantly, it is convenient to compare and analyze the pore structure characteristics, storage and percolation capacities of different types of ultradeep carbonate reservoirs (Wang et al., 2017). Ultimately, the carbonate core samples are divided into four types, namely matrix type, pore type, cavity type and fracture-cavity type according to the capillary pressure curves and related parameters.

1.2.6 Multiscale CT Scanning

Four types of carbonate core samples were selected for multiscale CT scanning experiments based on the classification results of the HPMI test. The purpose of CT scanning is to reconstruct the 2D and 3D pore throat structures of various types of carbonate core samples, and to quantify the value and distribution of pore throat radius, pore throat volume, coordination numbers, cavities and fractures. The principle of CT scanning is to use conical X-rays to penetrate the core sample, and then magnify the image through objective lenses of different magnifications. Finally, a large number of X-ray attenuation images obtained by 360-degree rotation are used to reconstruct a 3D microscopic model (Fig. 1.6). Carbonate samples contain both

Fig. 1.6 MicroXCT-200 micron CT scanner and CT scanning imaging schematic diagram

millimeter-scale cavities and fractures, as well as micron-scale pores and throats. Therefore, CT scanning experiments conducted at only one resolution scale cannot fully reflect the characteristics of multiscale storage and percolation media (Bai et al., 2013; Luo et al., 2017). In this study, CT scanning experiments were performed on the four types of carbonate samples at two resolution scales of 13.15 μm and 0.98 μm, which were used to observe and analyze large-scale and small-scale pore throat structures, respectively. CT scanning experiments at two resolution scales were conducted on a micron-CT scanner (MicroXCT-200, Zeiss, Germany). This scanner is suitable for samples with a diameter of 1–70 mm, with a working voltage of 40–150 kV and a resolution of 0.7–40 μm. These core samples (25 mm diameter × 45 mm length) were initially scanned with a resolution of 13.15 μm, and then they were cut into small samples (1.38 mm diameter × 3.35 mm length) for 0.98 μm resolution scanning.

In order to improve the modeling efficiency of pore throat network and ensure the ensure the accuracy of the pore throat distribution and connectivity, the "maximum-ball" method was selected to extract and reconstruct the topology of pore throat network in core samples (Al-Kharusi & Blunt, 2007; Silin et al., 2008). The principle of "maximum-ball" method is to fill all pore throats in the reconstructed digital model with variable size spheres at one time, and then these spheres adapt to the space by changing their diameters. Ultimately, the complex pore throat structures of a carbonate core sample could be characterized by a series of overlapping and containing spheres (Fig. 1.7a). The CT scanning differs from the HPMI test in that it can accurately differentiate between pores and throats. The determination of "pore" and "throat" in the digital model is achieved by finding the local maximum spheres and the minimum sphere between the two maximum spheres, thereby forming the pairing relationship of "pore-throat-pore" (Fig. 1.7b). Ultimately, the entire irregular pore throat system is quickly simplified into a regular digital pore throat network model through the ball-string structure. In order to visually distinguish between pores and throats in the digital network structure, the balls in the model represent the pores, the sticks represent the throats. The diameter of the ball reflects the size of the pore, and the length and diameter of the stick reflects the size of the throat.

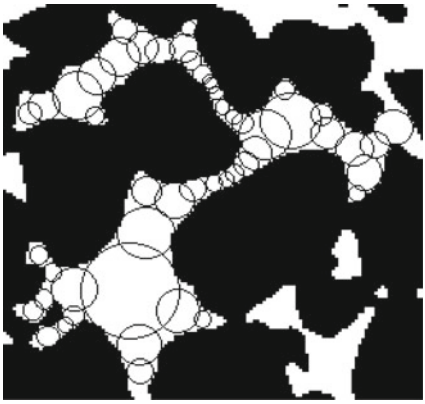

(a) Spheres of different sizes fill pore throats

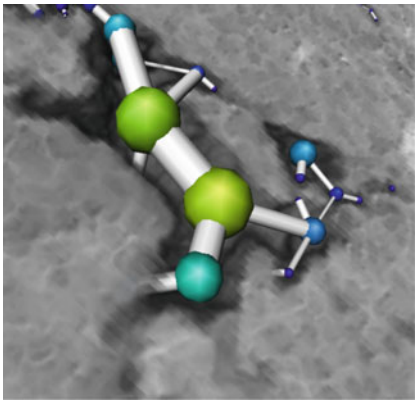

(b) Schematic diagram of the "ball-stick" model

Fig. 1.7 Extraction of pore throat network topology based on the "maximum-ball" method

Furthermore, the number of sticks connected to a ball is the coordination number that describes the pore throat connectivity. Balls that are not connected by sticks are considered as invalid pores. Therefore, the reconstructed 3D digital network model is also vividly called the "ball-stick" model.

The process of 3D digital network model reconstruction and pore throat structure characteristics analysis based on CT scanning is as follows (Wang et al., 2020): (a) analysis of apparent pores, cavities and fractures characteristics based on 2D CT scanning images; (b) select a high scanning quality and representative region to reconstruct the 3D digital network model; (c) smooth the selected sample to avoid noise effects during segmentation; (d) divide the 3D model into black pore space and white carbonate matrix; (e) calculation of basic pore parameters based on the image segmentation results, e.g., total porosity, connected porosity and pore throat radius; (f) extraction of pore throat network model using iCore software (iCore, Gothenburg Sweden) based on the "maximum-ball" method; (g) divide the extracted pore throat network model into a pore network model and a throat network model; (h) quantify the values and distributions of pore throat radius, volume and coordination number based on the extracted pore throat model, pore model and throat model; (i) Construction and analysis of a fracture network model (Fig. 1.8).

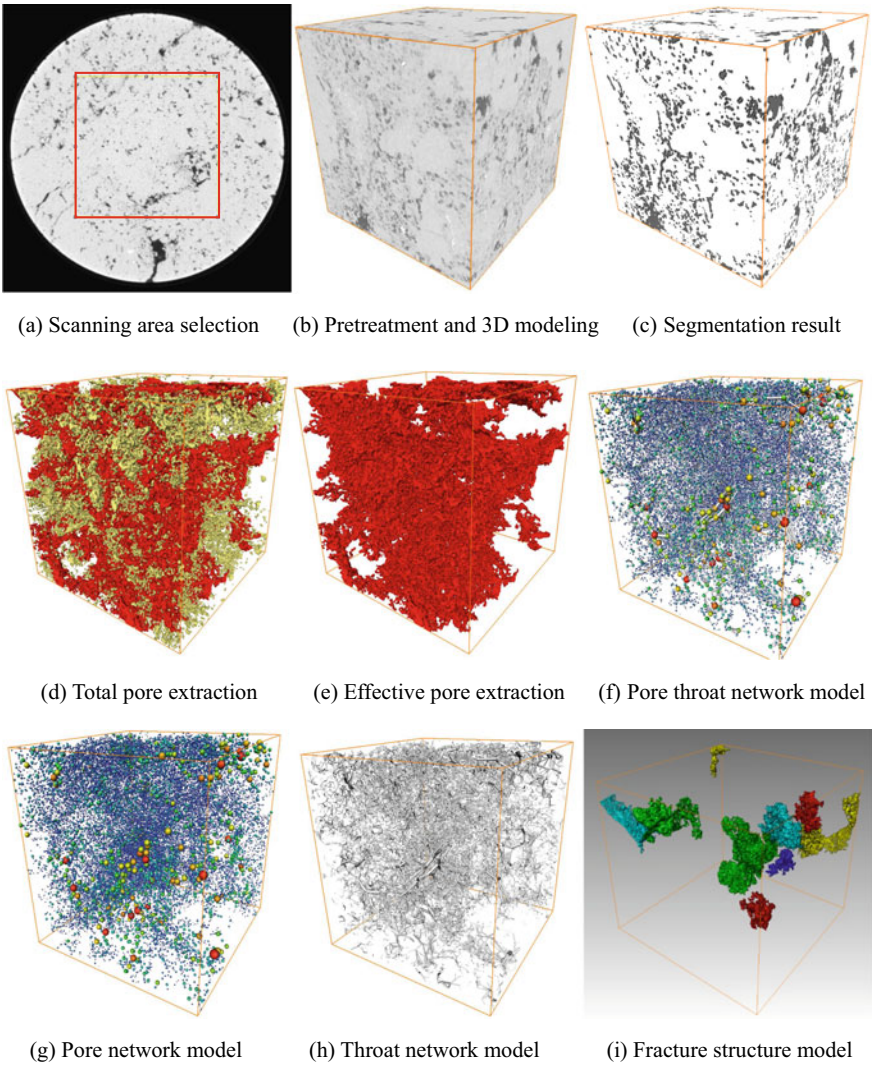

(a) Scanning area selection (b) Pretreatment and 3D modeling (c) Segmentation result

(d) Total pore extraction (e) Effective pore extraction (f) Pore throat network model

(g) Pore network model (h) Throat network model (i) Fracture structure model

Fig. 1.8 3D digital network model reconstruction and pore throat structure characteristic analysis process

1.3 Reservoir Characteristics of Ultradeep Carbonate Gas Reservoirs

1.3.1 Lithology and Mineral Composition of Reservoir Rocks

According to the comprehensive analysis based on core description (Fig. 1.9), petrochemical analysis, thin section identification (Fig. 1.10) and logging data, it could be found that the Deng IV Member carbonate gas reservoir is entirely developed in dolomite, and the dominant types of carbonate rocks are algal clotted dolomite, algal stromatolite dolomite and algal doloarenite. As shown in Fig. 1.11a, the most important reservoir rock in the ultradeep carbonate gas reservoir is algal clotted dolomite, accounting for 70.34% of all reservoir rocks. Algal clotted dolomite was significantly affected by karst reconstruction, and its dominant storage space is the residual pores between the clots and the later dissolved pore-cavities. The surface porosity of the samples is mainly distributed between 3 and 6%, and some pores and cavities were partially filled with asphalt or dolomite. Algal stromatolite dolomite is the second most common reservoir rock, accounting for 15.49% of all reservoir rocks. Algal stromatolite dolomite was obviously affected by bedding dissolution, and its dominant storage space is the bird's eye or fenestriform pore-cavities formed after the decay of algal filaments. The dissolution pores and cavities are developed in algal stromatolite dolomite, and the surface porosity of the samples is mainly distributed between 4 and 8%. Algal doloarenite was formed from sand grains in the algae growing environment. The dominant storage space is the interparticle dissolution pores. The similar sedimentary facies of the upper and lower submembers lead to similar petrological characteristics of the two submembers, and their reservoir rocks are still dominated by the above three lithologies. Although both the upper and lower submembers are dominated by algal clotted dolomite, the proportions of algal stromatolite dolomite and algal doloarenite are different. The content of algal clotted dolomite in the lower submember is higher than that in the upper submember, whereas the development of algal stromatolite dolomite is lower than that in the upper submember (Fig. 1.11b, c). These typical storage spaces and filling materials could also be clearly found in some images obtained from CTS and CT scanning tests.

In addition, the average porosity of carbonate core samples with different lithologies was compared and analyzed, as illustrated in Fig. 1.12. Algal clotted dolomite, algal stromatolite dolomite and algal doloarenite are not only highly developed, but their storage capacity is also better than other types of reservoir rocks, laying the foundation for the formation of high-quality gas reservoir in the Deng IV Member.

The mineral compositions of the samples taken from different depths in the three regions of the Deng IV Member were counted based on the analysis of casting thin sections, and the results are shown in Fig. 1.13. Dolomite is the dominant mineral in the Deng IV Member, and its content percentage is 75–96%, with an average of 88.63%. Although clay minerals were found in all samples, the content percentage is relatively low, only ranging from 1.07 to 3.94%, with an average of 1.43%. Organic matters were detected in all samples, but the percentage content of different samples

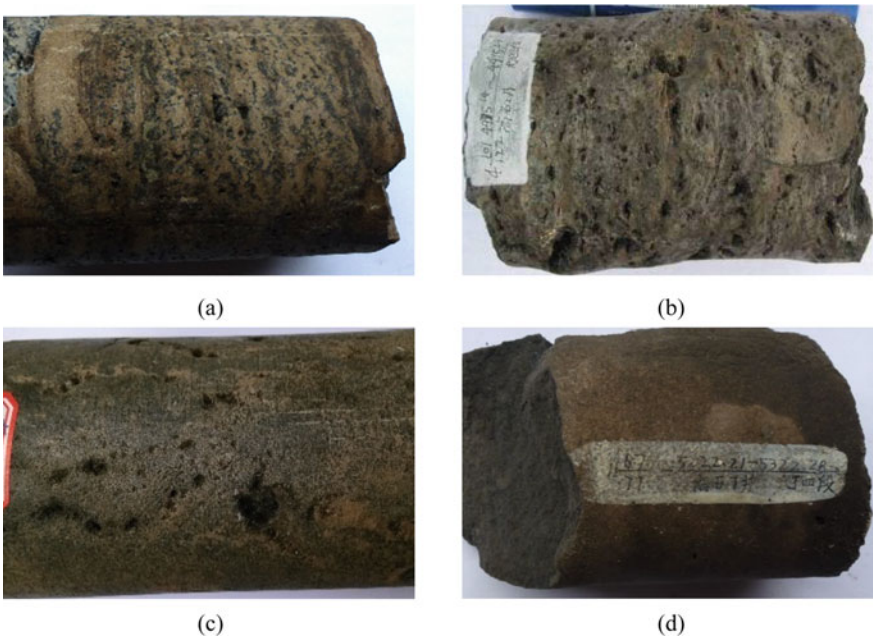

Fig. 1.9 Photographs of the main lithologies of carbonate reservoir rocks: **a** algal clotted dolomite filled with asphalt; **b** algal stromatolite dolomite with fenestriform and dissolution pore-cavities; **c** algal doloarenite with dissolution pore-cavities; **d** algal doloarenite with tiny pores

was quite different, ranging from 0.97 to 10.05%, with an average of 4.31%. The percentage of silicide content also varied greatly, ranging from 0 to 14.13%, with an average of 4.38%. Pyrite was only observed in six samples, and its content percentage is extremely low, ranging from 0 to 4.89%, with an average of 1.25%. Therefore, it could be concluded that the minerals in different regions of the Deng IV Member are relatively homogeneous.

1.3.2 Petrophysical Properties

The two most important parameters in petrophysical properties are porosity and permeability, which could directly reflect the reservoir storage capacity and percolation capacity, respectively (Zhang et al., 2015). Therefore, porosity and permeability data for 322 carbonate core samples were measured and plotted in Fig. 1.14. It can be seen from the figure that although the relationship between porosity and permeability of each sample is quite different, it shows the characteristics of regional distribution as a whole. The porosity of the Deng IV Member samples ranges from 2.00 to 13.90%, mainly distribute in 2–6%, with an average of 3.91%. The permeability of the Deng IV Member samples ranges from 0.0004 to 8990 mD, mainly distribute in 0.01 to

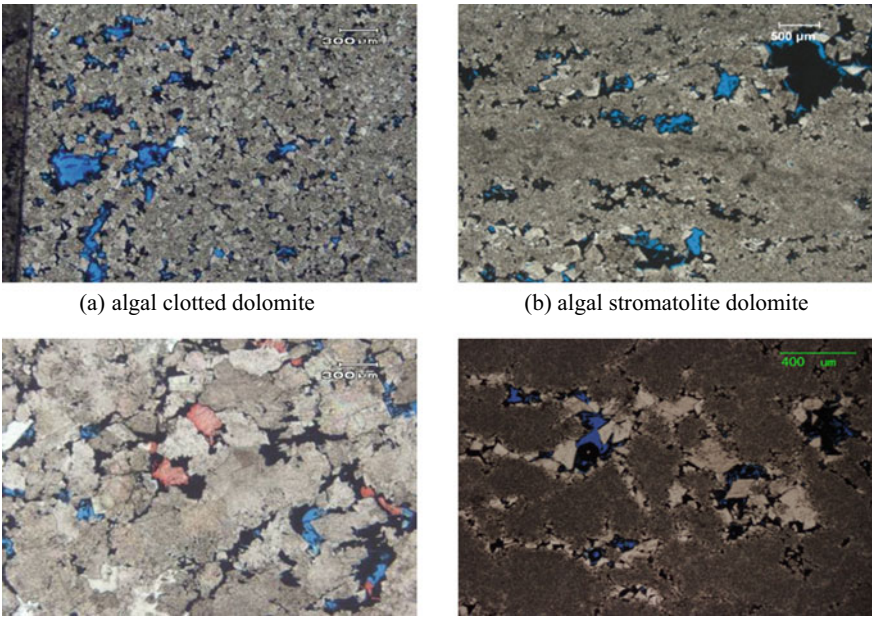

(a) algal clotted dolomite (b) algal stromatolite dolomite

(c) algal doloarenite or algal gobbet dolomite (d) sparry doloarenite

Fig. 1.10 Casting thin sections of the main lithologies of carbonate reservoir rocks

10 mD, with an average of 1.02 mD. The Deng IV Member should be classified as an ultralow to low porosity and low permeability gas reservoir according to the classification standards of natural gas reservoirs of the People's Republic of China (GB/T 26979-2011). Although most of the carbonate samples are tight (porosity < 6%, permeability < 1 mD), the porosity and permeability of a few samples can reach the ranges of 8–14% and 10–10,000 mD, respectively. The large distribution range of petrophysical properties is caused by the development of cavities and fractures, reflecting the strong heterogeneity of the Deng IV Member gas reservoir. However, there is little difference in petrophysical properties between the Gaoshiti area and Moxi area of the Deng IV Member reservoir.

The samples were divided into cores with fractures and cores without fractures to investigate the effect of fractures on the correlation between porosity and permeability (Fig. 1.14). The results show that the porosity and permeability of the cores without fractures have a strong correlation. Cavities can only improve the porosity and permeability of the reservoir simultaneously, and have little effect on the correlation between the two. The dominant percolation channel of these samples is throats. In contrast, the dominant percolation channel for the cores with fractures is the fracture, resulting in high permeability properties at low porosity. Therefore, the development of fractures is the dominant reason for the poor correlation between porosity and permeability.

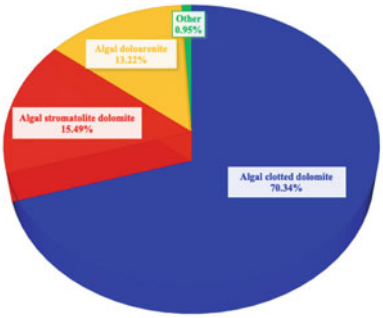

(a) Proportion of different types of lithology in the Deng IV Member

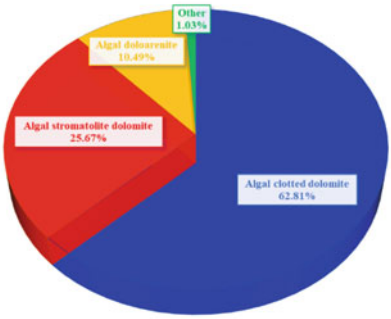

(b) Proportion of the upper submember

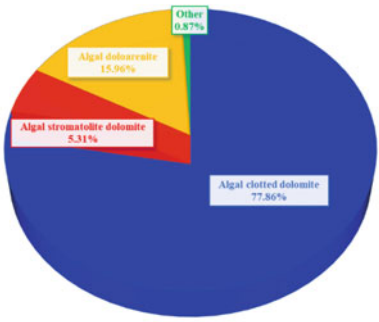

(c) Proportion of the lower submember

Fig. 1.11 Statistical results of proportion of various types of lithology

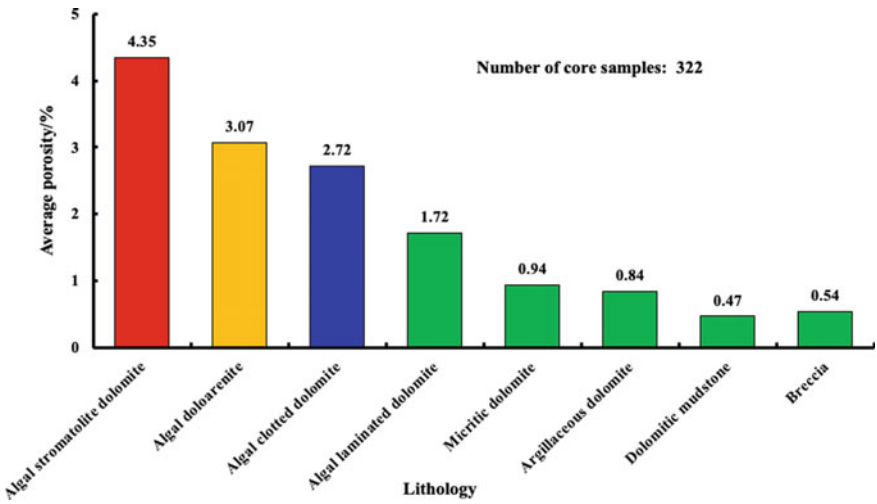

Fig. 1.12 Average porosity of different types of lithology in the Deng IV Member ultradeep carbonate gas reservoir

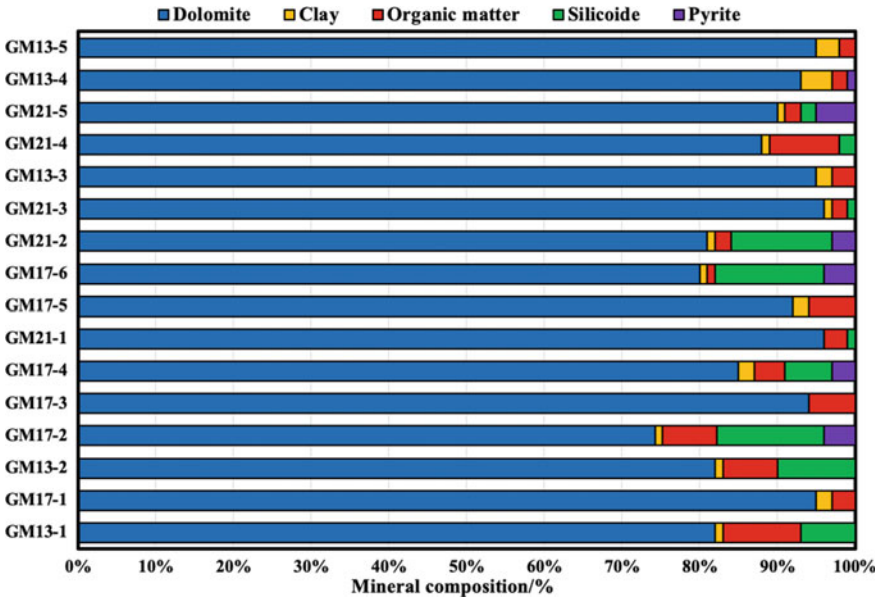

Fig. 1.13 Mineral composition in different regions of the Deng IV Member gas reservoir

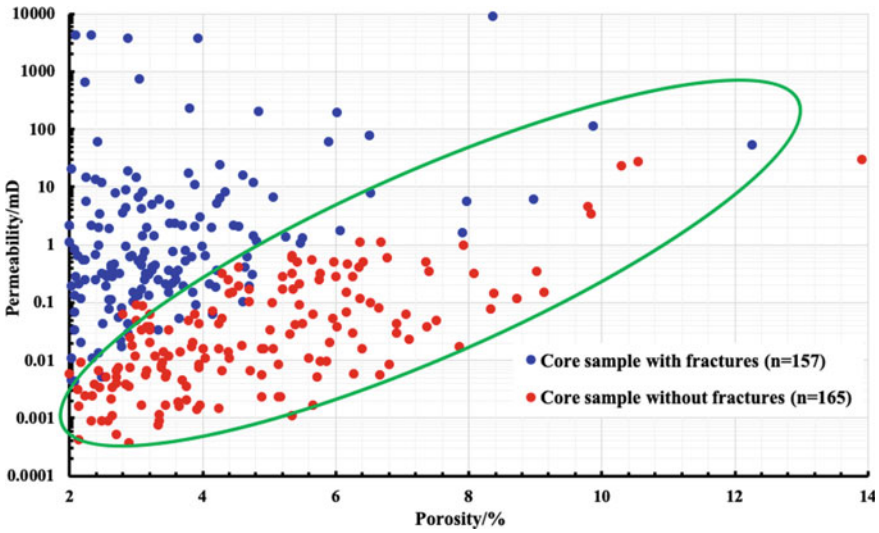

Fig. 1.14 Scatter plot of porosity and permeability of samples in the Deng IV Member reservoir

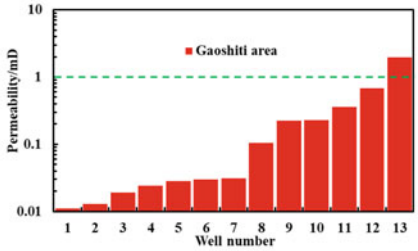

(a) Permeability data in the Gaoshiti area

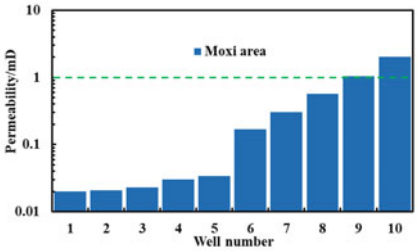

(b) Permeability data in the Moxi area

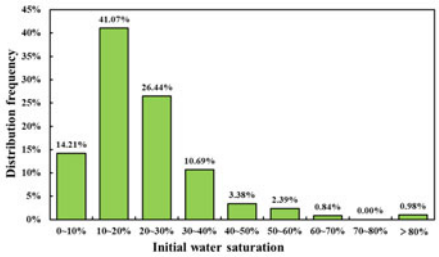

(c) Distribution frequency histogram of initial water saturation

Fig. 1.15 Permeability and initial water saturation explained by well logging data in the Deng IV Member reservoir

In conclusion, the petrophysical properties of the Deng IV Member reservoir are generally low porosity and low permeability, and high porosity and high permeability intervals are developed locally. The development of cavities and fractures in carbonate reservoirs reflects that the dominant reservoir type is fracture-cavity type. In addition, the permeability data of some gas wells explained by well logging was collected, as shown in Fig. 1.15a, b. It indicates that the Deng IV Member is dominated by low-permeability reservoirs with permeability less than 1 mD, and the vertical and horizontal heterogeneity of the reservoir is extremely strong.

In addition, the initial water saturation of the samples was analyzed based on the well interpretation data of well logging, as shown in Fig. 1.15c. The initial water saturation of the Deng IV Member reservoir ranges from 2.17 to 89.56%, mainly distribute in 10–30%, with an average of 23.26%. The initial water saturation in the high-permeability area with developed fractures is relatively low, while that in the low-permeability area with developed microscopic pores is relative high. The relatively low average initial water saturation means that the movable water content of the Deng IV Member reservoir is less. Therefore, the inhibiting effect of a small amount of movable water on the percolation capacity of gas phase is weak during the gas reservoir exploitation. However, some reservoirs with relatively high initial water saturation were discovered as the exploration and exploitation of the Deng IV Member gas reservoir move forward. Therefore, it is necessary to study the percolation characteristics and capacity of the gas phase under different water content conditions. These studies are specifically introduced in subsequent chapters.

1.3.3 Reservoir Space Types and Characteristics

Through the observation and analysis of CTS images, the reservoir space of the Deng IV Member can be divided into three categories, namely pores, cavities and fractures, according to the classification standards of carbonate reservoir space type (Choquette & Pray, 1970). The reservoir space of the Deng IV Member can also be subdivided into more types, including interparticle (interP) dissolution pores, intraparticle (intraP) dissolution pores and intercrystal (interC) dissolution pores that are controlled by fabric, as well as dissolution cavities, dissolution fractures and structural fractures that are not controlled by fabric. The development frequencies of various types of reservoir spaces are summarized in Table 1.1. The detailed characteristics of these reservoir spaces are then introduced according to the classification.

(1) The pores of the Deng IV Member are composed of interP (dissolution) pores, interC (dissolution) pores, intraP dissolution pores, fenestriform pores and nonfabric selectivity dissolution pores. The formation of these pores is mainly related to the preservation of interP or fenestriform pores, early diagenetic dissolution and multistage burial karst superimposition. The analysis results of CTS show that secondary pores dominated by interP dissolution and interC dissolution pores are the most significant types of reservoir space, followed by interC, interP and fenestriform pores (Fig. 1.16). The primary interP pores were formed under the support of the particles themselves after the original accumulation of carbonate particles. The development degree of interP cement directly affects the preservation degree of interP pores. Therefore, the interP pores were preserved

Table 1.1 Development frequency of various types of reservoir spaces in the Deng IV Member

Reservoir space			Frequency
Pore	Primary pore	Residual interP pore	Low
		Fenestriform pore	Low
	Secondary pore	InterP dissolution pore	High
		IntraP dissolution pore	Moderate
		InterC pore	Moderate
		InterC dissolution pore	High
Cavity	Primary cavity	Fenestriform cavity	Moderate
	Secondary cavity	Dissolution cavity	High
Fracture	Primary fracture	Structural fracture	Low
	Secondary fracture	Dissolution fracture	Moderate

to form residual interP pores when the cement is not developed or the content is quite small. InterP cements or some particles themselves were affected by acidic fluid dissolution or meteoric fresh water leaching-percolation to form interP dissolution pores after multiphase reformation and expansion. Therefore, the interP dissolution pores are the preservation and expansion of primary interP pores. The preservation of interP dissolution pores is mainly because of the filling of oil and gas, which changes the internal ion environment of pores and is not suitable for cementation. The phenomenon of the generally developed asphalt membranes at the edges of interP dissolution pores is a good demonstration of this process (Fig. 1.16a). The interC pores are mainly developed in the algal clotted dolomite with strong recrystallization and primary rock fabric severe destruction. Most of the interC pores are regular triangles, and some of them formed interC dissolution pores under the action of multistage dissolution (Fig. 1.16b). IntraP dissolution pores are commonly found in sparry algal doloarenite and doloarenite, which were formed by the selective dissolution of algal aromatics or aromatics (Fig. 1.16c). These pores could be called moldic pore when the outer contour of particles are well preserved. The intraP pores are generally small and poorly connected, and they need to be connected to the external reservoir space through later fractures or residual interP pores. Fenestriform pores are mainly developed in algal clotted dolomite and algal stromatolite dolomite (Fig. 1.16d). Although the storage capacity of fenestriform pores is better than other types of pores, their improvement in reservoir space is limited because the overall number is small. Both the upper and lower submember of the Deng IV Member reservoir are dominated by interP pores, interC pores and fenestriform pores. Therefore, the Deng IV Member reservoir could be studied as a whole because the sedimentary facies, petrophysical characteristics and pore types of the upper and lower submembers are similar.

(2) Different sizes and morphologies of primary fenestriform cavities and secondary dissolution cavities are generally developed in the Deng IV Member reservoir, and they are important supplements to the reservoir space. These cavities are layered or distributed along fractures, with oblate, elliptical, stripped, droplet and irregular shapes (Figs. 1.10b, c, and 1.17a, g). In order to quantify the development frequency of cavities in different areas of the Deng IV Member reservoir, the number of cavities per unit length of core samples from different wells is summarized in Fig. 1.18. It shows that the development frequency of cavities ranges from 11 per meter to 37 per meter, with an average of 24.67 per meter. These data indicate that the development degree of cavities in the Deng IV Member is relatively high, but there are obvious differences in different well areas. The statistical results of the size and number of cavities shows that the Deng IV Member reservoir is dominated by small cavities (78%) with a diameter of 2–5 mm and medium cavities with a diameter of 5–20 mm (15%). Large cavities with a diameter greater than 20 mm (7%) only locally developed. Most of the wells experienced mud loss at the top of the reservoir, but few wells experienced drilling breaks, which also proved that large cavities are not

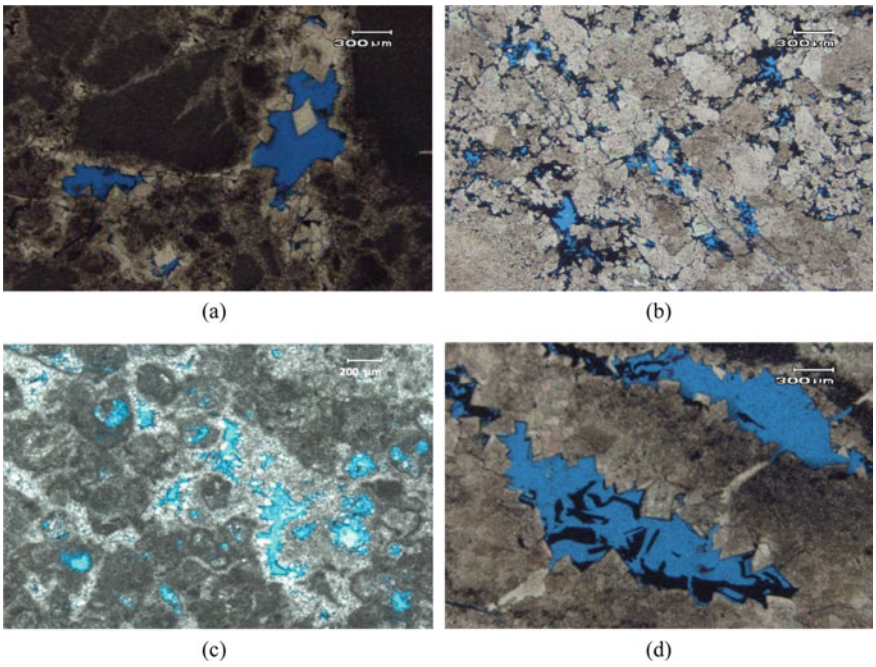

Fig. 1.16 Images of casting thin sections with different pore types: **a** InterP dissolution pores in algal doloarenite; **b** InterC pores and interC dissolution pores in fine-crystalline dolomite; **c** IntraP dissolution pores in doloarenite; **d** elongated fenestriform pores in algal clotted dolomite

developed. The poor contrast in the horizontal direction indicates that cavities are unevenly distributed in the plane.

(3) Various types of fractures are extensively developed in the Deng IV Member, and they effectively enhance the percolation capacity of the reservoir. Observation and statistical results of core samples from several wells show that the fracture density ranges from 1.5 to 7.5 per meter, with an average of 3.1 per meter (Fig. 1.19). Fractures could be subdivided into three types according to their formation cause, namely structural fractures, pressolutional fractures and structural dissolution fractures. The structural fracture section is generally straight and most of them appear as high-angles (Fig. 1.17b, c). In contrast, the walls of dissolution fractures are curved and harbor-shaped by the dissolution of fresh water or groundwater, and some are even connected in series with the dissolution pores. However, the excellent percolation capacity of dissolution fractures is suppressed to a certain extent because of the semi-filling of asphalt or dolomite (Fig. 1.17f). The pressolution fractures mainly appear in the form of stylolites or networks, and their contribution to the percolation capacity is little because they are generally filled with mud (Fig. 1.17d, e). Statistical results based on CTS images show that the development frequency of fractures is 63%, of which

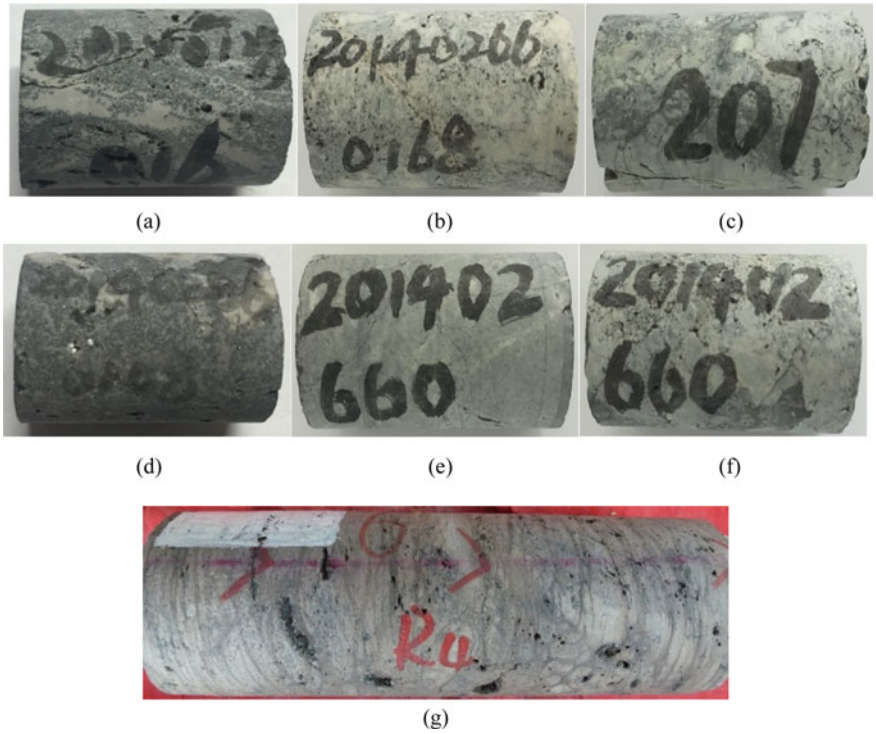

Fig. 1.17 Different types of cavities and fractures observed in core samples: **a** Fenestriform cavities and dissolution cavities; **b** high-angle structural fractures; **c** low-angle structural fractures; **d** stylolites; **e** pressolutional fracture network; **f** structural dissolution fractures; **g** bedding cavities

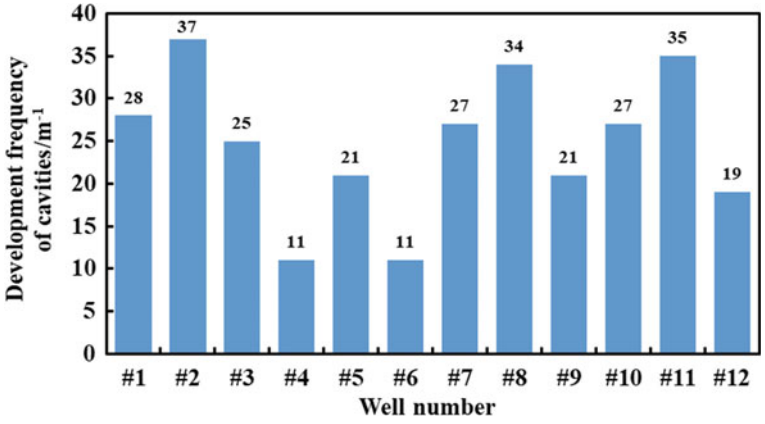

Fig. 1.18 Development frequency of cavities in different coring wells

structural fractures are dominant, according for 67% of the total number of fractures. The contribution of different types of fractures to the percolation capacity is different because of the different filling degree and development frequency (Table 1.2). The effective fractures that contribute significantly to the percolation capacity are mainly structural fractures partially filled with dolomite or asphalt and dissolution fractures distributed along the structural fractures.

In summary, the main reservoir spaces of the Deng IV Member are interP dissolution and interC dissolution pores. The primary fenestriform cavities and secondary dissolution cavities of different sizes are significant supplements to the reservoir space and further improve the storage capacity. Although widely developed fractures contribute little to the storage capacity, they can connect isolated pores and cavities

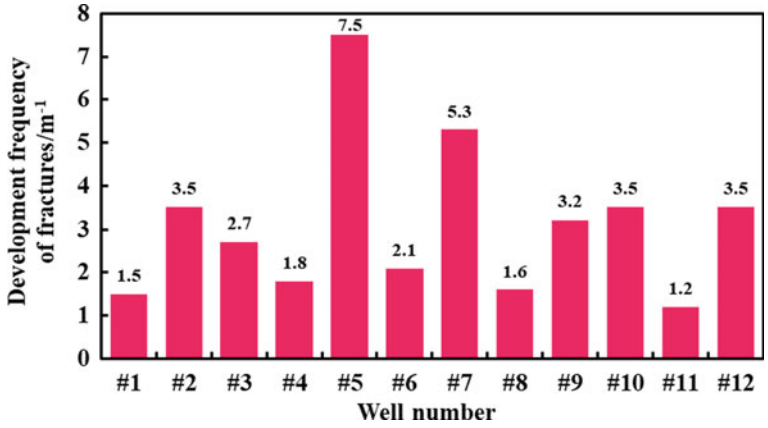

Fig. 1.19 Development frequency of fractures in different coring wells

Table 1.2 Development frequency of various types of fractures in the Deng IV Member and their contribution to percolation capacity

Category	Subcategory	Development frequency	Percolation contribution
Structural fracture	Fractures partially filled with asphalt	Locally developed	Moderate
	Fractures mostly filled with asphalt	Widely developed	Extremely small
	Fractures partially filled with dolomite	Commonly developed	Great
	Fractures without filling	Generally developed	Great
Pressolutional fracture	Network form	Widely developed	Moderate
	Stylolite form	Locally developed	Small
Structural dissolution fracture		Locally developed	Moderate

to effectively improve the percolation capacity. More information about cavities and fractures is presented in the SEM and CT scanning sections. Furthermore, the effect of pores, cavities and fractures on storage and percolation capacities were specifically analyzed in the subsequent sections.

1.3.4 Throat Types and Characteristics

The size and type of throat and its connectivity with pores directly affect the percolation capacity of the reservoir, especially for reservoirs with underdeveloped fractures. Therefore, the types and characteristics of reservoir throats in Deng IV Member were observed and analyzed by SEM images. The study area mainly developed three types of throats, namely necking, tubular and lamellar, as shown in Fig. 1.20. The necking throat is formed at the position where the pores are narrowed and has no obvious boundary with the pores. The enlarged part of the space is the pore, and the narrowed part of the space is the throat. The narrowing of the space is usually caused by the growth of crystals or the natural contact of particles. The necking throat is usually detected between the interP dissolution pores of the algal doloarenite, and is generally larger than 10 μm in width (Fig. 1.20a, c). The lamellar throat is formed between the dolomite crystal faces and usually connects the interC and interP pores. The width of lamellar throats is usually less than 1 μm, and they are widely distributed in crystalline dolomite reservoirs in the form of flakes (Fig. 1.20b). The tubular throat is a thin and long tube that connects two adjacent pores. The throat section is approximately circular and the width is commonly less than 10 μm. Tubular throats can be detected between the interP and intraP dissolution pores of doloarenite with strong cementation or compaction. In addition, some dissolution pores formed asphalt-contracted tubular throats because of asphalt filling (Fig. 1.20d). It could be found that the development frequency of necking throats and tubular throats is higher than that of tubular throats after analyzing many SEM images. In addition to the characteristics of pores and throats themselves, the connectivity between pores and throats also directly affects the storage and percolation capacities, which are specifically analyzed in the subsequent sections.

1.3.5 Reservoir Classification Based on HPMI Testing

HPMI tests are widely used to qualitatively and quantitatively investigate the characteristics and parameters of microscopic pore throat structures. Valuable information related to pore throats can be obtained directly or indirectly from mercury intrusion data and capillary pressure curves. In view of the fact that mercury conformance and ink-bottle effect can cause errors in the quantitative results of the HPMI test (Li et al., 2018), the capillary pressure curves of multiple samples were used only

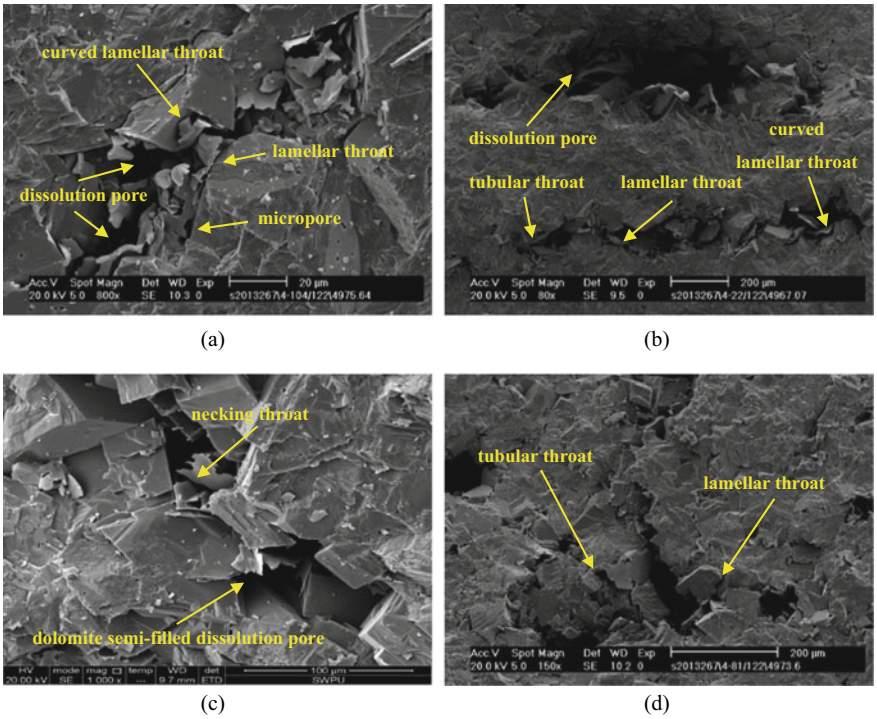

Fig. 1.20 Different types of pores and throats observed in SEM images: **a** Dissolution pores developed, lamellar and curved lamellar throats; **b** dissolution pores developed, tubular, lamellar and curved lamellar throats; **c** dolomite semi-filled dissolution pores, necking throats; **d** asphalt shrinkage tubular throats and lamellar throats

to qualitatively analyze the pore throat characteristics in our study. Then, reservoir classification standards were established based on these typical characteristic. Quantitative investigations on the pore radius and volume distribution, throat radius and volume distribution, and coordination number distribution of different types of reservoirs were conducted through multiscale CT scanning experiments.

The ultradeep carbonate gas reservoir was divided into four types of reservoirs based on the comprehensive analysis of the capillary pressure curves characteristics and other test results, namely matrix type, pore type, cavity type and fracture-cavity type (Wang et al., 2017). The lithology and petrophysical properties of the carbonate core samples used for HPMI testing are presented in Table 1.3. The capillary pressure curves of the 24 samples are illustrated in Fig. 1.21a. It could be seen from the figure that some capillary pressure curves are similar in morphology and value, indicating that these samples belong to the same reservoir type. Therefore, the 24 capillary pressure curves could be normalized into four types, representing four types of reservoirs (Fig. 1.21b).

Table 1.3 Lithology and petrophysical properties of carbonate core samples used for HPMI testing

Sample number	Lithology	Porosity/%	Permeability/mD	Category
#1	Algal clotted dolomite	2.03	0.006	Matrix
#2	Algal clotted dolomite	2.43	0.007	Matrix
#3	Algal clotted dolomite	2.11	0.003	Matrix
#4	Algal doloarenite	2.28	0.003	Matrix
#5	Algal clotted dolomite	2.34	0.002	Matrix
#6	Algal doloarenite	3.78	0.050	Pore
#7	Algal clotted dolomite	3.21	0.089	Pore
#8	Algal doloarenite	3.87	0.067	Pore
#9	Algal clotted dolomite	2.91	0.025	Pore
#10	Algal clotted dolomite	2.43	0.007	Pore
#11	Algal doloarenite	2.80	0.066	Pore
#12	Algal doloarenite	3.07	0.032	Pore
#13	Algal stromatolite dolomite	7.34	0.501	Cavity
#14	Algal stromatolite dolomite	6.01	0.279	Cavity
#15	Algal clotted dolomite	6.34	0.405	Cavity
#16	Algal stromatolite dolomite	5.32	0.182	Cavity
#17	Algal clotted dolomite	4.29	0.053	Cavity
#18	Algal clotted dolomite	4.71	0.107	Cavity
#19	Algal doloarenite	5.63	0.557	Cavity
#20	Algal clotted dolomite	4.66	0.626	Fracture-cavity
#21	Algal clotted dolomite	4.81	1.173	Fracture-cavity
#22	Algal stromatolite dolomite	5.25	1.376	Fracture-cavity
#23	Algal doloarenite	6.07	1.797	Fracture-cavity
#24	Algal clotted dolomite	5.06	6.796	Fracture-cavity

The type I capillary pressure curve reflects the pore throat characteristics of fracture-cavity type reservoirs. The minimum displacement pressure required for mercury to enter the reservoir space is usually around 0.1 MPa, reflecting that cavities and large pores are developed and well interconnected. Therefore, the threshold capillary resistance that mercury intrusion needs to overcome is relatively small. Subsequently, the saturation of mercury intrusion increases greatly as the mercury injection pressure increases from 0.1 to 1.0 MPa, and the type I curve shows an approximately horizontal stage with a gentle slope. This phenomenon reflects that the large pore throats of fracture-cavity type reservoirs are widely distributed and dominant. Therefore, a large amount of mercury enters the reservoir space within a low pressure range.

The type II capillary pressure curve with double-step characteristic reflects the pore throat characteristics of cavity type reservoirs. The two steps indicate that the reservoir has two different sets of pore throat systems, one is the cavities and coarse

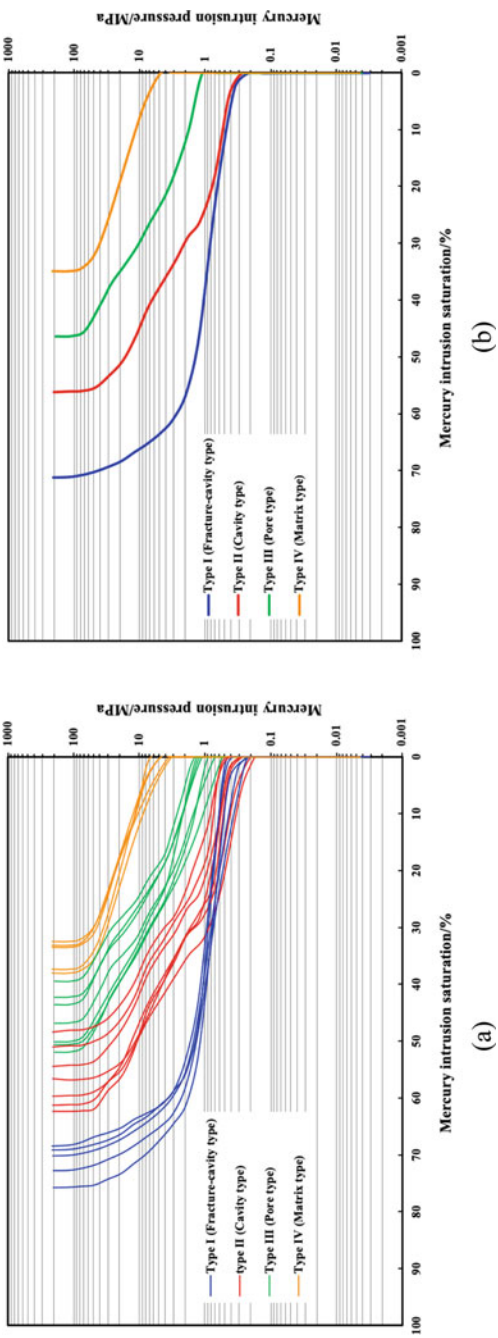

Fig. 1.21 Capillary pressure curves of four types of reservoirs in the Deng IV Member gas reservoir: **a** Capillary pressure curve of 24 samples; **b** normalized capillary pressure curves of four types of reservoirs

pores system, and the other is the fine pores and throats system. In the initial stage of mercury injection, the morphology of the type II curve is similar to that of the type I curve, except that the threshold value of the displacement pressure is slightly different. However, the cavity type requires higher injection pressure than the cavity-fracture type because the injected mercury can only enter small pores through throats in the intermediate and latter stages. Furthermore, the maximum mercury intrusion saturation of the normalized type I curve is 71.26%, which is higher than that of the type II curve. These differences indicate that fractures can effectively improve the connectivity of multiscale reservoir spaces, thereby allowing more natural gas in the reservoir space to participate in percolation under the same pressure conditions. This is also the reason why the Type I curve does not have the double-step characteristic. Therefore, the percolation capacity of fracture-cavity type reservoirs is stronger than that of cavity type reservoirs, but there is little difference in the storage capacity between the two (Wang et al., 2018a, 2018b).

The type III capillary pressure curve reflects the pore throat characteristics of pore type reservoirs. The threshold displacement pressure of pore type reservoirs is around 1.0 MPa, which is higher than that of cavity type and fracture-cavity type reservoirs. It reflects that the reservoir spaces and percolation channels are dominated by pores and throats with relatively small radii, respectively. Therefore, mercury requires higher injection pressure to overcome stronger capillary resistance to enter the reservoir space. The maximum mercury saturation of the normalized type III curve is 46.43%, which is 10% lower than that of the type II, reflecting that more than half of the reservoir space is ineffective or difficult to use. However, the maximum mercury saturation of several pore type samples is similar to that of cavity type samples, revealing that the pore throat size of some pore type reservoirs is small but widely distributed. Therefore, the storage and percolation capacities of pore type reservoirs are weaker than those of cavity type and fracture-cavity type reservoirs.

The type IV capillary pressure curve reflects the pore throat characteristics of matrix type reservoirs. The normalized threshold displacement pressure is 5 MPa, and the maximum mercury saturation is only 34.97%. Compared with the other three types of reservoirs, the reservoir space of matrix type reservoirs is dominated by ineffective tiny pores, and the connectivity between pores and throats is poor. Therefore, matrix type reservoirs are usually classified as reservoirs without development value.

In summary, ultradeep carbonate gas reservoirs with widely developed cavities and fractures can be classified into the above four types of reservoirs with typical pore throat structure characteristics. The accuracy and necessity of this classification method were also confirmed in the subsequent study of multiscale CT scanning. In addition, a significant conclusion can be drawn by comparing the capillary pressure curves of different types of reservoirs. The development of fractures could increase the maximum mercury saturation and make the capillary pressure curve present a relatively horizontal stage with a gentle slope. The development of cavities could decrease the threshold displacement pressure and make the capillary pressure curve present a double-step characteristic.

1.3.6 Two-Dimension CT Scanning Analysis

In order to further study the characteristics of various media in ultradeep carbonate gas reservoirs and quantify the parameters of pore throat structure, the fracture-cavity type, cavity type, pore type and matrix type carbonate core samples were selected for CT scanning at two scales. Then, some images with typical pore throat structures were selected from more than 8000 CT scanning images (1778 × 1800 pixels) for analysis. CT scanning experiments of different scales were conducted to investigate the reservoir spaces of different scales. The reservoir spaces observed by the 13.15 μm scale CT scanning can be subdivided into three types of cavities, macropores and fractures (Figs. 1.22a, 1.23a, 1.24a, 1.25a). Only small-sized pores and carbonate matrix could be detected by the 0.98 μm scale CT scanning (Figs. 1.22b, 1.23b, 1.24b, 1.25b). Furthermore, the aforementioned fillings, including dolomite and asphalt, were also detected. It could be founded that the pore structure characteristics of different types of reservoirs are significantly different by comparing the CT scanning apparent images and internal images of the four core samples.

(1) Widely developed structural fractures and dissolution fractures could be observed in the fracture-cavity type sample. The section of the structural fracture is relatively flat, and the fracture angle ranges from 30° to 70° (Fig. 1.22a). Dissolution fractures connect multiple dissolution pore-cavities in series to form beaded connections, thereby effectively improving the connectivity and percolation capacity of the reservoir space (Fig. 1.26a, b). The statistical results of a large number of fractures in the CT scanning images show that the average porosity is 1.07%, the width ranges from 20 to 332 μm, and the plane extension length is approximately 800 μm.

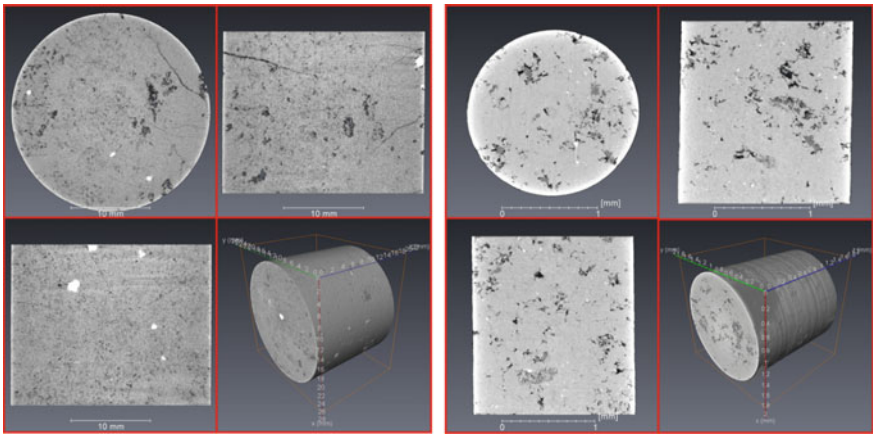

(a) Fracture-cavity type dolomite, 13.15 μm (b) Fracture-cavity type dolomite, 0.98 μm

Fig. 1.22 Apparent CT scanning images of the fracture-cavity type core sample with different observation directions under two scales

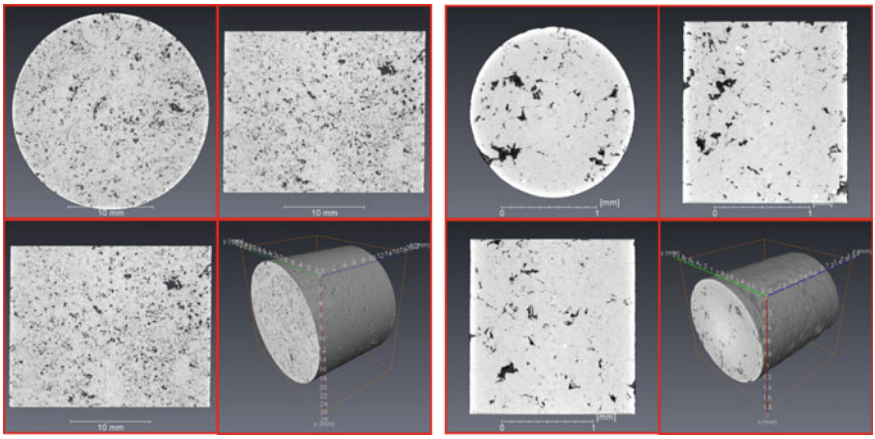

(a) Cavity type dolomite, 13.15 μm (b) Cavity type dolomite, 0.98 μm

Fig. 1.23 Apparent CT scanning images of the cavity type core sample with different observation directions under two scales

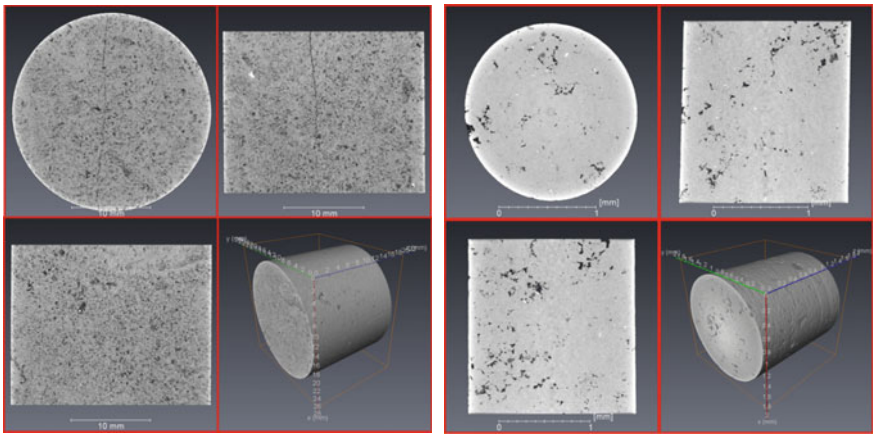

(a) Pore type dolomite, 13.15 μm (b) Pore type dolomite, 0.98 μm

Fig. 1.24 Apparent CT scanning images of the pore type core sample with different observation directions under two scales

(2) A certain number of dissolution cavities developed in both fracture-cavity type and cavity type core samples with elliptical, fenestriform, stripped and droplet shapes (Figs. 1.23a, 1.26c, d). These phenomena are consistent with the observation results of CTS. The dissolution cavities in the Deng IV Member reservoir are mainly bedding cavities or distributed around karst breccias, thereby improving the horizontal connectivity (Fig. 1.26c, d). The analysis results of CT scanning

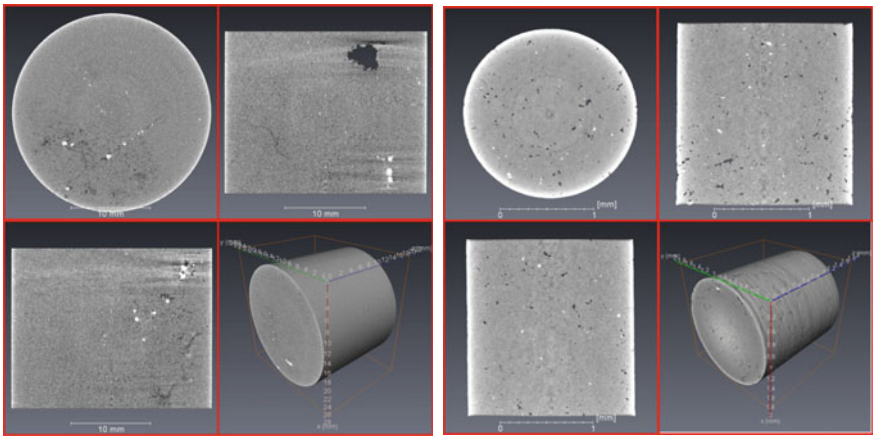

(a) Matrix type dolomite, 13.15 μm (b) Matrix type dolomite, 0.98 μm

Fig. 1.25 Apparent CT scanning images of the matrix type core sample with different observation directions under two scales

images show that the porosity and diameter of cavities are 1.55–2.02% and 2–5 mm, respectively. The plane porosity of different sections varies greatly, and cavities account for 20–70% of the plane porosities of the section. It reveals that the distribution of cavities is highly heterogeneous and difficult to predict accurately. The development frequency and distribution pattern of these cavities not only significantly enhance the storage capacity, but also play a certain role in improving the percolation capacity. In addition, the microscopic pores of the cavity type and fracture-cavity type samples observed at high resolution are still well developed, and large pores with diameters greater than 100 μm could be found. However, macroscopic fractures and cavities are difficult to observe (Figs. 1.22b, 1.23b).

(3) Although the reservoir space of both pore type and matrix type samples is dominated by pores, the size and distribution frequency of pores are quite different. The multiscale pores of the pore type sample are extremely developed, even a small amount of macroscopic pores could be observed, and the apparent porosity is approximately 6% (Fig. 1.24a). In contrast, most areas of the matrix sample are tight, and only a scattered distribution of tiny pores could be observed in some areas (Fig. 1.25a). A small amount of ellipsoid or triangular pores in the matrix type sample could be seen at high resolution. These pores are mostly dissolution pores developed between mineral particles and crystals, with diameters ranging from 0.7 to 4.6 μm (Fig. 1.25b). In addition, the dolomite filled in some pores further reduces the storage capacity of the matrix type reservoir.

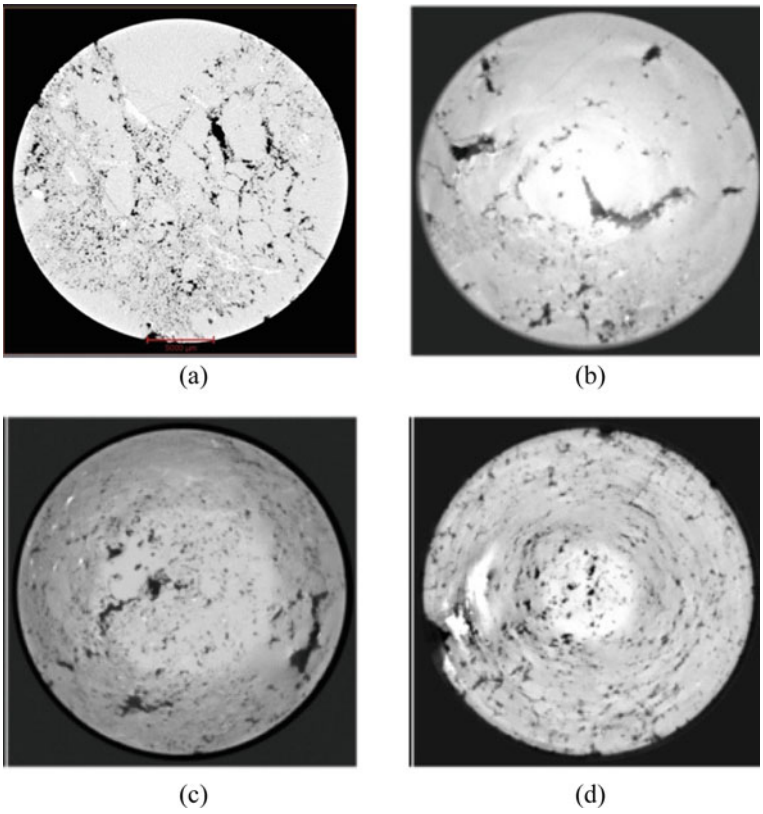

Fig. 1.26 CT scanning images of ultradeep carbonate core samples with typical pore structure characteristics: **a** Dissolution fractures developed in fracture-cavity type dolomite, 13.15 μm; **b** beaded combination of fractures and cavities in fracture-cavity type dolomite, 13.15 μm; **c** bedding cavities in fracture-cavity type dolomite, 13.15 μm; **d** cavities distribute around karst breccias in cavity type dolomite, 13.15 μm

1.3.7 Reservoir Temperature and Pressure Conditions

The measured temperature data of some gas wells in the Deng IV Member reservoir are summarized in Table 1.4. The reservoir temperature data of the upper submember was measured from gas wells #1 to #5, and the reservoir temperature data of the lower submember was measured from gas wells #6 to #8. The reservoir temperature data of the Deng IV Member was measured from gas wells #9 and #10 because of the commingled production of upper and lower submembers. The geothermal gradient of the upper submember ranges from 2.60 to 2.84 °C/100 m, with an average value of 2.68 °C/100 m. The geothermal gradient of the lower submember ranges from 2.64 to 2.73 °C/100 m, with an average value of 2.68 °C/100 m. Therefore, the geothermal gradients of the upper and lower submembers of the Deng IV Member

are similar. Overall, the geothermal gradient of the entire Deng IV Member reservoir ranges from 2.60 to 3.02 °C/100 m, with an average value of 2.71 °C/100 m. In order to facilitate the comparison of reservoir temperature data of the test gas wells, the temperature data of different depths were all converted into the data at the middle depth (− 4854.8 m) of the Deng IV Member reservoir. As illustrated in Fig. 1.27, the converted reservoir temperatures range from 149.5 to 164.2 °C, with an average value of 155.7 °C. Therefore, the Deng IV Member reservoir could be classified as a high-temperature gas reservoir.

The measured pressure data of some gas wells in the Deng IV Member reservoir are summarized in Table 1.5. The reservoir pressure data of the upper submember was measured from gas wells #1 to #5, and the reservoir temperature data of the lower submember was measured from gas wells #6 to #8. The reservoir pressure data of the Deng IV Member was measured from gas wells #9 and #10 because of the commingled production of upper and lower submembers. The pressure coefficient

Table 1.4 Statistics of temperature measured at different depth in the Deng IV Member reservoir

Position	Well number	Measuring point depth/m	Measuring point temperature/°C	Geothermal gradient/(°C/100 m)
Upper submember of Deng IV Member	#1	4744.7	142.3	2.64
	#2	4796.5	141.5	2.60
	#3	4573.3	147.5	2.84
	#4	4800.0	145.7	2.64
	#5	5043.9	149.1	2.66
Lower submember of Deng IV Member	#6	5111.6	156.6	2.73
	#7	5282.1	154.8	2.64
	#8	5182.7	152.7	2.67
Deng IV Member	#9	4887.6	147.1	2.66
	#10	4879.7	148.0	3.02
Average geothermal gradient/(°C/100 m)				2.71

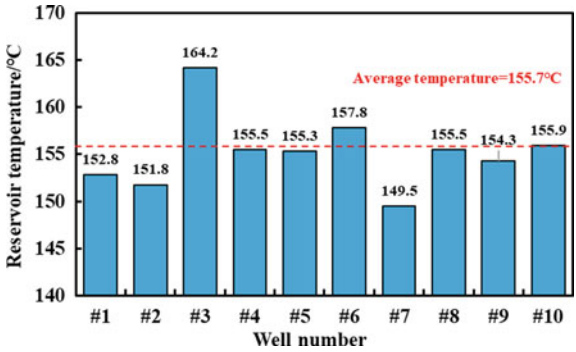

Fig. 1.27 Reservoir temperature of each gas well after conversion to the middle depth of reservoir

of the Deng IV Member ranges from 1.06 to 1.16, with an average value of 1.12. Therefore, the Deng IV Member reservoir could be classified as a normal-pressure gas reservoir. In order to facilitate the comparison of the reservoir pressure of the test gas wells, the pressure data of different depths were all converted into the data at the middle depth (− 4854.8 m) of the Deng IV Member reservoir. As illustrated in Fig. 1.28, the reservoir pressure of the upper submember ranges from 56.79 to 57.03 MPa, with an average value of 56.92 MPa. The reservoir pressure of the lower submember ranges from 56.50 to 56.78 MPa, with an average value of 56.66 MPa. In addition, the reservoir pressure of the upper and lower submembers of three wells were measured, and the pressure difference between the upper and lower submembers of the same well is between 0.16 and 0.33 MPa afrer conversion. It reflects that the upper and lower submembers are well connected and belong to the same pressure system. Overall, the reservoir pressure of the entire Deng IV Member reservoir ranges from 56.50 to 57.09 MPa, with an average value of 56.83 MPa. The reservoir pressures of the test wells only differ by 0.01–0.59 MPa, indicating that the pressure of different layers in the Deng IV Member reservoir are very close. It should be noted that these test gas wells are all located in the Gaoshiti area, and the reservoir temperature and pressure in the Moxi area were also measured later. The comparison of temperature and pressure data in Gaoshiti and Moxi areas is shown in Fig. 1.29. It reflects that the reservoir temperature in the Moxi area is similar to that in the Gaoshiti areas, but the reservoir pressure in the Moxi area is about 2.8 MPa higher than that in the Gaoshiti area. Therefore, the hydrocarbon accumulation backgrounds of the Gaoshiti area and the Moxi area are the same, but the pressure systems are different.

Table 1.5 Statistics of measured pressure in different depth of the Deng IV Member reservoir

Position	Well number	Measuring point depth/m	Measuring point pressure/MPa	Pressure gradient/(MPa/100 m)	Pressure coefficient
Upper submember of Deng IV Member	#1	4744.7	55.80	0.26	1.06
	#2	4796.5	55.90	0.27	1.13
	#3	4573.3	55.45	0.28	1.12
	#4	4800.0	54.74	0.26	1.13
	#5	5043.9	55.55	0.26	1.13
Lower submember of Deng IV Member	#6	5111.6	56.65	0.29	1.13
	#7	5282.1	56.60	0.26	1.09
	#8	5182.7	56.42	0.26	1.11
Deng IV Member	#9	4887.6	56.38	0.26	1.15
	#10	4879.7	56.55	0.27	1.16
Average pressure gradient/(°C/100 m)				0.27	
Average pressure coefficient				1.12	

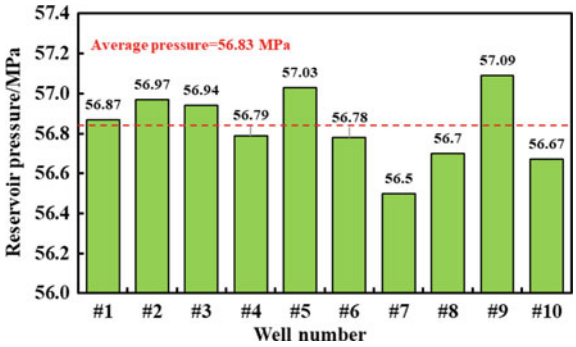

Fig. 1.28 Reservoir pressure of each gas well after conversion to the middle depth of reservoir

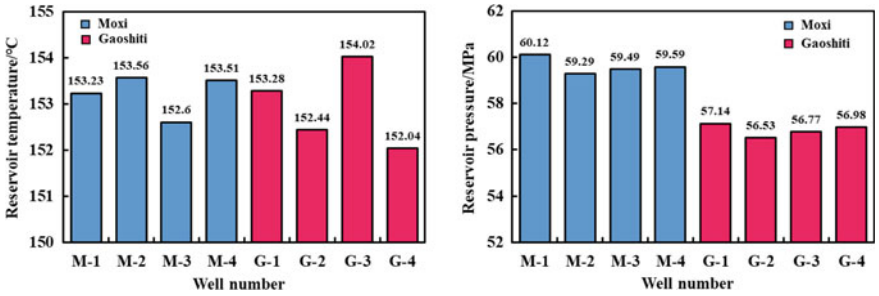

Fig. 1.29 Comparison of reservoir temperature and pressure between Gaoshiti area and Moxi area

1.3.8 Fluids Properties and Compositions

The natural gas composition analysis results of the upper and lower submembers of the Deng IV Member indicate that the natural gas composition of the wells in the Gaoshiti and Moxi areas is not significantly different. The relative density of natural gas ranges from 0.59 to 0.64, with an average value of 0.62. The range and average value of each component content of natural gas are summarized in Table 1.6. The natural gas in the Deng IV Member reservoir is generally dominated by methane, and contains moderate amounts of hydrogen sulfide and carbon doxide, as well as tiny amounts of ethane, propanem, helium and nitrogen. The hydrogen sulfide content in the Moxi area is slightly higher than that in the Gaoshiti area, whereas the carbon dioxide content in the Moxi area is slightly lower than that in the Gaoshiti area.

Table 1.6 Natural gas composition of the Deng IV Member gas reservoir

Component	CH_4/%	C_2H_6/%	C_3H_8/%	N_2/%	CO_2/%	H_2S/%	He/%
Range	90.00–93.77	0.03–0.41	0.00–0.05	0.02–3.23	4.11–8.16	0.62–3.19	0.01–0.05
Average	91.98	0.09	0.01	0.83	5.77	1.18	0.03

Table 1.7 Compositions and properties of formation water in the Deng IV Member gas reservoir

Sample number	Cl^-/(g/L)	Br^-/(mg/L)	Water type	PH	Mineralization degree/(g/L)	Density/(g/mL)	Residual acid concentration (%)
1	42.85	322.5	$CaCl_2$	7.00	73.85	1.07	0
2	48.85	402	$CaCl_2$	7.46	91.42	1.06	0
3	95.70	346	$CaCl_2$	5.57	107.4	1.08	0.08
4	164.34	807	$CaCl_2$	5.58	261	/	0.08
5	49.50	/	$CaCl_2$	5.75	49.5	/	0.08

There are five gas wells producing formation water in the Deng IV Member reservoir. The water samples of three wells were taken after acidification, which were greatly affected by residual acid. Therefore, water samples from the other two wells are representative. The analysis results of these water samples are shown in Table 1.7. The water type of these water samples is calcium chloride, indicating that the gas reservoir is well preserved. It should be noted that only one water sample was taken from the Gaoshiti area, and the rest were taken from the Moxi area. This is because only one gas well in the Gaoshiti area is connected to the water layer through fractures or faults in the lower submember. In contrast, the gas–water relationship in the Moxi area is relatively complex because of the edge water in the north and the local trapped water.

1.3.9 Reservoir Thickness Distribution Characteristics

Reservoir thickness distribution data was obtained according to the logging interpretation results of more than 60 wells in the Deng IV Member reservoir. The reservoirs in the Deng IV Member are distributed continuously, and the reservoir thickness is mainly in the range of 50–100 m. The cumulative thickness of the reservoirs drilled by different wells in the Gaoshiti area ranges from 11.50 to 68.12 m, with an average value of 34.80 m. The cumulative thickness of the reservoirs drilled by different wells in the Moxi area ranges from 11.80 to 116.80 m, with an average value of 46.84 m. The proportions of wells with different thickness ranges in the Gaoshiti and Moxi areas are summarized in Fig. 1.30. It shows that the overall reservoir thickness in the Moxi area is greater than that in the Gaoshiti area, and some reservoirs in the Moxi area are thicker than 80 m.

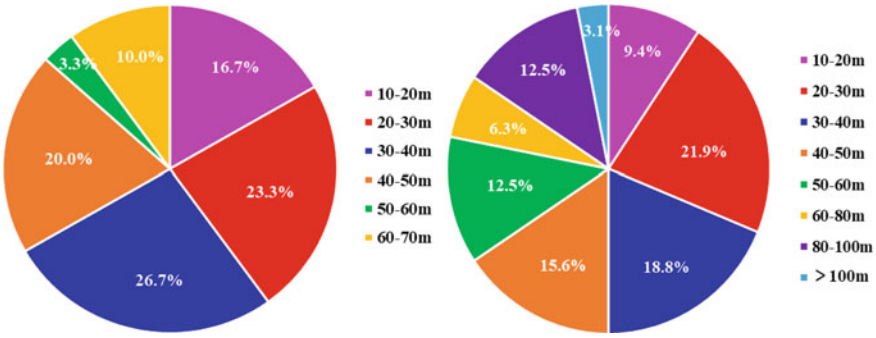

Fig. 1.30 Proportions of wells with different thickness ranges in the Gaoshiti and Moxi areas

1.4 Storage and Percolation Capacities of Ultradeep Carbonate Gas Reservoirs

1.4.1 Effect of Cavities and Fractures on Storage and Percolation Capacities

The effects of cavities and fractures on the storage and percolation capacities of ultradeep carbonate gas reservoirs were comprehensively analyzed based on petrophysical parameters and reservoir space characteristics. Porosity and permeability values are generally regarded as the basic petrophysical parameters that can directly reflect the storage and percolation capacities of reservoirs. The more core samples selected from different regions, the more representative the porosity and permeability obtained by statistics. However, the average porosity and permeability cannot fully represent the storage and percolation capacities of heterogeneous reservoirs, especially the ultradeep carbonate gas reservoirs with developed cavities and fractures. Therefore, the number and proportion of core samples with different porosity and permeability ranges were first determined, and then various petrophysical ranges were subdivided according to whether the core samples contain cavities or fractures. The frequency distribution histograms of the porosity and permeability of the Deng IV Member reservoir are shown in Fig. 1.31. Figure 1.31a shows that 34.48% of the core samples have cavities, reflecting the extensive development of cavities in the Deng IV Member reservoir. Moreover, the porosity of core samples without cavities are mainly distributed between 2 and 4%, and the proportion of core samples with cavities gradually increases with the increase of porosity. The majority of core samples with porosity greater than 6% contain cavities, indicating that cavities are a key factor in improving the storage capacity of reservoirs. In order to further study the cavity characteristics of the Deng IV Member reservoir, the size and proportion of cavities in several coring wells are summarized in Fig. 1.32. It reveals that the widely developed cavities in the Deng IV Member are mainly small cavities with a diameter of 2–5 mm, whereas the medium cavities (5–10 mm) and large cavities (> 10 mm)

were only found in local areas. However, the improvement of the overall porosity by the dominant small cavities is limited. The proportion of core samples with porosity greater than 8% is less than 5%. Medium and large cavities are mainly distributed in samples with porosity greater than 8%. It should be noted that the cavity data are all from plunger samples rather than full-diameter samples. Some large cavities were divided into multiple small cavities during plunger sample preparation. Therefore, the proportions of medium cavities and large cavities given in Fig. 1.32 are lower than the actual situation. In summary, the developed multiscale cavities increase the porosity of ultradeep carbonate gas reservoirs to a certain extent, and are an important supplement to the reservoir space. In addition, some bedding cavities can not only enhance the storage capacity, but also indirectly increase the percolation capacity by improving the horizontal connectivity.

Figure 1.31b shows that 48.76% of the core samples have fractures, reflecting that the development frequency of fractures in the Deng IV Member reservoir is higher than that of cavities. The permeability of core samples without fractures is mainly distributed below 0.1 mD, and the proportion of core samples with fractures gradually increases as the permeability increases. However, the permeability of some core samples with fractures are still low. This is because the fractures in these core samples are filled with asphalt or dolomite, thereby inhibiting the ability to improve the reservoir percolation capacity. In contrast, the permeability of a small number of core samples without visible fractures is also high. Some microscopic dissolution fractures could be detected in the rock after cutting these core samples. Therefore, the proportion of samples with fractures shown in Fig. 1.31b should be lower than in reality. There are structural fractures with different angles in the Deng IV Member reservoir, which greatly improves the percolation capacity of the reservoir. Low-angle structural fractures mainly develop and extend along the multilayer bedding, and high-angle structural fractures are mainly connected with low-angle fractures to form a network system (Luo et al., 2017). Furthermore, widely developed dissolution fractures could effectively connect pores and cavities, and enables the originally isolated reservoir space form an interconnected network structure, thereby increasing the reservoir permeability and reducing ineffective pores. In conclusion, all the effective structural fractures and dissolution fractures in the Deng IV Member reservoir positively affect the reservoir percolation capacity, and indirectly improve the storage capacity.

1.4.2 Pore and Throat Size Distribution and Connectivity Characteristics

The comprehensive analyses of storage and percolation capacities based on petrophysical parameters and reservoir space characteristics are on a macro scale. However, these petrophysical parameters and characteristics are macroscopic representations of microscopic pore throat parameters and characteristics. Therefore, it is

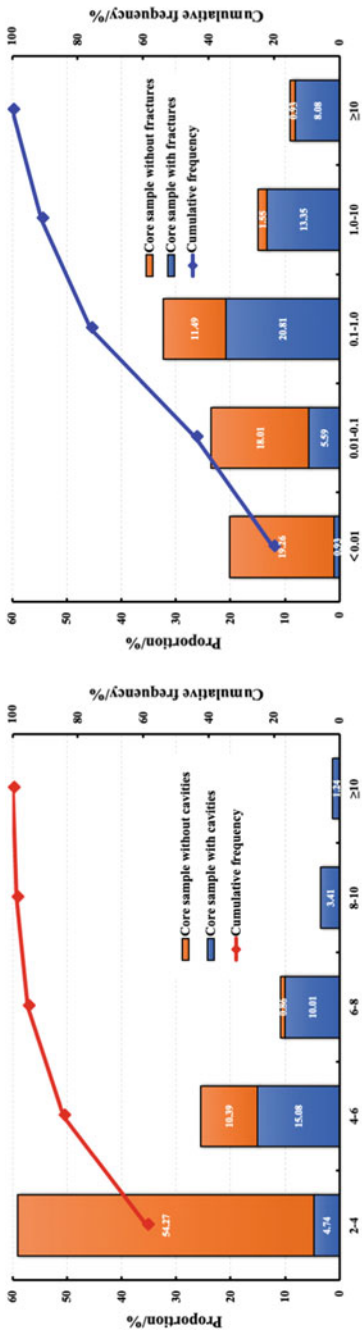

(a) Distribution characteristics of porosity

(b) Distribution characteristics of permeability

Fig. 1.31 Distribution frequency of different porosity and permeability ranges in the Deng IV Member reservoir

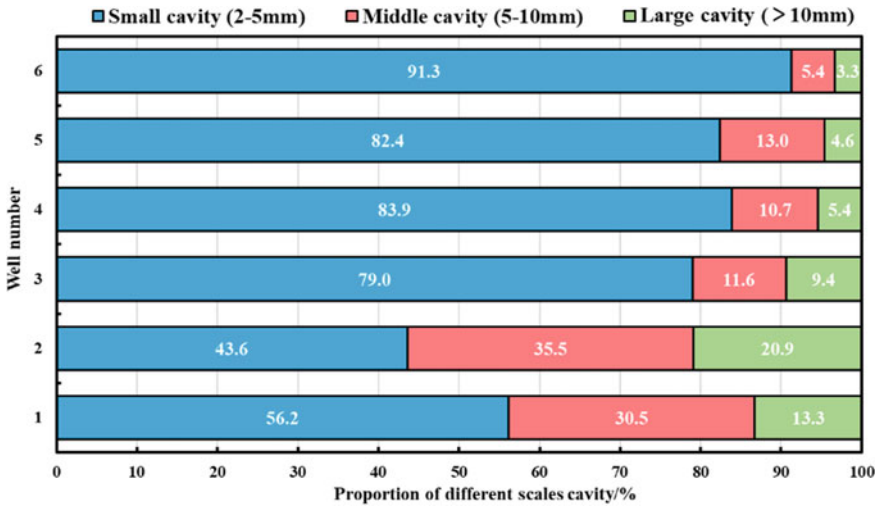

Fig. 1.32 Proportion of different sizes of cavities in the Deng IV Member reservoir

necessary to qualitatively and quantitatively study the storage and percolation capacities of various types of ultradeep carbonate reservoirs at a micro scale by using CT scanning technology. In order to quantify the size distribution and connectivity of the pore throats in the samples and realize the 3D visualization of the microscopic pore throat structure, the 3D pore throat network models of the four types of core samples were reconstructed based on the "maximum-ball" method. Subsequently, the CT scan data was processed by iCore software to obtain the distribution characteristics of the pore throat radii and volumes. The distribution results of matrix type, pore type, cavity type and fracture-cavity type samples at 13.15 μm scale are shown in Figs. 1.33, 1.34, 1.35 and 1.36, respectively.

The comparison results of the four types of samples at 13.15 μm scale reveal that the matrix type sample is similar to the pore type sample in the distribution pattern of pore throat radii and volumes, but the total number of pore throats is less than that of the pore type sample. The total pore throat number of the matrix type sample is approximately 188,300, which is only 70% of that of the pore type sample. The reason for this difference is that pore throats are widely developed in pore type reservoirs, but only locally developed in matrix type reservoirs. In the matrix type sample, 91.40% of the pore throats have radii of 0–18.81 μm but only occupy 69.83% of the total pore throat volume. There are only 131 pore throats with a radius greater than 100 μm, accounting for 0.07% of the total number of pore throats but 1.45% of the total pore throat volume. The maximum pore throat radius that could be detected is about 170.39 μm (Fig. 1.33). In the pore type sample, 89.41% of the pore throats have radii of 0–20.40 μm but only occupy 62.90% of the total pore throat volume. There are only 50 pore throats with a radius greater than 100 μm, accounting for 0.02% of the total number of pore throats but 0.87% of the total pore throat volume. The maximum pore throat radius that could be detected is about 185.80 μm (Fig. 1.34).

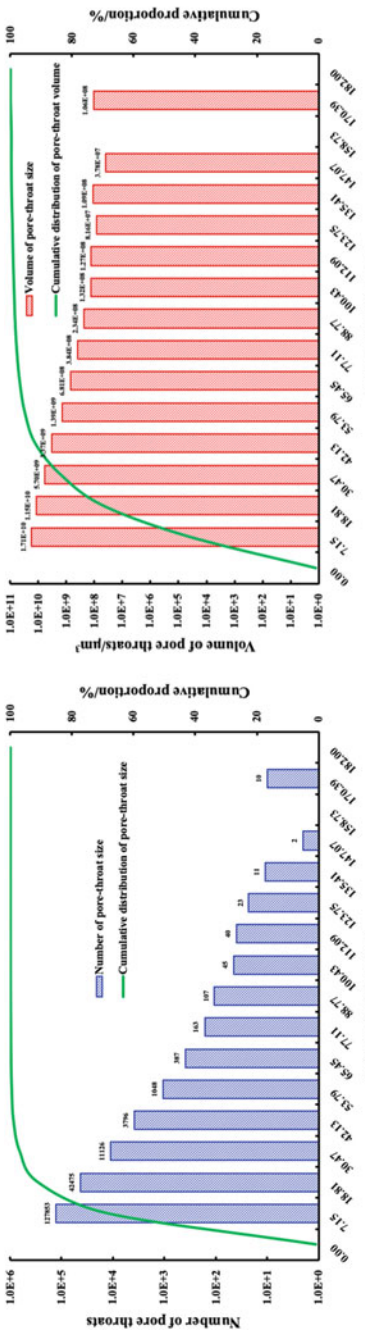

(a) Pore throat radii distribution (b) Pore throat volumes distribution

Fig. 1.33 Distribution of the pore throat radii and volumes of the matrix type sample at 13.15 μm scale

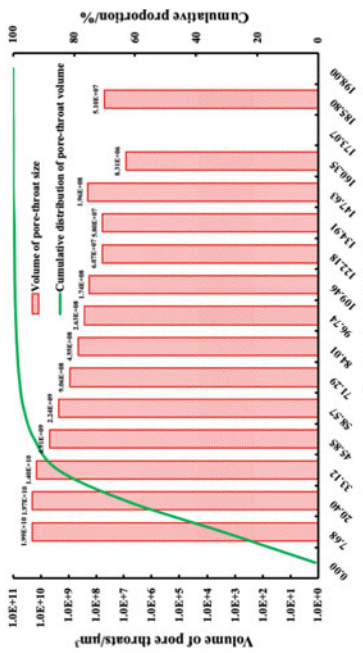

(a) Pore throat radii distribution (b) Pore throat volumes distribution

Fig. 1.34 Distribution of the pore throat radii and volumes of the pore type sample at 13.15 μm scale

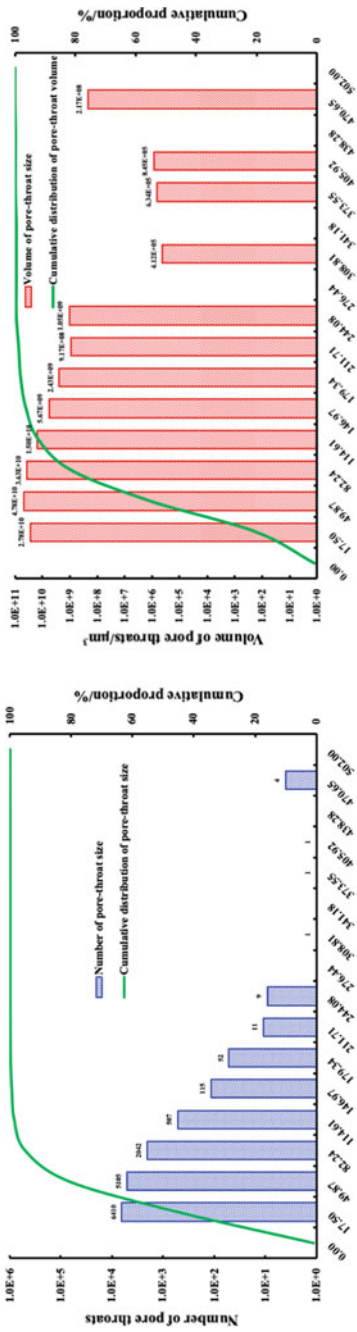

(a) Pore throat radii distribution

(b) Pore throat volumes distribution

Fig. 1.35 Distribution of the pore throat radii and volumes of the cavity type sample at 13.15 μm scale

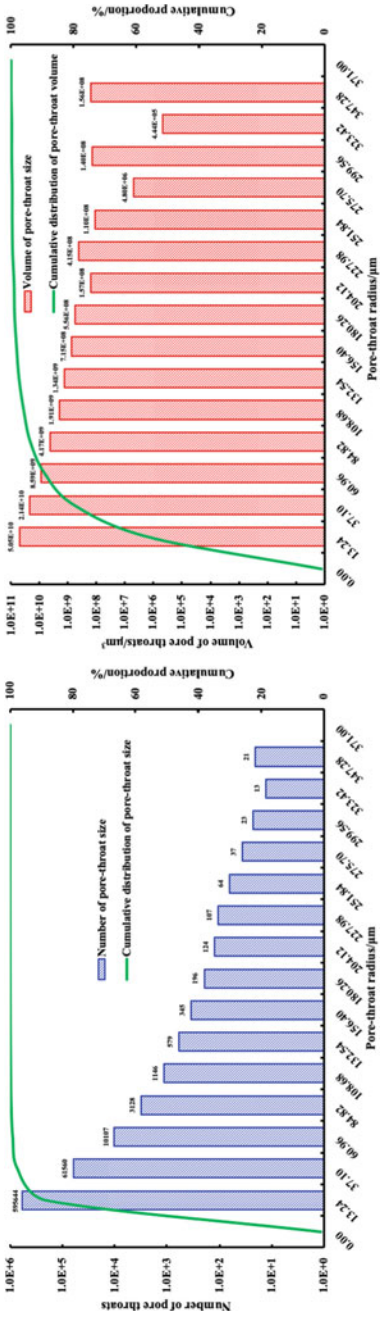

(a) Pore throat radii distribution (b) Pore throat volumes distribution

Fig. 1.36 Distribution of the pore throat radii and volumes of the fracture-cavity type sample at 13.15 μm scale

Therefore, the reservoir spaces of pore type and matrix type reservoirs are composed of abundant microscopic pores and a few macroscopic pores.

A total number of 14,258 pore throats and a total pore throat volume of 1.37 $\times$ 10^{11} μm^3 were detected in the cavity type sample through the CT scanning of 13.15 μm scale. The pore throat number of the cavity type sample is one order of magnitude lower than that of other samples, but the pore throat volume of the cavity type sample is one order of magnitude higher than that of the pore type and matrix type samples. Therefore, the storage capacity of the reservoir space depends not only on the number of pore throats, but also on the size of pore throats. The contribution of macroscopic pore throats to reservoir space is greater than that of microscopic pore throats. In the cavity type sample, 44.96% of the pore throats have radii of 0–17.50 μm but only occupy 19.71% of the total pore throat volume. There are more than 700 pore throats with a radius greater than 100 μm, accounting for 4.92% of the total number of pore throats but 18.69% of the total pore throat volume. The maximum pore throat radius that could be detected is about 470.65 μm, which is 2 to 3 times that of the pore type and matrix type samples (Fig. 1.35). It should be noted that the millimeter-level cavities of the cavity type sample were removed prior to the CT scanning experiments. The actual pore throat volume of the cavity type sample is larger than that measured by CT scanning. Consequently, the reservoir space of cavity type reservoirs is dominated by multiscale cavities and macroscopic pores. Although the pore throat volume of the cavity type sample is an order of magnitude higher than that of the pore type sample, its porosity is only 2 to 4 times that of the pore type sample. This is because the pore throat volume obtained by CT scanning includes effective connected pore throats and ineffective isolated pore throats, while the porosity obtained by conventional petrophysical measurement can only reflect the effective pore throats. This difference indicates that the reservoir space of cavity type reservoirs is large, but some pores lack effective connectivity.

The reservoir space of the fracture-cavity type sample is a complex combination of fractures, cavities, microscopic and macroscopic pores. A total number of 673,094 pore throats and a total pore throat volume of 9.01 $\times$ 10^{10} μm^3 were detected in the fracture-cavity type sample through the CT scanning of 13.15 μm scale. Although the pore throat volume of the fracture-cavity type sample is only 65.72% of that of the cavity type sample, the porosity of the fracture-cavity type sample is approximately 3% higher than that of the cavity type sample. This data strongly confirms the connection effect of generally developed fractures on the isolated reservoir spaces and the improvement effect on the storage capacity. In the fracture-cavity type sample, 88.49% of the pore throats have radii of 0–13.24 μm and only occupy 56.00% of the total pore throat volume. There are as many as 2655 pore throats with a radius greater than 100 μm, accounting for 0.39% of the total number of pore throats but 6.01% of the total pore throat volume. The maximum pore throat radius that could be detected is about 347.28 μm (Fig. 1.36). By comparing the total number of pore throats and the number of pore throats with different sizes, it could be concluded that the fracture-cavity type sample not only develops a large number of microscopic pores like the pore type sample, but also contains a certain number of macroscopic pores and cavities like the cavity type sample. Therefore, pore throats of various

sizes have corresponding contributions to the storage capacity of the fracture-cavity reservoirs.

As shown in Figs. 1.33, 1.34, 1.35 and 1.36, the detailed distribution characteristics of microscopic pore throats below 20 μm could not be obtained through the CT scanning at 13.15 μm scale. CT scanning is a test method that does not damage the pore throat structure of the sample. Therefore, CT scanning at 0.98 μm scale were conducted on the same 4 samples to observe and analyze microscopic pore throats with a radius of less than 20 μm. The distribution results of matrix type, pore type, cavity type and fracture-cavity type samples at 0.98 μm scale are shown in Figs. 1.37, 1.38, 1.39 and 1.40, respectively. The results show that the pore throat radii and volumes distribution characteristics at 0.98 μm scale are different from those at the 13.15 μm scale.

In the matrix type sample, 73.03% of the pore throats have radii of 0–2.02 μm but only occupy 42.97% of the total pore throat volume. There are only 14 pore throats with a radius greater than 10 μm, accounting for 0.33% of the total number of pore throats but 5.09% of the total pore throat volume. The maximum pore throat radius that could be detected is about 13.53 μm (Fig. 1.37). In the pore type sample, 82.63% of the pore throats have radii of 0–2.34 μm but only occupy 33.18% of the total pore throat volume. There are only 155 pore throats with a radius greater than 10 μm, accounting for 0.29% of the total number of pore throats but 8.62% of the total pore throat volume. The maximum pore throat radius that could be detected is about 13.53 μm (Fig. 1.38). Although the pore throat radii and volumes distribution characteristics of the matrix type sample and the pore type sample are similar, the difference between the two is mainly reflected in the number of pore throats. At the 0.98 μm scale, 4293 and 53,795 pore throats were detected in the matrix type and pore type samples, respectively. The difference in total pore throats mainly comes from pore throats with a radius less than 7 μm. It should be noted that the difference in the number of pore throats with a radius less than 7 μm at the 13.15 μm scale is far less than that at the 0.98 μm scale (Figs. 1.33a, 1.34a). The reason for this difference is that the scan area at the 0.98 μm scale comes from a part of the scan area at the 13.15 μm scale, but the microscopic pore throats in this part of area are not developed. This phenomenon reflects that the abundant pore throats are only developed in local areas of matrix type reservoirs, which could be observed in the 3D network topology model of the matrix type sample.

In the cavity type sample, 25.98% of the pore throats have radii of 0–1.91 μm but only occupy 8.43% of the total pore throat volume. There are as many as 920 pore throats with a radius greater than 10 μm, accounting for 22.96% of the total number of pore throats but 61.20% of the total pore throat volume. The maximum pore throat radius that could be detected is about 52.35 μm (Fig. 1.39). A total number of 4007 pore throats and a total pore throat volume of 1.07×10^8 μm^3 were detected in the cavity type sample through the CT scanning of 0.98 μm scale. The total number of pore throats of the cavity type sample is lower than that of the matrix type sample, but its pore throat volume is 10 and 4 times that of the matrix type and pore type samples, respectively. Although the number of pore throats of the cavity type sample is relatively small, the average pore throat radius, and the number and proportion of

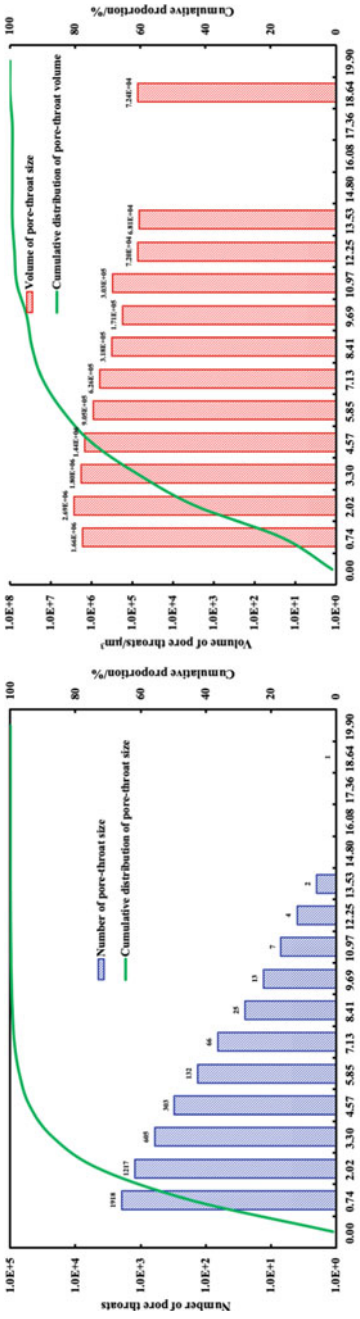

(a) Pore throat radii distribution

(b) Pore throat volumes distribution

Fig. 1.37 Distribution of the pore throat radii and volumes of the matrix type sample at 0.98 μm scale

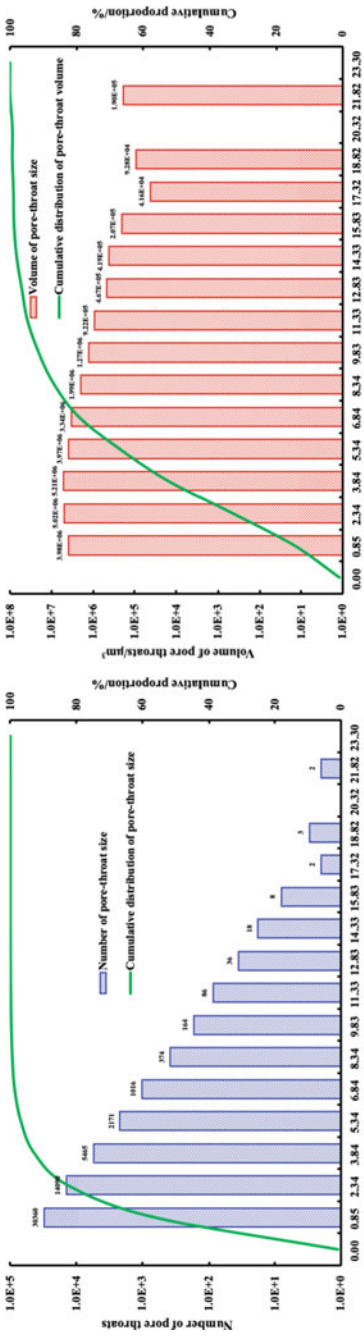

(a) Pore throat radii distribution

(b) Pore throat volumes distribution

Fig. 1.38 Distribution of the pore throat radii and volumes of the pore type sample at 0.98 μm scale

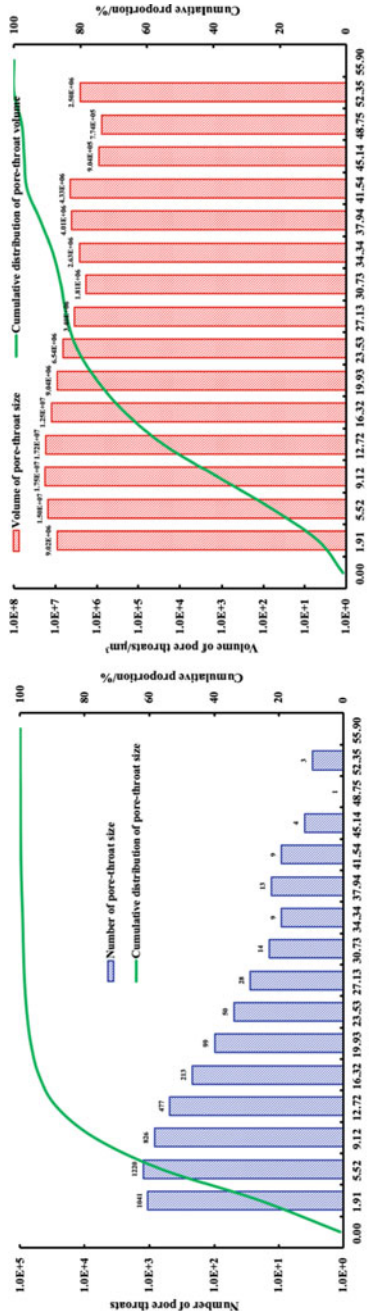

(a) Pore throat radii distribution

(b) Pore throat volumes distribution

Fig. 1.39 Distribution of the pore throat radii and volumes of the cavity type sample at 0.98 μm scale

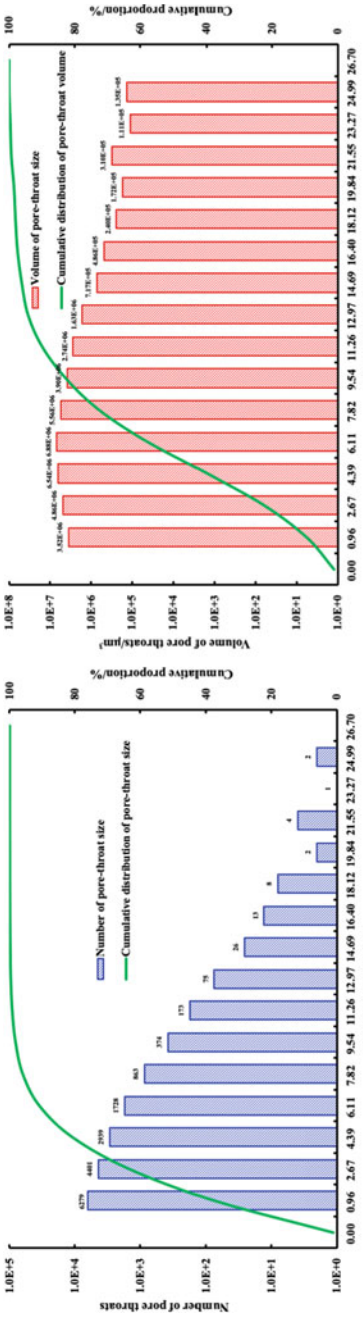

(a) Pore throat radii distribution

(b) Pore throat volumes distribution

Fig. 1.40 Distribution of the pore throat radii and volumes of the fracture-cavity type sample at 0.98 μm scale

relatively large pore throats of the cavity type sample are higher than those of the other samples.

In the fracture-cavity type sample, 63.24% of the pore throats have radii of 0–2.67 μm but only occupy 22.17% of the total pore throat volume. There are as many as 304 pore throats with a radius greater than 10 μm, accounting for 1.80% of the total number of pore throats but 17.30% of the total pore throat volume. The maximum pore throat radius that could be detected is about 24.99 μm (Fig. 1.40). A total number of 16,888 pore throats and a total pore throat volume of 3.78×10^7 μm^3 were detected in the fracture-cavity type sample through the CT scanning of 0.98 μm scale. The pore throats number, average pore throat radius, and total pore throat volume of the fracture-cavity type sample are between those of the cavity type sample and the pore type sample. Therefore, fracture-cavity type reservoirs have both the pore throat structure characteristics of pore type and cavity type reservoirs.

The pore throat radii and volumes distribution can reflect the storage capacity of the reservoir to a certain extent. However, the pore throat volume obtained by CT scanning is larger than the effective reservoir space if the pore throat connectivity is not considered. Therefore, the pore throat connectivity and effective storage capacity of the four types of samples were specifically analyzed later.

1.4.3 Analysis of Pore Throat Network Models

The 3D "ball-stick" network model established based on the "maximum-ball" method can intuitively investigate the size and distribution of pore throats. More importantly, the model can accurately distinguish between effective connected pore throats and ineffective isolated pore throats, and give the distribution data of pore throat coordination numbers. The extraction process of effective pore throats is shown in Fig. 1.41, and the total porosity and effective porosity of the four types of samples are summarized in Table 1.8. The proportion of effective pore throats of the four samples could indirectly reflect the pore throat connectivity. The connectivity of the fracture-cavity type sample is the best, followed by the pore type and cavity type samples, and the matrix type sample is the worst.

The 3D pore throat network models of the four types of samples at two scales are presented in Figs. 1.42, 1.43, 1.44 and 1.45. It can be seen from these figures that most conclusions obtained by the analyses of pore throat distribution characteristics could be intuitively verified through 3D pore throat network models. It can be seen from Fig. 1.42 that abundant pore throats only develop in the local area of the matrix sample, and only a small amount of pore throats could be observed in the 0.98 μm scale model. It can be seen from Fig. 1.43 that a large amount of pore throats are developed in the pore type model at both scales, and it can be judged that the radii of these pore throats are generally small based on the sphere size. It can be seen from Fig. 1.44 that the pore throat number of the cavity type model is relatively small, but the pore throat sizes are generally larger than those of other models. It can be seen

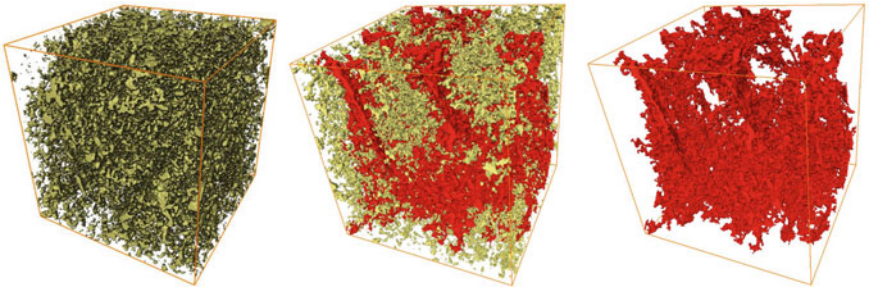

(a) Total pore throats (b) Effective and ineffective pore throats (c) Effective pore throats

Fig. 1.41 Extraction process of effective pore throats in 3D pore throat network model

Table 1.8 Total porosity and effective porosity of the four types of samples

Sample type	Matrix type	Pore type	Cavity type	Fracture-cavity type
Total porosity/%	2.18	5.12	10.71	10.30
Effective porosity/%	0.70	2.85	5.21	7.31
Proportion of effective pore throats/%	32.25	55.62	48.68	70.97

from Fig. 1.45 that the fracture-cavity type model simultaneously develops abundant microscopic pore throats and a certain number of macroscopic pore throats.

The fracture-cavity type sample contain a certain number of microscopic fractures, and conventional CT scanning cannot directly extract and characterize the fractures in the sample. Therefore, fracture CT scanning were conducted on the four types of samples later. The identification and extraction of fractures is achieved by binary segmentation of sample images during CT scanning. Taking the volume of 5 ×

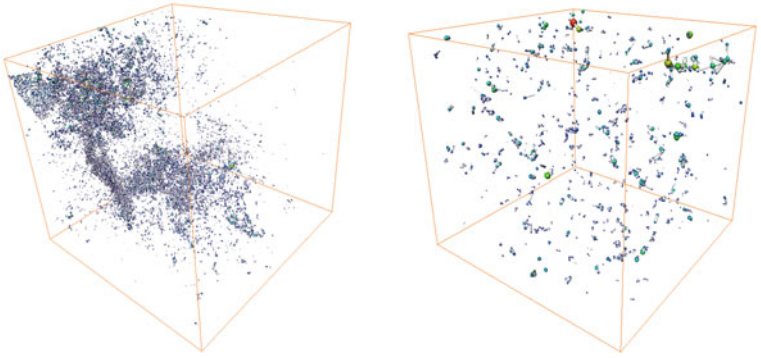

(a) 13.15 μm scale (b) 0.98 μm scale

Fig. 1.42 Pore throat network model of the matrix type sample at the two scales

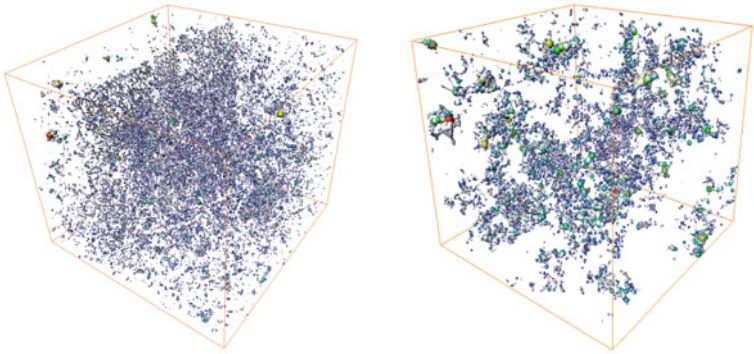

(a) 13.15 μm scale (b) 0.98 μm scale

Fig. 1.43 Pore throat network model of the pore type sample at the two scales

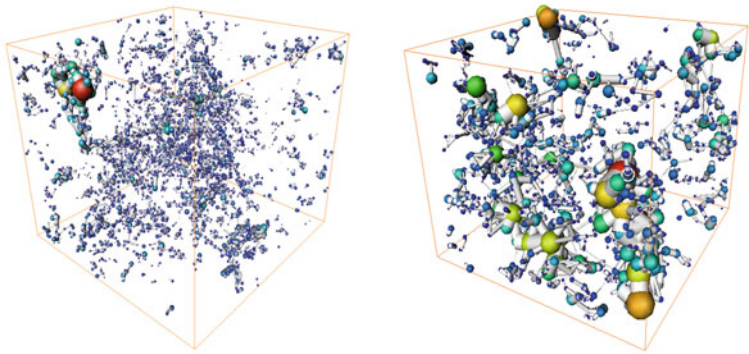

(a) 13.15 μm scale (b) 0.98 μm scale

Fig. 1.44 Pore throat network model of the cavity type sample at the two scales

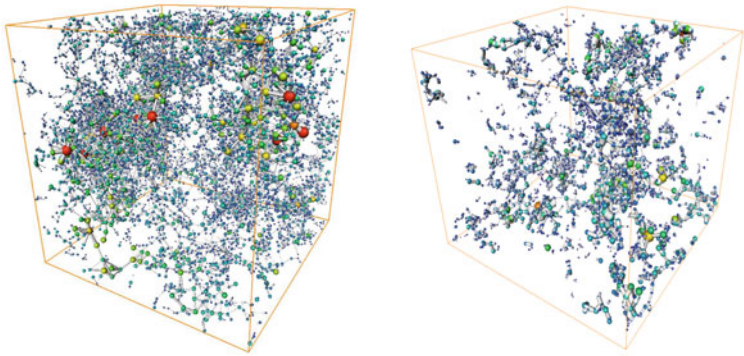

(a) 13.15 μm scale (b) 0.98 μm scale

Fig. 1.45 Pore throat network model of the fracture-cavity type sample at the two scales

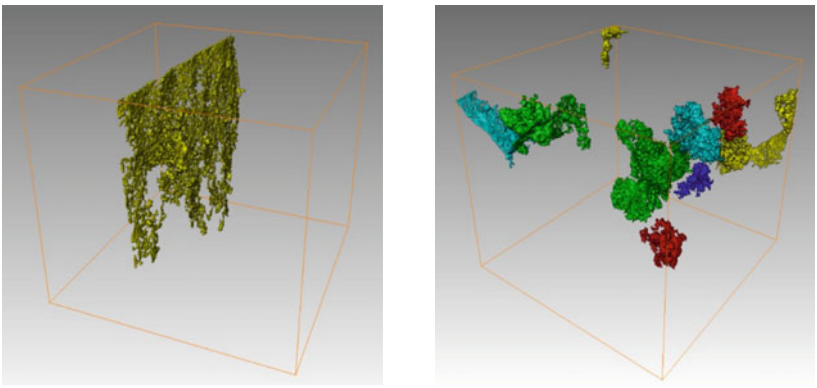

(a) one fracture in the pore type model (b) ten fractures in the fracture-cavity type model

Fig. 1.46 3D fracture network models of the pore type and fracture-cavity type samples

105 pixels as the threshold for the segmentation of fractures, the binary image was further segmented to preserve the fractures. Fractures were detected in both pore type and fracture-cavity type samples by CT scanning, and the 3D fracture network models and fracture parameters are shown in Figs. 1.46 and 1.47, respectively. Only one fracture was extracted from the pore type sample, and 92.14% of the fracture aperture is less than 100 μm. Fractures with apertures less than 100 μm should be classified as microscopic fractures according to the Industry Standard SY/T 6110-2002 of the P.R. of China (Table 1.9). A few microscopic fractures have limited contribution to storage and percolation capacities because they cannot form a fracture network structure and are easily filled with some minerals. A total of 10 fractures were extracted from the fracture-cavity type sample, and 35.78% of the fracture aperture are 100–500 μm. Therefore, these fractures can be classified as small-size fractures according to the standard. These fractures not only increase the effective porosity by connecting isolated reservoir spaces, but also increase the permeability by widening flow channels, thereby improving both the storage and percolation capacities of ultradeep carbonate gas reservoirs to a certain extent.

1.4.4 Analysis of the Pore Throat Connectivity

The pore-throat coordination number, defined as the number of throats connecting each pore, is an important parameter describing the connectivity degree between pores and throats (Luo et al., 2017). However, most pore throat structure characterization techniques cannot accurately measure the coordination number. The "maximum-ball" method based on CT scanning data could quantify the distribution of different coordination numbers, thereby assisting in evaluating the storage and percolation capacities of reservoirs. Therefore, the pore-throat coordination numbers

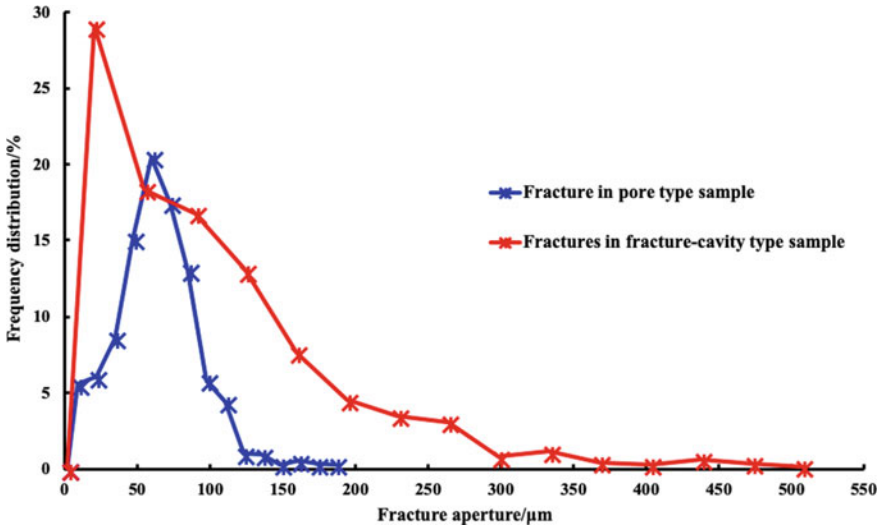

Fig. 1.47 Distribution of fracture apertures of the pore type and fracture-cavity type samples

Table 1.9 Classification standard of carbonate reservoir space (SY/T 6110-2002)

Pore		Cavity		Fracture		Throat	
Type	Pore/mm	Type	Cavity/mm	Type	Fracture/mm	Type	Throat/mm
Large	< 2–0.5	Huge	> 1000	Huge	> 100	Large	> 2
Medium	< 0.5–0.25	Large	< 1000–100	Large	< 100–10	Medium	< 2–0.5
Small	< 0.025–0.01	Medium	< 100–20	Medium	< 10–1	Small	< 0.5–0.05
Micro	< 0.01	Small	< 20–2	Small	< 1–0.1	Micro	< 0.05
–	–	–	–	Micro	< 0.1	–	–

distribution characteristics of the four types of samples at two scales are illustrated in Figs. 1.48 and 1.49. The average pore-throat coordination numbers of the matrix type, pore type, cavity type and fracture-cavity type samples at the 13.15 μm scale are 2.81, 3.59, 3.37 and 5.46, respectively (Fig. 1.48). In the matrix type sample, 51.95% of the pore throat coordination numbers are 1 and 2, while the proportion of coordination numbers greater than 10 is only 0.56%. The relatively low coordination number reflects that most pores are connected to adjacent pores through only a few throats, thereby reducing the connectivity of reservoir spaces and the efficiency of fluids migration, especially when some throats are blocked by formation water or minerals. The average value and distribution characteristics of pore-throat coordination numbers are similar for pore type and cavity type samples. Although the proportion of pore throat coordination numbers greater than 10 is only 2–3% for the two samples, the pores with coordination numbers of 5–10 are significantly more than those of the matrix type sample. Appropriate coordination number provides

necessary prerequisite for the effective connection of the reservoir space and the free migration of fluids. In the fracture-cavity type sample, 32.52% of the pore throat coordination numbers are between 5 and 10, and the proportion of coordination numbers greater than 10 is as high as 13.47%. The relatively high coordination number also verifies that fractures and bedding cavities in the fracture-cavity type sample are the key factors to improve the connectivity of the reservoir space. Pores are connected to each other through a plurality of throats to form a network structure, thereby greatly improving the effective reservoir space and fluid percolation capacity. The average pore-throat coordination numbers of the matrix type, pore type, cavity type and fracture-cavity type samples at the 0.98 μm scale are 2.44, 4.13, 4.51 and 4.79, respectively (Fig. 1.49). The data shows that connectivity of the fracture-cavity type sample is similar to that of the cavity type and pore type samples, because the areas with fractures and bedding cavities cannot be selected for CT scanning at the 0.98 μm scale. Therefore, the widespread development of fractures is the dominant reason why the coordination number of fracture-cavity type reservoirs is higher than that of other types of reservoirs.

In addition, the coordination number of cavities was analyzed based on the extraction of cavities with different sizes from the cavity type and fracture-cavity type network models. As shown in Fig. 1.50, the cavity coordination number of the cavity type sample is 1–5, with an average of 1.73. In contrast, the cavity coordination number of the fracture-cavity type sample is 1–10, with an average of 3.41. It indicates that the poor connectivity of cavities in cavity type reservoirs is not conducive to the percolation of gas in cavities, while the fractures in fracture-cavity type reservoirs improve the connectivity between pores and cavities. Therefore, fracture-cavity type reservoirs are the target areas for the exploration and development of ultradeep carbonate gas reservoirs. Although the geological reserves of cavity type reservoirs are similar to or even higher than those of fracture-cavity type reservoirs, it is still necessary to improve the connectivity of various reservoir spaces through reservoir reconstruction to form high-quality gas reservoirs.

In summary, the value of the pore throat coordination number reflects the reservoir space connectivity and fluid percolation capacity, and fractures can greatly increase the coordination number. Consequently, the percolation capacity of the four types of ultradeep carbonate reservoirs is fracture-cavity type, cavity type, pore type and matrix type from strong to weak. In addition, the proportion of effective pore throats of matrix type, pore type, cavity type and fracture-cavity type sample are 40.83%, 53.71%, 44.56% and 70.97%, respectively (Table 1.8). The effective pore volume could be calculated based on the effective pore throat proportion and the total pore throat volume. The effective pore volumes of matrix type, pore type, cavity type and fracture-cavity type samples are 1.32×10^{10} μm^3, 3.06×10^{10} μm^3, 7.63×10^{10} μm^3 and 6.39×10^{10} μm^3, respectively. Therefore, both fracture-cavity type and cavity type reservoirs have relatively strong storage capacity, followed by pore type and matrix type reservoirs.

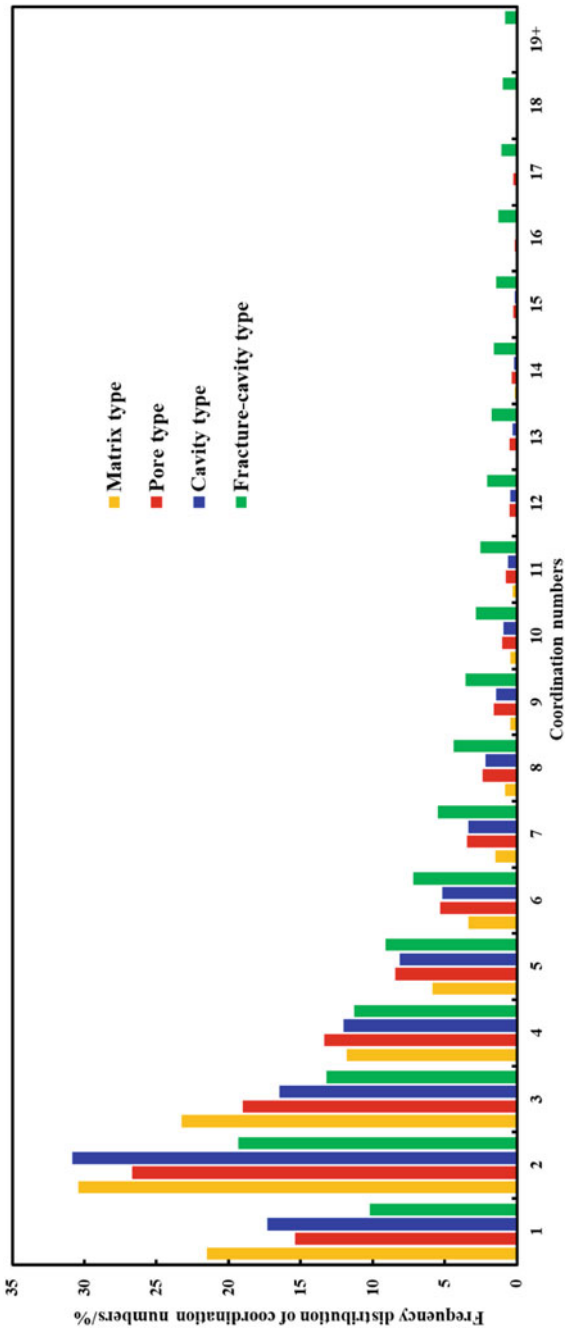

Fig. 1.48 Coordination number distribution of four types of samples at 13.15 μm scale

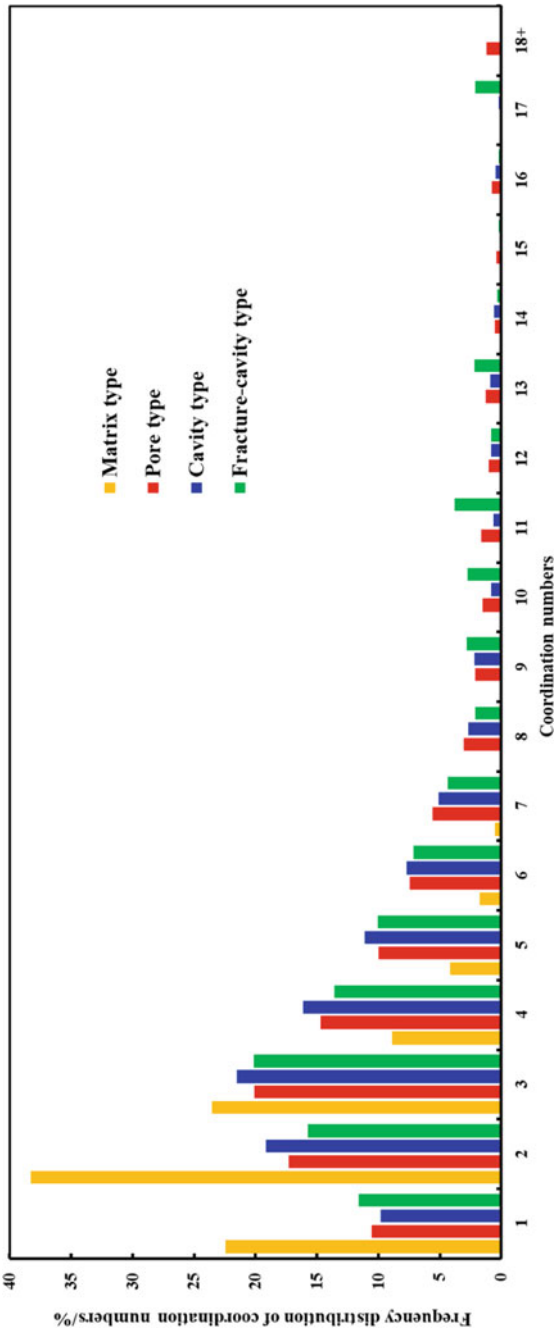

Fig. 1.49 Coordination number distribution of four types of samples at 0.98 μm scale

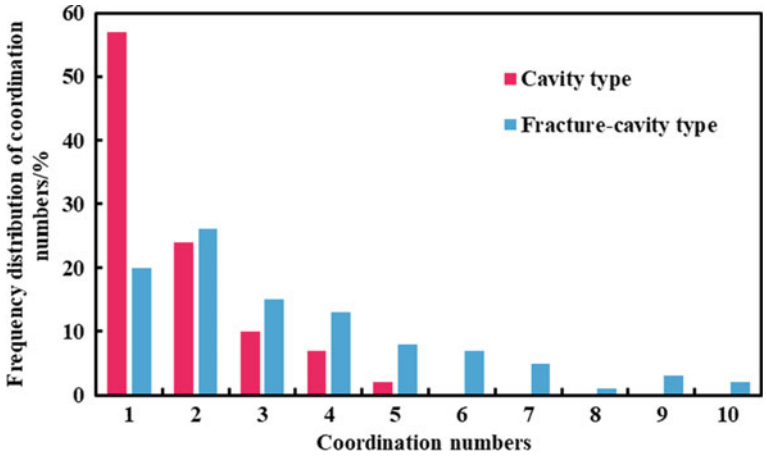

Fig. 1.50 Cavity coordination number distribution of the cavity type and fracture-cavity type samples at 13.15 μm scale

1.4.5 Proportion of Various Types of Reservoir Spaces

The CT scanning technique based on the "maximum-ball" method can also quantify the pore throat radii and volumes distribution characteristics through the pore network model and the throat network model, respectively. Therefore, the reservoir space proportion of pores, throats, cavities and fractures in the four types of samples are shown in Fig. 1.51. It could be found that fractures are more or less developed in various types of carbonate reservoirs. However, only the fractures in fracture-cavity type reservoirs can form an effective network structure from the perspective of fractures proportion. Therefore, widely developed fractures can not only improve the effective porosity and percolation capacity, but also provide a certain reservoir space by themselves. In contrast, a small number of isolated fractures in other types of reservoirs could only slightly improve the storage and percolation capacities of local areas, have a weak impact on the whole. Furthermore, the permeability of fracture-cavity type reservoirs is generally higher than that of cavity type reservoirs, but the throat proportion of the two are similar. It reflects the important role of fractures in improving the percolation capacity of ultradeep carbonate gas reservoirs. Cavities were not detected in both matrix type and pore type samples, but the proportion of throats in the matrix type sample is lower than that in the pore type sample. It explains the reason why the effective porosity and permeability of matrix type reservoirs are lower than those of pore type reservoirs.

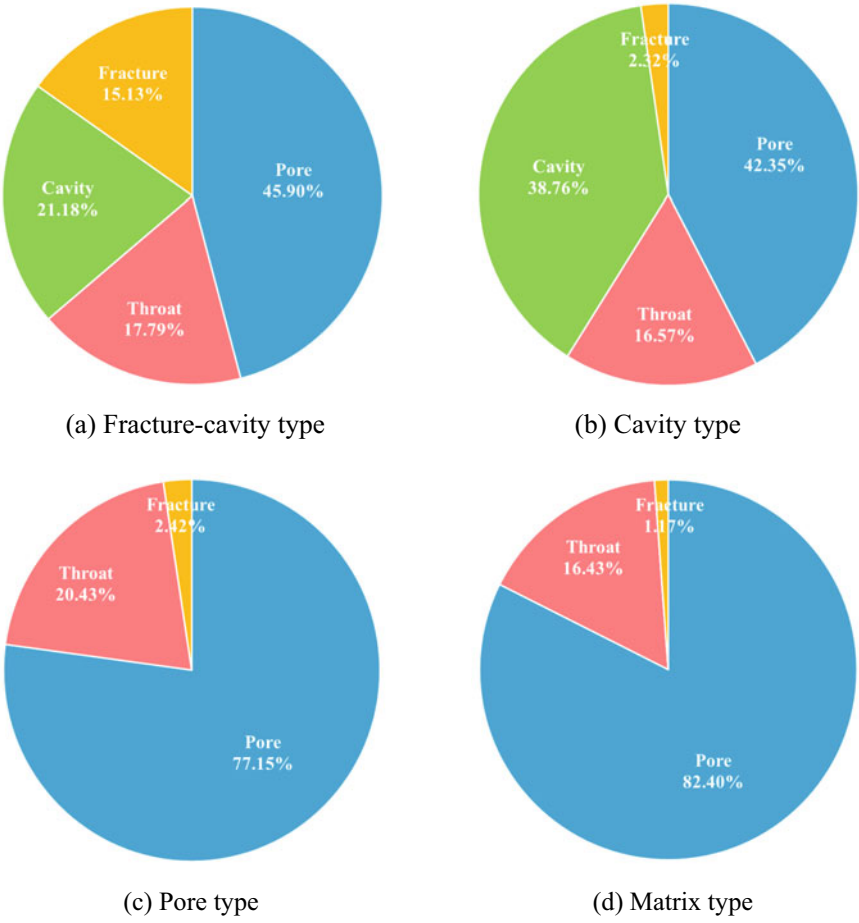

Fig. 1.51 Proportion of different reservoir spaces in the four types of carbonate samples

1.5 Characteristics and Classification Standard of Various Types of Ultradeep Carbonate Gas Reservoirs

Reservoir classification is the basis for reservoir evaluation and development scheme. The reservoir classification of conventional carbonate gas reservoirs refers to the Industry Standard SY/T 6110-2002 of the P.R. of China (Table 1.10). As shown in Fig. 1.52, 90% of the gas reservoirs in the Deng IV Member would be classified as the Type III reservoir according to the porosity range in Table 1.10. However, this classification method not only fails to reflect the heterogeneity of ultradeep carbonate reservoirs, but also classifies most of the reservoirs as ineffective or low-potential reservoirs. The open flow capacity and test production of multiple gas wells in the Deng IV Member show high development potential. Therefore, the existing

Table 1.10 Classification standard for carbonate gas reservoirs (SY/T 6110-2002)

Reservoir type	Permeability/mD	Porosity/%	Median throat width/μm	Threshold displacement pressure/MPa	Sorting coefficient
I	≥ 10	≥ 12	≥ 2	< 0.1	≥ 2.5
II	0.1–10	6–12	0.5–2	0.1–1	2–2.5
III	0.001–0.1	2–6	0.05–0.5	1–5	1–2
IV	< 0.001	< 2	< 0.05	≥ 5	< 1

reservoir classification standard is not fully applicable to ultradeep carbonate gas reservoirs. The reservoir classification of ultradeep carbonate gas reservoirs needs to comprehensively consider the reservoir characteristics, storage and percolation capacities of various types of reservoirs.

Finally, the reservoir characteristics of the four types of ultradeep carbonate gas reservoirs in the Deng IV Member are summarized in Table 1.11 based on the test data and analysis results of core description, conventional petrophysical measurement, CTS, SEM, HPMI, multiscale CT scanning and field gas well testing. It is concluded that cavities and fractures are widely developed in the Deng IV Member reservoir and the reservoir type is dominated by fracture-cavity type through comprehensive analysis of macro, micro, static and dynamic data. The matrix type reservoirs in the Deng IV Member are basically ineffective reservoirs, and the pore type reservoirs have relatively poor storage and percolation capacities. However, the widespread fractures and bedding cavities in the fracture-cavity type and cavity type reservoirs greatly improve the effective reservoir space and percolation capacity, and cavities with different sizes are an important supplement to the storage capacity. More importantly, a reasonable combination of cavities and fractures is the basis for the effective development of ultradeep carbonate gas reservoirs. Accurate exploration of favorable distribution areas of fractures and cavities is the prerequisite for efficient development of ultradeep carbonate gas reservoirs. Reservoir reconstruction in pore-cavities developed areas with high-porosity and low-permeability is the key to improving the gas recovery factor of ultradeep carbonate gas reservoirs.

1.6 Summary

In this chapter, a variety of experimental and analytical techniques were used to study the reservoir characteristics of ultradeep carbonate gas reservoirs, as well as the storage and percolation capacities of different types reservoir and their influencing factors. The important conclusions obtained are summarized as follows.

(1) Almost all the reservoirs in the Deng IV Member are developed in dolomite, and the dominant type of dolomite is algal clotted dolomite (average 70.34%), followed by algal stromatolite dolomite (average 15.49%) and algal doloarenite

Table 1.11 Pore throat structure characteristics of four types of ultradeep carbonate gas reservoir in Deng IV Member

Pore throat parameters	Matrix type	Pore type	Cavity type	Fracture-cavity type
Dominated porosity range/%	0–2	2–4	4–10	4–10
Dominated permeability range/%	< 0.01	0.001–0.1	0.01–1	0.1–100
Dominated reservoir lithology	Algal clotted dolomite > Algal stromatolite dolomite > Algal doloarenite			
Dominated mineral	Dolomite > Silicoide > Organic matter > Clay > Pyrite			
Pore type	InterP dissolution pore > InterC dissolution pore > InterC pore > InterP pore			
Cavity type	/	/	Fenestriform cavity > Dissolution cavity	
Dominated cavity diameter range/mm	/	/	2.0–5.0	
Fracture type	/	/	/	Structural fracture > Dissolution fracture
Dominated structural fracture aperture range/μm	/	/	/	100–500
Dominated dissolution fracture aperture range/μm	/	/	/	20–100
Dominated structural fracture density range/m^{-1}	/	/	/	1.5–7.5
Dominated structural fracture angle range/°	/	/	/	20–70
Throat type	Lamellar throat > Necking throat > Tubular throat			
Throat width/μm	Lamellar throat < 1.0; Necking throat > 10; Tubular throat < 10			
Threshold displacement pressure/MPa	5.0	2.0	0.3	0.1
Maximum mercury saturation/%	34.97	46.43	56.23	71.26
Dominated pore throat radius range at 13.15 μm scale/μm	0–18.81	0–20.40	0–49.87	0–13.24

(continued)

Table 1.11 (continued)

Pore throat parameters	Matrix type	Pore type	Cavity type	Fracture-cavity type
Proportion of pore throat volume occupied by dominated pore throats at 13.15 μm scale/%	69.83	62.90	54.89	56.00
Dominated pore throat radius range at 0.98 μm scale/μm	0–2.02	0–2.34	0–12.72	0–6.11
Proportion of pore throat volume occupied by dominated pore throats at 0.98 μm scale/%	42.97	33.18	54.80	57.66
Largest pore throat radius at 13.15 μm scale/μm	170.39	185.8	470.65	347.28
Largest pore throat radius at 0.98 μm scale/μm	13.53	21.82	52.35	24.99
Pore throat number at 13.15 μm scale	187,089	263,600	14,258	673,094
Pore throat number at 0.98 μm scale	4293	53,795	4007	16,888
Number of pore throats with a radius greater than 100 μm at 13.15 μm scale	131	50	701	2655
Proportion of the number of pore throats with a radius greater than 100 μm/%	0.07	0.02	4.92	0.39
Proportion of pore throat volume occupied by pore throats with a radius greater than 100 μm/%	1.45	0.87	18.69	6.10

(continued)

Table 1.11 (continued)

Pore throat parameters	Matrix type	Pore type	Cavity type	Fracture-cavity type
Number of pore throats with a radius greater than 10 μm at 0.98 μm scale	14	155	920	304
Proportion of the number of pore throats with a radius greater than 10 μm/%	0.33	0.29	22.96	1.80
Proportion of pore throat volume occupied by pore throats with a radius greater than 10 μm/%	5.09	8.62	61.20	17.30
Average coordination number at 13.15 μm scale	2.81	3.56	3.37	5.46
Proportion of coordination numbers greater than 10 at 13.15 μm scale /%	0.56	2.89	2.03	13.47
Average coordination number at 0.98 μm scale	2.44	4.13	4.51	4.79
Total pore throat volume/μm^3	3.23×10^{10}	6.29×10^{10}	1.37×10^{11}	9.01×10^{10}
Proportion of effective pore throats/%	40.83	53.71	44.56	70.97
Connected pore throat volume/μm^3	1.32×10^{10}	3.06×10^{10}	7.63×10^{10}	6.39×10^{10}
Reservoir space	Pore	Pore	Pore, cavity	Pore, cavity, fracture
Storage capacity	Weak	Moderate	Strong	Strong
Percolation channel	Throat	Throat	Throat, bedding cavity	Throat, fracture, bedding cavity
Percolation capacity	Weak	Weak	Moderate	Strong

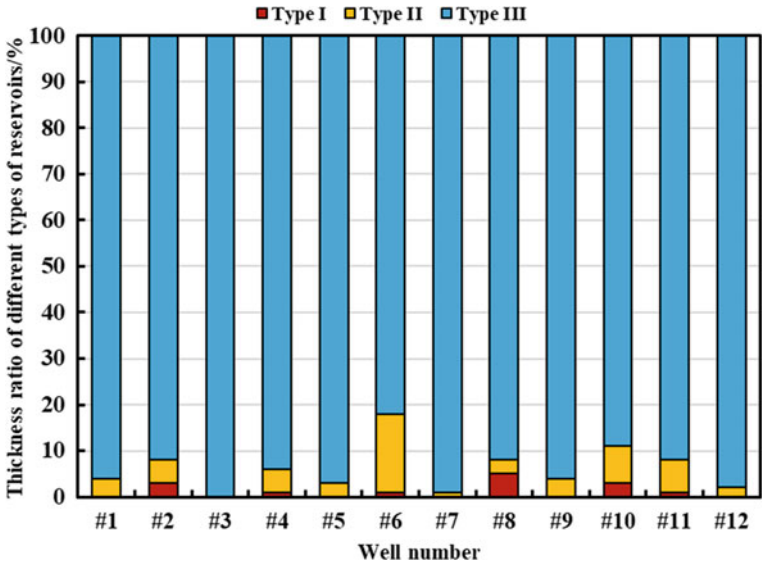

Fig. 1.52 Thickness proportions of the three types of reservoirs in different wells

(average 13.22%). The relatively high average porosity of the three types of dolomite directly reflects the storage capacity of the Deng IV Member reservoir, laying the foundation for the formation of high-quality natural gas reservoirs. There are small difference in mineral types and proportion of different areas in the Deng IV Member reservoir. The mineral composition is dominated by dolomite (average 88.63%), followed by silicoide (average 4.38%) and organic matter (average 4.31%). The initial water saturation in the high-permeability area with developed fractures is relatively low, while that in the low-permeability area with developed microscopic pores is relative high.

(2) The conventional petrophysical measurements of cores reflects that the extremely strong reservoir heterogeneity of ultradeep carbonate gas reservoirs is caused by widely developed fractures. The petrophysical properties of the Deng IV Member reservoir are generally low porosity (average 3.91%), low permeability (average 1.02 mD) and low water saturation (average 23.26%). However, the developed cavities and fractures can effectively increase the porosity and permeability of some reservoirs, thereby forming high-porosity and high-permeability intervals locally.

(3) The core observation and casting thin section images show that the reservoir spaces of the ultradeep carbonate reservoir are composed of pores, cavities and fractures. Secondary pores dominated by interP dissolution and interC dissolution pores are the most important reservoir space types. The primary fenestriform cavities and the secondary dissolution cavities with different sizes are important supplements to the reservoir space and further improve the storage capacity. The

generally developed fractures connect the isolated pores and cavities to effectively improve the percolation capacity. SEM images show that the reservoir develops three types of throats of necking (width > 10 μm), tubular (width < 1 μm) and lamellar (width < 10 μm). The development frequency of the necking throat and the tubular throat is higher than that of the tubular throat.

(4) The ultradeep carbonate gas reservoirs with widely developed fractures and cavities could be subdivided into four types of reservoirs based on the comprehensive analysis of capillary pressure curves and other test results, namely matrix type, pore type, cavity type and fracture-cavity type. Specifically, the development of fractures increases the maximum mercury saturation and make the capillary pressure curve present a relatively horizontal stage with a gentle slope. The development of cavities reduces the threshold displacement pressure and make the capillary pressure curve present a double-step characteristic.

(5) The reservoir temperature of the Deng IV Member ranges from 149.5 to 164.2 °C, with an average value of 155.7 °C. The pressure coefficient of the Deng IV Member ranges from 1.06 to 1.16, with an average value of 1.12. The reservoir pressure of the Deng IV Member range from 56.50 to 57.09 MPa, with an average value of 56.83 MPa. Therefore, the Deng IV Member reservoir could be classified as a high-temperature and normal-pressure gas reservoir. The composition of natural gas is dominated by methane, with moderate amounts of hydrogen sulfide and carbon dioxide, as well as tiny amounts of ethane, propane, helium and nitrogen. The water type of the formation water is calcium chloride, indicating that the gas reservoir is well preserved. The cumulative thickness of the reservoirs drilled by different wells in the Deng IV Member ranges from 11.50 to 116.80 m, with an average value of 41.05 m.

(6) The multiscale reservoir spaces of ultradeep carbonate gas reservoirs, including structural fractures, dissolution fractures, dissolution cavities, macroscopic pores, microscopic pores, and rock matrix, could be observed through 2D CT scanning images of representative core samples. More importantly, these dissolution fractures connect multiple dissolution pore-cavities in series to form a beaded connection, thereby effectively improving the connectivity and percolation capacity of the reservoir space. In addition, these dissolution cavities are mainly bedding cavities or distributed around karst breccias, thereby improving horizontal connectivity. Therefore, the development frequency and distribution pattern of these cavities not only significantly improve the storage capacity, but also play a certain role in improving the percolation capacity.

(7) The differences in pore throat radius, volume and coordination number distribution characteristics of the four types of reservoirs were quantified by reconstructing 3D pore throat network models. The reservoir space of fracture-cavity type reservoirs is mainly controlled by cavities and multiscale pore throats, with the best connectivity of reservoir space. The reservoir space of cavity type reservoirs is dominated by cavities and macroscopic pore throats, with the moderate connectivity. The reservoir space of pore type reservoirs is composed of multiscale pore throats, with the moderate connectivity. The reservoir space of matrix type reservoirs is dominated by locally developed microscopic pore throats, with

the worst connectivity. Although the reservoir space of cavity type reservoirs is similar to or even higher than that of fracture-cavity type reservoirs, the proportion of effective reservoir space affected by connectivity is relatively low. The widespread development of fractures is the main reason why the connectivity and effective reservoir space of fracture-cavity type reservoirs are higher than that of other types.

(8) It was concluded that the Deng IV Member is dominated by fracture-cavity type reservoirs through the comprehensive analysis of macro, micro, static and dynamic data. Matrix type reservoirs are basically ineffective reservoirs, and pore type reservoirs have relatively poor storage and percolation capacities. However, fractures and bedding cavities widely developed in fracture-cavity type and cavity type reservoirs greatly improves the percolation capacity of reservoir spaces, and the cavities are an important supplement to the storage capacity. More importantly, a reasonable combination of cavities and fractures is the basis for the effective exploitation of ultradeep carbonate gas reservoirs. Accurate exploration of favorable distribution areas of fractures and cavities is the prerequisite for efficient development of ultradeep carbonate gas reservoirs. Reservoir reconstruction in pore-cavities developed areas with high-porosity and low-permeability is the key to improving the gas recovery factor of ultradeep carbonate gas reservoirs.

References

Al-Kharusi, A. S., & Blunt, M. J. (2007). Network extraction from sandstone and carbonate pore space images. *Journal of Petroleum Science and Engineering, 56*, 219–231.

Bai, B., Zhu, R. K., Wu, S. T., Yang, W. J., Gelb, J., et al. (2013). Multiscale method of Nano(Micro)-CT study on microscopic pore structure of tight sandstone of Yanchang Formation, Ordos Basin. *Petroleum Exploration and Development, 40*, 354–358.

Choquette, P. W., & Pray, L. C. (1970). Geologic nomenclature and classification of porosity in sedimentary carbonates. *AAPG Bulletin, 54*, 207–250.

Corbett, P. W. M., Wang, H., Camara, R. N., Tavares, A. C., de Almeida, L. F. B., et al. (2017). Using the porosity exponent (m) and pore-scale resistivity modelling to understand pore fabric types in coquinas (Barremian-Aptian) of the Morro do Chaves Formation, NE Brazil. *Marine and Petroleum Geology, 88*, 628–647.

Du, J., Zou, C., Xu, C., He, H., Shen, P., Yang, Y., et al. (2014). Theoretical and technical innovations in strategic discovery of a giant gas field in Cambrian Longwangmiao Formation of central Sichuan paleo-uplift, Sichuan Basin. *Petroleum Exploration and Development, 41*(3), 294–305.

Gao, H., & Li, H. A. (2016). Pore structure characterization, permeability evaluation and enhanced gas recovery techniques of tight gas sandstones. *Journal of Natural Gas Science and Engineering, 28*, 536–547.

Garing, C., Luquot, L., Pezard, P. A., & Gouze, P. (2014). Electrical and flow properties of highly heterogeneous carbonate rocks. *AAPG Bulletin, 98*, 49–66.

Gundogar, A. S., Ross, C. M., Akin, S., & Kovscek, A. R. (2016). Multiscale pore structure characterization of middle east carbonates. *Journal of Petroleum Science and Engineering, 146*, 570–583.

Hulea, I. N., & Nicholls, C. A. (2012). Carbonate rock characterization and modeling: Capillary pressure and permeability in multimodal rocks—A look beyond sample specific heterogeneity. *AAPG Bulletin, 96*, 1627–1642.

Jiao, L., Adersen, P. Ø., Zhou, J., & Cai, J. (2020). Applications of mercury intrusion capillary pressure for pore structures: A review. *Capillarity, 3*(4), 62–74.

Jin, M., Tan, X., Tong, M., Zeng, W., Liu, H., Zhong, B., et al. (2017). Karst paleogeomorphology of the fourth Member of Sinian Dengying Formation in Gaoshiti-Moxi area, Sichuan Basin, SW China: Restoration and geological significance. *Petroleum Exploration and Development, 44*(1), 58–68.

Lai, J., Wang, G., Wang, Z., Jing, C., & Fan, X. (2018). A review on pore structure characterization in tight sandstones. *Earth-Science Reviews, 177*, 436–457.

Li, L., Tan, X., Zeng, W., Zhou, T., Yang, Y., Hong, H., et al. (2013). Development and reservoir significance of mud mounds in Sinian Dengying Formation, Sichuan Basin. *Petroleum Exploration and Development, 40*(6), 714–721.

Li, P., Sun, W., Wu, B. L., Gao, Y. L., & Du, K. (2018). Occurrence characteristics and influential factors of movable fluids in pores with different structures of Chang 63 reservoir, Huaqing Oilfield, Ordos Basin, China. *Marine and Petroleum Geology, 97*, 480–492.

Luo, B., Yang, Y., Luo, W., Wen, L., Chen, K., et al. (2015). Controlling factors and distribution of reservoir development in Dengying Formation of paleo-uplift in central Sichuan Basin. *Acta Petrolei Sinica, 36*(4), 416–426.

Luo, Q., Zhang, C., Dai, Q. Q., Liu, D. D., Yang, W., et al. (2017). Characterization of compact carbonate pore–throat network systems in the Xiagou Formation in Qingxi Sag, Jiuquan Basin, China. *Journal of Petroleum Science and Engineering, 159*, 853–868.

Makhloufi, Y., Collin, P. Y., Bergerat, F., Casteleyn, L., Claes, S., et al. (2013). Impact of sedimentology and diagenesis on the petrophysical properties of a tight Oolitic carbonate reservoir. The case of the Oolithe Blanche Formation (Bathonian, Paris Basin, France). *Marine and Petroleum Geology, 48*, 323–340.

Matonti, C., Guglielmi, Y., Viseur, S., Bruna, P. O., Borgomano, J., et al. (2015). Heterogeneities and diagenetic control on the spatial distribution of carbonate rocks acoustic properties at the outcrop scale. *Tectonophysics, 638*, 94–111.

Norbisrath, J. H., Eberli, G. P., Laurich, B., Desbois, G., Weger, R. J., et al. (2015). Electrical and fluid flow properties of carbonate microporosity types from multiscale digital image analysis and mercury injection. *AAPG Bulletin, 99*, 2077–2098.

Okolo, G. N., Everson, R. C., Neomagus, H. W., Roberts, M. J., & Sakurovs, R. (2015). Comparing the porosity and surface areas of coal as measured by gas adsorption, mercury intrusion and SAXS techniques. *Fuel, 141*, 293–304.

Peng, S., Zhang, T., Loucks, R. G., & Shultz, J. (2017). Application of mercury injection capillary pressure to mudrocks: Conformance and compression corrections. *Marine and Petroleum Geology, 88*, 30–40.

Ronchi, P., & Cruciani, F. (2015). Continental carbonates as a hydrocarbon reservoir, an analog case study from the travertine of Saturnia, Italy. *AAPG Bulletin, 99*, 711–734.

Schmitt, M., Fernandes, C. P., Neto, J. C., Wolf, F. G., & Santos, V. D. (2013). Characterization of pore systems in seal rocks using nitrogen gas adsorption combined with mercury injection capillary pressure techniques. *Marine and Petroleum Geology, 39*(1), 138–149.

Silin, D. B., Jin, G. D., & Patzek, T. W. (2008). Robust determination of the pore-space morphology in sedimentary rocks. *Journal of Petroleum Technology, 56*(5), 69–70.

Wang, L., He, Y. M., Peng, X., Deng, H., Liu, Y. C., et al. (2020). Pore structure characteristics of an ultradeep carbonate gas reservoir and their effects on gas storage and percolation capacities in the Deng IV member, Gaoshiti-Moxi area, Sichuan Basin, SW China. *Marine and Petroleum Geology, 111*, 44–65.

Wang, L., Yang, S. L., Liu, Y. C., Xu, W., Deng, H., et al. (2017). Experimental investigation on gas supply capability of commingled production in a fracture-cavity carbonate gas reservoir. *Petroleum Exploration and Development, 44*, 824–833.

Wang, L., Yang, S. L., Peng, X., Deng, H., Meng, Z., et al. (2018a). An improved visual investigation on gas–water flow characteristics and trapped gas formation mechanism of fracture–cavity carbonate gas reservoir. *Journal of Natural Gas Science and Engineering, 49*, 213–226.

Wang, L., Yang, S. L., Peng, X., Liao, Y., Liu, Y. C., et al. (2018b). Visual investigation of the occurrence characteristics of multi-type formation water in a fracture–cavity carbonate gas reservoir. *Energies, 11*, 661.

Xu, H., Wei, G., Jia, C., Yang, W., Zhou, T., et al. (2012). Tectonic evolution of the Leshan-Longnüsi paleo-uplift and its control on gas accumulation in the Sinian strata, Sichuan Basin. *Petroleum Exploration & Development, 39*(4), 436–446.

Yang, Y., Wen, L., Luo, B., Wang, W., & Shan, S. (2016). Hydrocarbon accumulation of Sinian natural gas reservoirs, Leshan-Longnüsi paleohigh, Sichuan Basin, SW China. *Petroleum Exploration and Development, 43*(2), 197–207.

Zhang, K., Pang, X. Q., Zhao, Z. F., Shao, X. H., Zhang, X., et al. (2018). Pore structure and fractal analysis of Lower Carboniferous carbonate reservoirs in the Marsel area, Chu-Sarysu Basin. *Marine and Petroleum Geology, 93*, 451–467.

Zhang, Y., Pe-Piper, G., & Piper, D. J. (2015). How sandstone porosity and permeability vary with diagenetic minerals in the Scotian Basin, offshore eastern Canada: Implications for reservoir quality. *Marine and Petroleum Geology, 63*, 28–45.

Zhang, Y. X., Yang, S. L., Zhang, Z., Li, Q., Deng, H., et al. (2022). Multiscale pore structure characterization of an ultra-deep carbonate gas reservoir. *Journal of Petroleum Science and Engineering, 208*, 109751.

Zou, C. N., Du, J. H., Xu, C. C., Wang, Z. C., Zhang, B. M., et al. (2014). Formation, distribution, resource potential, and discovery of Sinian-Cambrian giant gas field, Sichuan Basin, SW China. *Petroleum Exploration and Development, 41*, 306–325.

Chapter 2
Special Percolation Mechanism of the Ultradeep Carbonate Gas Reservoir

Deep reservoir burial, diverse reservoir media and complex gas–water relationship are the typical characteristics of ultradeep carbonate gas reservoirs. The burial depth of more than 4500 m makes the temperature and pressure conditions of this type of gas reservoir far higher than that of conventional gas reservoirs. The pore structure and fluids properties of the reservoir will change greatly under ultra-high temperature and pressure, thereby affecting the percolation characteristics of single-phase and multiphase fluids under reservoir conditions (Sidiq et al., 2017; Wang et al., 2020). In addition, the coexistence pattern of pores, fractures and cavities makes the ultradeep carbonate gas reservoirs could be divided into pore type, cavity type and fracture-cavity type. The flow types in porous media include percolation in microscopic pores and macroscopic fractures, and free flow in cavities. Multi-type reservoir characteristics and heterogeneity make the percolation mechanism of ultradeep carbonate gas reservoirs more complicated (Li et al., 2017b). The traditional percolation theory of hydrocarbon reservoirs cannot accurately describe the percolation characteristics of this type of gas reservoir (Fang et al., 2015; Wang et al., 2017c). It is necessary to deeply study the percolation mechanism considering the ultra-high temperature and pressure conditions, diverse pore structure characteristics and complex water content conditions of ultradeep carbonate gas reservoirs.

Currently, there are few investigations on the special percolation mechanism of ultradeep carbonate gas reservoirs in the world. The existing research cannot completely simulate the temperature and pressure conditions of ultradeep reservoirs because of the limitations of physical simulation experimental equipments and techniques (Li et al., 2017a). However, the results and conclusions obtained by conventional experimental studies are not suitable for ultradeep carbonate gas reservoirs. Therefore, the difficulties of ultra-high temperature and pressure physical simulation experiments were initially analyzed, and then the jointly developed ultra-high temperature and pressure physical simulation experimental system and experimental method were introduced. Subsequently, a series of physical simulation experiments of gas single-phase percolation under different water saturation conditions were conducted on the basis of completely simulating the temperature and

© The Author(s), under exclusive license to Springer Nature Singapore Pte Ltd. 2023

L. Wang, *Ultradeep Carbonate Gas Reservoirs*,
https://doi.org/10.1007/978-981-19-9708-2_2

pressure conditions of the reservoir. The gas phase percolation characteristics and percolation capacities of different types of carbonate gas reservoirs were revealed, and the influencing factors of gas phase percolation were analyzed. Then, a trinomial percolation mathematical model suitable for ultradeep carbonate gas reservoirs was established based on the physical simulation experimental results of gas phase percolation. The influence of various factors on gas production was evaluated through percolation mathematical model, and the dominant factors affecting gas production capacity of ultradeep carbonate gas reservoirs were determined. Finally, a series of gas–water two-phase percolation experiments were conducted on core samples of different types of carbonate reservoirs under conventional and reservoir conditions, respectively. The standard relative permeability curves and two-phase percolation characteristic parameters of various types of reservoirs were obtained. The influencing mechanism of pore structure, temperature and pressure conditions, and core sample size on the two-phase percolation law was analyzed.

2.1 Ultra-High Temperature and Pressure Physical Simulation Experiment Technique

2.1.1 Difficulties and Countermeasures in Physical Simulation Experiment of Ultra-High Temperature and Pressure

Experiment is a bridge to understand the material word, and physical simulation experiment is the most direct and effective method to investigate the percolation mechanism of fluid in the porous media. The accuracy and applicability of the physical simulation experiment results depend on whether the experimental materials and conditions are consistent with the actual oil and gas reservoirs. Therefore, rock cores obtained from coring wells are generally selected as experimental samples to simulate hydrocarbon reservoirs, and experimental fluids are prepared to simulate reservoir fluids according to the composition analysis results of produced fluids. However, the simulation of reservoir temperature and pressure is more difficult than the simulation of actual reservoir rocks and fluids, especially for the ultradeep carbonate gas reservoir. As introduced in Chap. 1, the average temperature and pore pressure of the Deng IV Member reach 155.7 °C and 56.83 MPa. Furthermore, it is necessary to simulate the overburden pressure of the reservoir by exerting confining pressure to the core in the physical simulation experiment. The average overburden pressure of the Deng IV Member reservoir is up to 138 MPa, which is much higher than other reported oil and gas reservoirs. Only by fully simulating the temperature and pressure conditions of ultradeep carbonate gas reservoirs, the experimental results obtained through physical simulation can truly reflect the fluids percolation characteristics and percolation capacities in actual reservoirs. Nevertheless, the ultra-high temperature and pressure conditions have strict requirements for experimental equipments and

materials, as well as experimental procedures and safety. Before our investigations on the Deng IV Member ultradeep carbonate gas reservoir were published, there was no physical simulation experiment research that can simulate ultra-high temperature and pressure conditions (Wang et al., 2017a). In previous physical simulation experiment studies, the experimental confining pressure and flowing pressure were simultaneously reduced to a certain extent to keep the effective stress consistent with the actual reservoir. In addition, the thermostat is the most commonly used core heating equipment in physical simulation experiments. The experimental temperature was also reduced appropriately to prevent the experimenter from being scalded when operating in the thermostat. However, the application effects of the relative permeability, percolation capacity and production characteristics obtained from physical simulation experiments under relatively low temperature and pressure conditions is not satisfactory in ultradeep reservoir.

Deep and ultradeep oil and gas reservoirs gradually replace shallow and medium oil and gas reservoirs and become an significant field of fossil fuels in the future. Relevant theoretical investigations on deep and ultradeep oil and gas reservoirs by reducing the experimental conditions of physical simulation cannot meet the requirements of the field. Therefore, ultra-high temperature and pressure physical simulation experiment technique is an important prerequisite for theoretical investigations of ultradeep carbonate gas reservoirs. The main difficults of ultra-high temperature and pressure physical simulation experiment technique were summarize through long-term theoretical studies and practice. These difficulties are reflected in two aspects, namely experimental equipments and experimental methods. The four main difficulties of experimental equipments are summarized as follows.

(1) The heating rate of the conventional thermostat gradually decreases after 100 °C, and every increase of 1 °C requires a lot of time. However, the prolongation of the experimental period further increases the risk of experimental failure, because the life of the sealing material under ultra-high temperature and pressure is greatly shortened. In addition, it is necessary to open the thermostat frequently to operate valves during the physical simulation experiment, resulting in the sharp fluctuation in the temperature of the experiment system. The temperature fluctuation may cause changes in the occurrence state and percolation characteristic of the fluid in the core, resulting in errors in the experimental results. The temperature fluctuations before and after opening and closing the thermostat are illustrated in Fig. 2.1. It reflects that the temperature fluctuated slightly in the range of ± 0.5 °C before the thermostat was opened, whereas the temperature dropped rapidly after the thermostat was opened. The temperature dropped by about 6 °C within 18 s after the thermostat was opened. The temperature would continue to decrease with the increase of valve operation time. It took tens of minutes for the temperature of the thermostat to rise to 150 °C again. Strictly speaking, the experimental data obtained during this period cannot meet the requirement. The more the thermostat is opened during the experiment, the more the accuracy of the experiment result cannot be guaranteed. Moreover, one thing that is easily overlooked is that the temperature of the thermostat

cannot represent the temperature of the sample in the core holder. In order to compare the temperature difference between the thermostat and the core holder, a temperature sensor was added and the probe was placed inside the core holder. Then the core holder was placed in the thermostat for heating, and the internal temperatures of the thermostat and the core holder were recorded simultaneously every 30 min. The temperature data of the thermostat and the core holder at the same time are illustrated in Fig. 2.2. It shows that the temperature in the core holder cannot reach the temperature set by the thermostat, and the temperature difference between the two slowly increases with the increase of temperature. The reason is that the heat transmit from the thermostat to the core sample needs to pass through the thick metal wall and rubber sleeve, and there is a hysteresis effect in the heat transmit in different media. Therefore, the thermostat can only maintain the internal ambient temperature at a certain preset value, and the temperature of the core sample is lower than this value. Although the temperature difference between the thermostat and the core holder decreases slowly as the heating time increases, a lot of time is wasted. However, long-term heating not only reduces the experiment efficiency, but also increases the risk of experiment failure. The reasons for the failure of the experiment are also explained later. More importantly, the heat escaping when opening the thermostat may scald the experimenter. Therefore, it is necessary to improve the heating method of the core system to improve the heating efficiency and avoid temperature fluctuations.

(2) Providing high and stable pressure for the experimental system is another difficulty in the ultra-high temperature and pressure physical simulation experiment. The experimental pressure system includes the confining pressure that simulates the overburden pressure, the flowing pressure that simulates the reservoir pressure, and the back pressure that simulates the bottom hole pressure. According to the pressure data of the Deng IV Member reservoir, the confining pressure

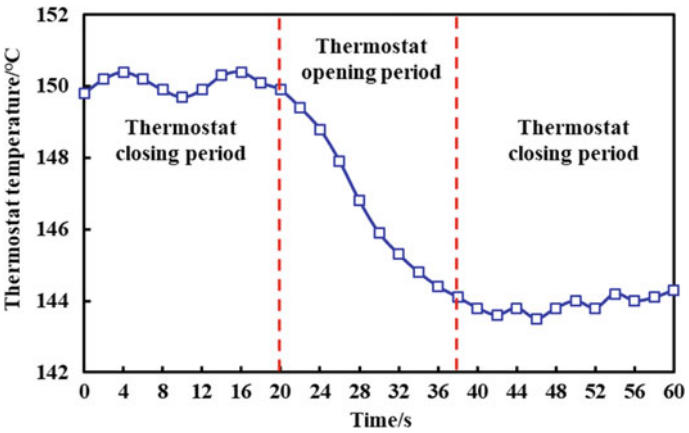

Fig. 2.1 Temperature fluctuations before and after opening and closing the thermostat

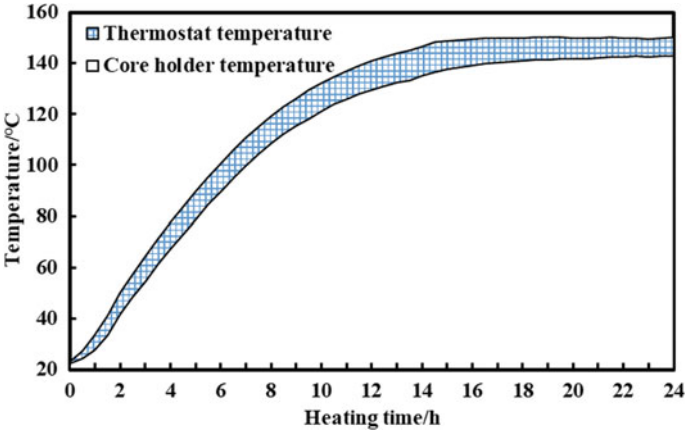

Fig. 2.2 Temperature difference between the thermostat and the core holder at different times

pump needs to provide a stable working pressure of 138 MPa, and the syringe pump and back-pressure pump need to provide an adjustable and stable working pressure of 58 MPa. Our laboratory took the lead in studying the reservoir characteristics and percolation mechanism of ultradeep carbonate gas reservoirs in 2015. However, the upper limit of the working pressure of the commonly used pump at that time was about 60 MPa, which was far lower than the requirement of the confining pressure. Furthermore, these pumps can barely meet the requirements of flowing pressure and back pressure, because the practical results show that maintaining the limit pressure for a long time may lead to fluid flow instability or even equipment breakdown. Therefore, it is necessary to develop sing-cylinder and double-cylinder pumps with ultra-high working pressure according to experimental requirements. In addition, the accessories and pipelines connecting various equipments in the experimental system should also be upgraded simultaneously with the significance increase in experimental pressure. This is because the thickness and materials of the conventional accessories and pipelines cannot meet the requirement of explosion protection under high pressure, and the narrow channel in the pipeline cannot allow the high pressure fluid to flow stably at high speed. These accessories mainly include plugs, three-way valves, six-way valves, back-pressure valves and sensors.

(3) Rubber sleeves and sealing rings are indispensable experimental materials in physical simulation experiments. The rubber sleeve is used to wrap the sample in the core holder and transmit the confining pressure to the sample. The sealing ring is used to seal each port of the equipment to prevent fluid leakage and pressure release. The quality of rubber sleeves and sealing rings directly affects the success rate of physical simulation experiments. However, the life of these experimental materials made of rubber is greatly shortened under ultra-high temperature and pressure. This is because the chemical bond between rubber atoms breaks at high temperature, leading to rubber aging. A certain range of

(a) Deformation of rubber sleeves (b) Aging and breakage of seal rings

Fig. 2.3 Deformation of rubber sleeves and breakage of seal rings after ultra-high temperature and pressure experiments

pressure variations in the experimental system may cause the fracture or deformation of the aged rubber. Figure 2.3 shows the deformed rubber sleeves and broken sealing rings taken out after the failure of ultra-high temperature and pressure experiments. Moreover, some rubber residues could be found at the ports of equipments and on the surfaces of core samples. This is because the rubber material may be carbonized or even lose its performance as the duration of ultra-high temperature and pressure experiments increases. The upper limit of working temperature of sleeves and sealing rings used in conventional experiments is generally lower than 100 °C. Therefore, in order to improve the success rate of ultra-high temperature and pressure experiments, it is necessary to select rubber materials with excellent heat resistance to make sleeves and sealing rings. The heat resistance of rubber can be evaluated by measuring its tensile strength, hardness and other physical properties under ultra-high temperature conditions.

(4) The accurate measurement of important parameters in physical simulation experiments is a the key to ensuring the accurate of experimental results. These parameters mainly include upstream pressure, downstream pressure and fluid flow rates at the outlet. The measurement error mainly comes from the experimental equipment, the experimental environment and the experimenter. Different from the physical simulation experiments of conventional oil and gas reservoirs, ultradeep carbonate gas reservoirs have both fracture-cavity type reservoirs with high petrophysical properties and pore type reservoirs with low petrophysical properties. The permeability difference between the two types of reservoirs is 2 to 4 orders of magnitude. Therefore, the experimental flow rates of different types of cores under the same pressure differential is quite different. If a measuring instrument with a fixed range is used to measure flow rates of different levels, certain errors will inevitably occur. Different measuring equipments with different measuring ranges should be selected for different types of core samples. Environmental error refers to the measurement error

caused by the variation of environmental conditions during the measurement process. Temperature fluctuations, especially pressure fluctuations, may cause large errors in flow rate. Accordingly, the temperature and pressure data should also be measured simultaneously with the flow rate data to ensure that each flow rate is obtained under stable temperature and pressure conditions. In addition, personal errors from experimenters are also inevitable, especially in the measurement of dynamic data. Therefore, it is necessary to select appropriate experimental equipments and methods to reduce these test errors.

In summary, it is necessary to develop a set of multi-functional physical simulation experimental platform with ultra-high temperature and pressure resistance, high heating and pressurization efficiency, accurate parameter measurement and high safety. In addition, the method of physical simulation experiments also needs to be targeted improved. The improvement of the conventional physical simulation experimental method includes the following three aspects.

(1) When the experimental equipments can reach the required temperature and pressure, it is crucial to adopt reasonable methods to raise the experimental system to the predetermined temperature and pressure conditions. The purpose of this is to ensure that the core will not change its basic petrophysical properties and pore structure during the heating and pressurization process. This is because all the physical simulation experiment results are based on the core with specific petrophysical properties and pore structure. Unreasonable heating and pressurization methods may change core permeability, or even close or form fractures. Gay-Lussac's Law states that a certain mass of gas expands with the increase of temperature under the premise of constant pressure. However, the core holder is sealed during the experiment, and the gas pressure increases with the increase of temperature according to Charles's Law. The pore pressure in the core system increases slowly and uncontrolled with the increase of heating time in the ultra-high temperature and pressure experiment. Therefore, it is necessary to increase the system temperature first and then increase the pore pressure during the experiment. Even so, the initial gas in the core holder before sealing may also increase the pore pressure to teens of megapascals at a high temperature of 150 °C. The gradually increasing pore pressure during heating process changes the initial effective stress of the core system established according to the actual reservoir conditions. Consequently, the basic petrophysical properties and pore structure of cores may change under the influence of the stress sensitivity effect. How to maintain the initial effective stress during the heating process is an important problem to be solved.
(2) Improving the pressurization efficiency and upper pressure limit is also the key to affect the efficiency and success rate of ultra-high temperature and pressure physical simulation experiments. The pressurization process of the conventional experiment is to inject a certain amount of gas into the upper part of the gas tank through the cylinder, and then inject high-pressure water into the lower part of the gas tank through the syringe pump to push the upper gas into the core system. However, this pressurization method is difficult to increase the pore pressure in

the core system to about 60 MPa in a short time. This is because the pressure of the standard gas cylinder under initial conditions is only approximately 15 MPa. Accordingly, injecting gas into the gas tank through the gas cylinder can only increase the pressure of 0.5 L gas tank to 10 MPa or even lower. However, the amount of gas in the gas tank cannot meet the requirements of gas volume of the experimental pipeline and core system under high pressure, especially in the long-term displacement experiment and multiple core experiment. Each set of experiment needs to replace the gas tank for many times, thereby prolonging the experiment period. In addition, every time the gas tank is replaced, the gas pressure in the gas tank needs to be increased to the core system pressure through the syringe pump, which further increases the experiment time. The higher the core system pressure, the slower the gas pressurization speed in the gas tank. As mentioned above, the success rate of ultra-high temperature and pressure physical simulation experiments decreases with the extension of the experiment time. Therefore, it is necessary to optimize the pressurization method of the experiment to reduce the time cost.

(3) The ultra-high temperature and pressure physical simulation experiments has high requirements on the length and flatness of core samples. The ultradeep carbonate rock is easily broken, which makes the coring process difficult and the coring effect poor. The carbonate cores obtained from the Deng IV Member have the characteristics of short length, uneven end faces and exposed cavities. Short core samples cannot meet the shortest core length requirement of the core holder ($\geq$ 40 mm), and they cannot represent heterogeneous reservoirs well (Fig. 2.4a). Furthermore, it may cause uneven force at both ends of the core with uneven end faces during the pressurization stage of the experiment (Fig. 2.4b). Consequently, the core sample broke in the core holder, leading to the failure of the experiment. The cutting grinding machine can adjust the flatness of the end face, but the blade cutting easily causes the broken of the brittle carbonate rock. Although the commonly used method of polishing the end face of the core with sandpaper can improve the flatness to a certain extent, the failure rate of the experiment is still high. In addition, some core samples with exposed large cavities could also cause the pressurization failure of confining pressure, because the confining pressure may penetrate the rubber sleeve at the location of the large cavity (Fig. 2.4c). As a result, the water that provides confining pressure enters the core and even damages the core. Therefore, it is necessary to further improve the flatness of the end face of carbonate core, and formulate core selection standard to reduce the rates of experimental failure and core damage.

2.1.2 Introduction of Ultra-High Temperature and Pressure Physical Simulation Experiment System

The difficulties in the experimental equipments and methods of ultra-high temperature and pressure physical simulation experiments were summarized through a large

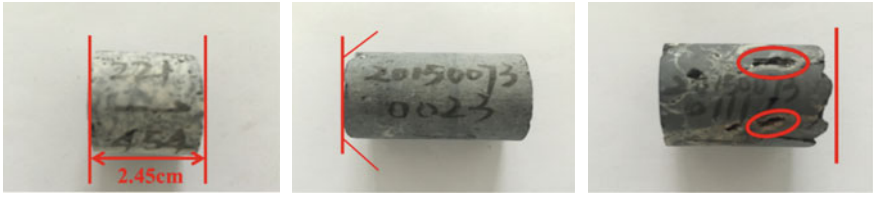

(a) Unqualified core length (b) Uneven core end face (c) Exposed large cavities

Fig. 2.4 Unfavorable characteristics of ultradeep carbonate rock cores

number of tentative experiments. In view of the above-mentioned experimental difficulties, we made improvements one by one. Eventually, a multi-functional physical simulation experiment system of ultra-high temperature and pressure was developed, and an efficient ultra-high temperature and pressure physical simulation experiment process was formed. The four major improvements of the experimental system are as follows.

(1) In order to improve the heating efficiency and avoid temperature fluctuation, it is recommended to use the electric heating jacket to wrap the core system for heating rather than the thermostat heating method (Fig. 2.5a). This heating method can avoid the heat loss and pressure fluctuation caused by opening the thermostat to operate the valve. In addition, the temperature sensor probe is installed inside the core holder to accurately record the core system temperature rather than the ambient temperature in the thermostat. More importantly, the heating efficiency of the electric heating jacket is higher than that of the thermostat, and the stability after reaching the target temperature is also better than the thermostat. Figure 2.6 illustrates the comparison of the time required for the electric heating jacket and the thermostat to heat to 150 °C. The electric heating jacket reached 150°C within 12 h, and the temperature fluctuation range after stabilization was only ± 0.2 °C. It took 17 h for the ambient temperature in the thermostat to reach 150 °C, and the pressure fluctuation range after stabilization was ± 0.5 °C. In addition, the test results show that the electric heating jacket can increase the ambient temperature in the core holder to more than 200 °C, which is higher than the upper limit of the working temperature of the conventional thermostats. More importantly, the heating method of the electric heating jacket gets rid of the space limitation of the thermostat, because the thermostat can accommodate only one large high-pressure core holder. However, multiple core holders are required to be connected in series or in parallel to simulate the horizontal or interlayer heterogeneity of ultradeep carbonate gas reservoirs. Another advantage that cannot be ignored is that the heating method of the electric heating jacket is more economical and safer. The thermal insulation material on the surface of the heating jacket effectively avoids the potential safety hazards caused by heat overflow.

(a) Ultra-high pressure core holder

(b) Confining pressure pump and syringe pump

(c) Intermediate container

(d) Back-pressure pump and air compressor

(f) Automatic data collection system

(g) Electronic flowmeter with multiple measuring ranges

Fig. 2.5 Important components of the ultra-high temperature and pressure physical simulation experiment system

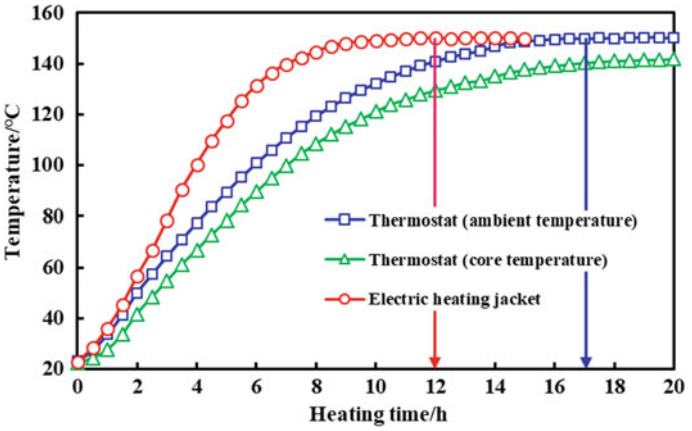

Fig. 2.6 Comparison of the time required for the electric heating jacket and the thermostat to heat to 150 °C

(2) All the experimental pipelines, pumps, intermediate containers, core holders, back-pressure valves and other accessories are made of titanium alloy (Fig. 2.5b–d). There are many reasons for using titanium alloys to develop experimental equipment and accessories. First of all, the specific strength of titanium alloy is far greater than that of other metal structural materials, and it could be used to manufacture equipment and components with high strength, good rigidity and light weight. The engine components, framework, fasteners and landing gear are all made of titanium alloy. The temperature resistance of titanium alloy is far higher than that of aluminum alloy. The titanium alloy can work at 450–500 °C for a long time, whereas the specific strength of aluminum alloy decreases significantly at 150 °C. The corrosion resistance of titanium alloy in humid environment is much better than that of stainless steel. Titanium alloys are extremely resistance to pitting corrosion, acid corrosion and stress corrosion, and are suitable for physical simulation of fluids with various components. Moreover, the heat preservation effect of titanium alloy is excellent because its thermal conductivity is far lower than that of iron and aluminum alloy. Therefore, the experimental equipments and accessories made of titanium alloy can meet all the requirements of ultra-high temperature and pressure physical simulation experiments. The double-cylinder syringe pump, single-cylinder confining pressure pump, single-cylinder back-pressure pump and their accessories were made of titanium alloy, which can provide a stable pressure of 150 MPa. The configuration and technical parameters of the experimental system are shown in Table 2.1.

(3) Fluororubber 246 was finally selected as the material for making sleeves and sealing rings after testing a variety of rubber materials under ultra-high temperature and pressure conditions. Fluororubber 246 is prepared by copolymerization of vinylidene fluoride, tetrafluoroethylene and hexafluoropropylene. The heat

Table 2.1 Configuration and technical parameters of the ultra-high temperature and pressure multi-functional physical simulation experiment system

Serial number	Equipment name	Technical parameters	Number of equipment
1	Confining pressure pump (Single cylinder)	✓ Model: D-250L ✓ Pressure range: 0.01–150 MPa ✓ Flow rate range: 0.001–25 mL/min	1
2	Syringe pump (Double cylinder)	✓ Model: D-250 M ✓ Pressure range: 0.01–150 MPa ✓ Flow rate range: 0.001–25 mL/min	1
3	Back-pressure pump (Single cylinder)	✓ Model: D-250L ✓ Pressure range: 0.01–150 MPa ✓ Flow rate range: 0.001–25 mL/min	1
4	Core holder (Plunger core)	✓ Model: TY-4 ✓ Maximum working pressure: 180 MPa ✓ Maximum working temperature: 200 °C ✓ Specification: Φ25 × 100 mm ✓ Equipped with high-pressure explosion-proof connectors and rubber sleeves	3
5	Core holder (Full-diameter core)	✓ Model: TY-6 ✓ Maximum working pressure: 180 MPa ✓ Maximum working temperature: 200 °C ✓ Specification: Φ70 × 10 mm ✓ Equipped with high-pressure explosion-proof connectors and rubber sleeves	1
6	Back-pressure valve	✓ Model: HY-180 ✓ Maximum working pressure: 150 MPa ✓ Pressure accuracy: ± 0.1 MPa	3

(continued)

Table 2.1 (continued)

Serial number	Equipment name	Technical parameters	Number of equipment
7	Pressure sensor	✓ Model: Senex-D ✓ Pressure range: 150 MPa ✓ Pressure accuracy: ± 0.25%	6
8	Pressure sensor	✓ Model: Senex-D ✓ Pressure range: 80 MPa ✓ Pressure accuracy: ± 0.25%	6
9	Ultra-high pressure pipelines and valves	✓ Model: TC-200 ✓ Maximum working pressure: 200 MPa ✓ Equipped with explosion-proof interface	/
10	Intermediate container (Piston type)	✓ Model: ZR-180 ✓ Maximum working pressure: 180 MPa ✓ Volume: 2000 mL	2
11	Flexible electric heating jacket	✓ Model: RT-120 ✓ Maximum working temperature: 200 °C ✓ Temperature control accuracy: ± 0.1 °C	4
12	Gas booster system	✓ Model: TC-60 ✓ Boost range: 10–60 MPa	1
13	Automatic data collection system	✓ Data collection of temperature, pressure and flow rate ✓ Minimum time interval: 0.5 s	1

resistance of fluororubber 246 is better than that of fluororubber 23 and fluororubber 26, and it can be used for a long time at 250 °C. In addition, fluororubber 246 has excellent stability to high temperature, strong acids, strong base, strong oxidant and solvent. Therefore, this material is widely used in special synthetic rubber products in aviation, aerospace, automotive and other industries. It should be noted although fluororubber 246 can withstand a high temperature of 250 °C, it still cannot maintain its performance for a long time under the dual influence of high temperature and high pressure. Therefore, the key to improve the success rate of ultra-high temperature and pressure experiment is to shorten the experimental period.

(4) In order to obtain flow rate data under stable and accurate temperature and pressure conditions, the temperature and pressure data should also be recorded in real time when measuring the flow rate. Therefore, the fully automatic data collection system and software were installed in the experimental system to monitor the

temperature and pressure data at different times. The minimum time interval for data recording is 0.5 s, and the temperature curve, as well as the pressure curves of upstream, downstream and confining can be drawn (Fig. 2.5e). In addition, the computer can be used to remotely control the opening and closing time of pumps, as well as the flow rate and pressure of pumps. The automation of the experimental system effectively reduces the potential safety hazards brought by the experimental operation under ultra-high temperature and pressure conditions. The experimental flow rate is measured by an electronic flowmeter with multiple measuring ranges (Fig. 2.5f). The flowmeter can automatically switch between a large range (0–30 mL/s) and a small range (0–5 mL/s) according to the actual flow rate, and all data can be transmitted to the computer. Therefore, it not only avoids the equipment error caused by the mismatch between measuring range and flow rate, but also avoids the personal error caused by dynamic data reading. The three major improvements in the experimental process are as follows.

(a) The initial effective stress could be maintained during the heating process through the dynamic monitoring of the data collection system and the dynamic tracking function of pumps. The data collection system can transmit the pore pressure of the core system at different heating times to the computer. Then, the computer automatically controls the pressure variation of the confining pressure pump according to the input effective stress value. The output pressure of the confining pressure pump increases simultaneously with the continuous increase of the pore pressure in the core during the heating process, therefore, the effective stress is always maintained at a value. When the temperature rises to the target value, the confining pressure and pore pressure are increased simultaneously by the computer controlled confining pressure pump and flow pressure pump, and finally the core system reaches the initial reservoir pressure condition.

(b) A two-stage pressurization process and a gas booster system (Fig. 2.7) were designed to improve the pressurization efficiency of flow pressure and reduce the frequency of gas tank replacement. The first stage pressurization means that the gas booster system transmits the gas in the gas cylinder to the intermediate container, and continuously increases the gas pressure in the upper part by controlling the piston of the gas tank. The gas booster system is designed for the high-pressure intermediate container, which can increase the gas pressure of the intermediate container to 60 MPa within 10 min. In addition, the capacity of the customized intermediate container was increased to 2000 mL, and the amount of high-pressure gas in the container can meet the demand for at least one set of ultra-high temperature and pressure experiments. The second stage pressurization means that the syringe pump further increases the gas pressure in the intermediate container to the pressure required for the experiment, and then transmits the gas to the core system. The actual operation process is to rapidly increase the gas pressure of the intermediate container to slightly lower than the

required pressure through the booster system, and then adjust the gas pressure of the intermediate container to meet the experimental requirements through the syringe pump.

(c) The selection and processing standards of experimental cores were formulated to ensure that the carbonate core samples meet the requirements of the ultra-high temperature and pressure physical simulation experiments. The length of carbonate cores must be greater than the minimum space length (40 mm) of the core holder, otherwise the core cannot be clamped by the plugs at both ends of the holder. The surface of the core shall not have large area depressions caused by large size cavities and large aperture fractures, otherwise the rubber sleeve at the core depressions may be punctured by the concentrated confining pressure. The end face of the core must not have gaps and must match exactly with the end face of the core holder plug. Therefore, a diamond wire cutting machine (STX-202A, Simit, China) was used to cut and polish the end face of the experimental core (Fig. 2.7). This machine has excellent applicability to brittle crystals with high hardness and breakable, and the minimum thickness of the cut slice is 0.08 mm. The core samples obtained by diamond wire cutting and polishing are rarely broken due to uneven end faces in the process of pressurization.

The preparation time for ultra-high temperature and pressure physical simulation experiments was shortened from 3–4 days to 1–2 days by improving the heating method, pressurization process and core treatment. Shortening the preparation time

Fig. 2.7 Gas booster system (left image) and small diamond wire cutting machine (right image)

before the formal experiment is the main way to reduce the failure rate of the experiment caused by rubber material denaturation. The ultra-high temperature and pressure physical simulation experiment system and its schematic diagram are shown in Figs. 2.8 and 2.9, respectively. The experimental system could be subdivided into four systems, namely the pressurization system, the injection system, the core system and the data collection system. The customized experimental system and the improved experimental procedure constitute the ultra-high temperature and pressure physical simulation experimental technique suitable for studying the complex percolation mechanism and production characteristics of ultradeep carbonate gas reservoirs.

2.2 Nonlinear Percolation Mechanism of Single-Phase Gas

2.2.1 Experimental Objective

The characteristics of deep burial depth, ultra-high temperature and pressure conditions, strong heterogeneity and diverse reservoir types in the Deng IV Member ultradeep carbonate gas reservoir lead to complex percolation mechanism of gas sing-phase and gas–water two-phase. The purpose of this section is to reveal the gas-phase percolation characteristics and percolation capacities of different types of gas reservoirs in the Deng IV Member, and analyze the influencing factors of gas-phase percolation. Four types of cores (fracture-cavity type, cavity type, pore type and matrix type) with different porosity ranges were selected for the physical simulation experiment of gas-phase percolation under actual reservoir temperature and pressure conditions. The gas-phase percolation capacity of different cores was determined by measuring the stable gas flow rates at the outlet end of the core system under different displacement pressure differentials, and the percolation characteristics of different types of cores were revealed by analyzing the relationship curve between gas flow rate and pressure differential. In addition, the influence of reservoir type, water saturation and displacement pressure differential on gas-phase percolation characteristics and percolation capacity was studied by changing experimental conditions.

2.2.2 Experimental Samples and Conditions

Some carbonate core samples were collected from both the Moxi area and Gaoshiti area in the Deng IV Member reservoir for gas-phase percolation physical simulation experiments. These samples were numbered for identification and use. However, not all samples meet the requirements according to the selection and processing standards of experimental cores. Therefore, it is necessary to use the diamond wire cutting machine to cut and polish the end faces of these samples. The porosity and permeability of each sample were measured by helium porosimeter and overburden

Fig. 2.8 Ultra-high temperature and pressure physical simulation experiment system

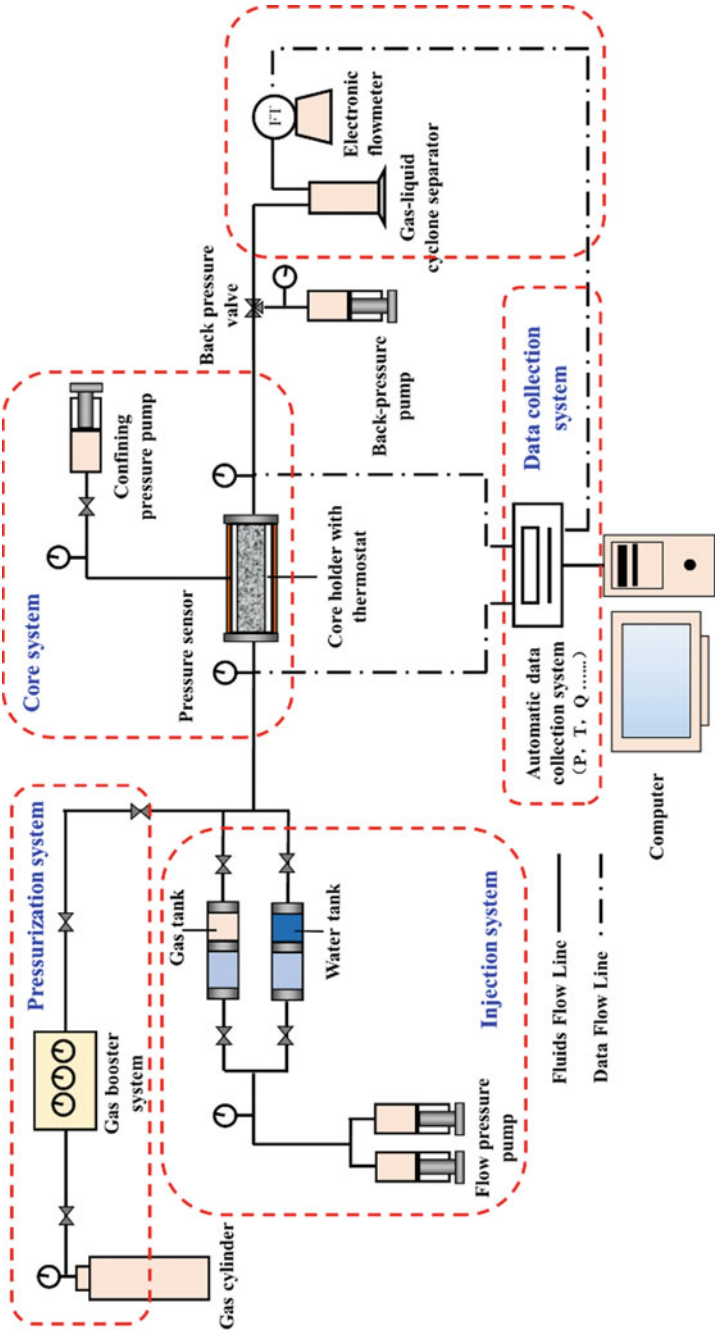

Fig. 2.9 Schematic diagram of the ultra-high temperature and pressure physical simulation experiment system

pulse method before and after core treatment. The comparison results of porosity and permeability before and after core treatment are illustrated in Fig. 2.10. There is little difference in permeability before and after core treatment, but the porosity after treatment is lower than that before treatment. This is because the gap on the end face was cut and the uneven area was also polished during the core treatment. These operations eliminate the influence of the additional volume formed by irregular end faces on porosity measurement. Therefore, the porosity value measured after core treatment is more accurate.

Subsequently, the qualified samples were selected according to the core length and core surface conditions. Furthermore, the petrophysical properties of experimental samples should cover the main petrophysical properties of the Deng IV Member reservoir. The petrophysical parameters of the core samples for the gas-phase percolation experiment are summarized in Table 2.2. These samples not only include four reservoir types, but also cover the main porosity range and permeability range (Fig. 2.11), ensuring the representativeness of the experimental results. The photographs of four types of representative core samples are shown in Fig. 2.12.

The temperature and pressure settings of gas-phase percolation experiments refer to the ultra-high temperature and pressure conditions of Deng IV Member reservoir. The experimental temperature is 150 °C, the confining pressure is 138 MPa and the pore pressure is 56 MPa. High-purity nitrogen was used as experimental gas to simulate natural gas, because the use of natural gas for ultra-high temperature and pressure experiments can easily cause powerful combustion and explosions. The experimental water was prepared in the laboratory based on the chemical composition of the formation water in Deng IV Member formation, as shown in Table 2.3. It should be noted that the experimental water preparation was performed in a reactor rather than in a glass container. The temperature and pressure of the reactor should be maintained continuously after water sample preparation to prevent salt precipitation from the water. Salt precipitation not only changes the experimental water properties, but also may block the flow channel in the pipeline and core sample.

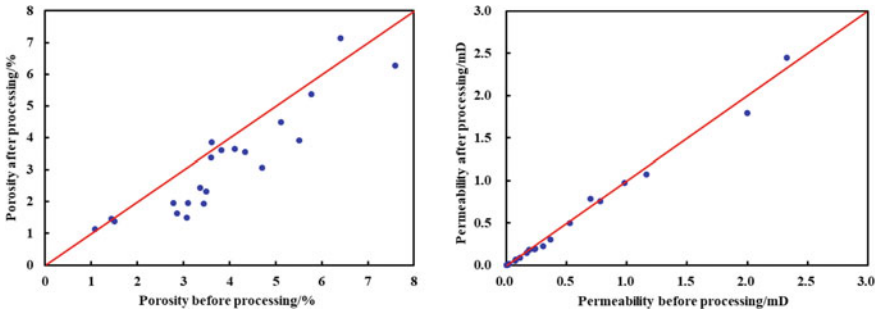

Fig. 2.10 Comparison of porosity (left image) and permeability (right image) before and after core treatment

Table 2.2 Petrophysical parameters of core samples for gas-phase percolation experiments

Core number	Core type	Length/mm	Diameter/mm	Weight/g	Permeability/mD	Porosity/%	Depth/m
28	Fracture-cavity type	37.40	25.10	50.87	1.271	4.30	/
1	Fracture-cavity type	49.54	25.00	63.89	0.739	9.89	5509.47
11	Cavity type	48.92	25.00	63.65	0.287	7.34	5509.47
54	Cavity type	47.10	25.20	65.16	0.105	4.64	5521.56
39	Pore type	38.10	25.04	52.41	0.356	2.42	5518.49
53	Pore type	47.56	25.20	67.26	0.124	2.11	5521.36
118	Pore type	49.10	25.20	68.14	0.084	3.79	5537.05
55	Pore type	48.90	25.20	66.54	0.030	4.21	/
95	Matrix type	46.30	25.20	63.25	0.042	1.64	5531.63
51	Matrix type	47.40	24.96	65.59	0.005	1.89	5516.66

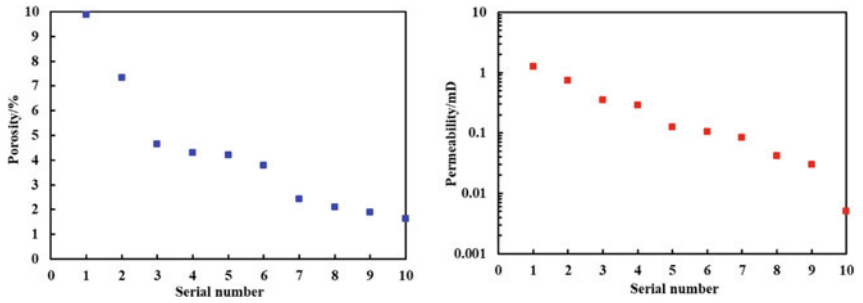

(a) Porosity distribution (b) Permeability distribution

Fig. 2.11 Scatter plots of petrophysical property distribution of experimental cores

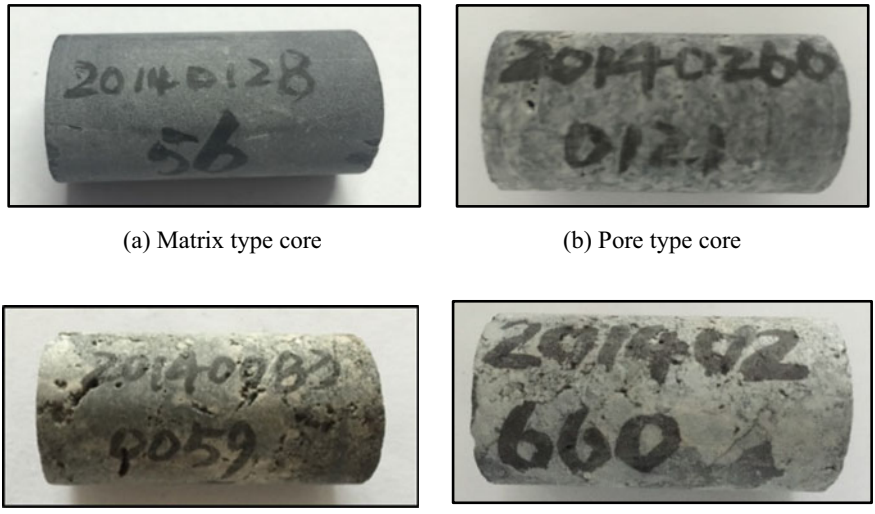

(a) Matrix type core (b) Pore type core

(c) Cavity type core (d) Fracture-cavity type core

Fig. 2.12 Photographs of four types of representative cores from the Deng IV Member reservoir

Table 2.3 Chemical composition of formation water in Deng IV Member

Positive ions (mg/L)					Negative ions (mg/L)			Mineralization degree (mg/L)	Water type
K^+	Na^+	Ca^{2+}	Mg^{2+}	Ba^{2+}	HCO_3^-	Cl^-	SO_4^{2-}		
2596	34,527	1762	233	1467	716	63,596	119	106,241	$CaCl_2$

2.2.3 Experimental Scheme

The frequency distribution histograms of water saturation and porosity in the platform margin belt and intra-platform belt of the Deng IV Member reservoir are illustrated

in Fig. 2.13. The platform margin belt is the key area for the first stage development of the Deng IV Member reservoir, and the intra-platform belt is the area for the second stage development. The comparison results of porosity distribution show that the average porosity values of the platform margin belt and intra-platform belt are 4.13% and 3.41%, respectively. The main difference in porosity is that the proportion of low porosity (2–3%) in the intra-platform belt is higher than that in the platform margin belt. The comparison results of water saturation distribution show that the average water saturations of the platform margin belt and intra-platform belt are 21.47% and 33.03%, respectively. The main difference in water saturation is that the proportion of high water saturation (40–70%) in the intra-platform belt is higher than that in the platform margin belt. Therefore, three types of cores were selected to conduct percolation experiments with different displacement pressure differentials under different water conditions. The water conditions of reservoirs were divided into three types, namely non-water conditions, irreducible water conditions and movable water conditions. The experimental scheme of gas-phase percolation physical simulation is summarized in Table 2.4. Therefore, the effect of reservoir type, water saturation and displacement pressure differential on gas-phase percolation characteristics and percolation capacity were analyzed by comparing experimental results.

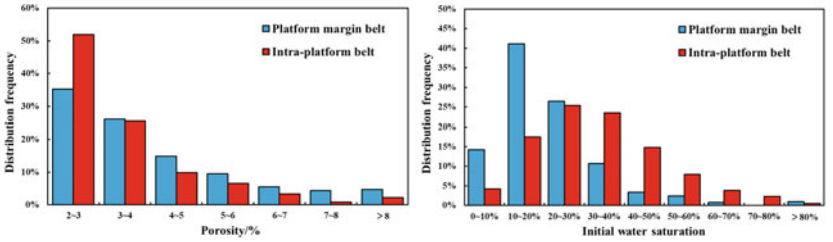

(a) Porosity distribution frequency (b) Water saturation distribution frequency

Fig. 2.13 Frequency distribution histograms of water saturation and porosity in the platform margin belt and intra-platform belt of the Deng IV Member reservoir

Table 2.4 Gas-phase percolation physical simulation experimental scheme

Core sample type	Matrix type	Pore type	Cavity type	Fracture-cavity type
Porosity range/%	0–2	2–4	4–8	4–10
Permeability range/mD	< 0.01	0.01–1.0	0.1–1.0	0.1–10
Number of cores	2	4	2	2
Initial water saturation condition	Water saturations: 0, 10, 20, 30, 40, 50, and 60% Water conditions: non-water, irreducible water, and movable water			
Displacement pressure differential (MPa)	0.2, 0.4, 0.6, 0.8, 1.0, 1.2, 1.4, 1.6, 1.8, 2.0, 2.5, 3.0, 3.5, 4.0, 4.5, 5.0, 6.0, 7.0, 8.0, 9.0 and 10.0 MPa			

2.2.4 Experimental Procedure

The detailed experimental procedure of the gas-phase percolation experiment under ultra-high temperature and pressure conditions is as follows. (1) The gas in the intermediate container was pressurized to 50 MPa through the gas booster system, and then connected to the experimental system. (2) The experimental core was placed in the core holder after being cleaned and dried, and then the experimental system was connected according to Fig. 2.9. (3) The confining pressure of the core system was increased to 5 MPa by the confining pressure pump. (4) The temperature of the core system was increased to 150 °C through the electric heating jacket, and the confining pressure was automatically increased with the increase of the pore pressure during the heating process through the pressure tracking function during the heating process. (5) The valve of the intermediate container was opened slowly to allow the gas to enter the core system when the temperature stabilizes at 150 °C. The pore pressure of the core system was gradually increased to 50 MPa, and the confining pressure was also increased to 55 MPa with the increase of pore pressure. (6) The pore pressure and the confining pressure were gradually increased to 56 and 138 MPa by the flow pressure pump and the confining pressure pump. The initial temperature and pressure conditions of the reservoir were finally established when the upstream and downstream pressures of the core system stabilized. This pressure and temperature increase process can effectively reduce the irreversible damage to the pore throat structure of the core sample caused by excessive initial effective stress and rapid increase of effective stress. (7) The upstream pressure was maintained at 56 MPa, and multiple downstream pressures were set through the back-pressure pump and back-pressure valve to simulate different displacement pressure differentials (0.1–5.0 MPa). Three flow rates were recorded and averaged after the gas flow rate at the outlet end of the core system stabilized.

The experimental core was cleaned and dried again. Different water saturations should be established in the core before conducting gas-phase percolation experiments under different water conditions. (8) When the initial water saturation of the core is equal to or lower than the irreducible water saturation, it is difficult for the water in the porous media to participate in percolation. In other words, the initial water saturation of the core remains basically unchanged under different displacement pressure differentials, and the non-steady state method could be used to conduct gas-phase percolation experiments under conditions equal to or lower than irreducible water saturation. Therefore, the capillary imbibition method was used to establish different initial water saturations of the core, and then the above steps 3 to 7 were repeated. (9) When the initial water saturation of the core is higher than the irreducible water saturation, the water in the porous media will participate in percolation and form gas–water two-phase flow. In other words, the water saturation of the core will gradually decrease under different displacement pressure differentials if the non-steady state method is used for the experiment. Because the movable water in porous media can be gradually driven out of the core as the displacement experiment progresses. In order to ensure that the water saturation of the core under different displacement

pressure differentials is consistent, it is necessary to use the steady state method to conduct gas-phase percolation experiments under the condition of higher than irreducible water saturation. Therefore, the two-cylinder syringe pump was used to control the gas tank and water tank respectively. The steady state method was used to inject the corresponding proportion of gas and water into the core system at a constant rate according to the required water saturation. The pressure differential can be adjusted by changing the injection rate. The pressure differential and gas flow rate were measured after the pressure was stabilized.

2.2.5 Gas-Phase Percolation Mechanism Under Irreducible Water Condition

(1) Fracture-cavity type sample

The gas-phase percolation experiment results of fracture-cavity type cores under the maximum irreducible water saturation are illustrated in Fig. 2.14. The parameters describing percolation stage and percolation capacity are summarized in Table 2.5. The experimental results show that there is no threshold pressure gradient and low-velocity non-Darcy stage in fracture-cavity type reservoirs. The relationship between gas-phase flow rate and displacement pressure differential is basically linear and consistent with Darcy's law under low displacement pressure differentials. However, the increase of gas flow rate is significantly suppressed with the increase of displacement pressure differential. The gas-phase flow rate and the displacement pressure differential gradually deviate from the linear relationship and enter the high-velocity non-Darcy flow stage. In the case of sample No. 28 as an example, when the displacement pressure differential was 2.0 MPa, the gas-phase percolation was in the Darcy flow stage and the flow rate was 5.652 mL/s. When the displacement pressure differential was increased to 4.0 MPa, the gas-phase percolation entered the high-velocity non-Darcy flow stage and the flow rate was 10.012 mL/s. When the displacement pressure differential was further increased to 8.0 MPa, the non-Darcy flow effect of gas phase was enhanced and the flow rate only increased to 16.417 mL/s.

By comparing the experimental results of the two fracture-cavity type cores, it could be concluded that the higher the permeability of fracture-cavity type reservoirs, the lower the pressure differential required for the gas phase to enter the high-velocity non-Darcy flow stage, and the greater the deviation from the Darcy flow. The fluid flow in porous media is affected by both inertial resistance and the viscous resistance. When the fluid velocity is low, it is mainly affected by viscous resistance, and the fluid flow follows Darcy's law. When the fluid velocity is high, it is mainly affected by the inertial resistance, and the fluid flow deviates from the Darcy flow. Therefore, the comparison of inertial resistance and viscous resistance determines whether the pressure differential and flow rate are in a linear relationship. There are two main reasons for the non-Darcy flow phenomenon of fracture-cavity type reservoirs under relatively high pressure differential. One of the reasons is that the gas-phase flow rate

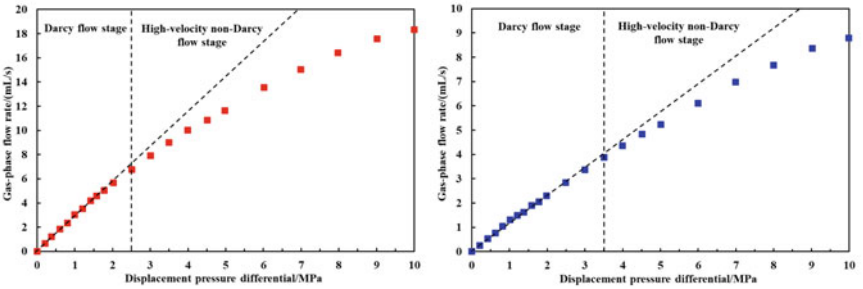

(a) Sample No. 28 (b) Sample No. 1

Fig. 2.14 Percolation characteristic curves of fracture-cavity type core samples under irreducible water saturation

Table 2.5 Parameters describing percolation stage and percolation capacity (fracture-cavity type)

Core sample number	28	1
Porosity/%	4.30	9.89
Permeability/mD	1.271	0.739
Threshold pressure/MPa	/	/
Low-velocity non-Darcy flow stage/MPa	/	/
Darcy flow stage/MPa	0–2.5	0–3.5
High-velocity non-Darcy flow stage/MPa	> 2.5	> 3.5
Gas flow rate under displacement pressure differential of 2 MPa/(mL/s)	5.652	2.290
Gas flow rate under displacement pressure differential of 4 MPa/(mL/s)	10.012	4.355
Gas flow rate under displacement pressure differential of 8 MPa/(mL/s)	16.417	7.677

in the fracture-cavity type reservoir with high permeability is high under high pressure differential. The inertial resistance gradually increases and the negative impact on the percolation capacity cannot be ignored. The gas-phase flow enters the high-velocity non-Darcy flow dominated by inertial resistance, and the higher the flow rate, the greater the loss of percolation capacity caused by inertial resistance. Consequently, there is a binomial relationship between gas flow rate and pressure differential, rather than a linear relationship. Another reason is that fractures are developed in fracture-cavity type reservoirs, and the fracture system contributes most of the percolation capacity. However, the stress sensitivity of the fracture system is far stronger than that of pores and cavities. The displacement pressure differential was controlled by maintaining the upstream injection pressure and changing the downstream back pressure. The effective stress of the core sample near the downstream increases as the back pressure decreases. Accordingly, the fracture system at the downstream end of the core gradually closes under the high pressure differential, resulting in a further increase in the loss of percolation capacity. The gas-phase flow in fracture-cavity type reservoirs deviates from Darcy flow and loses certain percolation capacity under the

combined action of the two mechanisms. Therefore, the fracture-cavity type reservoir is the dominant gas supply reservoir under low production pressure differential in the initial stage of ultradeep carbonate gas reservoir development. The production pressure differential should be reasonably controlled to prevent the gas-phase flow from entering the high-velocity non-Darcy flow stage early. This is because the production increase is not significant in the high-velocity non-Darcy flow stage, and the fracture closure is irreversible under the high production pressure differential.

(2) Cavity type sample

The gas-phase percolation experiment results of cavity type cores under the maximum irreducible water saturation are illustrated in Fig. 2.15. Parameters describing percolation stage and percolation capacity are summarized in Table 2.6. The experimental results show that there is no threshold pressure gradient in the cavity type reservoir, but there is a low-velocity non-Darcy flow stage under low displacement pressure differentials. The gas-phase gradually gets rid of the low-velocity non-Darcy flow stage and enters the Darcy flow stage when the displacement pressure differential continues to increase. Although cavities of various sizes are developed in cavity type reservoirs, their percolation channels are still dominated by throats. By comparing the experimental results of sample No. 11 and sample No. 54, it could be concluded that the lower the reservoir permeability, the more obvious the low-velocity non-Darcy flow stage, and the higher the pressure differential required to enter the Darcy flow stage. The formation mechanism of low-velocity non-Darcy percolation is that the irreducible water in porous media imposes additional viscous resistance on the gas-phase flow. The inhibition effect of viscous resistance on gas-phase percolation capacity is relatively obvious when the displacement pressure differential is low, but it can be ignored with the increase of displacement pressure differential. Moreover, the smaller the pore throat size, the higher the irreducible water saturation, the greater the additional viscous resistance, and the higher the displacement pressure differential required to overcome this viscous resistance. Therefore, sample No. 11 with relatively high permeability entered the Darcy flow stage when the pressure differential was 0.6 MPa, whereas sample No. 54 with relatively low permeability only got rid of the low-velocity non-Darcy stage when the pressure differential was 1.0 MPa.

When the displacement pressure differential is further increased, the gas-phase flow in cavity type reservoirs also gradually deviates from the Darcy flow stage. However, the deviation degree of the cavity type reservoir is far lower than that of the fracture-cavity type reservoir, and the displacement pressure differential required for deviation is also far higher than that of the fracture-cavity type reservoir. In the case of sample No. 11 as an example, when the displacement pressure differential was 5.0 MPa, the gas-phase percolation was in the Darcy flow stage and the flow rate was 1.555 mL/s. When the displacement pressure differential was increased to 10.0 MPa, although the gas-phase percolation had deviated from the Darcy flow, the flow rate still increased to 2.790 mL/s. The reason why the non-linear percolation process of the cavity type reservoir under high pressure differentials cannot be defined as high-velocity non-Darcy percolation is that the gas-phase flow rate is lower

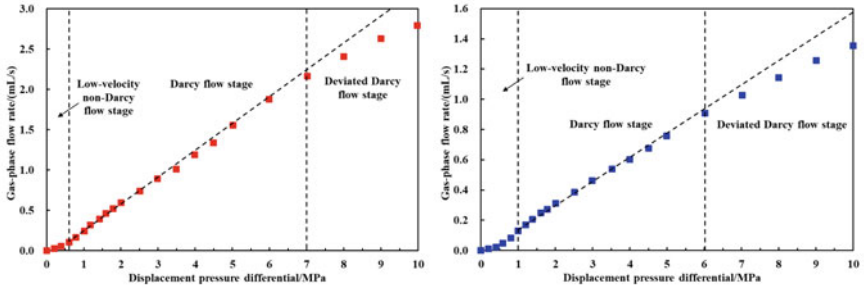

(a) Sample No. 11 (b) Sample No. 54

Fig. 2.15 Percolation characteristic curves of cavity type core samples under irreducible water saturation

Table 2.6 Parameters describing percolation stage and percolation capacity (cavity type samples)

Core sample number	11	54
Porosity/%	7.37	4.64
Permeability/mD	0.287	0.105
Threshold pressure/MPa	/	/
Low-velocity non-Darcy flow stage/MPa	0–0.6	0–1.0
Darcy flow stage/MPa	0.6–7.0	1.0–6.0
Deviated Darcy flow stage under high displacement pressure differential/MPa	> 7.0	> 6.0
Gas flow rate under displacement pressure differential of 2 MPa/(mL/s)	0.597	0.312
Gas flow rate under displacement pressure differential of 5 MPa/(mL/s)	1.555	0.758
Gas flow rate under displacement pressure differential of 10 MPa/(mL/s)	2.790	1.355

than the turbulent flow standard. This deviation stage is only caused by the stress sensitivity effect of core samples near the downstream end under high displacement pressure differentials. Furthermore, cavity type reservoirs are dominated by cavities and macroscopic pores, and their stress sensitivity effect is weaker than that of fracture-cavity type reservoirs. The non-Darcy flow caused only by the stress sensitivity effect has a weak inhibition on the gas production capacity of cavity type reservoirs. Therefore, the cavity type reservoir can supply gas at all stages of ultra-deep carbonate gas reservoir development. However, the gas production capacity of the cavity type reservoir is relatively weak under low production pressure differential in the initial development stage. Cavity type reservoirs could be used as the dominant gas supply reservoir under high production pressure differentials in the middle and late development stages.

(3) Pore type sample

The gas-phase percolation experiment results of pore type cores under the maximum irreducible water saturation are illustrated in Fig. 2.16. The parameters describing

percolation stage and percolation capacity are summarized in Table 2.7. The experimental results show that the percolation characteristic curves of most pore type samples are similar to those of cavity type samples. The gas-phase percolation of these samples showed the low-velocity non-Darcy flow stage, the Darcy flow stage and the deviated Darcy flow stage in turn with the increase of displacement pressure differential. It indicates that the cavity of the cavity type reservoir can improve the storage capacity, but has little influence on the gas-phase percolation characteristics and percolation capacity. The flow channels of both the cavity type and pore type reservoirs are dominated by throats. However, the deviation degree of gas-phase flow from Darcy flow in the cavity type reservoir is stronger than that of the cavity type reservoir under the condition of high displacement pressure differentials, but weaker than that of the fracture-cavity type reservoir. In the case of sample No. 118 as an example, when the displacement pressure differential was 5.0 MPa, the gas-phase percolation was in the Darcy flow stage and the flow rate was 0.270 mL/s. When the displacement pressure differential was increased to 10.0 MPa, the gas-phase percolation had entered the deviated Darcy flow stage, and the flow rate was 0.440 mL/s, which is 1.63 times the flow rate at the displacement pressure differential of 5.0 MPa. The percolation characteristics of the No. 54 cavity type sample are similar to those of the No. 118 pore type sample, which could be used as a reference. When the displacement pressure differential was 5.0 MPa, the gas-phase percolation was in the Darcy flow stage and the flow rate was 0.758 mL/s. When the displacement pressure differential was increased to 10.0 MPa, the gas-phase percolation had entered the deviated Darcy flow stage, and the flow rate was 1.355 mL/s, which is 1.79 times the flow rate at the displacement pressure differential of 5.0 MPa. There are also two main reasons for the non-Darcy flow phenomenon of pore type reservoirs under relatively high pressure differentials. One reason is the loss of percolation capacity caused by the stress sensitivity effect of the core sample near the downstream end under high displacement pressure differentials. The high irreducible water saturation and small pore throat size result in the thick irreducible water film in the pore type reservoir. When the displacement pressure differential increases to the critical value, the irreducible water at the gas–water contact surface may get rid of the constraint and turn into secondary movable water to participate in the flow. The tiny amount of water droplets observed in the condensing device could confirm this hypothesis. Therefore, another reason is that a small amount of secondary movable water forms gas–water two-phase percolation, thereby reducing the relatively permeability of the gas phase.

The comparison of the experimental results of 4 pore type samples shows that the lower the reservoir permeability, the higher the displacement pressure differential required to get rid of the low-velocity non-Darcy stage, the lower the critical pressure differential that deviates from Darcy flow, and the greater the effect of non-Darcy flow on percolation capacity. In addition, some pore type reservoirs have relatively high storage capacity, but there is a threshold pressure effect under low displacement pressure differentials. This is because the throat size of these high-porosity and low-permeability pore type reservoirs is small, and the coordination number is low. Therefore, some key percolation channels are easily blocked by irreducible water

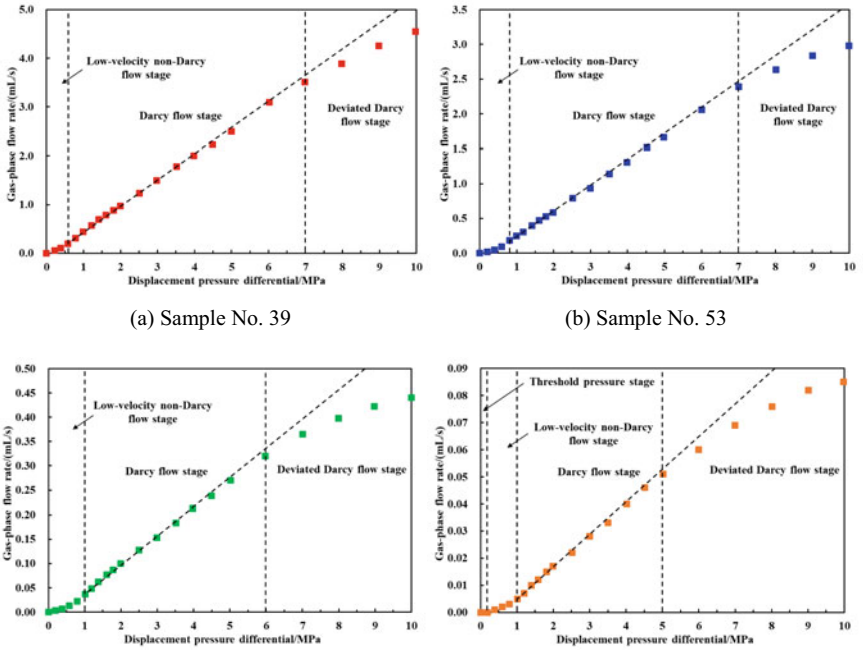

(a) Sample No. 39 (b) Sample No. 53

(c) Sample No. 118 (d) Sample No. 55

Fig. 2.16 Percolation characteristic curves of pore type core samples under irreducible water saturation

Table 2.7 Parameters describing percolation stage and percolation cavity (pore type samples)

Core sample number	39	53	118	55
Porosity/%	2.42	2.11	3.79	4.21
Permeability/mD	0.356	0.124	0.084	0.03
Threshold pressure/MPa	0	0	0	0.2
Low-velocity non-Darcy flow stage/MPa	0–0.6	0–0.8	0–1.0	0.2–1.2
Darcy flow stage/MPa	0.6–7.0	0.8–7.0	1.0–6.0	1.2–5.0
Deviated Darcy flow stage under high displacement pressure differential /MPa	> 7.0	> 7.0	> 6.0	> 5.0
Gas flow rate under displacement pressure differential of 2 MPa/(mL/s)	0.973	0.587	0.100	0.017
Gas flow rate under displacement pressure differential of 5 MPa/(mL/s)	2.495	1.663	0.270	0.051
Gas flow rate under displacement pressure differential of 10 MPa/(mL/s)	4.547	2.977	0.440	0.085

to form capillary resistance. The macroscopic performance of capillary resistance in key percolation channels is the threshold pressure effect, which could be overcome by increasing the displacement pressure differential. For example, when the displacement pressure differential was less than 0.2 MPa, the gas in sample No. 55 could not overcome the capillary resistance caused by the blockage of irreducible water, and no gas flow was detected at the outlet end of the core system. In summary, the storage capacity of pore type reservoirs is not only weaker than that of cavity and fracture-cavity type reservoirs, but also some low-permeability pore type reservoirs have obvious low-velocity non-Darcy stage and threshold pressure gradient. Therefore, the pore type reservoir has a weak gas supply capacity under low production pressure differentials in the initial development stage, but it plays a role in replenishing high-quality reservoirs under high production pressure differentials in the middle and late development stages.

(4) Matrix type sample

Ultradeep carbonate reservoirs with porosity less than 2% in the Deng IV Member are generally classified as ineffective reservoirs, because CT scanning results show that this type of reservoir is dominated by rock matrix and only a small number of microscopic pore throats are locally developed (Figs. 1.25 and 1.42). Two matrix type core samples were selected for gas-phase percolation experiments in order to compare the gas-phase percolation characteristics and percolation capacities of effective and ineffective reservoirs. The gas-phase percolation experiment results of pore type cores under the maximum irreducible water saturation are illustrated in Fig. 2.17. The parameters describing percolation stage and percolation capacity are summarized in Table 2.8. The experimental results show that the threshold pressure effect only exists in the matrix type reservoirs with extremely low permeability. For example, the threshold pressure of sample No. 31 is 1.0 MPa, whereas sample No. 95 has no threshold pressure effect. It could be concluded that the parameter directly related to the threshold pressure effect is permeability rather than porosity based on the threshold pressure data of pore type and matrix type samples. In addition, both the low-velocity non-Darcy flow stage and the deviated Darcy flow stage of matrix type reservoirs are more obvious than those of pore type and cavity type reservoirs. For example, sample No. 31 got rid of the low-velocity non-Darcy flow stage when the displacement pressure differential was 1.6 MPa, but entered the deviated Darcy flow stage when the displacement pressure differential increased to 4.5 MPa. This is because the pore throat size and coordination number of matrix type reservoirs are mostly lower than those of effective reservoirs, which enhances the effect of irreducible water on gas-phase percolation characteristics and percolation capacity. The viscous resistance and irreducible water blockage during the gas-phase percolation process are the main reasons for the formation of low-velocity non-Darcy effect and the threshold pressure effect, respectively. The worse the petrophysical properties of the matrix type reservoir, the thicker the irreducible water film, the greater the viscous resistance of the gas-phase percolation, and the easier the key percolation channels are blocked by the irreducible water. Moreover, the influence of a small amount of secondary movable water converted from the irreducible water under high pressure

differentials on the gas-phase percolation capacity of low-permeability reservoirs is further increased. The combined effect of gas–water two-phase percolation and stress sensitivity leads to an increase in the deviation degree of gas phase from Darcy flow and a decrease in the critical pressure differential deviating from Darcy flow. In summary, the permeability of matrix type reservoirs is generally low, the irreducible water saturation is generally high, and the gas-phase percolation capacity is extremely low. Although a few matrix type reservoirs have relatively high permeability, their storage capacity is limited. Therefore, the matrix type reservoir has no development value under the current economic and technical conditions.

(5) Comparison and analysis of gas-phase percolation mechanism

In order to compare the gas-phase percolation characteristics and percolation capacities of four types of ultradeep carbonate reservoirs, ten percolation characteristic curves are illustrated in Fig. 2.18. The figure shows that the percolation capacity of fracture-cavity type reservoirs is far higher than that of other types of reservoirs, and

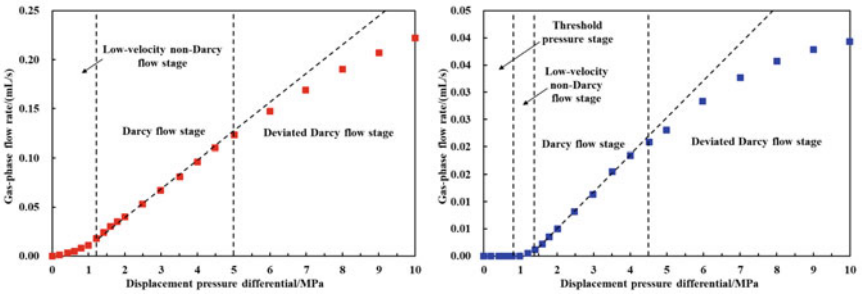

(a) Sample No. 95 (b) Sample No. 31

Fig. 2.17 Percolation characteristic curves of matrix type core samples under irreducible water saturation

Table 2.8 Parameters describing percolation stage and percolation capacity (matrix type samples)

Core sample number	95	31
Porosity/%	1.64	1.89
Permeability/mD	0.042	0.005
Threshold pressure/MPa	0	1.0
Low-velocity non-Darcy flow stage/MPa	0–1.2	1.0–1.6
Darcy flow stage/MPa	1.2–5.0	1.6–4.5
Deviated Darcy flow stage under high displacement pressure differential/MPa	> 5.0	> 4.5
Gas flow rate under displacement pressure differential of 2 MPa/(mL/s)	0.040	0.005
Gas flow rate under displacement pressure differential of 5 MPa/(mL/s)	0.123	0.023
Gas flow rate under displacement pressure differential of 10 MPa/(mL/s)	0.222	0.039

there is an obvious binomial relationship between the flow rate and pressure differential of fracture-cavity type reservoirs. The percolation characteristics and percolation capacities of cavity type reservoirs are similar to those of pore type reservoirs. Small-sized cavities could only improve the reservoir storage capacity, but have little effect on the percolation characteristics. It should be noted that the large-sized bedding cavity could improve the percolation capacity, but cores containing such cavities cannot be used for ultra-high temperature and pressure physical simulation experiments. The matrix type reservoir with the worst percolation capacity still cannot reach the profitable productivity under high pressure differentials. The summary of percolation characteristics and analysis of percolation mechanism of ultradeep carbonate gas reservoirs are shown in Table 2.9.

The above investigation results show that the gas-phase flow characteristics and percolation capacity are closely related to reservoir permeability, but poorly related to porosity. Therefore, the core permeability was taken as the abscissa, and the critical pressure differential of each percolation stage was taken as the ordinate. The relationship curve between the percolation stage and the core permeability is illustrated in Fig. 2.19. The following conclusions could be drawn from Fig. 2.19. ① The lower the reservoir permeability, the more obvious the low-velocity non-Darcy flow stage. When the permeability is lower than a certain value, the threshold pressure gradient will be generated and affect the gas production capacity of the well under low pressure differentials. ② The lower the permeability of reservoirs without fractures, the lower the critical pressure differential of the gas phase deviates from

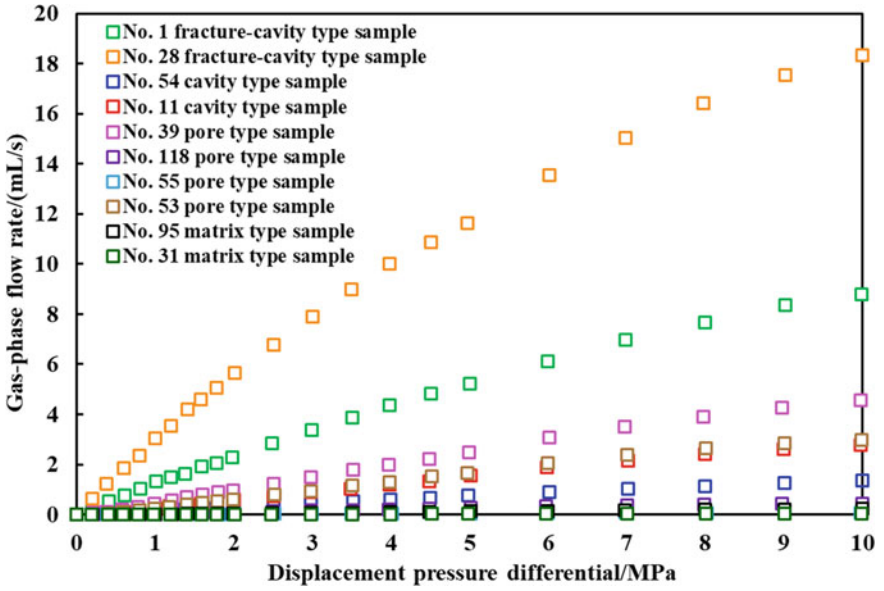

Fig. 2.18 Gas-phase percolation characteristic curves of four types of core samples under irreducible water saturation

Table 2.9 Gas-phase percolation characteristics and mechanisms of different types of ultradeep carbonate gas reservoirs

Reservoir type	Percolation stage	Percolation mechanism
Fracture-cavity type	Darcy flow stage	✓ Darcy flow mechanism
	High-velocity non-Darcy flow stage	✓ Inertial resistance under high gas-phase flow rates ✓ Strong stress sensitivity of fracture systems
Cavity type and pore type	Low-velocity non-Darcy flow stage	✓ Irreducible water narrows gas-phase percolation channels ✓ Viscous resistance caused by irreducible water during gas-phase percolation
	Darcy flow stage	✓ Darcy flow mechanism
	Deviated Darcy flow stage	✓ Stress sensitivity of pores and cavities ✓ A certain amount of irreducible water is converted into secondary movable water under high pressure differential
Matrix type	Threshold pressure stage	✓ Irreducible water blocks key percolation channels
	Low-velocity non-Darcy flow stage	✓ Irreducible water narrows gas-phase percolation channels ✓ Viscous resistance caused by irreducible water during gas-phase percolation
	Darcy flow stage	✓ Darcy flow mechanism
	Deviated Darcy flow stage	✓ Stress sensitivity of pores and throats ✓ A certain amount of irreducible water is converted into secondary movable water under high pressure differential

the Darcy flow stage. On the contrary, the higher the permeability of reservoirs with fractures, the lower the critical pressure differential of the gas phase deviates from the Darcy flow stage, and the stronger the inhibition of high pressure differential on gas production capacity. ③ The percolation curve of Darcy flow stage is roughly straight, but slightly inclines to the X axis. This is because the gas-phase percolation is affected by the gradually enhanced stress sensitivity.

It is possible to determine the reasonable production pressure differential suitable for development of different types of actual reservoirs according to the range of experimental pressure differential in Darcy flow stage. The conversion of experimental pressure differential and production pressure differential, as well as the experimental gas-phase flow rate and gas well production could be realized by similarity

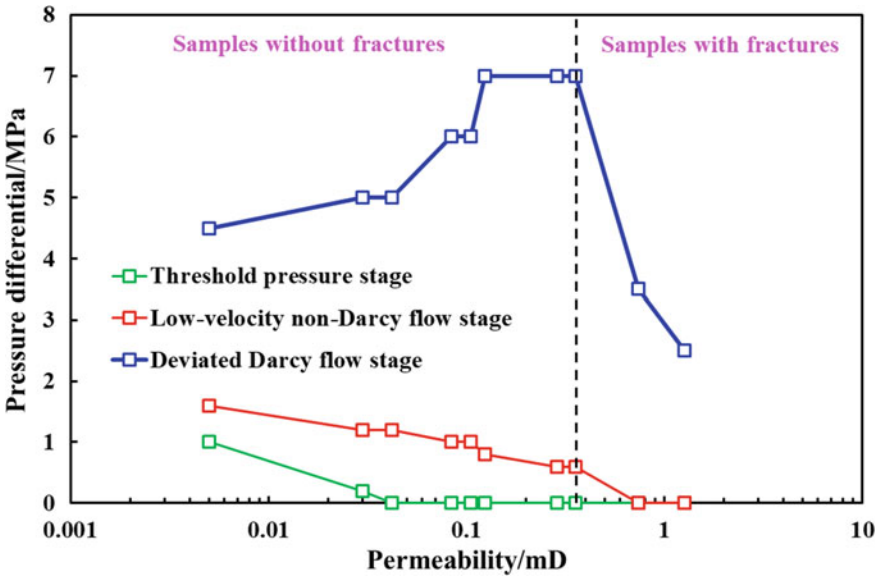

Fig. 2.19 Critical pressure differential of samples with different permeability at different percolation stages

principle and conversion formula (Wang et al., 2017b). The reasonable pressure differential range and the gas production under the production pressure differential of 30 MPa after similarity conversion are summarized in Table 2.10. The gas production of a gas well is directly related to the effective thickness of the reservoir. Therefore, it is assumed that the average reservoir thickness is 50 m and the well type is the commonly used horizontal well in the study area. The following conclusions could be drawn from Table 2.10. ① The daily gas production of fracture-cavity type reservoirs can reach 10–5–100 $\times$ 10^4 m^3/d, but it is severely affected by stress sensitivity and high-velocity non-Darcy flow effects. Therefore, the fracture-cavity type reservoir is suitable for the low pressure differential production stage in the initial stage of ultradeep carbonate gas reservoir development. ② The daily gas production of cavity type and the pore type reservoirs can reach 0.1–10 $\times$ 10^4 m^3/d, but they are severely affected by the low-velocity non-Darcy flow effect. Therefore, the cavity type and pore type reservoirs are suitable for the high pressure differential production stage in the middle and late stage of ultradeep carbonate gas reservoir development. In addition, the cavity type reservoir has excellent storage capacity, and the gas production capacity of this type of reservoir could be improved through reservoir reconstruction. ③ The matrix type reservoirs has worst storage capacity and percolation capacity, and are more seriously affected by threshold pressure and low-velocity non-Darcy flow effects. Therefore, the daily gas production of matrix type reservoirs is generally less than 0.1 $\times$ 10^4 m^3/d (Table 2.10).

Table 2.10 Reasonable production pressure differential and predicted gas production of reservoirs with different petrophysical properties based on gas-phase percolation experiment results and similar principle

Core number	28	1	11	54	39	53	118	55	95	31
Reservoir type	Fracture-cavity type		Cavity type		Pore type				Matrix type	
Permeability/mD	1.271	0.739	0.287	0.105	0.356	0.124	0.084	0.030	0.042	0.005
Porosity/%	4.30	9.89	7.34	4.64	2.42	2.11	3.79	4.21	1.64	1.89
Pressure differential range of Darcy flow/MPa	0–2.5	0–3.5	0.6–7.0	1.0–6.0	0.6–7.0	0.8–7.0	1.0–6.0	1.2–5.0	1.2–5.0	1.6–4.5
Reasonable production pressure differential range/MPa[a]	0–21.6	0–27.5	6.2–40.1	9.9–37.5	6.2–40.1	8.1–40.1	9.9–37.5	11.7–34.2	11.7–34.2	15.0–32.2
Gas-phase flow rate when the experimental pressure differential is 4 MPa/(mL/s)	10.012	4.355	1.187	0.602	2.000	1.307	0.213	0.040	0.096	0.019
Horizontal well production when the production differential is 30 MPa/(m^3/d)[b]	199,565	86,806	23,660	12,000	39,865	26,052	4,246	798	1,914	369

[a]The reasonable production pressure differential was converted from the pressure differential range of Darcy flow stage by the similarity conversion formula
[b]The horizontal well production was converted from the experimental flow rate of gas-phase through the similarity conversion formula. The reservoir thickness was assumed to be 50 m

2.2.6 Gas-Phase Percolation Mechanism Under Different Water Saturation Conditions

The proportion of reservoirs with water saturation between 30 and 60% in the intra-platform belt of the Deng IV Member reservoir is higher than that in the platform margin belt. The difference of initial water saturation has a great influence on gas-phase percolation characteristics and percolation capacity (Volkov et al., 2014). Therefore, it is necessary to compare the gas-phase percolation mechanism of fracture-cavity type, cavity type and pore type reservoirs under different initial water saturations. The reason why the matrix type reservoir was not studied is that the gas-phase flow rate under high water saturation is too low to be measured by electronic flowmeter. The experimental cores were taken from 3 of the above 10 samples, and their petrophysical parameters are shown in Table 2.11. The corresponding relationship between water content condition and water saturation of three types of cores is shown in Table 2.12.

(1) Fracture-cavity type sample

The gas-phase percolation experiment results of the fracture-cavity type sample under different water saturations are illustrated in Fig. 2.20. The critical pressure differentials for each percolation stage of the fracture-cavity type sample under different water saturations are summarized in Table 2.13. The experimental results show that there is no low-velocity non-Darcy flow stage and threshold pressure stage when the fracture-cavity type reservoir does not contain water. The gas-phase flow in fracture-cavity type reservoirs approximates Darcy flow at low displacement pressure differentials, but deviates from Darcy flow at high displacement pressure differentials due to fracture system closure and inertial resistance. The gas-phase percolation characteristics under irreducible water conditions are similar to those under non-water conditions, except that the deviation degree of Darcy flow and the percolation capacity of gas-phase are both weaker than those under non-water conditions. This is because the viscous resistance generated by the irreducible water in porous media reduces the gas-phase percolation velocity, thereby weakening the influence of inertial resistance. In the case of sample No. 1 under non-water condition as an example, when the displacement pressure differential was 2.0 MPa, the gas-phase percolation was in the Darcy flow stage and the flow rate was 3.053 mL/s. When the displacement pressure differential was increased to 4.0 MPa, the gas-phase percolation had entered the high-velocity non-Darcy flow stage, and the flow rate was 5.393 mL/s, which is 1.766 times the flow rate at the displacement pressure differential of 2.0 MPa. In contrast, sample No. 1 was in the Darcy flow stage under irreducible water conditions (S_{wi} = 10%) when the displacement pressure differential was 2.0 MPa, and the gas flow rate was 2.290 mL/s. When the displacement pressure differential was increased to 4.0 MPa, the gas-phase percolation had entered the high-velocity non-Darcy flow stage, and the flow rate was 4.355 mL/s, which is 1.902 times the flow rate at the displacement pressure differential of 2.0 MPa. When the movable water content in the fracture-cavity type reservoir is small, the movable water mainly exists in the

Table 2.11 Petrophysical parameters of core samples for gas-phase percolation experiments under different water saturation conditions

Core number	Core type	Length/mm	Diameter/mm	Permeability/mD	Porosity/%	Depth/m	Irreducible water saturation/%
1	Fracture-cavity type	49.54	25.00	0.739	9.89	5509.47	17.63
54	Cavity type	47.10	25.20	0.105	4.64	5521.56	22.25
118	Pore type	49.10	25.20	0.084	3.79	5537.05	27.84

Table 2.12 Corresponding relationship between water content condition and water saturation

Core number	Non-water condition	Irreducible water condition	Movable water condition	
			Low movable water content	High movable water content
1	$S_{wi} = 0$	$S_{wi} = 10\%, 20\%$	$S_{wi} = 30\%, 40\%$	$S_{wi} = 50\%, 60\%$
54	$S_{wi} = 0$	$S_{wi} = 10\%, 20\%$	$S_{wi} = 30\%, 40\%$	$S_{wi} = 50\%, 60\%$
118	$S_{wi} = 0$	$S_{wi} = 10\%$	$S_{wi} = 20\%, 30\%$	$S_{wi} = 40\%, 50\%, 60\%$

S_{wi} represents the initial water saturation

cavities and large pores, and has little influence on the gas-phase percolation capacity of the fracture system. When the movable water content is high, the movable water participates in the percolation in the fracture system and forms gas–water two-phase percolation, thereby greatly reducing the gas-phase percolation capacity, as well as the degree of deviation from Darcy flow caused by inertial force. Although the increase of water saturation in fracture-cavity type reservoirs reduces the gas-phase percolation capacity, it also weakens the impact of high-velocity non-Darcy flow. This conclusion could also be drawn by comparing the critical pressure differentials entering the high-velocity non-Darcy flow stage at different water saturations. The relationship between percolation stage and water saturation of the fracture-cavity type sample is illustrated in Fig. 2.21. There is a low-velocity non-Darcy flow stage of 0–0.2 MPa when the water saturation increases to 60%. Therefore, the water in the fracture system under high water saturations will also impose certain additional viscous resistance on the gas-phase percolation, and inhibit the percolation capacity under low displacement pressure differentials. In summary, fracture-cavity type reservoirs with low water saturations are not suitable for large pressure differential production, while the production pressure differential could be appropriately amplified under high water saturations.

(2) Cavity type sample

The gas-phase percolation experiment results of the cavity type sample under different water saturations are illustrated in Fig. 2.22. The critical pressure differentials for each percolation stage of the cavity type sample under different water saturations are summarized in Table 2.14. The experimental results show that there is no low-velocity non-Darcy flow stage and threshold pressure stage when the cavity type reservoir does not contain water. The gas-phase flow in the cavity type reservoir without water is approximately Darcy flow under low displacement pressure differentials, but it starts to deviate from Darcy flow under high displacement pressure differentials because of the gradually enhanced stress sensitivity effect. The subsequent sensitivity experiment results show that the stress sensitivity of the cavity type reservoir is weaker than that of the fracture-cavity type reservoir. Therefore, the degree of deviation of gas flow from the Darcy flow in the cavity type reservoir is far lower than that in the fracture-cavity type reservoir, and the critical pressure

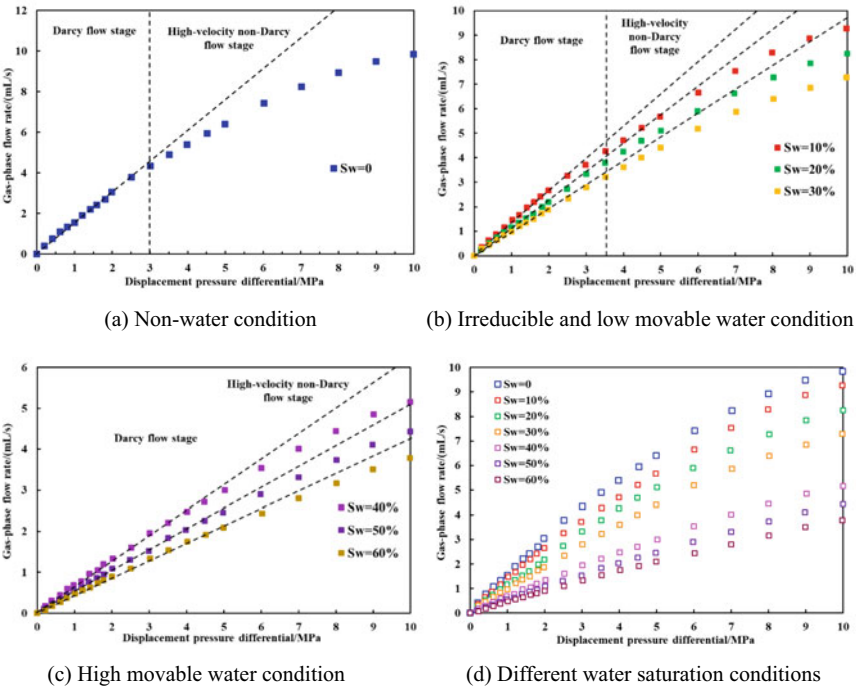

(a) Non-water condition

(b) Irreducible and low movable water condition

(c) High movable water condition

(d) Different water saturation conditions

Fig. 2.20 Percolation characteristic curves of the fracture-cavity type sample under different water saturations

Table 2.13 Critical pressure differentials of each percolation stage under different water saturations (fracture-cavity type sample)

Water saturation/%	Water condition	Threshold pressure stage/MPa	Low-velocity non-Darcy flow stage/MPa	High-velocity non-Darcy flow stage/MPa
0	Non-water	/	/	3.0
10	Irreducible water	/	/	3.0
20	Movable water	/	/	3.5
30	Movable water	/	/	3.5
40	Movable water	/	/	4.5
50	Movable water	/	/	5.0
60	Movable water	/	0.2	5.5

differential of gas phase deviates from Darcy flow in the cavity type reservoir is also far higher than that in the fracture-cavity type reservoir. When the cavity type reservoir contains irreducible water, the gas-phase percolation exhibits low-velocity non-Darcy flow under low displacement pressure differentials. This is because the gas flow under low displacement pressure differentials cannot completely overcome

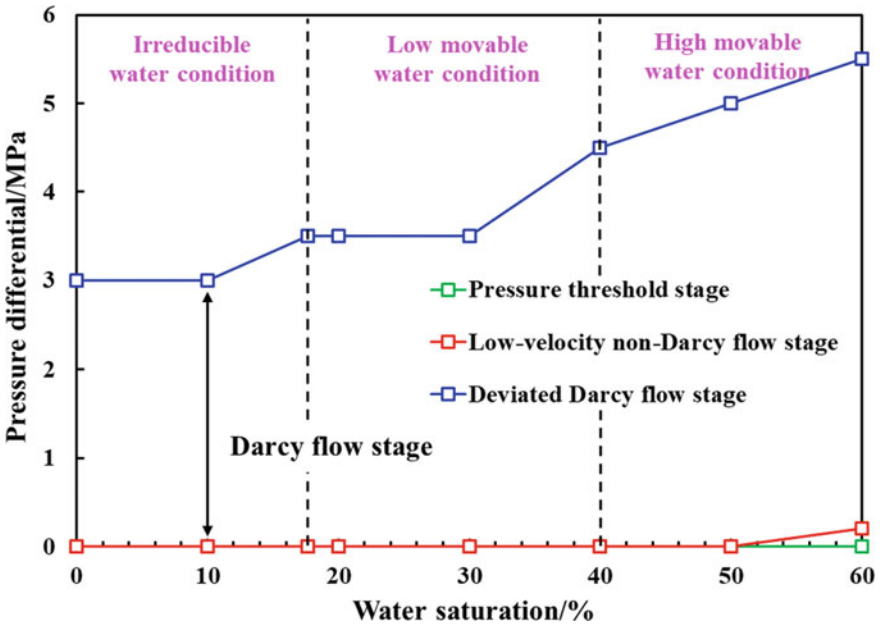

Fig. 2.21 Relationship between gas-phase percolation stage and water saturation of the fracture-cavity type sample

the additional viscous resistance caused by irreducible water. Gas-phase percolation also deviates from Darcy flow under high displacement pressure differentials, but the deviation degree under irreducible water conditions is slightly stronger than that under non-water conditions. This is because a small amount of irreducible water may be converted to secondary movable water under high displacement pressure differentials, thereby forming gas–water two-phase flow and reducing the relative permeability of gas phase. When the irreducible water saturation is low and the displacement pressure differential is small, the converted movable water will participate in the percolation in the form of dispersed phase, which has a weak inhibition on the gas-phase percolation capacity. When the irreducible water saturation is high and the displacement pressure differential is large, the converted movable water can form a continuous phase, which significantly increases the inhibition of gas-phase percolation. This phenomenon could be explained by the results of subsequent microscopic visualization experiments. In the case of sample No. 54 under non-water condition as an example, when the displacement pressure differential was 5.0 MPa, the gas-phase percolation was in the Darcy flow stage and the flow rate was 1.427 mL/s. When the displacement pressure differential was increased to 10.0 MPa, the gas-phase percolation had entered the deviated Darcy flow stage, and the flow rate was 2.675 mL/s, which is 1.875 times the flow rate at the displacement pressure differential of 5.0 MPa. In contrast, sample No. 54 was in the Darcy flow stage under irreducible water conditions ($S_{wi} = 20\%$) when the displacement pressure

differential was 5.0 MPa, and the gas flow rate was 0.860 mL/s. When the displacement pressure differential was increased to 10.0 MPa, the gas-phase percolation had entered the deviated Darcy flow stage, and the flow rate was 1.628 mL/s, which is 1.893 times the flow rate at the displacement pressure differential of 5.0 MPa. When the cavity type reservoir contains movable water, the movable water may form a water column at small pore throats or a water wedge between rock particles, thereby blocking dominant percolation channels. The gas phase must overcome certain capillary resistance to pass through these channels, thereby forming a threshold pressure gradient. The relationship between percolation stage and water saturation of the cavity type sample is illustrated in Fig. 2.23. The range of pressure differential in Darcy flow stage decreases with the increase of water saturation. It indicates that the movable water in the cavity type reservoir not only enhances the low-velocity non-Darcy flow stage under low pressure differentials, but also reduces the critical pressure differential that deviates from Darcy flow. The more movable water, the higher the relative permeability of water phase, and the greater the deviation from Darcy flow. In addition, the initial movable water in the cavity reservoir triggers the threshold pressure effect, and the threshold pressure gradually increases with the increase of the movable water saturation. Therefore, the difference of initial water condition has a great influence on the percolation characteristics of cavity type reservoirs. Controlling the production pressure differential to avoid threshold pressure effect and non-Darcy flow stage is the key to the efficient development of cavity type reservoirs.

(3) Pore type sample

The gas-phase percolation experiment results of the pore type sample under different water saturations are illustrated in Fig. 2.24. The critical pressure differentials for each percolation stage of the pore type sample under different water saturations are summarized in Table 2.15. The experimental results show that the gas-phase flow in pore type reservoirs without water is approximately Darcy flow, and only slightly deviates from Darcy flow under high displacement pressure differentials. In the case of sample No. 118 under non-water condition as an example, when the displacement pressure differential was 5.0 MPa, the gas-phase percolation was in the Darcy flow stage and the flow rate was 0.553 mL/s. When the displacement pressure differential was increased to 10.0 MPa, the gas-phase percolation had entered the deviated Darcy flow stage, and the flow rate was 1.077 mL/s, which is 1.984 times the flow rate at the displacement pressure differential of 5.0 MPa. In contrast, the gas-phase flow rates of No. 54 cavity type sample and No. 1 fracture-cavity type sample under the displacement pressure differential of 10 MPa are 1.875 and 1.536 times that under the displacement pressure differential of 5 MPa, respectively. When the pore type reservoir contains irreducible water, the gas-phase percolation exhibits low-velocity non-Darcy flow under low displacement pressure differentials, and deviates from Darcy flow under high displacement pressure differentials. When the pore type reservoir contains movable water, the effective gas-phase percolation in pore type reservoirs also needs to overcome the threshold pressure effect. Therefore, the percolation characteristics of pore type and cavity type reservoirs are also

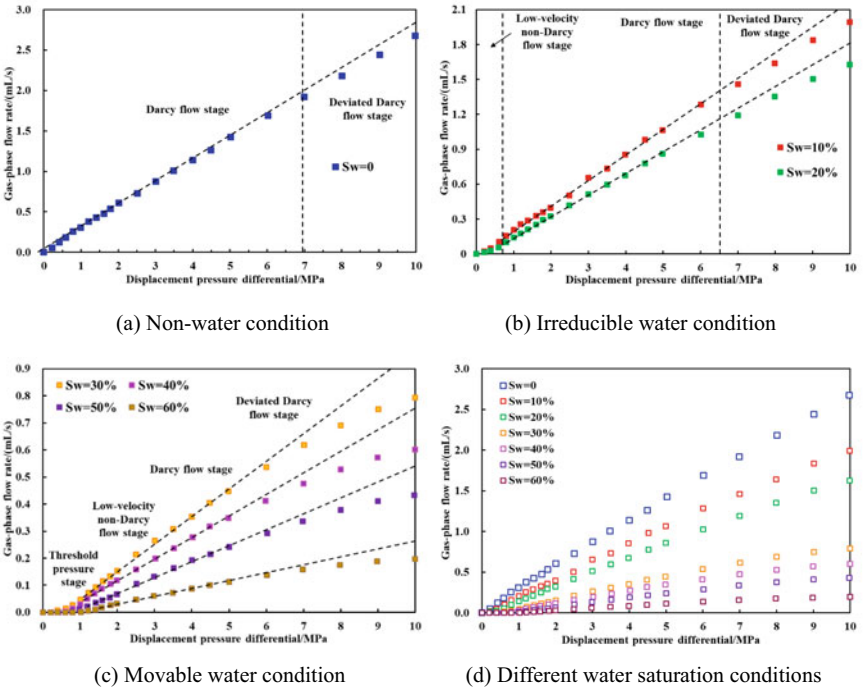

(a) Non-water condition (b) Irreducible water condition

(c) Movable water condition (d) Different water saturation conditions

Fig. 2.22 Percolation characteristic curves of the cavity type sample under different water saturations

Table 2.14 Critical pressure differentials of each percolation stage under different water saturations (cavity type sample)

Water saturation/%	Water condition	Threshold pressure stage/MPa	Low-velocity non-Darcy flow stage/MPa	High-velocity non-Darcy flow stage/MPa
0	Non-water	/	/	7.0
10	Irreducible water	/	0.6	6.5
20	Irreducible water	/	0.8	6.0
30	Movable water	0.2	1.0	6.0
40	Movable water	0.4	1.0	6.0
50	Movable water	0.6	1.2	6.0
60	Movable water	0.8	1.6	5.5

similar under different water saturations. However, the secondary movable water converted from irreducible water under high pressure differentials has a stronger inhibitory effect on the gas-phase percolation capacity of pore type reservoirs than that of cavity type reservoirs. In the case of No. 118 sample under irreducible water

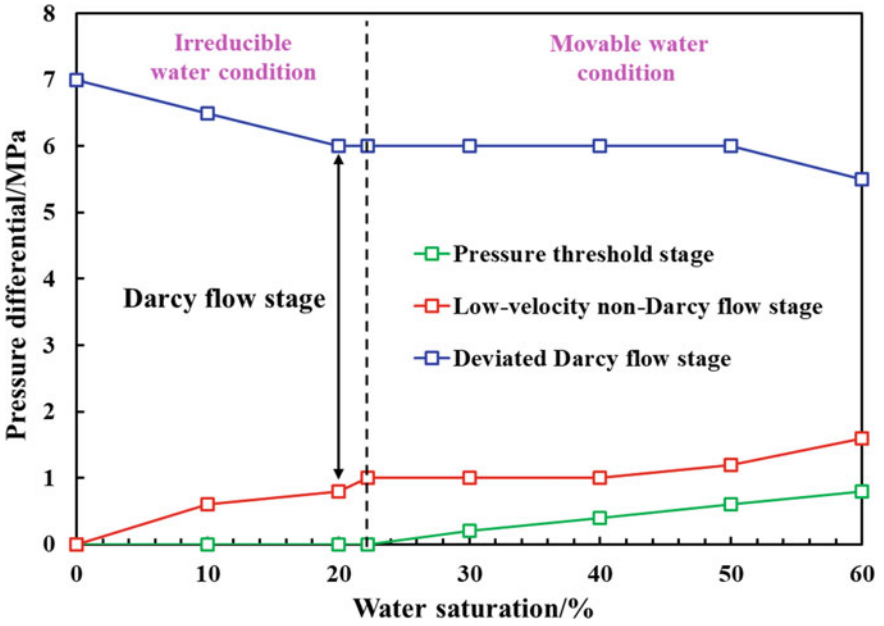

Fig. 2.23 Relationship between gas-phase percolation stage and water saturation of the cavity type sample

condition ($S_{wi} = 20\%$) as an example, when the displacement pressure differential was 5.0 MPa, the gas-phase percolation was in the Darcy flow stage and the flow rate was 0.303 mL/s. When the displacement pressure differential was increased to 10.0 MPa, the gas-phase percolation had entered the deviated Darcy flow stage, and the flow rate was 0.542 mL/s, which is 1.789 times the flow rate at the displacement pressure differential of 5.0 MPa. In contrast, the gas-phase flow rate of No. 54 cavity type sample containing irreducible water under the displacement pressure differential of 10 MPa is 1.893 times that under the displacement pressure differential of 5 MPa. The relationship between percolation stage and water saturation of the pore type sample is illustrated in Fig. 2.25. The range of pressure differential in Darcy flow stage decreases with the increase of water saturation. However, the threshold pressure effect and non-Darcy flow effect of pore type reservoirs are slightly stronger than those of cavity type reservoirs. This difference in percolation characteristics is caused by the difference of pore throat structure between pore type and cavity type reservoirs. In summary, it is necessary to determine a reasonable range of production pressure differential before the exploitation of these two types of reservoirs, while avoiding the development of reservoirs with high water saturation.

(4) Comparison and analysis of percolation mechanism

It could be seen from Figs. 2.20d, 2.22d and 2.24d that the percolation capacities of the three types of reservoirs all decrease in varing degrees with the increase of water

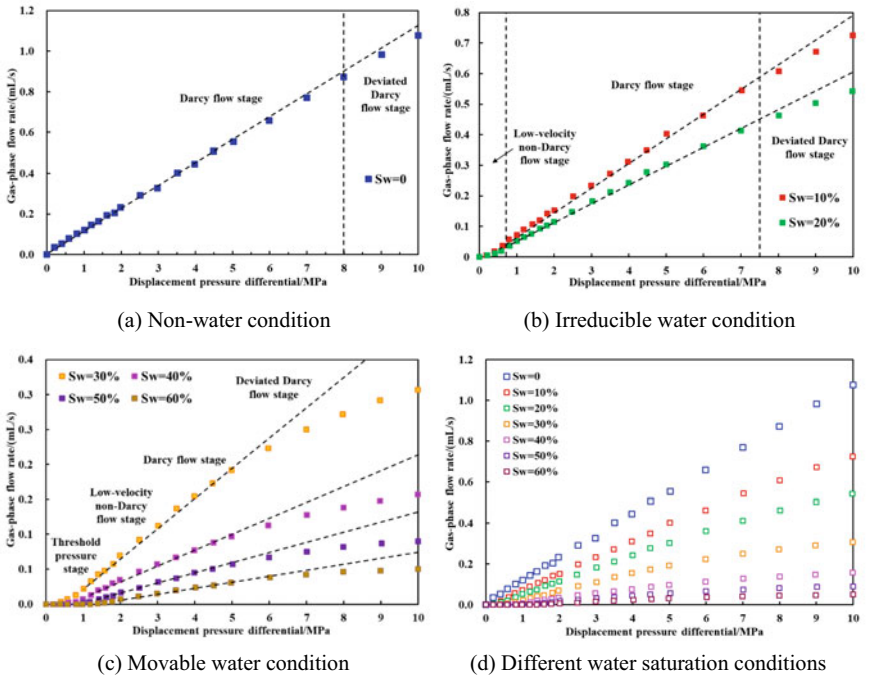

(a) Non-water condition

(b) Irreducible water condition

(c) Movable water condition

(d) Different water saturation conditions

Fig. 2.24 Percolation characteristic curves of the pore type sample under different water saturations

Table 2.15 Critical pressure differentials of each percolation stage under different water saturations (pore type sample)

Water saturation/%	Water condition	Threshold pressure stage/MPa	Low-velocity non-Darcy flow stage/MPa	High-velocity non-Darcy flow stage/MPa
0	Non-water	/	/	8.0
10	Irreducible water	/	0.6	7.5
20	Irreducible water	/	0.8	7.0
30	Movable water	0.2	1.0	6.0
40	Movable water	0.4	1.2	6.0
50	Movable water	0.8	1.4	5.5
60	Movable water	1.0	1.8	5.5

saturation. In order to compare the influence of water saturation difference on gas flow capacity of three types of reservoirs, the gas-phase flow rate of samples under non-water condition is defined as the lossless flow rate, and the gas-phase percolation capacity loss rate is defined as the ratio of the gas-phase loss flow rate under a certain water saturation to the lossless gas-phase flow rate. The effect of water saturation on the gas-phase percolation capacity loss rate of three types of reservoirs

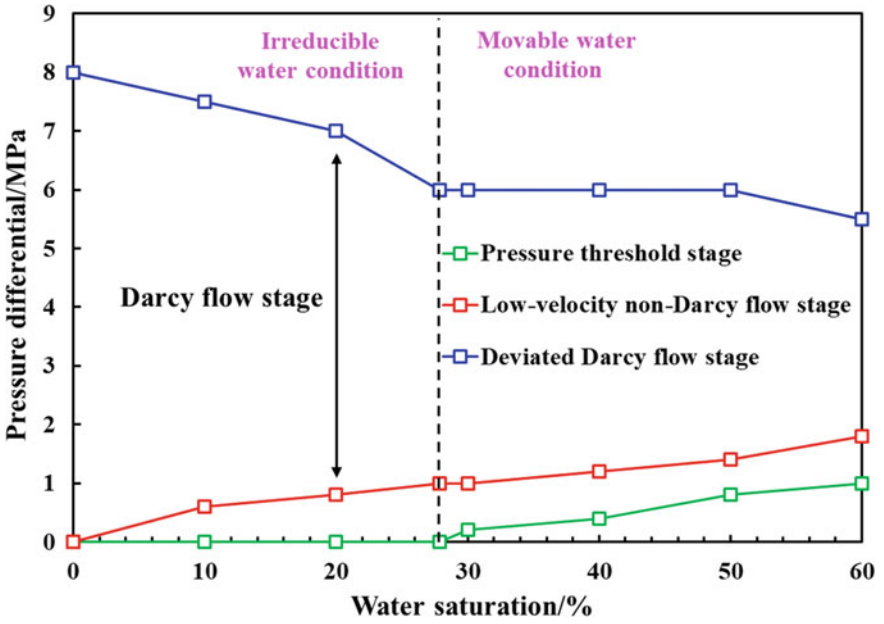

Fig. 2.25 Relationship between gas-phase percolation stage and water saturation of the pore type sample

under different displacement pressure differentials is illustrated in Fig. 2.26. The position of hexagonal stars in the figure are data points corresponding to irreducible water saturations of different types of reservoirs. The experimental results under three pressure differentials all show that the inhibition of reservoir water on the gas-phase percolation capacity of pore type and cavity type reservoirs is significantly stronger than that of fracture-cavity type reservoirs. This is because the percolation channel of fracture-cavity type reservoirs is dominated by fracture network with relatively high coordination number, whereas the percolation channel of cavity type and pore type reservoirs is dominated by pore throat network with relatively low coordination number. Reservoir water is difficult to completely block the fracture system, and therefore it has relatively little influence on the gas-phase percolation channel. In addition, the percolation capacity loss rate of the cavity type reservoir is lower than that of the pore type reservoir because the permeability of the cavity type sample selected in the experiment is better than that of the pore type sample. In fact, the petrophysical properties of most cavity type reservoirs in the Deng IV Member are better than those of pore type reservoirs. The loss rate of gas-phase percolation capacity of cavity type and pore type reservoirs increases significantly when irreducible water and movable water begin to exist in the reservoir. This phenomenon indicates that whether the reservoir contains water or not and whether it contains movable water has a significant impact on the gas-phase percolation characteristics and percolation capacity. In contrast, the gas-phase percolation capacity loss rate

of the fracture-cavity type reservoir increases steadily with the increase of water saturation, and only increases rapidly when the movable water content is high.

Finally, the gas-phase percolation characteristics and percolation mechanism under different water conditions of ultradeep carbonate gas reservoirs are summarized in Fig. 2.27 by analyzing the physical simulation experiment results of gas-phase percolation under different water saturations. In conclusion, the main factors affecting gas-phase percolation include viscous force, inertial force, stress sensitivity, secondary movable water, percolation channel size and pore throat connectivity. These factors have different effects on different types of reservoirs under different water conditions and displacement pressure differentials, thereby forming complex and special gas-phase percolation characteristics of ultradeep carbonate gas reservoirs.

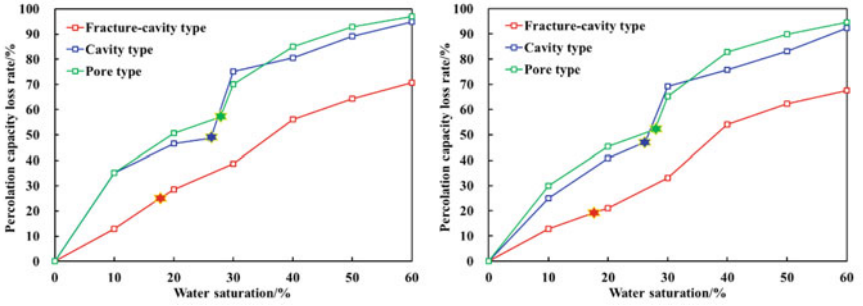

(a) Displacement pressure differential is 2 MPa (b) Displacement pressure differential is 4 MPa

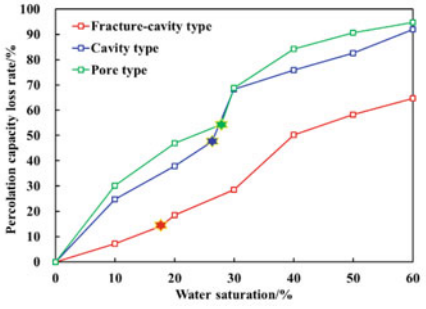

(c) Displacement pressure differential is 8 MPa

Fig. 2.26 Relationship between water saturation and production capacity loss rate of three types of reservoirs under different displacement pressure differentials

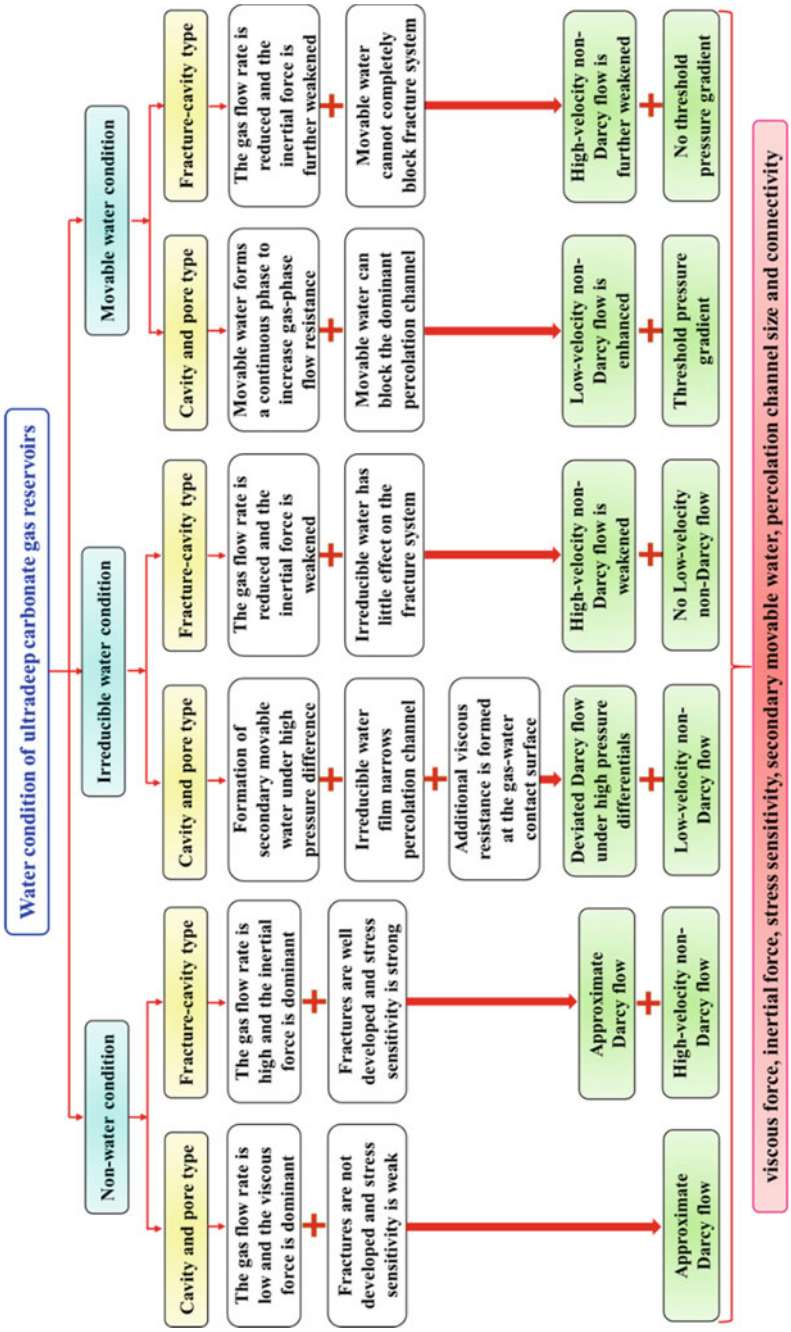

Fig. 2.27 Gas-phase percolation characteristics and percolation mechanism under different water conditions of ultradeep carbonate gas reservoirs

2.3 Mathematical Model of Gas-Phase Nonlinear Percolation

The physical simulation experiment of gas-phase percolation can obtain the gas-phase percolation characteristics and percolation capacity of a certain type of reservoir under the comprehensive influence of multiple factors. However, the percolation characteristic curve under any petrophysical properties cannot be obtained because of the limited number of physical simulation experiments. Furthermore, it is impossible to quantitatively analyze the influence of a single factor on gas-phase percolation through experimental data alone. Therefore, it is of great significance to establish a percolation mathematical model suitable for ultradeep deep carbonate gas reservoirs based on the limited experimental data. More importantly, the mathematical model of gas-phase percolation could be used to predict the production capacity of gas wells and analyze the influence of various factors on gas production. Gas well production capacity is the most critical and direct indicator to evaluate the development performance and effect of gas reservoirs.

At present, there are various mathematical models of conventional gas reservoirs with good applicability. These models can effectively predict the production capacities of gas wells under different geological, fluid and exploitation conditions. However, the special percolation mechanism of ultradeep carbonate gas reservoirs makes the applicability of these models poor. Therefore, some scholars have conducted related studies on the percolation mathematical model of ultradeep carbonate gas reservoirs. Liu et al. (2014) developed a binomial gas-phase percolation mathematical model considering stress sensitivity and high-velocity non-Darcy flow percolation based on the stress sensitivity and gas-phase percolation physical simulation experimental results of the Longwangmiao Formation ultradeep carbonate gas reservoir in the Sichuan Basin. However, this model does not consider the multiple reservoir types of ultradeep carbonate gas reservoirs. Subsequently, Gao et al. (2015) subdivided the ultradeep carbonate gas reservoir of Longwangmiao Formation into pore type, fracture type and cavity type, and then established a binomial gas-phase percolation mathematical model. However, this model does not consider the effect of well deviation angle, and therefore its applicability to deviated wells and horizontal wells is poor. Therefore, Meng et al. (2017) established a binomial gas-phase percolation mathematical model considering well deviation, stress sensitivity, and high-velocity non-Darcy flow. Nonetheless, the previous percolation mathematical model ignored the threshold pressure effect of pore type and low-permeability cavity type reservoirs under irreducible water conditions, did not analyze the influence of various factors on gas production capacity, and did not judge whether the mathematical model is generally applicable to the ultradeep carbonate gas reservoirs in different regions and different formations.

In view of the deficiencies of existing studies, a more applicable trinomial percolation mathematical mode for ultradeep carbonate gas reservoirs was re-established. The new model is based on the Forchheimer differential equation of gas phase (Forchheimer, 1901), and a threshold pressure gradient term was added. The threshold

pressure characteristics, stress sensitivity characteristics and non-Darcy flow characteristics of different types of carbonate gas reservoirs considered in the new model are all obtained through core physical simulation experiments. In addition, a large number of deviated wells have been drilled in ultradeep carbonate gas reservoirs in order to improve the gas productivity of single well. Therefore, a negative skin factor was introduced into the new model to describe the effect of well deviation angle on gas-phase flow rate. Then the new model was used to predict the gas production capacity of gas wells and evaluate the influence of various factors on the gas production. Subsequently, the sensitivity of gas production capacity to various factors was compared, and the main controlling factors for gas production capacity of different types of reservoirs were clarified. The accuracy and universality of the new model were verified by the prediction of gas production of gas wells in three different ultradeep carbonate gas reservoirs. Finally, the sensitivity of gas production capacity in three types of reservoirs to different influencing factors was studied by using orthogonal analysis method, and then the dominant factors that affect gas productivity of ultradeep carbonate gas reservoirs were determined.

2.3.1 Reservoir and Percolation Characteristics of Ultradeep Carbonate Gas Reservoirs

(1) Characteristics of various reservoir types

The research results of reservoir characteristics in Chap. 1 indicate that the ultradeep carbonate gas reservoir could be subdivided into matrix type, pore type, cavity type and fracture-cavity type reservoirs. The physical simulation experiment results of gas-phase percolation in Chap. 2 show that the difference in pore throat structure of four types of reservoirs results in different percolation characteristics and percolation capacity. Therefore, the establishment of gas-phase percolation mathematical model must consider the percolation characteristics and stress sensitivity characteristics of these reservoirs respectively. The matrix type reservoir, as an ineffective reservoir, is not necessary for further study. It should be noted that the new percolation mathematical model is only for gas single-phase rather than gas–water two-phase. This is because the initial water saturation of most gas wells in the Deng IV Member is below the irreducible water saturation, and these wells are less affected by external water. Figure 2.28 shows that the initial water saturations of several gas wells in the Gaoshiti and Moxi areas are all below 25%. Moreover, the mathematical model of gas-phase percolation is the basis of the mathematical model of gas–water two-phase percolation. For some reservoirs with relatively high initial water saturation, the new model can be further improved according to the relationship between gas relative permeability and water saturation in the gas–water two-phase flow curve introduced later.

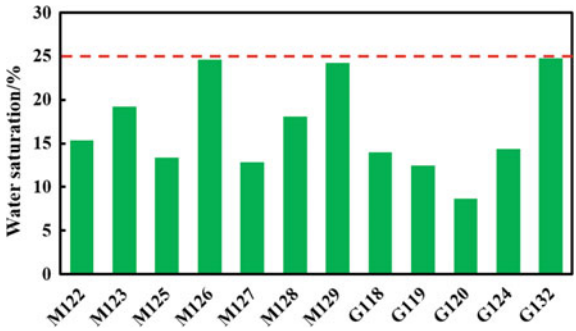

Fig. 2.28 Initial water saturations of several gas wells in the Gaoshiti and Moxi areas

(2) Characteristics of threshold pressure and non-Darcy flow

In order to ensure the universality of the new model, the physical simulation experimental data of gas-phase percolation in three different areas were selected to comprehensively analyze the threshold pressure and non-Darcy flow characteristics of ultradeep carbonate gas reservoirs. The experimental results show that the gas-phase flow in pore type and some low-permeability cavity type core samples exhibits an obvious threshold pressure effect at low displacement pressure differentials. Therefore, the commonly used binomial percolation mathematical model is not completely suitable for ultradeep carbonate gas reservoirs with threshold pressure effect. The threshold pressure gradient term should be added to the Forchheimer differential equation of gas phase. The relationship between threshold pressure gradient and permeability of samples for the three different areas is shown in Fig. 2.29. The data fitting results show that the threshold pressure gradient and permeability are approximately exponential, indicating that the threshold pressure effect of ultradeep carbonate gas reservoirs in different areas has similar laws.

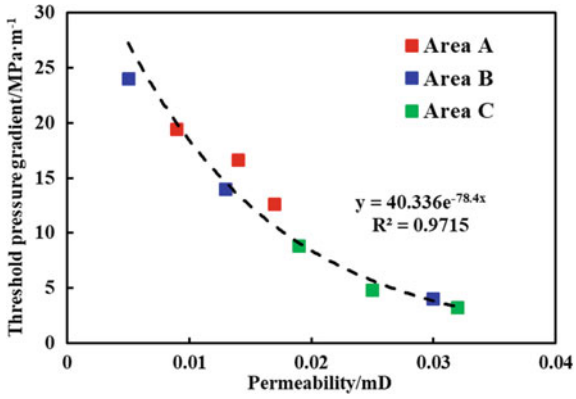

Fig. 2.29 Relationship between threshold pressure gradient and sample permeability in different areas

In addition, the relationship between gas-phase flow rate and pressure squared difference of the samples in intra-platform belt is illustrated in Fig. 2.30. The data fitting results reveal that the pressure squared difference and gas-phase flow rate of different types of samples are all in binomial relationship, indicating that the gas-phase percolation after overcoming the threshold pressure follows the Forchheimer differential equation. In order to compare the binomial percolation characteristics of samples in the three areas, the nonlinear percolation coefficient was calculated by using the binomial coefficient in the fitting formula. The relationship between nonlinear percolation coefficient and permeability of three different areas is illustrated in Fig. 2.31. The comparison results show that the nonlinear percolation coefficient and permeability of different types of reservoirs in the same area have an approximately linear relationship on the double logarithmic coordinate. The nonlinear percolation coefficient decreases with the increase of sample permeability. However, the nonlinear percolation coefficients of different areas are different under the same permeability (Fig. 2.32). Therefore, the corresponding nonlinear coefficients should be determined for carbonate gas reservoirs in different areas and applied to the gas-phase percolation mathematical model. The threshold pressure gradient term in different areas can adopt the same expression. Furthermore, the relationship between nonlinear percolation coefficient and permeability of an ultradeep sandstone gas reservoir in the Sichuan Basin (Area D) is also shown in Fig. 2.32. The comparison results reveal that the relationship between nonlinear percolation coefficient and permeability of the ultradeep carbonate and ultradeep sandstone gas reservoirs is similar. However, the nonlinear percolation effect of the ultradeep sandstone reservoirs is obviously stronger than that of ultradeep carbonate reservoirs. One reason is that the hardness of carbonate rock makes its percolation channel smoother than that of sandstone rock. Therefore, the additional resistance caused by the rough surface of the percolation channel is small during the gas-phase percolation process. Another reason is that the buffering effect of cavities and large-scale pores is significant when the gas-phase flows rapidly in the porous media of carbonate rock. The buffering effect could effectively reduce the non-Darcy flow effect. The nonlinear coefficients of ultradeep carbonate gas reservoirs in Sichuan Basin are generally smaller than those in foreign sandstone reservoirs.

(3) Characteristics of stress sensitivity

The stress sensitivity characteristics of ultradeep carbonate gas reservoirs were specifically introduced in Chap. 4 later. The ultradeep carbonate gas reservoir is generally moderate stress sensitivity, but the stress sensitive characteristics of the three types of reservoirs are different. Therefore, it is necessary to consider the influence of stress sensitivity on gas-phase percolation in the new mathematical model, and select corresponding stress sensitivity coefficients for different types of reservoirs.

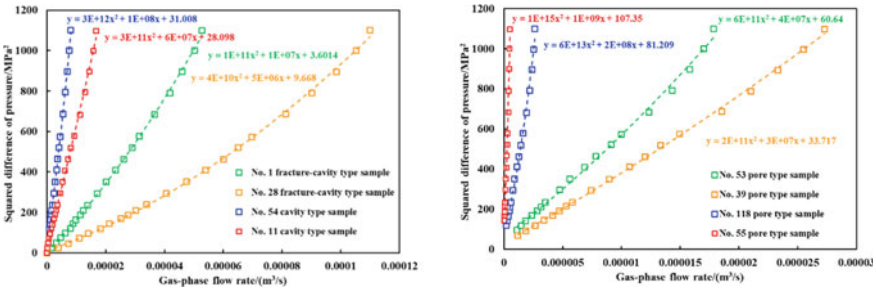

(a) Fracture-cavity and cavity type samples (b) Pore type samples

Fig. 2.30 Relationship between gas-phase flow rate and squared difference of pressure

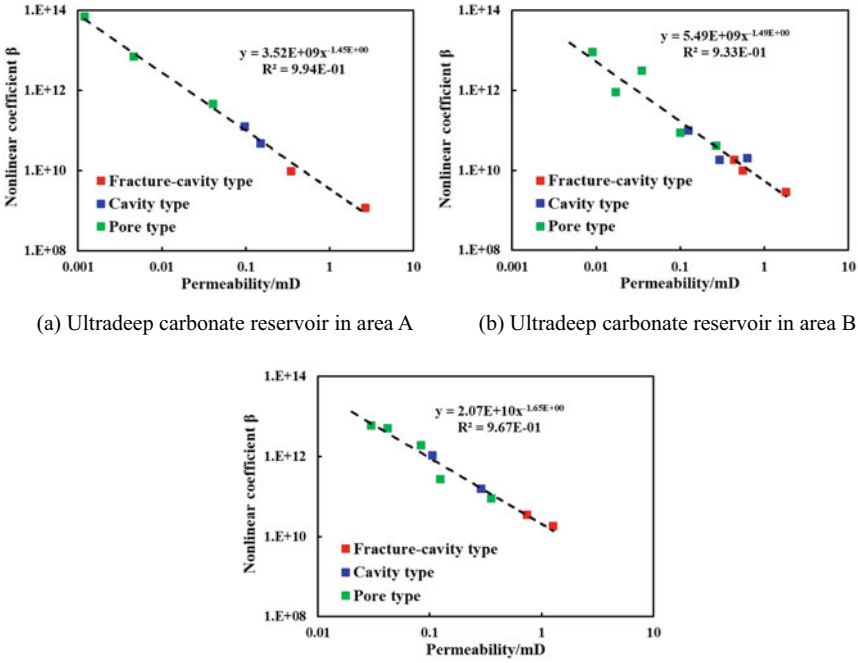

(a) Ultradeep carbonate reservoir in area A (b) Ultradeep carbonate reservoir in area B

(c) Ultradeep carbonate reservoir in area C

Fig. 2.31 Relationship between nonlinear percolation coefficient and permeability of ultradeep carbonate core samples in different areas

2.3.2 Trinomial Percolation Mathematical Modeling

The establishment of the trinomial percolation mathematical model requires seven physical assumptions. (1) There is only gas single-phase percolation in carbonate

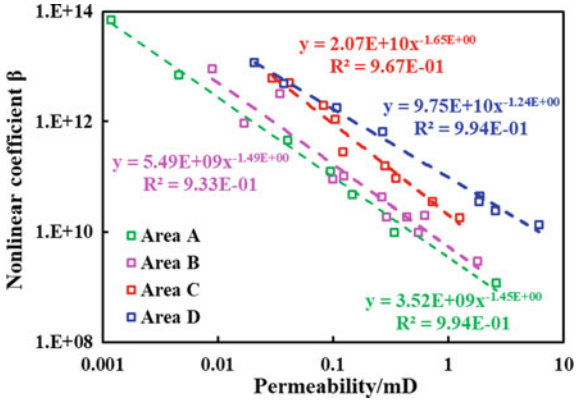

Fig. 2.32 Comparison of nonlinear percolation coefficients between ultradeep carbonate and ultradeep sandstone gas reservoirs (Area D is a ultradeep sandstone gas reservoir in Sichuan Basin)

porous media. (2) The gas-phase percolation process follows the law of non-Darcy flow. (3) The gas-phase percolation process is an isothermal plane radial steady percolation process. (4) There is a skin effect near the bottom of the gas well. (5) The pressure is evenly distributed at any position of the reservoir before production. (6) The effect of gravity and capillary forces are ignored. (7) The gas reservoir is quivalent to a circular homogeneous reservoir with equal thickness. The trinomial percolation mathematical model after introducing the threshold pressure gradient term is as follows.

$$\frac{\mathrm{d}p}{\mathrm{d}r} = \lambda + \frac{\mu}{K}\upsilon + \beta\rho\upsilon^2 \tag{2.1}$$

The first term of the Eq. (2.1) is the threshold pressure gradient term, which represents the threshold pressure effect. The second term of the Eq. (2.1) is the linear percolation term, which represents the viscous force. The last term of the Eq. (2.1) is the nonlinear percolation term, which represents the inertial force. Where p is the reservoir pressure, MPa; r is the reservoir radius, m; λ is the threshold pressure gradient, MPa/m; μ is the gas viscosity, mPa·s; υ is the gas-phase percolation velocity, m/s; K is the reservoir permeability, mD; β is the nonlinear percolation coefficient, 1/m; ρ is the gas density, kg/m^3. The threshold pressure gradient λ and the nonlinear percolation coefficient β in Eq. (2.1) need to be obtained through the physical simulation experiment of gas-phase percolation, and the permeability K in Eq. (2.1) needs to be expressed as a function related to pressure because of the stress sensitivity effect.

The threshold pressure gradient λ could be expressed by the fitting formula (Eq. (2.2)) in Fig. 2.29.

$$\lambda = 40.336e^{-78.4K} \tag{2.2}$$

The nonlinear percolation coefficient β could be calculated by the binomial fitting formula of samples with different permeability in Fig. 2.30. The calculation process is

based on the Forchheimer differential equation of gas phase. The gas-phase flow rate and the square difference of displacement pressure during the nonlinear percolation stage satisfies Eq. (2.3).

$$\left(p_{\mathrm{L}}^2 - p_0^2\right) = Cq_{\mathrm{sc}} + Dq_{\mathrm{sc}}^2 \tag{2.3}$$

The coefficient C and coefficient D in Eq. (2.3) could be expressed by Eqs. (2.4) and (2.5) (Gao et al., 2015).

$$C = 2\frac{\mu L}{KA}\frac{ZTp_{\mathrm{sc}}}{T_{\mathrm{sc}}} \tag{2.4}$$

$$D = \frac{2L\beta M}{ZRT}\left(\frac{ZTR_{\mathrm{sc}}}{AT_{\mathrm{sc}}}\right)^2 \tag{2.5}$$

where L is the length of the core sample, cm; A is the cross-sectional area of the core samples, cm^2; T is the experimental temperature, K; Z is the compressibility of the gas; p_{sc} is standard atmospheric pressure, 0.1013 MPa; T_{sc} is the reference temperature when testing the volume flow rate, 273.15 K; M is the molecular weight of the gas; R is a constant value, 8.314 J/(mol·K). The coefficient D is the binomial coefficient of the fitting formula in Fig. 2.30. Therefore, the nonlinear percolation coefficient β could be inversely calculated by Eq. (2.5).

$$\beta = \frac{DZRT}{2ML}\left(\frac{AT_{\mathrm{sc}}}{ZTP_{\mathrm{sc}}}\right)^2 \tag{2.6}$$

The nonlinear percolation coefficients of the ultradeep carbonate gas reservoirs in three different areas were obtained by using Eq. (2.6) and binomial coefficients in Fig. 2.30. Then, the relationship curve between the nonlinear percolation coefficient and the sample permeability was drawn (Fig. 2.31). Finally, the relational expression of nonlinear permeability coefficient and core permeability in three different areas was established by fitting the data points in Fig. 2.31.

$$\beta = \frac{2.07 \times 10^{10}}{K^{1.65}} \tag{2.7}$$

$$\beta = \frac{5.49 \times 10^{9}}{K^{1.49}} \tag{2.8}$$

$$\beta = \frac{3.52 \times 10^{9}}{K^{1.45}} \tag{2.9}$$

The stress sensitivity experimental results indicate that although the stress sensitivity of the three types of reservoirs is different, they all satisfy the Eq. (2.10).

$$\frac{K}{K_i} = \left(\frac{\sigma_s - P}{\sigma_s - P_i}\right)^{-\alpha} \tag{2.10}$$

where K_i is the sample permeability measured under the initial flowing pressure, mD; P_i is the initial flowing pressure, MPa; σ_s is the overburden pressure, MPa; α is the stress sensitivity coefficient. The experimental results of stress sensitivity show that the relationship between dimensionless permeability and Terzaghi effective stress conforms to a power function. The dimensionless permeability of the reservoir initially decreased rapidly with the increase of effective stress, then decreased slowly, and finally stabilizes. The relationship expressions of effective pressure and dimensionless permeability of three types of reservoirs were established by fitting experimental data points. Equations (2.11), (2.12) and (2.13) are stress sensitivity expressions of fracture-cavity type, cavity type and pore type reservoirs, respectively.

$$\frac{K}{K_i} = \left(\frac{\sigma_s - P}{\sigma_s - P_i}\right)^{-0.738} \tag{2.11}$$

$$\frac{K}{K_i} = \left(\frac{\sigma_s - P}{\sigma_s - P_i}\right)^{-0.591} \tag{2.12}$$

$$\frac{K}{K_i} = \left(\frac{\sigma_s - P}{\sigma_s - P_i}\right)^{-0.493} \tag{2.13}$$

The ultradeep carbonate gas reservoir has strong heterogeneity, and the horizontal and vertical anisotropy of the reservoir is significant. Well deviation can produce negative skin factor, and pseudo-skin factor can be calculated by Cinco-Lee model (Cinco & Miller, 1975) or Besson model (Besson, 1990). The calculation accuracy of the Cinco-Lee model is higher than that of the Besson model when the well deviation angle is less than 75°, whereas the Besson model is suitable for wells with a well deviation angle ranging from 0 to 90°. However, the Besson model requires many parameters and the calculation process is complicated, which increases the uncertainty of the calculation results. The well deviation angle in the study area is mostly less than 75°. Therefore, the Cinco-Lee model (Eqs. (2.14) and (2.15)) was selected to calculate the pseudo-skin factor S_θ caused by well deviation.

$$S_\theta = -\left(\frac{\theta'_w}{41}\right)^{2.06} - \left(\frac{\theta'_w}{56}\right)^{1.865} \times \lg\left(\frac{h_D}{1000}\right) \tag{2.14}$$

$$\theta'_w = \tan^{-1}\left(\sqrt{\frac{K_v}{K_h}}\tan\theta_w\right), h_D = \frac{h}{r_w}\sqrt{\frac{K_h}{K_v}} \tag{2.15}$$

where S_θ is the pseudo-skin factor; θ_W is the well deviation angle, °; θ'_w is the equivalent well deviation angel, °; K_h is the horizontal permeability of the reservoir, mD;

K_v is the vertical permeability of the reservoir, mD; h is the effective reservoir thickness, m; h_D is the dimensionless reservoir thickness; r_w is the gas well radius, m. In addition, the skin factor S_d was introduced to represent the reservoir pollution near the gas well caused by human factors. The equivalent wellbore radius r_{we} is defined to consider the combined effects of the skin factor S_d and the pseudo-skin factor S_θ.

$$r_{we} = r_w e^{-(S_d+S_\theta)} \tag{2.16}$$

Finally, Eq. (2.2) for the threshold pressure effect effect, Eqs. (2.7)–(2.9) for the nonlinear percolation effect, Eqs. (2.11)–(2.13) for the stress sensitivity effect, and Eq. (2.16) for the equivalent wellbore radius were substituted into the trinomial percolation differential Eq. (2.1). Equation (2.17) defines a modified pseudo-pressure function m to consider the effect of stress sensitivity on gas-phase percolation. m can be simplified to a common pseudo-pressure function when the value of α is 0.

$$m = \int_{P_0}^{P} \frac{2P}{\mu Z}\left(\frac{\sigma_s - P}{\sigma_s - P_i}\right)^{-\alpha} \mathrm{d}P \tag{2.17}$$

The derived trinomial percolation mathematical model of ultradeep carbonate gas reservoir is shown in Eq. (2.18). When the value of α is 0, Eq. (2.18) could be simplified to a model that does not consider stress sensitivity. When the value of C, α and β are all set to 0, Eq. (2.18) is simplified to the gas well productivity equation corresponding to the Darcy flow model.

$$m_e - m_w = C + Aq_{sc} + Bq_{sc}^2 \tag{2.18}$$

The expressions of the coefficients A, B and C are shown in Eqs. (2.19), (2.20) and (2.21), respectively.

$$A = \frac{P_{sc}T}{\pi K_i h Z_{sc} T_{sc}} \ln \frac{r_e}{r_{we}} \tag{2.19}$$

$$B = \frac{\beta M \gamma_g P_{sc}^2 T}{2\pi^2 h^2 T_{sc}^2 \mu R Z_{sc}^2} \frac{1}{r_{we}} \left(\frac{\sigma_s - \overline{P}}{\sigma_s - P_i}\right)^{-\alpha} \tag{2.20}$$

$$C = \lambda^2\left(r_e^2 - r_{we}^2\right) \frac{1}{\overline{\mu_B} \overline{Z_B}} \left(\frac{\sigma_s - \overline{P}}{\sigma_s - P_i}\right)^{-\alpha} \tag{2.21}$$

where m is the modified pseudo-pressure function; A represents the inertial resistance term; B represents the viscous resistance term; C represents the threshold pressure gradient term. q_{sc} is the gas well productivity under standard conditions, m^3/d; r_e is the single well control radius, m; $\overline{p}$ is the average reservoir pressure, MPa; γ_g is the ratio of natural gas density to dry air density under standard conditions; μ_B is the average viscosity of gas corresponding to $\lambda(r_e + r_w)/2$, mPa·s; Z_B is the average

deviation coefficient of gas corresponding to $\lambda(r_e + r_w)/2$; $\overline{P}$ is the average flowing pressure, MPa.

In order to verify the accuracy and universality of the trinomial percolation mathematical model in predicting the gas production of different types of reservoirs, six ultradeep carbonate gas wells in three different areas of Sichuan Basin were selected to compare the tested productivity and the predicted productivity. The reservoir properties and production parameters required by the new model were extracted by analyzing geological data and test data (Table 2.16). The single well control radius and reservoir permeability in the table were obtained through modern production decline analysis by TopazeNL production analysis software (Kappa workstation 5.10). The selected dynamic analysis method and model are the analytical method and the dual-porosity model, which are suitable for ultradeep carbonate gas reservoirs. Figure 2.33 shows the fitting effect of two gas wells in the Deng IV Member gas reservoir. Finally, the reservoir properties and production parameters, as well as the experimental results of stress sensitivity and gas-phase percolation were substituted into the trinomial percolation mathematical model to calculate the predicted productivity of each gas well. The comparison results of predicted productivity and gas well test productivity are shown in Table 2.17. The comparison results show that the relative errors of the productivity predictions of six gas wells are all within 3%, indicating that the new model is applicable to different types of ultradeep carbonate gas reservoirs located in multiple areas.

In addition, the new model was also used to calculate multiple IPR (Inflow Performance Relationship) curves considering different influencing factors. Figure 2.34 shows the IPR curve of a pore type reservoir. The comparison results show that the threshold pressure effect, stress sensitivity effect and non-Darcy flow effect all inhibit the gas well productivity to varying degrees. The gas production calculated by the new model is about 35% lower than that calculated by the Darcy flow model because the

Table 2.16 Reservoir properties and production parameters of carbonate gas reservoirs in three different areas of Sichuan Basin

Area number	A		B		C	
Well number	G3	X3	M11	G18	M13	X1
Reservoir type	Fracture-cavity type	Cavity type	Pore type	Cavity type	Pore type	Cavity type
Reservoir Depth/m	5023	5097	5179	5161	5103	5134
Reservoir thickness/m	47.37	28.5	61.01	34.4	54.18	56.80
Well deviation angel/°	68.4	60	6	5.4	3.33	59.5
Permeability/mD	2.51	1.075	0.14	1.22	0.098	0.821
Well control radius/m	933	945	1023	950	1057	902
Skin factor	5.06	4.21	4.96	3.64	5.01	7.08

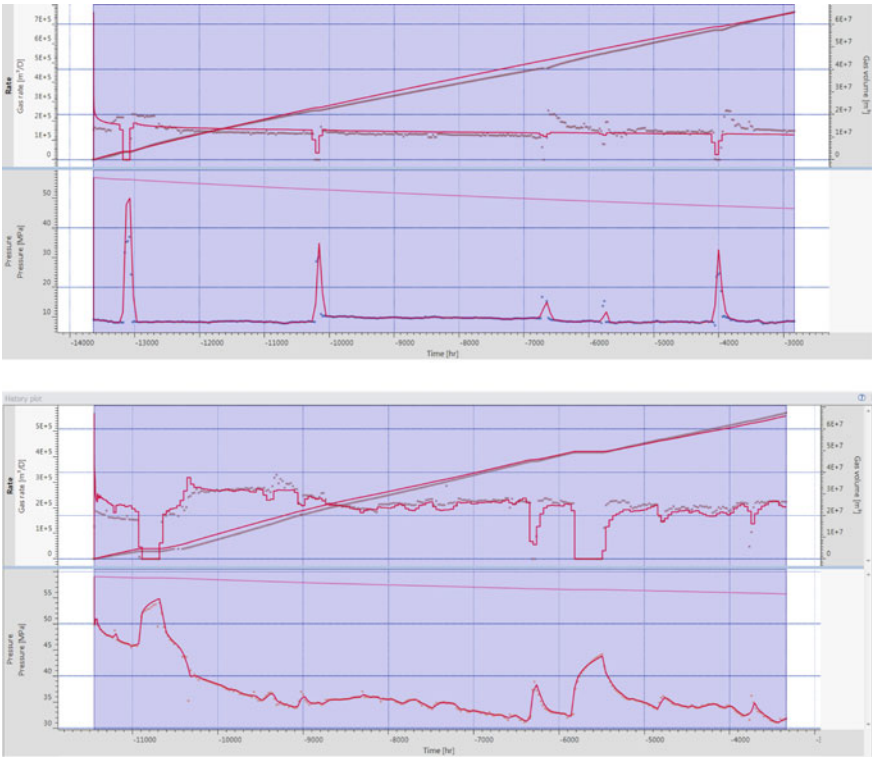

Fig. 2.33 Fitting effect of the combination of analytical method and dual-porosity model

Table 2.17 Productivity prediction results and relative errors of gas wells in different types of reservoirs

Area number	A		B		C	
Well number	G3	X3	M11	G18	M13	X1
Reservoir type	Fracture-cavity type	Cavity type	Pore type	Cavity type	Pore type	Cavity type
Tested productivity of gas well/10^4 m^3/d	157.66	51.10	9.19	60.60	6.92	46.5
Predicted productivity of model/10^4 m^3/d	160.66	49.57	8.95	59.15	6.74	45.24
Relative errors/%	1.91	− 2.99	− 2.62	− 2.39	− 2.62	− 2.71

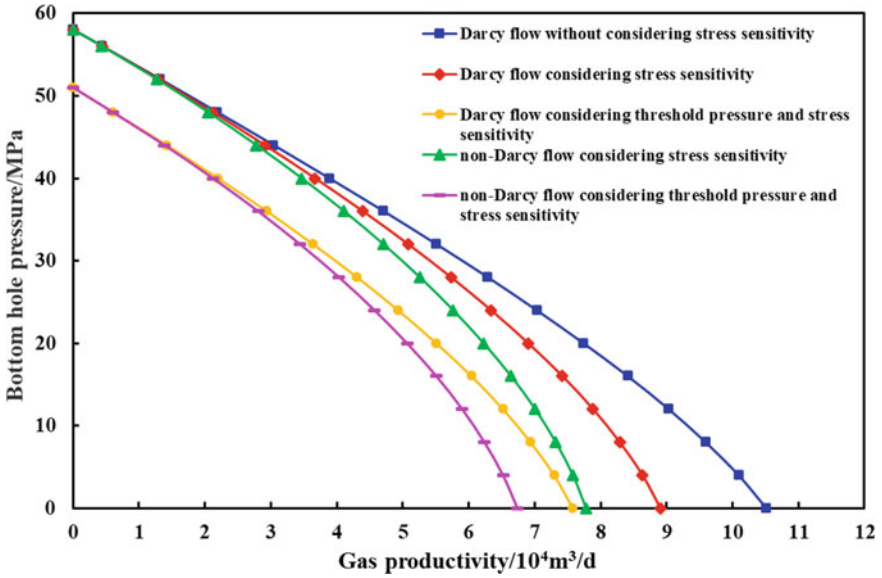

Fig. 2.34 IPR curves of a pore type reservoir under the influence of different factors

comprehensive influence of these three factors is considered. The trinomial model is more applicable than the binomial model because the threshold pressure effect can further reduce the productivity of pore type and low-permeability cavity type reservoirs, resulting in a significant difference in gas production calculated by the two models under the same production pressure differential. The inhibition of stress sensitivity and non-Darcy flow effects on production capacity is mainly reflected in the stage of high production pressure differential, because these two effects are not significant under low pressure differentials. Therefore, it is necessary to fully consider the influence of these three effects of different reservoirs when predicting gas well production, otherwise the predicted production under high production pressure differentials will be significantly higher than the actual production.

2.3.3 Analysis of Influencing Factors of Gas-Phase Percolation Capacity

In order to quantify the influence of threshold pressure effect, stress sensitivity effect, nonlinear percolation effect and well deviation angle on the productivity of different types of ultradeep carbonate gas reservoirs, multiple threshold pressure gradients, stress sensitivity coefficients, nonlinear percolation coefficients and well deviation angles were substituted into the trinomial percolation mathematical model. The influence of threshold pressure effect of pore type and low-permeability cavity

type reservoirs on gas production capacity is illustrated in Fig. 2.35a. The productivity of gas wells decreases with the increase of threshold pressure gradient, but the rate of productivity decline is different within different threshold pressure gradient ranges. The gas productivity is less affected by the threshold pressure effect when the threshold pressure gradient is lower than 0.01 MPa/m. However, the gas production capacity drops rapidly when the threshold pressure gradient is between 0.01 and 0.048 MPa/m. The control radius of gas wells in the Deng IV Member reservoir are between 800 and 1000 m. Therefore, the impact of threshold pressure effect on gas productivity cannot be ignored when the threshold pressure gradient is greater than 8 MPa. The gas productivity drops to zero when the threshold pressure gradient increases to greater than 0.048 MPa/m, because the gas phase in the reservoir cannot form effective percolation even under high production pressure differentials.

In contrast, the non-Darcy flow effect mainly affects the gas production capacity of fracture-cavity type and high-permeability cavity type reservoirs, and the relationship curve is illustrated in Fig. 2.35b. The productivity of gas wells decreases with the increase of nonlinear percolation coefficient, but the rate of productivity decline is different within the different ranges of different nonlinear percolation coefficient. The gas production capacity is less affected by the non-Darcy flow effect when the nonlinear percolation coefficient is lower than 1×10^9 m^{-1}. When the nonlinear percolation coefficient is between 1×10^9 and 1×10^{12} m^{-1}, the inhibition of inertial resistance on gas productivity increases rapidly. When the nonlinear percolation

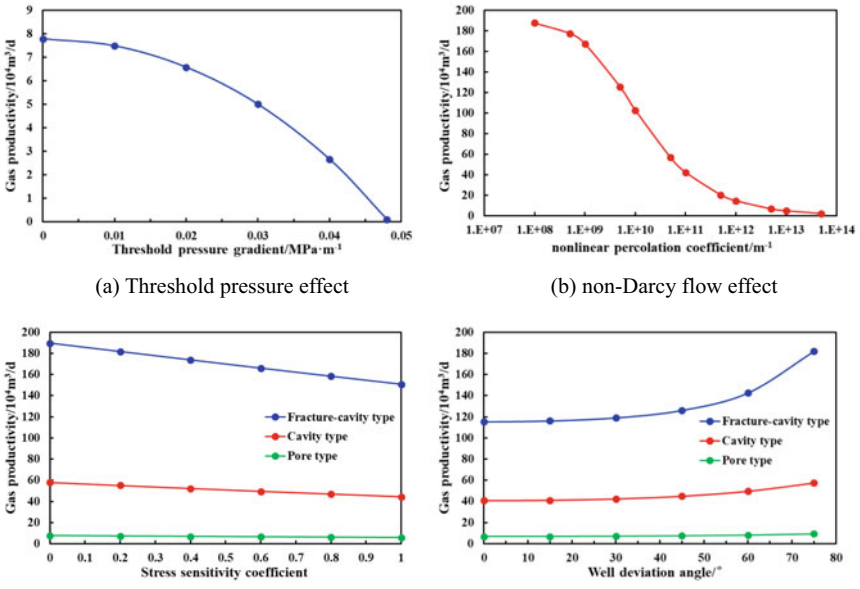

(a) Threshold pressure effect

(b) non-Darcy flow effect

(c) Stress sensitivity effect

(d) Well deviation angle

Fig. 2.35 Relationship curves between gas productivity and different influencing factors

coefficient increases to greater than 1×10^{12} m^{-1}, the rate of productivity decline gradually slows down and is infinitely close to zero.

The influence laws of stress sensitivity effect on gas production capacity of three types of reservoirs is shown in Fig. 2.35c. The figure shows that the gas production capacity of the three types of reservoirs decreases approximately linearly with the increase of stress sensitivity coefficient. When the stress sensitivity coefficient increases to 1.0, the productivity decline of each type of reservoir is less than 30%, indicating that the effect of stress sensitivity on the gas productivity of ultradeep carbonate gas reservoirs is not as large as expected. This conclusion is consistent with the actual production characteristics on site. Figure 2.35c also shows that there is little difference in gas productivity decline of the three types of reservoirs under the same stress sensitivity coefficient. However, the effect of stress sensitivity on the gas production capacity of fracture-cavity type reservoirs is greater than that of pore type and cavity type reservoirs. This is because the stress sensitivity coefficient of the fracture-cavity type reservoir is generally higher than that of pore type and cavity type reservoirs.

The improvement effect of different well deviation angles on the gas productivity of three types of reservoirs is illustrated in Fig. 2.35d. It can be seen from the figure that the productivity of gas wells increases with the increase of the well deviation angle, but the productivity growth rate is different within the different ranges of well deviation angles. The improvement effect of gas production capacity in three types of reservoirs are not obvious when the well deviation angle is lower than 50°. When the well deviation angle increases to greater than 50°, the gas productivity of the three types of reservoirs starts to increase rapidly with the increase of the well deviation angle. When the well deviation angle is increases to 75°, the gas productivity of fracture-cavity type, cavity type and pore type reservoirs increases by 57.73%, 40.72% and 37.85%, respectively. The data shows that highly deviated wells can greatly increase the gas productivity of ultradeep carbonate gas reservoirs, and the improvement effect of highly deviated wells on the gas production capacity of fracture-cavity type reservoirs is better than that of pore type and cavity type reservoirs.

This is the first time to analyze the influencing factors of gas production capacity of ultradeep carbonate gas reservoirs based on the trinomial percolation mathematical model. In addition, the orthogonal analysis method was used to compare the sensitivity of gas productivity to various factors, and then the dominant factors affecting the gas production capacity of the ultradeep carbonate gas reservoir in Deng IV Member were determined. The factors affecting gas productivity in the trinomial percolation mathematical model include reservoir permeability, effective thickness, well control radius, skin factor, well deviation angle, stress sensitivity coefficient, nonlinear percolation coefficient and threshold pressure gradient. The process of determining the dominant factors of gas productivity through orthogonal analysis is as follows. Firstly, the influencing factors and levels were selected according to the reservoir type. Then, the orthogonal analysis table was selected according to the number of factors and levels. Subsequently, the orthogonal test scheme was designed based on the value range of each factor. Finally, the influence order of each factor

on gas production capacity was determined according to the range of the orthogonal test.

Seven factors should be considered for fracture-cavity type reservoirs, namely, reservoir permeability, effective thickness, well control radius, skin factor, well deviation angle, stress sensitivity coefficient and nonlinear percolation coefficient. Three levels were designed for each influencing factor. Therefore, the orthogonal analysis table of L18(3^7) was selected to compare these factors affecting gas production capacity. The orthogonal analysis results of fracture-cavity type reservoirs are shown in Table 2.18. The results of range ranking show that the dominant factors affecting the gas productivity of fracture-cavity type reservoirs are skin factor, effective thickness and reservoir permeability. It could be concluded that the pollution and blockage of the reservoir near the wellbore have the greatest impact on the gas productivity of the fracture-cavity type reservoir. On the contrary, acidification, fracturing and other reservoir stimulation operations have obvious effects on gas productivity improvement. The product of reservoir permeability (K) and effective thickness (H) is the formation coefficient (K·H), which is an important parameter that intuitively reflects the reservoir productivity. In addition to the above three parameters related to reservoir properties, the nonlinear percolation coefficient also has a great impact on the gas production capacity of fracture-cavity type reservoirs. Therefore, the efficient development of fracture-cavity type reservoirs not only requires the optimization of the well location, but also avoids the pollution and damage to the reservoir near the wellbore during the drilling process. In addition, the production pressure differential should be controlled to avoid the negative effect of high-velocity non-Darcy flow on gas productivity and reservoir energy.

The influencing factors of gas production capacity that need to be considered in cavity type reservoirs are the same as those in fracture-cavity type reservoirs. Therefore, the orthogonal analysis table of L18(3^7) was also selected to compare these factors in cavity type reservoirs. The orthogonal analysis results of cavity

Table 2.18 Orthogonal analysis results of dominant factors of gas well productivity in fracture-cavity type reservoirs

Influence factor	Level 1	Level 2	Level 3	Range	Ranking of influence factors
Reservoir permeability/mD	1	5	10	837	3
Effective thickness/m	20	60	100	972	2
Well control radius/m	600	900	1200	535	5
Skin factor	− 4	2	8	1395	1
Well deviation angle/°	0	30	75	358	7
Stress sensitivity coefficient	0	0.5	1.0	488	6
Nonlinear percolation coefficient/m^{-1}	1×10^8	1×10^9	1×10^{10}	583	4

type reservoirs are shown in Table 2.19. The results of range ranking show that the dominant factors affecting the gas production capacity of cavity type reservoirs are also the skin factor and formation coefficient. The cavity type reservoir has strong storage capacity but weak percolation capacity. Well location optimization and reservoir stimulation are the key to achieve profitable gas productivity for cavity type reservoirs.

In addition to the above seven factors, the threshold pressure gradient also affects the gas production capacity of pore type reservoirs. Therefore, the orthogonal analysis table of L27(3^8) was selected to compare these factors affecting gas production capacity. The orthogonal analysis results of pore type reservoirs are shown in Table 2.20. The results of range ranking show that the dominant factors affecting the gas productivity of pore type reservoirs are skin factor, effective thickness and well deviation angle. In addition, the threshold pressure gradient and reservoir permeability are similar in the value of range, indicating that the threshold pressure effect has a relative strong effect on the gas production capacity of pore type reservoirs. The effect of non-Darcy flow on pore type reservoirs is obviously weaker than that of cavity type and fracture-cavity type reservoirs. Therefore, pore type reservoirs are suitable for replenishing high-permeability reservoirs under high production pressure differentials in the middle and late development stages. This is because the pore type reservoir is affected by the threshold pressure effect and low permeability under the low production pressure differential, and there is no gas production or the gas production capacity is lower than the profitable productivity.

In summary, the orthogonal analysis results of the three types of reservoirs show that the stress sensitivity has relatively weak influence on the gas production capacity of ultradeep carbonate gas reservoirs. The skin factor and the formation coefficient are the key factors that affect the gas productivity of three types of reservoirs in Deng IV Member. Besides, the effect of non-Darcy flow on high-permeability reservoirs

Table 2.19 Orthogonal analysis results of dominant factors of gas well productivity in cavity type reservoirs

Influence factor	Level 1	Level 2	Level 3	Range	Ranking of influence factors
Reservoir permeability/mD	0.4	1.2	2.0	146	3
Effective thickness/m	20	60	100	222	2
Well control radius/m	600	900	1200	85	6
Skin factor	− 4	2	8	333	1
Well deviation angle/°	0	30	75	72	7
Stress sensitivity coefficient	0	0.5	1.0	98	5
Nonlinear percolation coefficient/m^{-1}	1×10^9	5×10^9	2×10^{10}	108	4

Table 2.20 Orthogonal analysis results of dominant factors of gas well productivity in pore type reservoirs

Influence factor	Level 1	Level 2	Level 3	Range	Ranking of influence factors
Reservoir permeability/mD	0.05	0.075	0.1	16.3	4
Effective thickness/m	20	60	100	21.8	2
Well control radius/m	600	900	1200	13.0	6
Skin factor	− 4	2	8	24.0	1
Well deviation angle/°	0	30	75	17.1	3
Stress sensitivity coefficient	0	0.5	1.0	12.3	7
Nonlinear percolation coefficient/m^{-1}	1×10^{11}	3×10^{11}	5×10^{11}	1.66	8
Threshold pressure gradient/MPa/m	0	0.024	0.048	16.1	5

and the effect of threshold pressure gradient on low-permeability reservoirs should be carefully considered.

2.4 Gas–Water Two-Phase Percolation Mechanism

Relative permeability curve of gas–water two-phase is the most significant parameter for production performance prediction, exploitation scheme design and gas–water distribution characteristics analysis. There are two main methods to obtain the relative permeability curve, namely direct measurement method and indirect calculation method. The indirect calculation method is generally based on the capillary pressure curve, production data and empirical formula. The direct measurement method is divided into steady state method and non-steady state method, generally referring to the National Standard GB/T 28912-2012 of the P.R. of China. However, the test temperature and pressure conditions required in the standard are relatively low, and the effects of high temperature, high pressure and stress sensitivity are not considered. Therefore, the test results obtained according to the standard cannot truly reflect the gas–water two-phase percolation characteristics under reservoir conditions, especially in the ultradeep gas and heavy oil reservoir. Therefore, Sola et al. (2007) obtained the oil–water relative permeability curves under different temperatures using the JBN method. The results revealed that the oil–water relative permeability of heavy oil carbonate systems is a functions of temperature. Guo et al. (2014) established a conversion formula that can convert the relative permeability curve under experimental conditions to that under different reservoir conditions. Then, they studied the effects of temperature and pressure on the relative permeability of

gas–water two-phase. However, these calculation results have not been verified by the experimental results. Fang et al. (2015) tested the relative permeability curves of the same tight sandstone samples under conventional conditions and reservoir conditions, respectively. These study results all show that the change of temperature and pressure leads to the change of relative permeability curve. Therefore, it is of great significance to accurately measure the relative permeability curve of gas–water two-phase under reservoir conditions for predicting the development performance of gas reservoirs.

Edge and bottom water bodies are developed in some areas of the Cambrian Longwangmiao Formation and Sinian Dengying Formation carbonate gas reservoirs in Sichuan Basin. Intense water encroachment in some layers seriously affects the efficient and stable development of gas reservoirs. However, the water breakthrough characteristics and water production performance of gas wells in ultradeep carbonate gas reservoirs are difficult to predict because of the diversity of reservoir types and strong reservoir heterogeneity. The multiscale storage spaces and percolation channels of pores, throats, fractures and cavities make the gas–water two-phase percolation mechanism more complex. Furthermore, the ultra-high reservoir temperature and pressure conditions make the relative permeability curve measured under conventional conditions inapplicable to the ultradeep carbonate gas reservoir. Historical experience has confirmed that the use of conventional relative permeability curves will bring varying degrees of errors to reservoir numerical simulation and production performance prediction.

At present, the research on the gas–water two-phase percolation mechanism mainly focuses on the fileds of tight sandstone (Fang et al., 2015; Guo et al., 2014; Ji, 2018; Zhang et al., 2018b;), coalbed methane (Chen et al., 2014; Sun et al., 2018a, 2018b), and shale gas reservoirs (Zhang et al., 2018a). However, the water encroachment of these gas reservoirs is mainly caused by limited water bodies, which is quite different from the intense edge and bottom water encroachment characteristics of carbonate gas reservoirs. Therefore, the relevant research results of other types of gas reservoirs have limited reference value for the study of gas–water two-phase percolation mechanism of ultradeep carbonate gas reservoirs. The investigations on the relative permeability of gas–water two-phase in ultradeep carbonate gas reservoirs is rare and incomplete (Wan et al., 2019). Li et al. (2017b) obtained gas–water two-phase relative permeability curves of different types of carbonate core samples in Sichuan Basin under high temperature and pressure conditions. However, the test temperature and confining pressure are 50 °C and 50 MPa, respectively. Although the testing conditions were improved, they are still far lower than the actual reservoir conditions. Wang et al. (2017c) studied the gas–water two-phase percolation mechanism of carbonate core samples under actual reservoir temperature and pressure conditions. However, they only selected fracture-cavity type samples for investigation, and did not consider different types of carbonate gas reservoirs. Therefore, it is necessary to study the gas–water two-phase percolation mechanism of different types of carbonate gas reservoirs under the actual reservoir temperature and pressure conditions, and compare and analyze the influence of reservoir types and experimental conditions on the relative permeability curve.

In this work, the testing method of gas–water two-phase relative permeability under reservoir temperature and pressure was developed by improving the operation process of the conventional test method. In addition, the ultra-high temperature and pressure physical simulation experimental system breaks through the upper limit of the testing conditions of the relative permeability curve. Firstly, the relative permeability curves of different types of carbonate samples were measured by conventional methods under normal temperature and pressure conditions. Then, these samples were processed and tested for relative permeability curves under reservoir temperature and pressure conditions. Finally, the difference in relative permeability curves of different types of reservoirs under the two test conditions were compared, and the effects of temperature, pressure and reservoir type on gas–water two-phase percolation characteristics were analyzed. More importantly, some full-diameter core samples were also selected for testing experiments to avoid the measurement error caused by too small pore volume and the boundary effect caused by too short plunger core length. Full-diameter cores could better reflect the reservoir heterogeneity of ultradeep carbonate gas reservoirs than plunger cores. The study results are of great significance to the exploitation scheme formulation and production performance prediction of ultradeep carbonate gas reservoirs.

2.4.1 Experimental Samples and Conditions

Plunger cores of the Cambrian Longwangmiao Formation and full-diameter cores of the Sinian Dengying Formation in Sichuan Basin were selected for gas–water two-phase percolation experiments under conventional conditions and reservoir conditions. The end faces of these core samples were cut and polished using a diamond wire cutting machine. The porosity and permeability of each sample were measured by helium porosimeter and overburden pulse method after core treatment. The reservoir properties of the Longwangmiao Formation are generally better than those of the Dengying Formation. The reservoir classification standard of the Longwangmiao Formation is different from that of the Dengying Formation. The reservoir of the Longwangmiao Formation could be divided into three types, namely pore type, fracture-pore type and fracture-cavity type (Fig. 2.36). However, the development frequency of cavities in this areas is lower than that of the Dengying Formation, whereas the development frequency of fractures is higher than that of the Dengying Formation. Only a small number of plunger cores contain cavities. Therefore, the cavity type plunger core was not selected for the two-phase percolation experiment. The effect of cavities on two-phase percolation characteristics could also be analyzed by comparing the experimental results of fracture-pore type and fracture-cavity type core samples. The full-diameter cores taken from the Dengying Formation could still be divided into pore type, cavity type and fracture-cavity type. However, most full-diameter cores contain fractures and cavities because the length and diameter of these cores are much larger than those of plunger cores (Fig. 2.37). The petrophysical parameters of core samples for two-phase percolation experiments are summarized

in Tables 2.21 and 2.22. The reason for not selecting the matrix type core for the experiment is that the complete saturation of formation water cannot be achieved for this type of sample.

The temperature and pressure of gas–water two-phase percolation experiments were designed according to the ultra-high temperature and pressure conditions of ultradeep carbonate gas reservoirs. The experimental temperature, confining pressure and pore pressure of the Longwangmiao Formation reservoir are 140 °C, 126 MPa and 76 MPa, respectively. The experimental temperature, confining pressure and pore pressure of the Dengying Formation reservoir are 150 °C, 138 MPa and 56 MPa, respectively. The experimental temperature, confining pressure and pore pressure of the conventional conditions are 25 °C, 3 MPa and 0.5 MPa, respectively. High-purity nitrogen was used as experimental gas to simulate natural gas because the

(a) Pore type core

(b) Fracture-cavity type core

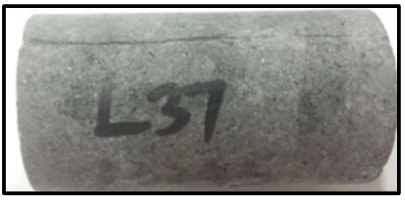

(c) Fracture-pore type core

Fig. 2.36 Photographs of three types of representative plunger cores from the Longwangmiao Formation reservoir

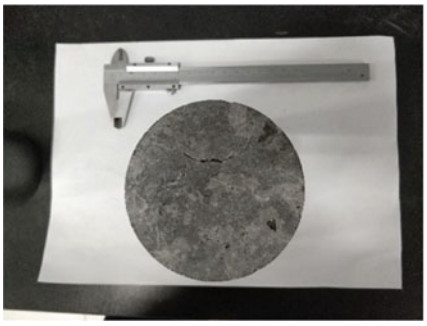

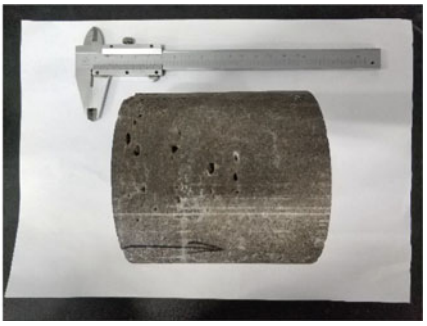

Fig. 2.37 Photographs of representative full-diameter cores from the Dengying Formation reservoir

Table 2.21 Petrophysical parameters of plunger cores for two-phase percolation experiments

Core number	Core type	Length/mm	Diameter/mm	Permeability/mD	Porosity/%
L50	Pore type	48.54	24.90	0.054	4.86
L58	Pore type	46.68	24.90	0.031	4.82
L62	Pore type	47.32	25.10	0.028	4.01
L90	Fracture-cavity type	47.40	25.10	3.135	8.19
L92	Fracture-cavity type	47.59	25.00	2.629	7.38
L93	Fracture-cavity type	46.83	25.10	6.535	9.65
L7	Fracture-pore type	45.41	25.20	1.687	2.90
L73	Fracture-pore type	44.72	25.10	3.029	2.40
L37	Fracture-pore type	46.98	25.20	1.633	1.91

Table 2.22 Petrophysical parameters of full-diameter cores for two-phase percolation experiments

Core number	Core type	Length/mm	Diameter/mm	Permeability/mD	Porosity/%
G4	Pore type	101.2	65.4	0.005	2.24
G11	Pore type	103.6	70.0	0.013	4.52
G1	Cavity type	102.9	65.1	0.042	7.33
G7	Cavity type	103.4	69.2	0.261	6.21
G6	Fracture-pore type	104.1	69.5	0.301	1.83
G9	Fracture-cavity type	103.5	69.3	0.865	6.51

use of natural gas for ultra-high temperature and pressure experiments can easily cause powerful combustion and explosions. The experimental water was prepared in the laboratory according to the analysis results of the chemical composition of formation water, as shown in Table 2.3. The fluid viscosity, compressibility factor and interfacial tension under ultra-high temperature and pressure conditions and conventional conditions were calculated by PVTsim, and the calculation results are shown in Table 2.23. It should be noted that the experimental water preparation was performed in a reactor rather than in a glass container. The temperature and pressure of the reactor should be maintained continuously after water sample preparation to prevent salt precipitation from the water. Salt precipitation not only changes the experimental water properties, but also may block the flow channel in the pipeline and core sample.

Table 2.23 High pressure properties of experimental fluids

Experimental condition	Experimental fluid	Viscosity/cp	Compressibility factors	Interfacial tension/(mN/m)
Ultra-high temperature and pressure conditions	Nitrogen	0.054	1.287	42.36
	Brine	0.337	0.264	
Conventional temperature and pressure conditions	Nitrogen	0.019	1.000	71.25
	Brine	0.934	/	

2.4.2 Experimental Scheme

In order to compare the gas–water two-phase percolation characteristics of different types of reservoirs under conventional conditions and reservoir conditions, the experimental samples were allocated, as shown in Table 2.24. Comparative experiments were conducted under the two conditions on plunger and full-diameter core samples of each reservoir type.

2.4.3 Experimental Method

There are two methods for measuring the relative permeability of gas–water two-phase in the laboratory, namely the steady state method and the unsteady state method. The unsteady state method could be divided into the displacement method of gas by water and the displacement method of water by gas. However, there is basically no gas produced at the outlet end of the core sample after water breakthrough in the displacement method of gas by water, thereby making it difficult to obtain and process experimental data. Previous experiments show that the data points obtained by the displacement method of gas by water are few, and the two-phase percolation region in the relative permeability curve is not obvious. Therefore, the displacement method of water by gas was adopted in most gas–water two-phase percolation experiments, and most of the relative permeability curves used in gas reservoir engineering calculation are also measured by the displacement method of water by gas. Regardless of whether the relative permeability curve is measured by the displacement method of gas by water or the displacement method of water by gas, the irreducible water saturation and the two-phase percolation region range obtained by the two methods are basically the same.

The displacement method of water by gas is based on Buckerly-Leverette theory. The theory assumes that the fluid is incompressible and ignores gravity and capillary forces. The theory also requires that the distribution of gas and water on any section of the core sample is uniform, and the distribution of gas and water saturation in

Table 2.24 Experimental scheme of gas–water two-phase percolation under conventional and reservoir conditions

Core number	Core size	Core type	Conventional conditions	Reservoir conditions
L50	Plunger core	Pore type	√	√
L58		Pore type		√
L62		Pore type		√
L90		Fracture-cavity type		√
L92		Fracture-cavity type	√	√
L93		Fracture-cavity type		√
L7		Fracture-pore type		√
L73		Fracture-pore type	√	√
L37		Fracture-pore type		√
G4	Full-diameter core	Pore type	√	√
G11		Pore type	√	√
G1		Cavity type	√	√
G7		Cavity type	√	√
G6		Fracture-pore type	√	√
G9		Fracture-cavity type	√	√

the core is a multivariate function of time and distance. The flow rate of each phase fluid at the outlet and the pressure change at both ends of the core holder should be recorded at different times, and then the gas–water two-phase relative permeability under different gas saturation could be calculated by the JBN method (Johnson et al., 1959). In order to reduce the influence of end effect to improve the accuracy and representativeness of the obtained relative permeability curve, the displacement pressure differential of the two-phase percolation experiment should conform to the Eq. (2.22).

$$\pi_1 = \frac{10^{-3}\sigma_{gw}}{\Delta p_0 \sqrt{K_a/\phi}} \tag{2.22}$$

where π_1 is the ratio of capillary pressure and displacement pressure, which is required to be less than or equal to 0.6. Where σ_{gw} is the interfacial tension between gas phase and water phase, mN/m; K_a is the permeability of the core sample, D; ϕ is the porosity of core sample, %; Δp_0 is the initial displacement pressure differential of the experiment, MPa.

In addition, the cumulative liquid production needs to be corrected by Boyle's law. There is always a pressure difference between the inlet and outlet of the core sample

during the displacement process. The gas volume changes gradually as the gas flows from the inlet through the core sample to the outlet. Therefore, it is necessary to correct the volume of cumulative production measured at the outlet to the volume under the average pressure of the core sample. The Boyle correction formula is shown in Eq. (2.23).

$$V_t = \Delta V_{wt} + V_{t-1} + \frac{2P_a}{\Delta p + 2p_a}\Delta V_{gt} \tag{2.23}$$

where V_t is the cumulative liquid production under average pressure of the core sample at time t, mL; V_{t-1} is the cumulative liquid production under average pressure of the core sample at time $t-1$, mL; ΔV_{wt} is the volume of water production in the time interval from $t-1$ to t, mL; p_a is atmospheric pressure, MPa; Δp is the displacement pressure differential, MPa; ΔV_{gt} is the volume of gas production in a period of time interval under atmospheric pressure, mL.

More importantly, the gas dissolution in water and the volume change of water and gas should be considered under ultra-high temperature and pressure. Therefore, it is necessary to convert the volume of water production and gas production measured under conventional conditions into those under reservoir conditions. The conversion formulas are shown in Eqs. (2.24) and (2.25).

$$W'(t) = W(t)B_{\mathrm{w}} \tag{2.24}$$

$$G'(t) = [G(t) - W(t)GWR]B_{\mathrm{g}} \tag{2.25}$$

Then, the JBN method was used to calculate the gas saturation at the outlet of the core sample, as well as the relative permeability of water phase and gas phase at different times. The detailed calculation formulas are as follows.

$$K_{\mathrm{rg}} = K_{\mathrm{rw}} \cdot \frac{\mu_{\mathrm{g}}}{\mu_{\mathrm{w}}} \cdot \frac{1 - f_{\mathrm{w}}(S_{\mathrm{g}})}{f_{\mathrm{w}}(S_{\mathrm{g}})} \tag{2.26}$$

$$K_{\mathrm{rw}} = f_{\mathrm{w}}(S_{\mathrm{g}}) \frac{d[1/V(t)]}{d\{1/[I \cdot V(t)]\}} \tag{2.27}$$

$$f_{\mathrm{w}}(S_{\mathrm{g}}) = \frac{dV_{\mathrm{w}}(t)}{dV(t)} \tag{2.28}$$

$$I = \frac{Q(t)}{Q_0} \cdot \frac{\Delta P_0}{\Delta P(t)} \tag{2.29}$$

$$Q(t) = \frac{W'(t) - W'(t-1) + G'(t) - G'(t-1)}{\Delta t} \tag{2.30}$$

$$S_{\mathrm{ge}} = V_{\mathrm{w}}(t) - V(t) f_{\mathrm{w}}\left(S_g\right) \tag{2.31}$$

$$V_{\mathrm{w}}(t) = \frac{W'(t)}{V_{\mathrm{p}}} \tag{2.32}$$

$$V(t) = \frac{W'(t) + G'(t)}{V_{\mathrm{p}}} \tag{2.33}$$

where $W'(t)$ and $W(t)$ represent the cumulative water production before and after conversion, respectively, mL; $G(t)$ and $G'(t)$ represent the cumulative gas production before and after conversion, respectively, mL; B_{g} and B_{w} represent the volume coefficients of gas and water, respectively; GWR is the gas–water ratio in equilibrium water phase; $f_{\mathrm{w}}(S_{\mathrm{g}})$ represents the water cut, which is a function of gas saturation, f; S_{g} is the gas saturation, f; $V_{\mathrm{w}}(t)$ is the dimensionless cumulative water production; $V(t)$ is the dimensionless cumulative liquid production; K_{rw} and K_{rg} represent the relative permeability of water-phase and gas-phase, respectively, f; I is the mobility ratio; μ_{w} and μ_{g} represent the viscosity of formation water and natural gas, respectively, mPa·s; Q_0 is the water flow rate at the outlet of the core sample at the initial time, mL/s; Q(t) is the flow rate of water and gas at the outlet of the core sample at time t; ΔP is the initial displacement pressure differential, MPa; $\Delta P(t)$ is the displacement pressure differential at time t, MPa; Δt is the time difference, s; S_{ge} is the gas saturation at the outlet of the core sample, f; V_{p} is the effective pore volume of the core sample, mL.

2.4.4 Experimental Procedure

The detailed experimental procedure of gas–water two-phase percolation experiment under conventional temperature and pressure conditions can refer to the National Standard GB/T 28912-2012 of the P.R. of China. (1) The core sample was weighed after cleaning and drying, and then evacuated and saturated with formation water. The amount of water saturated in the sample was calculated by weighing its wet weight. (2) The sample was placed in the core holder and then the experimental system was connected according to Fig. 2.9. (3) The water flooding was conducted after the confining pressure of core system was increased to 3 MPa. The water-phase permeability obtained by water flooding was used as the basic value for calculating the relative permeability of gas–water two-phase. (4) The valve of the gas cylinder was switched to conduct the displacement experiment of water by gas under a reasonable displacement pressure differential. The pressure difference shall be large enough to overcome the capillary end effect, and small enough to prevent turbulence and satisfy the requirement of Eq. (2.22). (5) During the experiment, the pressure differential, gas production and water production at different times were recorded through the pressure sensor, wet flowmeter and gas–liquid separator, respectively. The interval between data recordings after gas breakthrough needs to be shortened. (6) When the water volume in the gas–liquid separator no longer increased, the irreducible water

saturation in the core system had been established, and the gas-phase permeability under the irreducible water condition was measured. (7) The sample was weighed again with an electronic balance after the experiment. (8) Repeat the experiment on the same sample according to steps (1)–(7). The data is repeatable and reliable if the error of the two experimental results is less than 5%. Otherwise, the reasons should be analyzed and the experiment should be repeated. (9) The relative permeability of gas–water two-phase was calculated according to the experimental data and JBN method.

The main process of the gas–water two-phase percolation experiment under ultra-high temperature and pressure conditions is similar to that under conventional conditions. However, there are still some different steps that require attention. (1) The gas and water in the intermediate containers should be pressurized to 50 MPa through the pressurization system before being connected to the experimental system. (2) The pore pressure was provided by the high-pressure syringe pump instead of the gas cylinder. (3) A humidifier was installed at the inlet of the core system to maintain the equilibrium state between gas and water during water flooding and gas flooding. Besides, a condenser was installed at the outlet of the core system to prevent the water vapor formed by pressure drop from being carried away by the gas flow. (4) It is necessary to establish the temperature system first and then establish the pressure system to avoid the pressure fluctuation caused by the gas compressibility when the temperature and pressure rise at the same time. (5) It is necessary to simultaneously and slowly increase the confining pressure and pore pressure to avoid core damage caused by stress sensitivity when establishing the pressure system. (6) When the displacement process is completed, it is necessary to gradually reduce the back pressure and collect produced water. The sample is taken out and weighed after the temperature of core system drops to room temperature. (7) The rubber sleeve and sealing ring need to be replaced after each experiment to ensure the tightness of the experimental system because of the long experimental period under ultra-high temperature and pressure conditions.

2.4.5 Characteristics of Gas–Water Two-Phase Percolation in Different Types of Carbonate Reservoirs

(1) Pore type sample

Figure 2.38 shows the relative permeability data of pore type samples under reservoir conditions obtained through gas–water two-phase percolation experiments on three pore type core samples. In order to facilitate the comparison and analysis of two-phase percolation characteristics of different samples, the discrete data points were fitted by the Corey model. The fitting formula of Corey model is shown in Eqs. (2.34) and (2.35). The standard relative permeability curves of the three samples after fitting are shown in Fig. 2.39. In addition, the key parameters of two-phase percolation characteristics are summarized in

Table 2.25 according to these standard curves. It can be seen that the irreducible water saturation (S_{wi}) of pore type reservoirs ranges from 41.89 to 47.72%, and the gas-phase relative permeability (K_{rg}) under irreducible water saturation ranges from 0.285 to 0.315. With the increase of core permeability, the S_{wi} decreases, the K_{rg} under S_{wi} increases, and the displacement efficiency of water by gas increases. The point on the relative permeability curve where the gas-phase relative permeability and the water-phase relative permeability (K_{rw}) are equal is called the iso-permeability point. The saturation and relative permeability corresponding to the iso-permeability point are represented by S_e and K_e, respectively. The S_e of pore type reservoirs ranges from 30.74 to 35.92%, and the K_e ranges from 0.11 to 0.16. The values of S_e and K_e could reflect the reservoir wettability and two-phase percolation capacity, respectively. When the reservoir wettability is hydrophilic, the S_e is less than 50%. The smaller the value of S_e, the stronger the hydrophilicity. In summary, the curve characteristics and key parameters of the three samples are similar, and they can represent the gas–water two-phase relative permeability curve of pore type reservoirs after normalization.

$$K_{rg}(S_w) = K_{rge}\left(\frac{1 - S_{gr} - S_w(i)}{1 - S_{gr} - S_{wi}}\right)^{n_g} \tag{2.34}$$

$$K_{rw}(S_w) = K_{rwe}\left(\frac{S_w(i) - S_{wi}}{1 - S_{gr} - S_{wi}}\right)^{n_w} \tag{2.35}$$

where $K_{rg}(S_w)$ and $K_{rw}(S_w)$ represent the relative permeability of gas phase and water phase under a certain water saturation (S_w), respectively, f; K_{rge} and K_{rwe} represent the gas-phase relative permeability under irreducible water saturation and the water-phase relative permeability under residual gas saturation, respectively; S_{gr} and S_{wi} represent residual gas saturation and irreducible water saturation, respectively; n_g and n_w are the fitting exponents of the gas-phase relative permeability and water-phase relative permeability, respectively.

(2) Fracture-cavity type sample

Figure 2.40 shows the relative permeability data of fracture-cavity type samples under reservoir conditions obtained through gas–water two-phase percolation experiments on three fracture-cavity type core samples. The standard relative permeability curves of the three samples after fitting are shown in Fig. 2.41. In addition, the key parameters of two-phase percolation characteristics are summarized in Table 2.26 according to these standard curves. It can be seen that the S_{wi} of fracture-cavity type reservoirs ranges from 27.58 to 40.03%, and the K_{rg} under S_{wi} ranges from 0.442 to 0.768. With the increase of core permeability, the S_{wi} decreases, the K_{rg} under S_{wi} increases, and the displacement efficiency of water by gas increases. The S_e of fracture-cavity type reservoirs ranges from 24.07 to 27.70%, and the K_e ranges from 0.11 to 0.16. The curve characteristics and key parameters of the three samples are similar, and they can

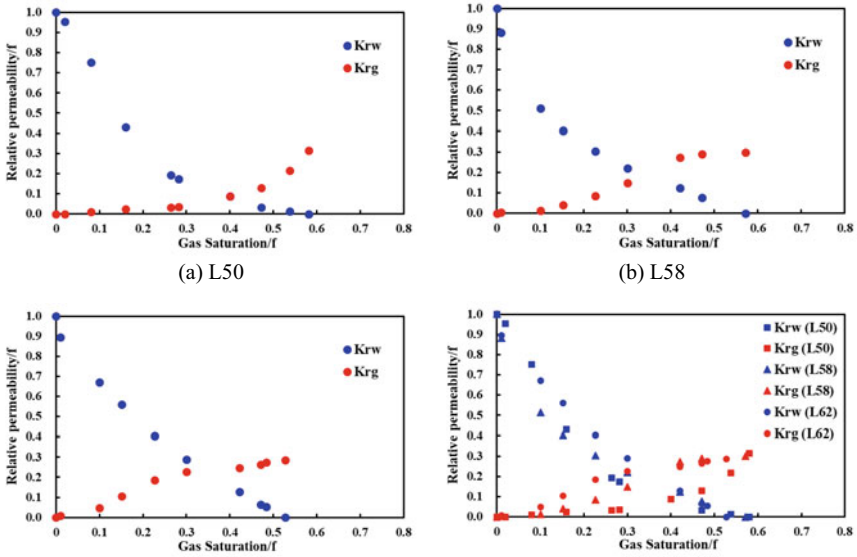

Fig. 2.38 Experimental data on relative permeability of pore type samples under reservoir conditions

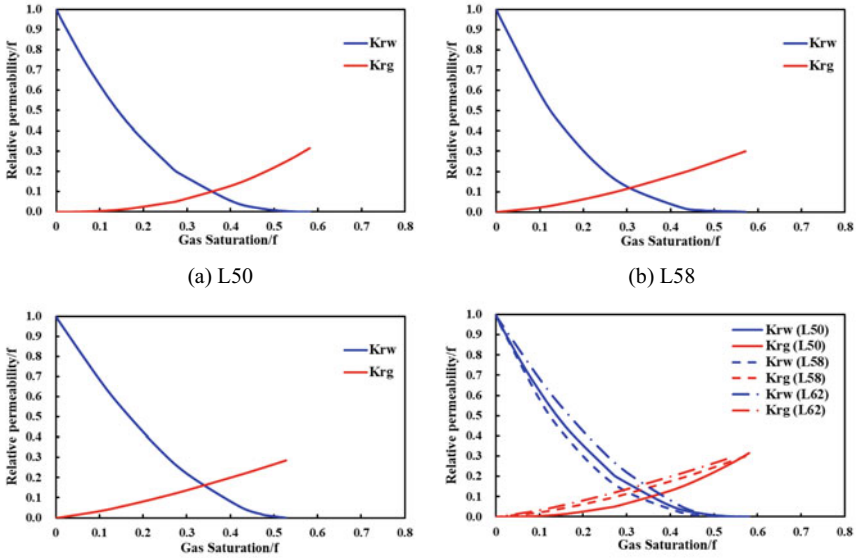

Fig. 2.39 Standard relative permeability curves of pore type samples under reservoir conditions

Table 2.25 Two-phase percolation characteristic parameters of pore type samples under reservoir conditions

Core number	L50	L58	L62
Porosity/%	4.86	4.82	4.01
Permeability/mD	0.054	0.031	0.028
S_{wi}/%	41.89	42.97	47.22
K_{rg} under S_{wi}/f	0.315	0.299	0.285
S_e/%	35.92	30.74	34.11
K_e under S_e/f	0.11	0.13	0.16
Two-phase percolation region/%	58.11	57.03	52.78

represent the gas–water two-phase relative permeability curve of fracture-cavity type reservoirs after normalization.

(3) Fracture-pore type sample

Figure 2.42 shows the relative permeability data of fracture-pore type samples under reservoir conditions obtained through gas–water two-phase percolation experiments on three fracture-pore type core samples. The standard relative permeability curves of the three samples after fitting are shown in Fig. 2.43. In addition, the key parameters of two-phase percolation characteristics are summarized in Table 2.27 according to these standard curves. It can be seen that the S_{wi} of fracture-pore type reservoirs ranges from 42.98 to 51.24%, and the K_{rg} under S_{wi} ranges from 0.350 to 0.613. With the increase of core permeability,

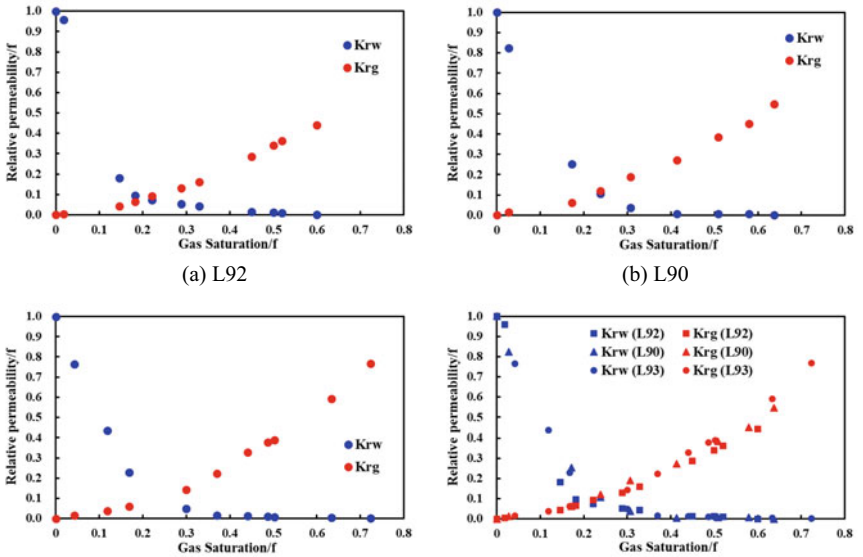

Fig. 2.40 Experimental data on relative permeability of fracture-cavity type samples under reservoir conditions

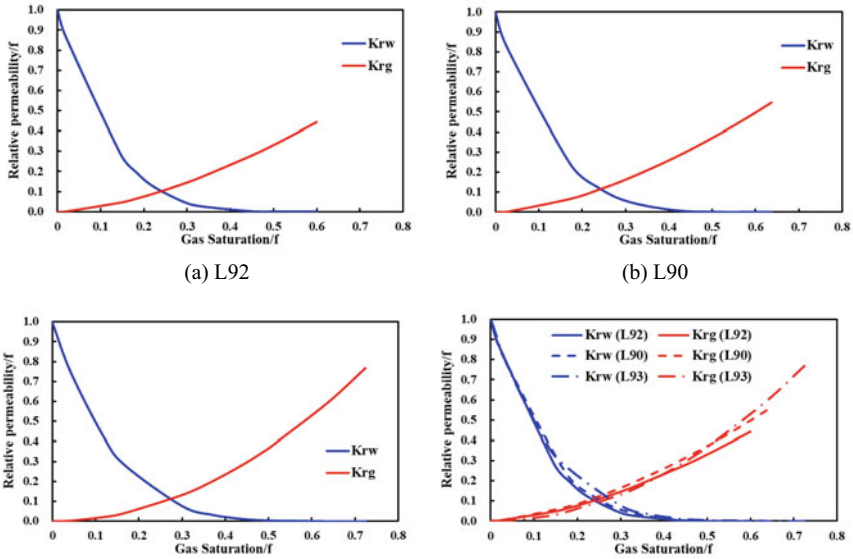

(a) L92 (b) L90

(c) L93 (d) Summary of relative permeability curves

Fig. 2.41 Standard relative permeability curves of fracture-cavity type samples under reservoir conditions

Table 2.26 Two-phase percolation characteristic parameters of fracture-cavity type samples under reservoir conditions

Core number	L92	L90	L93
Porosity/%	7.38	8.19	9.65
Permeability/mD	2.629	3.135	6.535
S_{wi}/%	40.03	36.34	27.58
K_{rg} under S_{wi}/f	0.442	0.547	0.768
S_e/%	24.07	24.22	27.70
K_e under S_e/f	0.11	0.12	0.12
Two-phase percolation region/%	59.97	63.66	72.42

the S_{wi} decreases, the K_{rg} under S_{wi} increases, and the displacement efficiency of water by gas increases. The S_e of fracture-pore type reservoirs ranges from 22.41 to 25.76%, and the K_e ranges from 0.12 to 0.16. The curve characteristics and key parameters of the three samples are similar, and they can represent the gas–water two-phase relative permeability curve of fracture-pore type reservoirs after normalization.

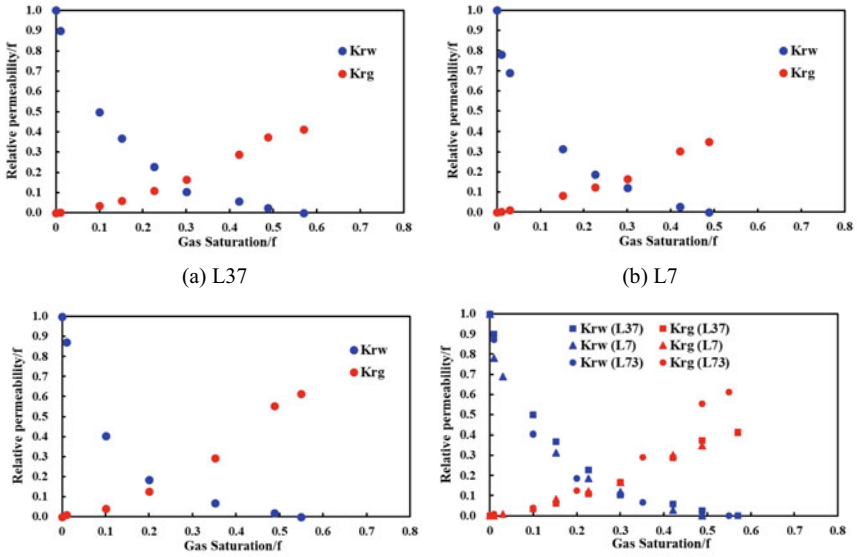

(a) L37 (b) L7

(c) L73 (d) Summary of experimental data

Fig. 2.42 Experimental data on relative permeability of fracture-pore type samples under reservoir conditions

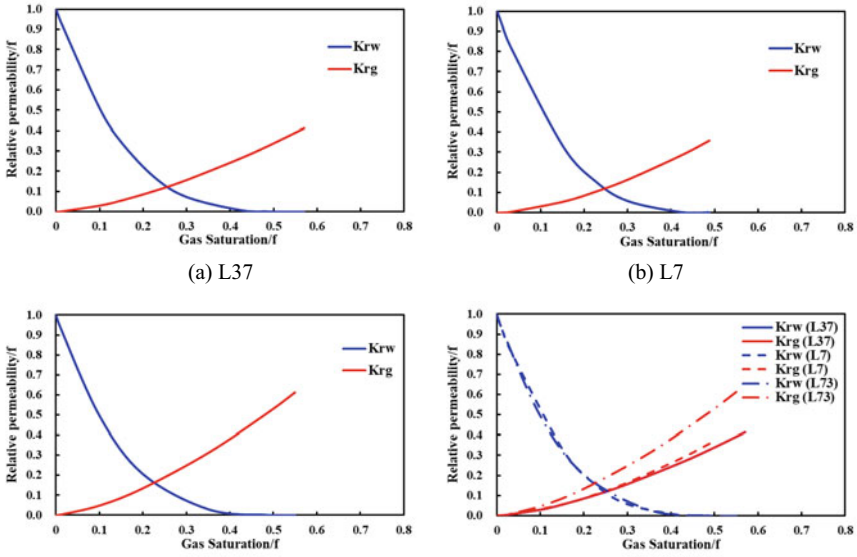

(a) L37 (b) L7

(c) L73 (d) Summary of relative permeability curves

Fig. 2.43 Standard relative permeability curves of fracture-pore type samples under reservoir conditions

Table 2.27 Two-phase percolation characteristic parameters of fracture-pore type samples under reservoir conditions

Core number	L37	L7	L73
Porosity/%	1.91	2.90	2.40
Permeability/mD	1.633	1.687	3.092
S_{wi}/%	42.98	51.24	45.03
K_{rg} under S_{wi}/f	0.413	0.350	0.613
S_e/%	25.76	24.33	22.41
K_e under S_e/f	0.13	0.12	0.16
Two-phase percolation region/%	57.02	48.76	54.97

2.4.6 *Effect of Reservoir Type on Gas–Water Two-Phase Percolation Characteristics*

The gas–water two-phase relative permeability curves of the same type of core sample are similar, but the curve characteristics of different types of carbonate cores are obviously different. The representative relative permeability curves of different types of reservoirs are indispensable tools for gas reservoir engineering calculation and numerical simulation of ultradeep carbonate gas reservoirs. Therefore, the curves of the same type of samples were normalized and averaged to obtain standard charts of relative permeability curves for the three types of reservoirs (Fig. 2.44). The key parameters of two-phase percolation characteristics are summarized in Table 2.28 according to these normalized curves. The following conclusions could be drawn by comparing the normalized curves and characteristic parameters of different types of reservoirs. ① The wettability of ultradeep carbonate gas reservoirs is hydrophilicity because the S_e is less than 50%. The S_e of the reservoir with fractures is lower than that of the reservoir without fractures. This reflects that the gas-phase percolation capacity of the reservoir with fractures is stronger than the water-phase percolation capacity in a relatively wide range of S_g. ② The S_{wi} of the fracture-cavity type reservoir is the lowest, and the two-phase percolation region is the largest. In contrast, the S_{wi} of the fracture-pore type reservoir is the highest, and the two-phase percolation region is the narrowest. The S_{wi} and two-phase percolation region of the pore type reservoir are between the other two types of reservoirs, but closer to those of the fracture-pore reservoir. This is because the gas–water two-phase percolation in the fracture-pore type reservoir mainly occurs in the fracture system, but the reservoir space connected by fractures is limited. The water in the pores not connected by fractures is difficult to be displaced, resulting in the highest S_{wi} in the fracture-pore type reservoir. However, fractures in the fracture-cavity type reservoir effectively connect isolated storage spaces, especially isolated cavities with excellent storage capacity. The microscopic visual investigation of gas–water two-phase percolation confirms that the cavity can reduce the water encroachment intensity and increase the sweep range. Therefore, not only most of the water in cavities, but also some of the water in pores could be displaced. The reasonable combination of fractures and cavities makes the displacement effect of fracture-cavity type reservoirs the best.

③ The two-phase percolation characteristics of pore type reservoirs are similar to those of homogeneous tight sandstone gas reservoirs. ④ The K_{rg} under the S_{wi} of the fracture-cavity type reservoir is the largest, followed by the fracture-pore type reservoir and the pore type reservoir. Furthermore, Fig. 2.44d shows that the K_{rg} of the reservoir with fractures is relatively large and the K_{rw} is relatively small under the same saturation. All these indicate that the fracture system could improve the gas-phase percolation capacity and relatively reduce the water-phase percolation capacity in the gas–water two-phase system under the reservoir conditions. However, the weakening effect of cavities on fluid encroachment intensity in fracture system makes the gas-phase and water-phase percolation capacities of fracture-cavity type reservoirs weaker than those of fracture-pore type reservoirs. The two-phase percolation region of the fracture-cavity type reservoir is larger than that of the fracture-pore type reservoir, and therefore the gas-phase percolation capacity of the former exceeds the maximum value of the latter under high gas saturation. In summary, the two-phase percolation characteristics of different types of carbonate reservoirs are significantly different. Therefore, the corresponding relative permeability curve should be selected according to the dominant types of carbonate reservoirs in the study area when conducting gas reservoir engineering calculation and numerical simulation research.

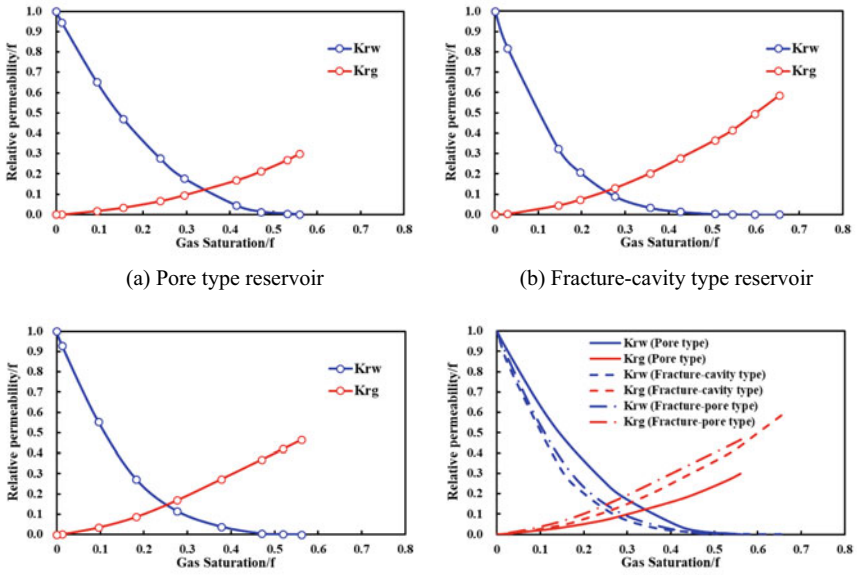

(a) Pore type reservoir

(b) Fracture-cavity type reservoir

(c) Fracture-pore type reservoir

(d) Summary of relative permeability curves

Fig. 2.44 Averaged relative permeability curves of different types of samples under reservoir conditions

Table 2.28 Two-phase percolation characteristic parameters of different types of samples under reservoir conditions

Reservoir type	Pore type	Fracture-cavity type	Fracture-pore type
S_{wi}/%	43.96	34.58	46.44
K_{rg} under S_{wi}/f	0.299	0.586	0.465
S_e/%	34.22	25.27	25.83
K_e under S_e/f	0.13	0.12	0.15
Two-phase percolation region/%	56.04	65.42	53.56

2.4.7 Effect of Temperature and Pressure Conditions on Gas–Water Two-Phase Percolation Characteristics

In order to compare the two-phase percolation characteristics of three types of reservoirs under different temperature and pressure conditions, the relative permeability curves of the same core sample under reservoir conditions and conventional conditions is illustrated in Fig. 2.45. The key parameters of two-phase percolation characteristics are summarized in Table 2.29 according to these standard curves. The following conclusions can be drawn by comparing the normalized curves and characteristic parameters of three types of reservoirs under different temperature and pressure conditions. ① The S_e of three types of reservoirs decreased under high temperature and pressure conditions. This indicates that the hydrophilicity of reservoir conditions is weaker than that of conventional conditions. ② The S_{wi} of three types of reservoirs decreased and the two-phase percolation region increased under high temperature and pressure conditions. These differences also reflect that the displacement efficiency of water by gas under reservoir conditions is higher than that under conventional conditions. ③ The gas-phase relative permeability curves of three types of reservoirs measured under high temperature and pressure conditions rise slowly. Although S_{wi} is relatively low under high temperature and pressure conditions, the K_{rg} under the S_{wi} is still relatively small. These differences indicate that the gas-phase percolation capacity under reservoir conditions is weakened, while the water-phase percolation capacity is relatively enhanced. Two types of water encroachment phenomena during the exploitation of ultradeep carbonate gas reservoirs in the Longwangmiao Formation could be explained by this conclusion. One is that the advance of gas–water front in the reservoir is relatively slow before the formation water breaks through the gas well. The other is that the gas production decreases rapidly and the water–gas ratio continues to rise after the formation water breaks through the gas well (Li et al., 2017b). ④ The S_e of three types of reservoirs increased under high temperature and pressure conditions. This means that the water-phase percolation capacity is stronger than the gas-phase percolation capacity in a relatively wide range of S_g under reservoir conditions. This explains why the

water–gas ratio of ultradeep carbonate gas wells rises earlier and faster. Therefore, the two-phase percolation characteristics obtained under these two conditions verify that the water encroachment intensity of ultradeep carbonate gas reservoirs is generally stronger than that of conventional gas reservoirs. Some ultradeep carbonate gas wells were completely flooded within a month or even several days after the formation water breakthrough.

The gas–water two-phase percolation characteristics of the three types of reservoirs under reservoir condition are obviously different from those under conventional conditions. The main reason for these differences is that the pore structure and fluid properties of ultradeep carbonate gas reservoirs under high temperature and pressure conditions are completely different from those under conventional conditions. The effective stress increases greatly under high pressure conditions, resulting in different degrees of compression and deformation in the throats, pores, cavities and fractures. The reservoir property parameters (porosity, permeability and heterogeneity) that affect two-phase percolation characteristics change with the pore structure. The stress sensitivity of fractures in the reservoir is far stronger than that of other reservoir media, and some fractures may be completely closed under high effective stress. Therefore, the difference between the relative permeability curves of fractured reservoirs under the two conditions is more obvious. However, this difference in fracture-cavity type reservoirs is relatively small because the fluid preservation and compression resistance of cavities are strong. In addition, the fluid properties of gas phase and liquid phase will also change significantly under ultra-high temperature

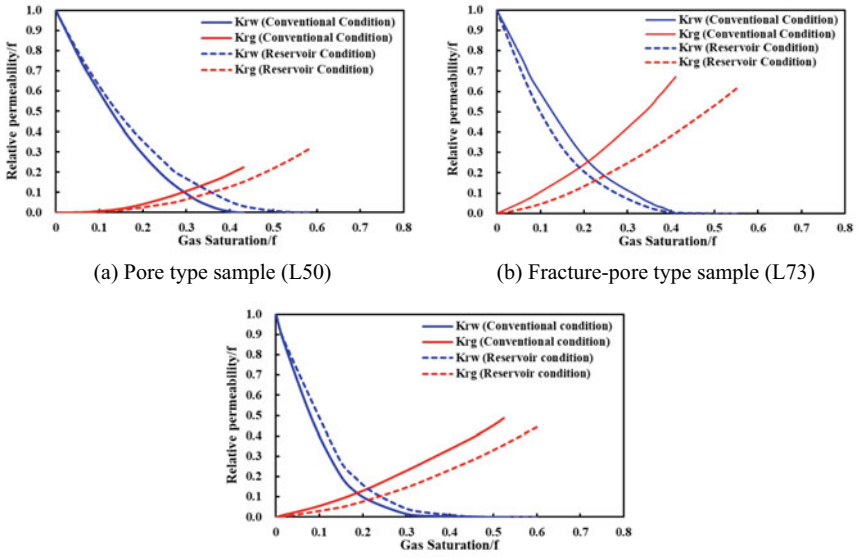

(a) Pore type sample (L50)

(b) Fracture-pore type sample (L73)

(c) Fracture-cavity type sample (L92)

Fig. 2.45 Relative permeability curves of the same core sample under reservoir conditions and conventional conditions

Table 2.29 Two-phase percolation characteristic parameters of different types of samples under different conditions

Reservoir type	Experimental condition	S_{wi}/%	K_{rg} under S_{wi}/f	S_e/%	K_e under S_e/f	Two-phase percolation region/%
L50 Pore type K = 0.054 mD Φ = 4.86%	Conventional condition	56.91	0.224	29.85	0.10	43.09
	Reservoir condition	41.89	0.360	35.92	0.10	58.11
L73 Fracture-pore type K = 3.029 mD Φ = 2.40%	Conventional condition	59.04	0.682	20.83	0.26	40.96
	Reservoir condition	45.03	0.613	22.41	0.16	54.97
L92 Fracture-cavity type K = 2.629 mD Φ = 7.38%	Conventional condition	47.66	0.485	18.78	0.12	52.34
	Reservoir condition	40.03	0.442	24.07	0.11	59.97

and pressure conditions. The fluid properties of nitrogen and brine under these two conditions are summarized in Table 2.23. The solubility of gas in water increases with the increase of pressure. High temperature conditions can intensify molecular motion and promote gas dissolution, thereby reducing the interfacial tension between gas and water. Both the viscosity ratio and density ratio of water and gas are close to 1 under reservoir conditions, which means that the fluid properties of the water and gas in the reservoir are closer. Low interfacial tension and similar fluid properties can improve the sweep range and displacement efficiency of gas phase, and reduce the water trapped in pores and adhered to rock surfaces. Therefore, the S_{wi} measured under reservoir conditions is lower than that obtained under conventional conditions. The mechanism of this process is similar to that of gas flooding reservoirs. Although the effects of ultra-high temperature and pressure conditions on gas-phase percolation capacity are opposite, the negative effect of stress sensitivity under high pressure is still widespread, especially in the reservoir developed with fractures.

2.4.8 Characteristics of Gas–Water Two-Phase Percolation in Full-Diameter Cores

The gas–water two-phase relative permeability curve measured by physical simulation experiment with full-diameter core is more representative than that measured with plunger core, because the number and size of the cavities and fractures in the plunger core have strong randomness and uncertainty. However, physical simulation experiments using full-diameter cores cannot be carried out in large quantities

because they are more difficult and time-consuming. The long experiment period means that the success rate of experiments under ultra-high temperature and pressure is further reduced. The relative permeability curves of six full-diameter cores tested under two experimental conditionsQuery are illustrated in Fig. 2.46. The two-phase percolation characteristic parameters of different types of full-diameter samples under conventional conditions and reservoir conditions are summarized in Table 2.30.

The following conclusions could be drawn by comparing the relative permeability curves and two-phase percolation characteristic parameters of full-diameter cores under two experimental conditions. ① Both the S_{wi} and K_{rg} measured under

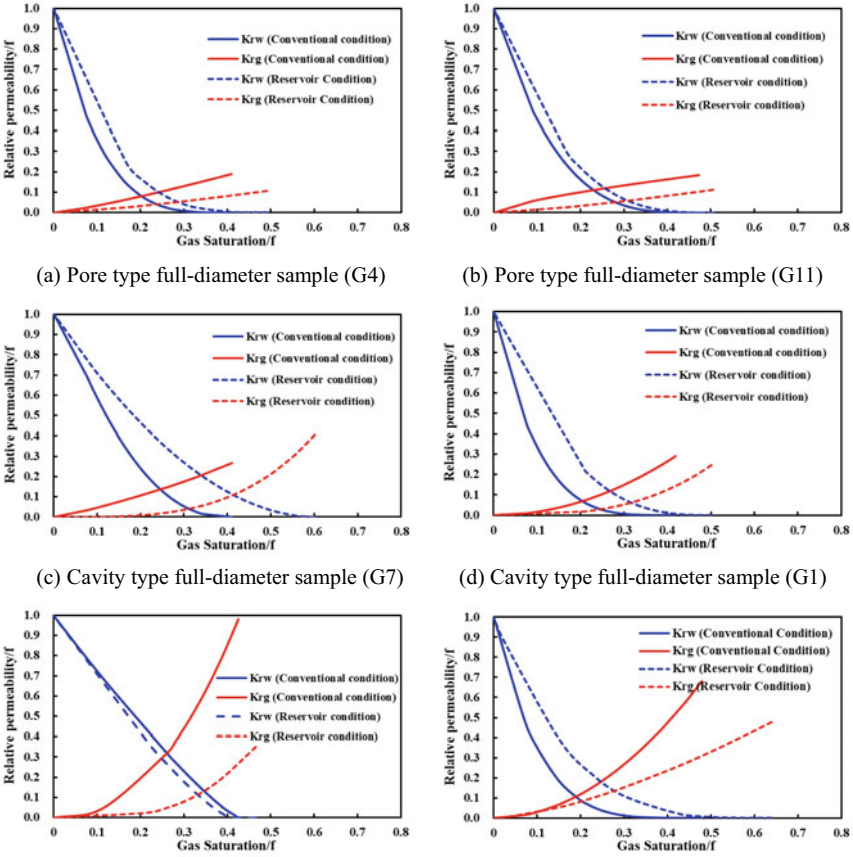

(a) Pore type full-diameter sample (G4)

(b) Pore type full-diameter sample (G11)

(c) Cavity type full-diameter sample (G7)

(d) Cavity type full-diameter sample (G1)

(e) Fracture-pore type full-diameter sample (G6)

(f) Fracture-cavity type full-diameter sample (G9)

Fig. 2.46 Relative permeability curves of the same full-diameter core sample under reservoir conditions and conventional conditions

Table 2.30 Two-phase percolation characteristic parameters of different types of full-diameter samples under conventional conditions and reservoir conditions

Core introduction	Experimental condition	S_{wi}/%	K_{rg} under S_{wi}/f	S_e/%	K_e under S_e/f	Two-phase percolation region/%
G4 Pore type K = 0.005 mD Φ = 2.24%	Conventional condition	59.05	0.190	20.09	0.08	40.95
	Reservoir condition	50.87	0.107	28.68	0.06	49.13
G11 Pore type K = 0.013 mD Φ = 4.52%	Conventional condition	52.70	0.184	23.04	0.12	47.30
	Reservoir condition	49.42	0.113	31.05	0.06	50.58
G7 Cavity type K = 0.261 mD Φ = 6.21%	Conventional condition	59.97	0.461	20.46	0.20	40.03
	Reservoir condition	39.89	0.405	41.71	0.11	60.11
G1 Cavity type K = 0.042 mD Φ = 7.33%	Conventional condition	58.11	0.290	20.62	0.07	41.89
	Reservoir condition	49.82	0.245	31.96	0.06	50.18
G6 Fracture-pore type K = 0.301 mD Φ = 1.83%	Conventional condition	57.38	0.981	26.19	0.32	42.62
	Reservoir condition	53.40	0.351	33.23	0.12	46.60
G9 Fracture-cavity type K = 0.865 mD Φ = 6.51%	Conventional condition	52.11	0.681	18.97	0.11	47.89
	Reservoir condition	35.96	0.478	27.93	0.14	64.04

conventional conditions are relatively high, reflecting that the gas-phase percolation capacity decreases but the displacement efficiency increases under reservoir conditions. ② The S_e under conventional conditions is relatively low, indicating that the hydrophilicity under reservoir conditions is weakened. The percolation capacity of water phase is stronger than that of gas phase in a relatively wide range of S_g under reservoir conditions. ③ The relative permeability curves of fracture-pore type samples obtained under the two conditions differ the most, followed by fracture-cavity type samples. Moreover, this difference is further amplified in full-diameter cores, indicating that the effect of ultra-high temperature and pressure conditions on the two-phase percolation characteristics of carbonate reservoirs with fractures is greater than that obtained through plunger cores. In contrast, full-diameter cores will not magnify this difference in pore type samples because of the strong homogeneity of such reservoirs.

The following conclusions could be drawn by comparing the relative permeability curves and two-phase percolation characteristic parameters of different types of full-diameter cores under reservoir conditions. ① Fracture-cavity type reservoirs have the lowest S_{wi} and S_e, as well as highest K_{rg}. The two-phase percolation characteristics of high-permeability cavity type reservoirs (e.g. G7) are similar to those of fracture-cavity type reservoirs. Therefore, these reservoirs have a relatively long gas–water co-production period and a relatively slow water cut growth under the influence of external water encroachment. Besides, these reservoirs are rich in natural gas due to generally low initial water content. ② Pore type reservoirs have relatively high S_{wi} and K_{rg}. The two-phase percolation characteristics of low-permeability cavity type reservoirs (e.g. G1) are similar to those of pore type reservoirs. Therefore, the initial water content of these reservoirs is generally high, and the gas-phase percolation capacity is greatly affected by water. These conclusions are consistent with those obtained from the study of gas-phase percolation mechanism under different initial water saturation. ③ The S_{wi} and K_{rg} of fracture-pore type reservoirs are similar to those of pore type and fracture-cavity type reservoirs, respectively. This is because the injected gas mainly flows in high-permeability fractures, and displaces the water in the fracture system and surrounding pores. It is difficult for gas to enter the region far from the fracture system to displace water because of excessive permeability differences. When the effective stress of fracture-pore type reservoirs further increases, the fractures will gradually narrow or even close. In this case, the two-phase percolation characteristics of fracture-pore type reservoirs are basically the same as those of pore type reservoirs.

The following conclusions could be drawn by comparing the relative permeability curve and two-phase percolation characteristic parameters of plunger and full-diameter cores. ① The two-phase percolation laws are basically the same, but there are differences in numerical values. ② The stronger the reservoir heterogeneity, the more obvious the difference between the experimental results of two sizes of cores. ③ The differences caused by heterogeneity and measurement error can be reduced by normalizing and averaging the relative permeability curves of multiple plunger cores of the same type. Therefore, full-diameter cores or multiple plunger cores should be used when studying two-phase percolation characteristics through physical simulation experiments.

2.5 Summary

In this chapter, a multi-functional ultra-high temperature and pressure physical simulation experiment system was developed based on the difficulties and requirements of physical simulation experiments of ultradeep carbonate gas reservoirs. Subsequently, an efficient physical simulation experiment technique and analysis method of ultra-high temperature and pressure were formed to study the complex percolation mechanism of gas single-phase in ultradeep carbonate gas reservoirs. Then, a trinomial percolation mathematical model that considers the threshold pressure effect,

stress sensitivity effect and non-Darcy flow effect of different types of carbonate reservoirs was developed based on the physical simulation experimental results. Finally, the plunger and full-diameter carbonate cores of different reservoir types were selected to conduct physical simulation experiments of gas–water two-phase percolation under reservoir conditions and conventional conditions, respectively. The effects of pore structure characteristics, temperature and pressure conditions on gas–water two-phase percolation mechanism were analyzed. The important conclusions obtained are summarized as follows.

(1) The gas-phase percolation characteristics and percolation capacity of fracture-cavity type, cavity type, pore type and matrix type reservoirs were revealed by conducting the physical simulation experiment of gas-phase percolation under reservoir conditions. There is no threshold pressure gradient stage and low-velocity non-Darcy flow stage in the fracture-cavity type reservoir under irreducible water conditions. However, the surge of inertial resistance and the closure of fracture system under high pressure differentials make the gas phase in the fracture-cavity type reservoir enter the high-velocity non-Darcy flow stage. The daily gas production of fracture-cavity type reservoirs can reach 10–100 $\times$ 10^4 m^3/d. Therefore, the fracture-cavity type reservoir is the dominant gas supply reservoir under low production pressure differentials in the initial stage of ultradeep carbonate gas reservoir development. There is a low-velocity non-Darcy flow stage but no threshold pressure gradient in the cavity type reservoir under irreducible water conditions. However, the stress sensitivity and secondary movable water under high pressure differentials make the gas phase in cavity type reservoirs deviated from the Darcy flow stage. The percolation characteristics and percolation capacity of pore type reservoirs with relatively high permeability are similar to those of cavity type reservoirs. The daily gas production of cavity type and pore type reservoirs can reach 0.1–10 $\times$ 10^4 m^3/d. Therefore, the cavity type reservoir could be used as the dominant gas supply reservoir, while the pore type reservoir could replenish the high-permeability reservoir in the middle and late development of ultradeep carbonate gas reservoirs. There are threshold pressure gradient stage and low-velocity non-Darcy flow stage in the matrix type reservoir under irreducible water conditions. The daily gas production of matrix type reservoirs is less than 0.1 $\times$ 10^4 m^3/d. Therefore, the matrix type reservoir have no development value under the current economic and technical conditions.

(2) The gas-phase percolation characteristics and percolation capacity of different types of reservoirs under non-water conditions, irreducible water conditions and movable water conditions were compared and analyzed. The inhibitory effect of reservoir water on the gas-phase percolation capacity of pore type and cavity type reservoirs is significantly stronger than that of fracture-cavity type reservoirs. The threshold pressure effect and non-Darcy flow effect of cavity type and pore type reservoirs also gradually enhances with the increase of water saturation. Furthermore, the complex and special gas-phase percolation characteristics of ultradeep carbonate gas reservoirs are caused by many factors,

namely viscous force, inertial force, stress sensitivity, secondary movable water, percolation channel size and pore throat connectivity, and these factors have different effects on different types of reservoirs under different water conditions and displacement pressure differentials.

(3) The influence laws of threshold pressure effect, stress sensitivity effect, nonlinear percolation effect and well deviation angle on the productivity of different types of ultradeep carbonate gas reservoirs were studied respectively based on the newly established trinomial percolation mathematical model. The threshold pressure effect significantly inhibits the gas production capacity of pore type and low-permeability cavity type reservoirs when the threshold pressure gradient reaches 10–48 kPa/m. The non-Darcy flow effect obviously inhibits the gas production capacities of fracture-cavity type and high-permeability cavity type reservoirs when the nonlinear percolation coefficient reaches 1×10^9–1×10^{12} m^{-1}. The effect of stress sensitivity on the gas production capacity of ultradeep carbonate gas reservoirs is lower than expected because the loss of gas production capacity under extreme conditions is less than 30%. The gas productivity is significantly improved when the well deviation angle is greater than 50°, and the highly deviated well has the best improvement effect on the gas production capacity of fracture-cavity type reservoirs.

(4) The sensitivity of gas production capacity of three types of reservoirs to different influencing factors was obtained through orthogonal analysis experiments. Skin factor and formation coefficient are the key factors that affect the gas productivity of ultradeep carbonate gas reservoirs. In addition to the parameters related to reservoir properties, the effects of non-Darcy flow on high-permeability reservoirs and the effect of threshold pressure gradient on low-permeability reservoirs should be seriously considered. The stress sensitivity has relatively weak influence on the gas production capacity of ultradeep carbonate gas reservoirs. It is necessary to determine a reasonable production pressure differential and formulate an efficient development scheme according to the dominant factors affecting the gas production capacity of different types of reservoirs

(5) The fracture-cavity type reservoir has the lowest S_{wi} and S_e, as well as highest K_{rg}. These characteristics indicate that fracture-cavity type reservoirs have a relatively long gas–water co-production period, a relatively slow water cut growth and a relatively high displacement efficiency under the influence of external water encroachment. The pore type reservoir has high S_{wi} and low K_{rg}. These characteristics indicate that the initial water content of these reservoirs is generally high, and the gas-phase percolation capacity is greatly affected by water. The two-phase percolation characteristics of the pore type reservoir are similar to those of the homogeneous tight sandstone reservoir. The fracture-pore type reservoir has high K_{rg} and S_{wi}. These characteristics indicate that the gas production capacity of this type reservoirs is high before water breakthrough, but the gas mainly comes from fracture system and surrounding pores. The water cut of the gas well rises rapidly after water breakthrough. Ultimately, the gas in a large number of pores is trapped by the water in the fracture system,

resulting in the lowest effective development degree of fracture-pore type reservoirs under the influence of external water. The two-phase percolation characteristics of high-permeability and low-permeability cavity type reservoirs are similar to those of fracture-cavity type and pore type reservoirs, respectively. Therefore, the relative permeability curve suitable for the target reservoir should be selected when conducting gas reservoir engineering calculation and numerical simulation research.

(6) The fractures and cavities developed in ultradeep carbonate gas reservoirs make the gas–water two-phase percolation characteristics complex and diverse. The fracture system can simultaneously increase the K_{rg} and S_{wi}. This is because the injected gas mainly flows in high-permeability fractures and displaces water in the fracture system and surrounding pores. The water in the pores not connected by fractures is difficult to be displaced, resulting in relatively high S_{wi} of fractured reservoirs. However, fractures in the fracture-cavity type reservoir effectively connect isolated storage spaces, especially isolated cavities with excellent storage capacity. Therefore, not only most of the water in cavities, but also some of the water in pores could be displaced. In addition, the cavity can weaken the intensify of water encroachment. The reasonable combination of fractures and cavities makes the displacement effect of the fracture-cavity type reservoir the best.

(7) The ultra-high temperature and pressure in ultradeep carbonate gas reservoirs makes the gas–water two-phase percolation characteristics under reservoir conditions significantly different from those under conventional conditions. The relative permeability curve under reservoir conditions has a relatively large two-phase percolation region and a relatively low S_{wi}, reflecting that the displacement efficiency of water by gas is improved under reservoir conditions. The relative permeability curve of gas phase is relatively low under reservoir conditions, indicating that the gas-phase percolation capacity is inhibited under high temperature and pressure conditions. The percolation capacity of water phase is relatively improved under reservoir conditions, reflecting that the water encroachment degree in ultradeep carbonate gas reservoirs is enhanced. The main reason for these differences is that the pore structure and fluid properties under reservoir conditions are completely different from those under conventional conditions. Therefore, it is necessary to select the relative permeability curve under reservoir conditions for application and analysis.

References

Besson, J. (1990). Performance of slanted and horizontal wells on an anisotropic medium. *SPE, 20965*, 219–231.

Chen, D., Shi, J. Q., Durucan, S., & Korre, A. (2014). Gas and water relative permeability in different coals: Model match and new insights. *International Journal of Coal Geology, 122*, 37–49.

Cinco, H., & Miller, F. G. (1975). Unsteady-state pressure distribution created by a directionally drilled well. *Journal of Petroleum Technology, 27*(11), 1392–1400.

Fang, J. L., Guo, P., Xiao, X. J., Du, J. F., Dong, C., et al. (2015). Gas-water relative permeability measurement of high temperature and high pressure tight gas reservoirs. *Petroleum Exploration and Development, 42*(1), 92–96.

Forchheimer, P. H. (1901). Wasserbewegung durch boden. *Zeitschrift Des Vereines Deutscher Ingenieure, 49*, 1781–1793.

Gao, S. S., Liu, H. X., Ren, D., Hu, Z. M., & Ye, L. Y. (2015). Deliverability equation of fracture-cave carbonate reservoirs and its influential factor. *Natural Gas Industry, 35*(9), 48–54.

Guo, X., Du, Z. M., Jiang, Y. W., Sun, L. J., Liu, X. H., et al. (2014). Can gas-water relative permeability measured under experiment conditions be reliable for the development guidance of a real HPHT reservoir? *Natural Gas Industry, 34*(6), 60–64.

Ji, W. (2018). Gas water relative flow of tight sandstone gas reservoirs and its influencing factors. *Journal of Jilin University: Earth Science Edition, 49*(6), 1540–1551.

Johnson, E. F., Bossler, D. P., & Bossler, V. (1959). Calculation of relative permeability from displacement experiments. *Transactions of the AIME, 216*(1), 370–372.

Li, C., Zhou, X., You, S., & Ibragimov, J. J. (2017a). Analysis of two-phase gas-water flow in carbonate reservoirs. *Journal of Mining Science, 53*, 643–654.

Li, C. H., Li, X. Z., Gao, S. S., Liu, H. X., You, S. Q., et al. (2017b). Experiment on gas-water two-phase seepage and inflow performance curves of gas wells in carbonate reservoirs: A case study of Longwangmiao Formation and Dengying Formation in Gaoshiti-Moxi block, Sichuan Basin. *SW China. Petroleum Exploration and Development, 44*(6), 983–992.

Liu, H. S., Ren, D., Hu, Z. M., & An, W. G. (2014). Establishment and application of seepage mathematical model of Longwangmiao Fm gas reservoirs in the Sichuan Basin. *Natural Gas Industry, 34*(3), 110–114.

Meng, F. K., Lei, Q., Yan, H. J., He, D. B., & Deng, H. (2017). Productivity assessment for inclined wells in Gaoshiti-Moxi carbonate gas reservoirs. *Special Oil and Gas Reservoirs, 24*(5), 111–115.

Sidiq, H., Amin, R., & Kennaird, T. (2017). The study of relative permeability and residual gas saturation at high pressures and high temperatures. *Advances in Geo-Energy Research, 1*(1), 64–68.

Sola, B. S., Rashidi, F., & Babadagli, T. (2007). Temperature effects on the heavy oil/water relative permeabilities of carbonate rocks. *Journal of Petroleum Science and Engineering, 59*, 27–42.

Sun, X. X., Yao, Y. B., Ripepi, N., & Liu, D. M. (2018a). A novel method for gas-water relative permeability measurement of coal using NMR relaxation.*Transport in Porous Media, 124*(1), 1–18.

Sun, Z., Shi, J., Zhang, T., et al. (2018b). A fully-coupled semi-analytical model for effective gas/water phase permeability during coal-bed methane production. *Fuel, 2018*(223), 44–52.

Volkov, R. S., Kuznetsov, G. V., & Strizhak, P. A. (2014). The influence of initial sizes and velocities of water droplets on transfer characteristics at high-temperature gas flow. *International Journal of Heat and Mass Transfer, 79*, 838–845.

Wan, T., Yang, S. L., Wang, L., & Sun, L. T. (2019). Experimental investigation of two-phase relative permeability of gas and water for tight gas carbonate under different test conditions. *Oil & Gas Science and Technology—Revue d'IFP Energies Nouvelles, 74*, 23.

Wang, L., He, Y. M., Peng, X., Deng, H., Liu, Y. C., et al. (2020). Pore structure characteristics of an ultradeep carbonate gas reservoir and their effects on gas storage and percolation capacities in the Deng IV member, Gaoshiti-Moxi area, Sichuan Basin, SW China. *Marine and Petroleum Geology, 111*, 44–65.

Wang, L., Yang, S. L., Liu, Y. C., Xu, W., Deng, H., et al. (2017a). Experimental investigation on gas supply capability of commingled production in a fracture-cavity carbonate gas reservoir. *Petroleum Exploration and Development, 44*(5), 824–833.

Wang, L., Yang, S. L., Xu, W., Meng, Z., Han, W., et al. (2017b). Application of improved productivity simulation method in determination of the lower limits of reservoir physical properties in Moxi district of An'yue gas field. *Xinjiang Petroleum Geology, 38*(3), 358–362.

Wang, Z. H., Xiao, Y., Guo, P., Du, J. F., & Yang, H. Z. (2017c). Gas-water flowing characteristics under high temperature and high pressure in fractured-cavity carbonate gas reservoir. *Reservoir Evaluation and Development, 7*(2), 47–52.

Zhang, T., Li, X. F., Li, J., Feng, D., Wu, K. L., et al. (2018a). A fractal model for gas-water relative permeability in inorganic shale with nanoscale pores. *Transport in Porous Media, 122*(2), 305–331.

Zhang, T., Li, X. F., Wang, X. Z., Hu, K. Y., Sun, F. R., et al. (2018b). Gas-water relative permeability model for tight sandstone gas reservoirs. *Scientia Sinica: Technologica, 48*(10), 1132–1140.

Chapter 3
Complex Gas–Water Relationship of the Ultradeep Carbonate Gas Reservoir

Most of the ultradeep carbonate gas reservoirs in the Sichuan Basin are connected with edge and bottom water bodies, and the reserves of gas reservoirs with water account for 80% of the total reserves (Zou et al., 2014). The Cambrian Longwangmiao Formation gas reservoir with severe water encroachment is a typical representative (Li et al., 2017). The water encroachment characteristics of gas reservoirs are not only affected by external water bodies, but also closely related to their own initial water content conditions. Therefore, revealing the gas–water relationship in the reservoir under initial conditions and during exploitation is crucial for clarifying the water encroachment characteristics. The complex gas–water relationship in ultradeep carbonate gas reservoirs is mainly caused by the multiple types of reservoir media and strong heterogeneity (Han et al., 2022). Insufficient understanding of the gas–water relationship not only affects the predictions of gas percolation characteristics and gas well production performance, but also restricts the long-term and efficient development of this type of gas reservoir.

At present, the research on gas–water relationship mostly focuses on exploitation technique, numerical simulation, prediction model establishment and physical simulation experiment. However, the gas reservoir numerical model and gas–water two-phase percolation mathematical model can neither truly reflect the pore structure characteristics of the reservoir, nor can they accurately describe the real two-phase percolation law in porous media, especially for strongly heterogeneous reservoirs (Liu et al., 2015). The reliability of the gas–water two-phase percolation physical simulation experiment is relatively strong because the core and fluid in the study area are used as samples. However, core experiments can only describe the gas–water relationship by collecting and analyzing pressure, flow rate and time data during the water encroachment simulation process, but cannot intuitively study the gas–water occurrence state and two-phase percolation process in complex porous media (Fang et al., 2016). Currently, there are few investigations on the complex gas–water relationship in ultradeep carbonate gas reservoirs in the world.

© The Author(s), under exclusive license to Springer Nature Singapore Pte Ltd. 2023

L. Wang, *Ultradeep Carbonate Gas Reservoirs*,
https://doi.org/10.1007/978-981-19-9708-2_3

Therefore, microscopic visualization technique was introduced in this chapter to study the complex gas–water relationship in the processes of hydrocarbon accumulation and water encroachment. The microscopic visualization experiment is a special technique to intuitively study fluid flow and enhanced hydrocarbon recovery from the microscopic level. However, there is no report on the gas–water relationship in carbonate gas reservoirs because of the limitations of microscopic visual models and visualization experiments. The existing microscopic visual models is difficult to simulate the complex pore structure of the actual reservoir and bear a certain effective stress, and the visualization experiment cannot simulate the gas–water flow process under the micro flow control and conduct real-time quantitative monitoring. Therefore, a novel microscopic visualization technique of multiphase fluid percolation was developed based on CT scanning and microelectronic lithography to overcome the existing technical difficulties. Three microscopic visual models representing the pore structure of three types of ultradeep carbonate gas reservoirs were fabricated. The visualization experiments of gas flooding water and water flooding gas were conducted to simulate hydrocarbon accumulation and water encroachment processes, respectively. The gas–water two-phase percolation law, water encroachment characteristics, initial occurrence state of formation water, formation mechanism of trapped gas and residual water, etc. were intuitively studied by electron microsope during visualization experiments. Then, the fluid distribution characteristics, irreducible water and trapped gas saturations, water breakthrough times and gas recovery factors were quantitatively studied by ImageJ gray analysis method. Furthermore, the influence of the occurrence state of formation water on the gas percolation capacity and the recovery mechanism of trapped gas were also revealed. Finally, development strategies for different types of carbonate reservoirs with water were proposed according to the complex gas–water relationship in different types of visual models.

3.1 Microscopic Visualization Technique of Fluid Percolation Based on CT Scanning and Microelectronic Lithography

Various types of microscopic visual models have been fabricated and widely applied for micro-scale investigations of multiphase flow characteristics and fluids distribution in porous media, because they can structurally simulate the microscopic pore structures of fossil fuel reservoirs. The prominent advantage of visualization experiments is that they allow the direct observation of the processes, phenomena and mechanisms that occur in porous media, which is difficult to achieve in other physical simulation experiments (Mosavat & Torabi, 2016).

Microscopic visual model with regular network channels were pioneered by Mattax and Ktye (1961). They observed the oil–water interface in porous media and analyzed the effect of wettability on oil production performance during water injection. Davis and Jones (1968) improved the accuracy and efficiency of pattern

etching through photoresist and acid etching techniques. Bonnet and Lenormand (1977) introduced photolithography to improve the fabrication process of microscopic visual models. They developed a large visual model with channel size and pore structure similar to those of an actual oil reservoir. Subsequently, an increasing number of scholars have adopted a variety of methods and techniques to fabricate microscopic visual models with different features and applications (Mahers et al., 1981; Wan et al., 1996). Recently, Buchgraber et al. (2012) developed an etched-silicon visual model based on the dual-porosity structure characteristics of carbonate oil reservoirs using the microelectronic lithography technique (Fig. 3.1). They intuitively study the percolation mechanism at the pore level and the fluid exchange process between pores and fractures through visualization experiments. Mohammadi et al. (2013a, 2013b) fabricated an ideal visual model considering fracture heterogeneity by laser technique and then studied the enhanced oil recovery mechanism of carbonated water injection in heterogeneous reservoirs accordingly (Fig. 3.2). Mosavat and Torabi (2016) designed a random and irregular pore pattern through CAD software (Fig. 3.3) and then imported the pattern into a laser machine to create a visual model for the investigation of carbonated water injection. Wang et al. (2016) filled regular glass beads between two glass plates to create a visual model and studied the mechanisms and effects of various enhanced oil recovery methods accordingly. Spaces created by contact between glass beads can simulate porous media in reservoirs. However, the pore patterns of these visual models are all regular structures or randomly generated irregular structures, which cannot represent the pore structure of actual reservoirs. Therefore, the observed phenomena and summarized conclusions from these visual models are insufficient and limited (Fig. 3.4).

At present, the microscopic visual model, as a multifunctional simulation physical model, has been widely used in various fields of petroleum engineering. The microscopic visualization experiment has been proven to be a technique that can intuitively study oil and gas percolation and enhanced oil recovery from a mechanism level,

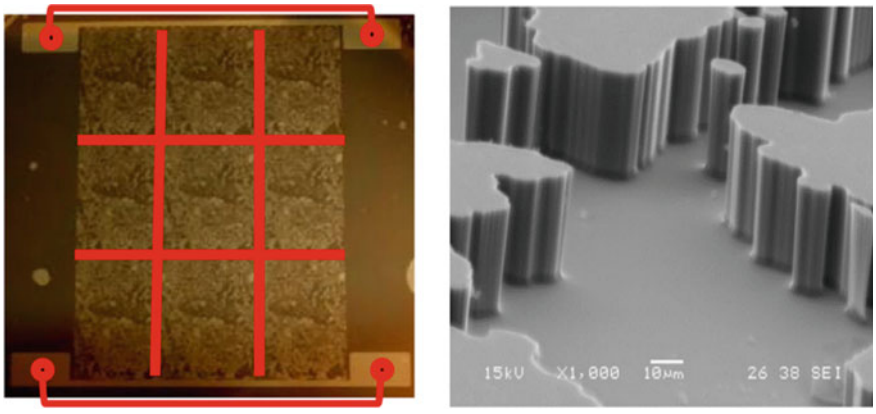

Fig. 3.1 Silicon visual model and its microscopic pore structure (Buchgraber et al., 2012)

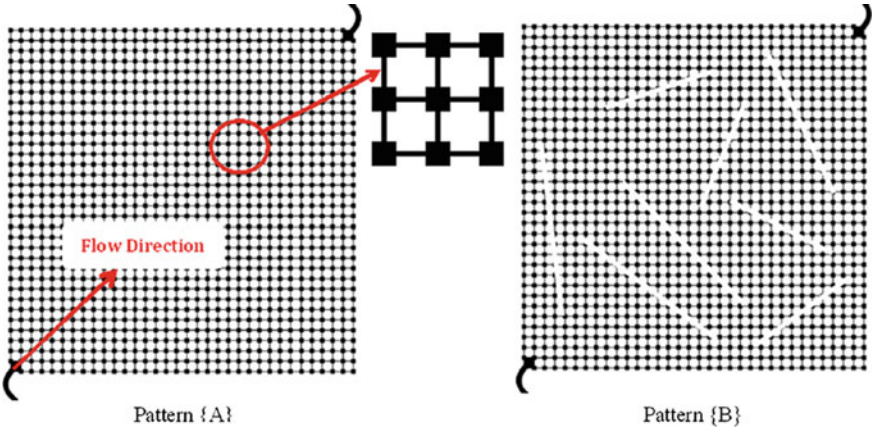

Fig. 3.2 Ideal visual model considering fracture heterogeneity (Mohammadi et al., 2013a)

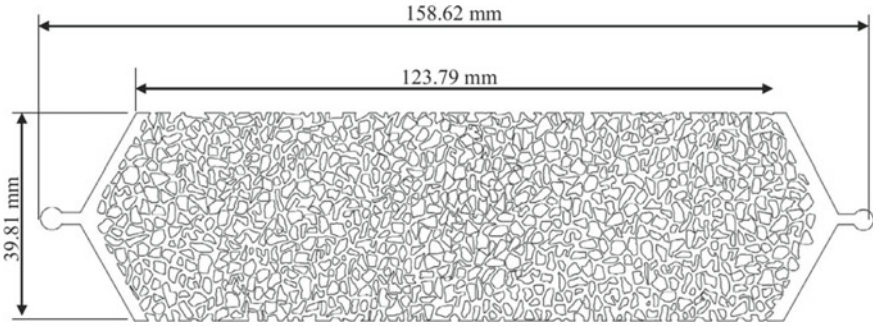

Fig. 3.3 Irregular porous media pattern designed by CAD software (Mosavat & Torabi, 2016)

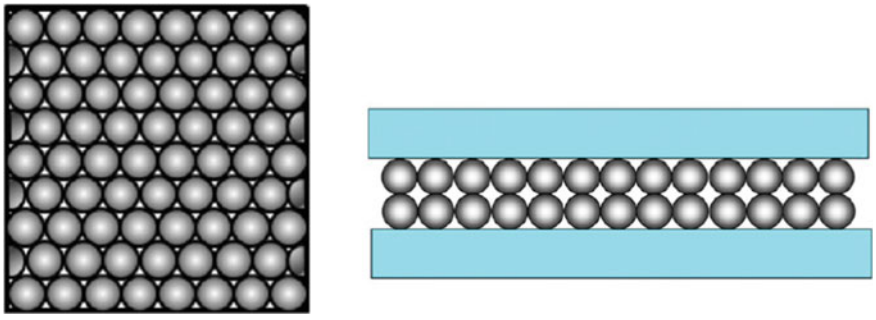

Fig. 3.4 A visual model fabricated by filling glass beads between two glass plates (Wang et al., 2016)

including water injection (Wang et al., 2006), gel injection (Bai et al., 2007), steam injection (Wu et al., 2019), foam injection (Wu et al., 2016), carbonated water injection (Mosavat & Torabi, 2016; Sohrabi et al., 2012), solution gas drive (George et al., 2005), miscible flooding (Mohammadi et al., 2013a and 2013b) and spontaneous imbibition (Hatiboglu & Babadagli, 2010). The visual investigations of these reservoir development methods could not only observe the flow characteristics of various injected materials in porous media and reveal the enhanced recovery mechanism, but also provide theoretical basis for parameter optimization. In addition, microscopic visual models could also be used to intuitively study the interactions between multiple fluids and between rock and fluids in porous media, including wettability conversion (Romero-Zeron & Kantzas, 2007), polymer retention (Yun & Kovscek, 2015), capillary force (Smith et al., 2005), asphaltene precipitation (Doryani et al., 2016), and interfacial tension (Mosavat & Torabi, 2016). The percolation characteristics and action mechanisms obtained by microscopic visualization experiments are more convincing than those obtained by conventional physical simulation experiments.

However, most of the previous microscopic visual investigations have focused on oil reservoir, and few studies have used visual models to simulate hydrocarbon accumulation and water encroachment processes in gas reservoirs, especially fracture-cavity type carbonate gas reservoirs. This is because the implementation of microscopic visual investigations of gas–water relationship in gas reservoirs has encountered some difficulties: (1) the microscopic visual model used to study the relationship between gas and water needs to be further improved in sealability to prevent gas leakage; (2) the strong compressibility of gas requires the visual model to have a high allowable stress; (3) the high mobility of natural gas and the low pore volume of the visual model make the duration of visualization experiments too short for fluid quantification with conventional measurement methods; (4) the reservoir heterogeneity and medium diversity of ultradeep carbonate gas reservoirs require the visual model to have a pore structure similar to the actual reservoir; and (5) only static images of fluid distribution after the visualization experiment can be presented, and dynamic images of fluid flow process and distribution at different times cannot be given.

Therefore, a novel microscopic visualization technique of multiphase fluid percolation was developed based on CT scanning and microelectronic lithography to address the above difficulties. First, visual model patterns were designed based on CT scan images of three types of reservoirs to simulate the pore structure of actual carbonate gas reservoirs. Subsequently, visual models representing the three types of reservoirs were fabricated by float glass and microelectronic lithography, and the sealability and stress resistance of these visual models were enhanced by improving the sintering method. Then, a high-resolution microscope camera and a digital video recorder were used to precisely captures local microscopic images and record the overall percolation process, respectively. Finally, the ImageJ gray analysis method was introduced to quantitatively characterize the images captured at different moments in the video, including fluid saturation and gas recovery factor. The microscopic visualization technique introduced in this chapter can serve as a reference in other aspects of visual investigations. For example, we also reported a series of

visualization experiments using this technique to simulate the water injection, CO_2 injection and WAG injection processes (Wang et al., 2020).

3.1.1 Mask Design and Creation Based on Typical CT Scan Images

An important function of microscopic visualization technique is that it can be used to simulate and observe the 2D flow process of fluids in complex porous media. The application of microscopic visualization technique in the field of hydrocarbon reservoirs would assist in obtaining an enhanced insight into the percolation law and distribution characteristics of multiphase fluids. This application provides a theoretical basis for the investigation of the complex oil–water or gas–water relationship in the reservoir, as well as the analysis of the formation mechanism of the residual oil and trapped gas. Microscopic visual model is the basis and premise of the application of microscopic visualization technique, and its design and fabrication level directly affect the accuracy and representativeness of visualization experimental results. Therefore, a novelty method for microscopic visual model fabrication based on CT scan images and microelectronic lithography is proposed. The entire fabrication process includes basic image selection, binary image conversion, mask creation, microelectronic lithography, high temperature sintering, and quality inspection (Wang et al., 2018a, 2018b).

Mask creation is one of the most critical steps in the model development process, and the creation level of the mask directly affects the representativeness of the microscopic pore structure in the model. Basic image selection and binary image conversion are required before mask creation. These images can be digitally modified by a computer to adjust microscopic pore structure characteristics and improve pore throat connectivity. Compare with CTS and SEM techniques, CT scanning is the most accurate and comprehensive technique for obtaining 2D and 3D images of reservoir pore structure at this stage. Therefore, representative images were selected from the 2D CT scan images of fracture type, cavity type and fracture-cavity type samples as basic images to accurately describe the microstructural characteristics of various types of reservoirs in ultradeep carbonate gas reservoirs, and restore the distribution of pores, cavities, and fractures in the reservoirs. A total of 6000 CT scan images were obtained. Each CT scan image is 1778 $\times$ 1800 pixels with a pixel size of 13.15 μm. However, it was found that the distribution characteristics of pores, cavities and fractures in most images were not significant during image screening. There is usually only one typical structure in a single image and cannot fully represent the complex pore structure of the actual reservoir. If a microscopic visual model is developed with reference to these CT scan images, it is impossible to accurately simulate the gas–water two-phase percolation process, nor to obtain the comprehensive occurrence characteristics of irreducible water and trapped gas. Therefore, three types of CT scan images with obvious microstructure features and

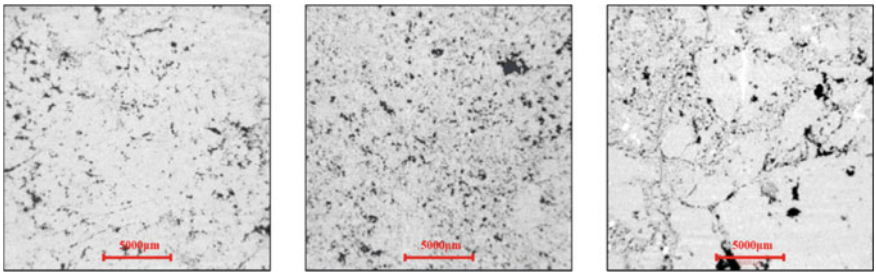

(a) Fracture type (b) Cavity type (c) Fracture-cavity type

Fig. 3.5 Optimized CT scan images for three types of ultradeep carbonate reservoirs

complex distribution patterns of pores, cavities and fractures were selected as the basic images for mask creation. Representative basic images of the three types of carbonate reservoirs are shown in Fig. 3.5. The reason for not making a pore type model is that the cavity type model can simultaneously display the flow characteristics and fluids distribution in pores and cavities. It should also be noted that there are essential differences between the cavity type model and the fracture-cavity type model in terms of structural characteristics and research objects. In terms of structural characteristics, the cavity type model consists of a large number of pore throats and a small number of cavities. The small-scale pores are widely distributed in the model and are the main channels for fluid flow. The fracture-cavity type model is mainly composed of cavities and fractures. Large-scale fractures are discretely distributed in the model and are the dominant channels for fluid flow. In terms of research objects, the cavity type model is mainly used to study the gas–water relationship between pores and cavities, while the fracture-cavity type model focuses on the investigation of the gas–water relationship between fractures and cavities.

These basic images were then imported into a computer, where they were converted into binary images by setting the threshold for the gray value. The black areas in the binary image represent porous media, whereas the white areas represent rock matrix. Binary images were digitized to remove invalid pores and filled minerals, and to reconnect fractures and throats that were isolated in the 2D images based on the 3D CT scan images. After the binary image was modified, the mask frame diagram was designed according to the requirements of the visualization experiment. Figure 3.6 shows that flow channels were added to the inlet and outlet ends on both sides of the model, and multiple ports were added to the flow channel that allow fluid to enter and exit the valid region of the model. This design of the model not only improves the fluid exchange capacity, but also establishes linear flow boundary conditions. Compare with the traditional point boundary condition, the displacement process simulated by the linear boundary condition is more consistent with the actual gas accumulation and water encroachment processes. It should be noted that CNC (Computer Numerical Control) milling machines cannot identify tiny pore throats in high-resolution CT scan images due to their resolution limitations. Therefore, the pixel size of the basic image was appropriately enlarged under the premise that the

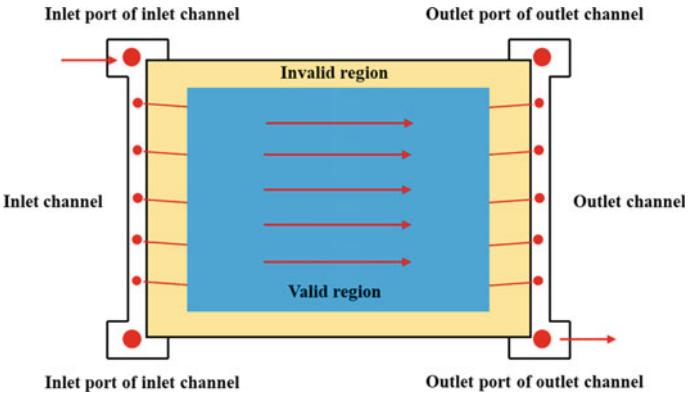

Fig. 3.6 Schematic of the mask frame and typical fluid flow direction

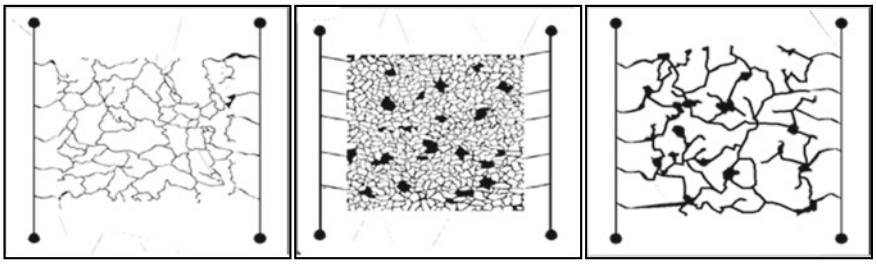

(a) Fracture type (b) Cavity type (c) Fracture-cavity type

Fig. 3.7 Design of three types of masks based on CT scan images

microstructural characteristics and relative pore size distribution remain constant. These high-resolution basic images will be used in the future given the advances in mask writing technique. Finally, the mask design patterns representing the three types of reservoir microstructure were obtained by Corel Draw X8 software (Fig. 3.7).

3.1.2 Visual Model Fabrication Based on Microelectronic Photolithography

These visual models were fabricated at the State Key Laboratory of Petroleum Resources and Exploration in Beijing. The material used for the substrate and cover of the visual model is float glass. This glass material has excellent flatness and transparency, and is not easily broken when its surface is etched. The fabrication process of the visual model mainly includes the steps of pretreatment, etching, cleaning, sintering, and testing, as shown in Fig. 3.8. It should be noted that the fabrication

process of the three types of models is the same, but the mask used in DUV (deep ultra-violet) exposure is different. Details of the fabrication steps are as follows.

(a) The glass substrate was initially cleaned to remove surface contaminants, and then pre-baked at 200 °C for a few minutes to keep the surface dry.
(b) The cleaned and dried substrate was coated by hexamethyldisilane (HMDS) vapor deposition at an ambient temperature of 250 °C for 0.2 min.
(c) Krypton fluoride (KrF) photoresist was evenly spin coated on the substrate. The substrate was then soft-baked at 100 °C for 45 s in a vacuum insulating plate to release the stress in the photoresist and improve the adhesion.

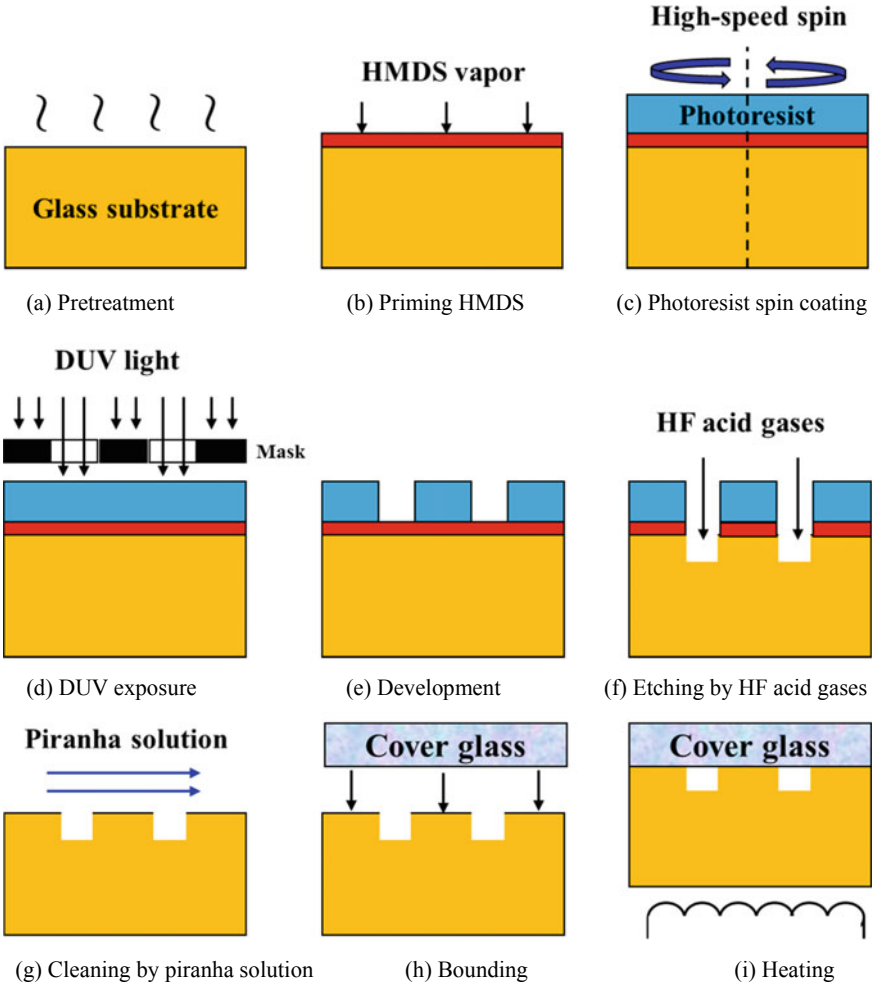

Fig. 3.8 Fabrication process of the microscopic visual model

Table 3.1 Temperature and duration of each heating stage

Temperature/°C	Heating time/min	Retention time/min
300	100	35
500	80	40
600	60	40
700	60	40
750	45	45

(d) The fabricated mask was placed over the substrate, and then the model was fully exposed to the DUV radiator so that the light can pass through the mask and irradiate the substrate coated with photoresist.
(e) The excess photoresist was removed and undergone post-exposure baking at 120 °C for 1 min. Subsequently, the substrate was cooled to 23 °C before being ready for etching.
(f) The regions exposed to DUV light were etched into the desired microstructures with hydrofluoric acid (HF) acid gas. The duration and number of acid etching processes depend on the depth and complexity of the etched microstructures. Besides, ports and channels were etched at the four corners and on both sides of the substrate, respectively.
(g) The substrate was thoroughly cleaned to remove residual photoresist and glass particles after etching was complete. The cleaning solution, called Piranha solution, is made up of 90% sulfuric acid (H_2SO_4) and 10% hydrogen peroxide (H_2O_2).
(h) Another float glass with the same size was placed on the cleaned substrate as a cover plate. Ports were also etched at the four corners of the cover glass.
(i) The model was then placed in a heating furnace for sintering, and the temperature and duration of each heating stage are shown in Table 3.1. The substrate and cover glasses adhered gradually as the furnace temperature gradually increased.

In addition, it is necessary to conduct sealability and pressure resistance tests on the sintered model to meet the requirements of the visualization experiments of gas–water two-phase percolation under a certain pressure. Finally, the three types of microscopic visual models and their size parameters are shown in Fig. 3.9 and Table 3.2. The wettability of the model was also measured. The model is hydrophilic and has a wetting angle of 36.4°–36.7° (Fig. 3.10), which is similar to the wettability of carbonate gas reservoirs (Schneider et al., 2011). The initial wettability of the model was kept identical for different visualization experiments.

3.1.3 Advantages of Microscopic Visual Models

Compared with traditional models, the microscopic visual model developed based on CT scanning and microelectronic lithography has the following improvements. (1)

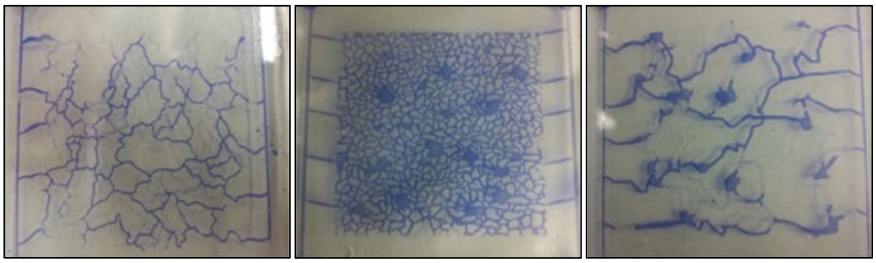

(a) Fracture type (b) Cavity type (c) Fracture-cavity type

Fig. 3.9 Three types of microscopic visual models based on microelectronic photolithography technique

Table 3.2 Dimensional parameters of the microscopic visual model

Model dimension/cm	Valid region dimension/cm	Pore diameter range/μm	Cavity diameter range/μm	Fracture diameter range/μm
6.00 × 6.00	4.50 × 4.50	99–181	1161–1657	325–492

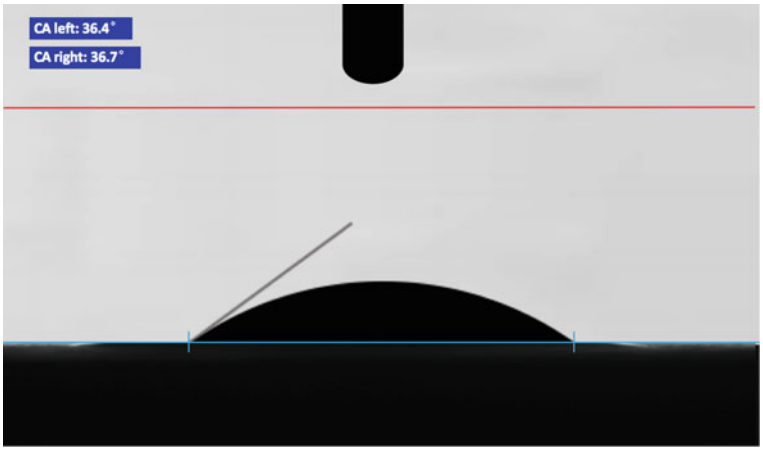

Fig. 3.10 Wettability and wetting angle of the microscopic visual model (water-wetting)

The sealing performance of the model is further enhanced by improving the sintering technique, which can be used to simulate the gas–water two-phase percolation under certain temperature and pressure conditions. This technique solves the defects of poor pressure resistance and gas sealing of most visual models. (2) The microscopic pore structure distribution and characteristics of the new model are similar to those of ultradeep carbonate reservoirs. Therefore, the gas–water relationship and distribution characteristics obtained by the new model can truly reflect the actual situation of the reservoir. (3) Three types of microscopic visual models were developed according to

the characteristics of various types of reservoirs in ultradeep carbonate gas reservoirs. At present, there are no reports on the microscopic visualization investigation of this type of gas reservoir.

3.1.4 Quantitative Methods for Microscopic Visualization Experimental Results

Quantitative characterization of visualization experimental results is another difficulty in microscopic visualization technique of multiphase fluid percolation. This is because of the high mobility of the gas and the small pore volume of the model, resulting in a short experimental duration and a small amount of fluid. It is impossible to quantitatively measure fluids by conventional methods, and it is also difficult to achieve accurate calculation of material balance. For example, the total pore volume of the model is about 0.07 mL when the average pore size and porosity of the model are 140 μm and 14%, respectively. However, the volume of a single inlet or outlet port is about 0.1 mL, which occupies a large volume in the microscopic visual model. Therefore, applying the material balance method to measure fluids in microscopic visualization experiments inevitably results in errors.

In view of the poor applicability of traditional measurement methods in microscopic visualization experiments, an image analysis method was introduced to quantitatively characterize images captured at different moments in the video. The image analysis method used in the study was ImageJ gray analysis. Pore volume, saturation, recovery factor, percolation and occurrence patterns could be obtained by this method. The procedures for quantitative characterization are as follows. (1) The image was processed by Photoshop software (CS6, Adobe, USA) to improve the quality and adjust the brightness. (2) The colorless gas in the flow channel was converted to yellow by the software to distinguish the gas from the glass particles in the model (Fig. 3.11a). (3) The image recognition function of ImageJ software (v1.8.0, National Institutes of Health, USA) was used to determine the gray value distribution of the image. Pixels of glass particles were converted to white pixels, and pixels of voids were converted to red pixels after setting the threshold (Fig. 3.11b). (4) The number of red pixels was counted to calculate the area occupied by the voids, and then the porosity was calculated based on the area ratio of the voids to the valid region of the model. (5) Photoshop and ImageJ software were reused to separate the gas from the fluid and convert the pixels of the gas to red pixels (Fig. 3.11c). (6) The number of red pixels was counted to calculate the area occupied by the gas, and then the gas saturation was calculated based on the area ratio of the gas to the voids. Similarly, the water saturation can also be calculated. ImageJ gray analysis is a simple and practical method that does not require extensive computational resources. The water and gas saturation and recovery factor at different times could be obtained through this image analysis method.

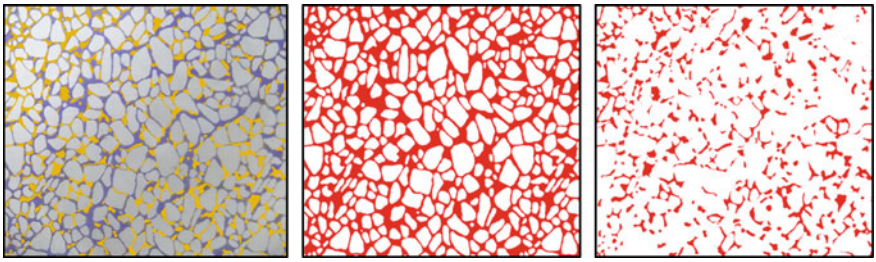

(a) Gas-water distribution image (b) Area occupied by voids (c) Area occupied by gas

Fig. 3.11 Schematic diagram of the method for quantitative characterization of visual images

3.2 Microscopic Visualization of Gas–Water Relationship During Accumulation Process

It is important to clarify the occurrence characteristics and formation mechanism of formation water in gas reservoirs and analyze the influence of initial formation water on gas percolation capacity for revealing the gas–water relationship and predicting production performance. At present, most reports on formation and occurrence of formation water focus on low-permeability tight sandstone gas reservoirs. Displacement experiments, magnetic resonance imaging (MRI) and mercury intrusion porosimetry are commonly used methods to study water occurrence in porous media. Hu et al. (2011) found that formation water in low-permeability gas reservoirs is composed of movable water and residual water, and petrophysical properties and displacement pressure are the main factors affecting the water occurrence state. They believe that the occurrence pattern of formation water in different types of pores has different effects on the gas-phase percolation mechanism. Wang et al. (2012) subdivided the formation water occurrence pattern of tight sandstone gas reservoirs into irreducible water, capillary water and free water. The gas test results show that the reservoir containing irreducible water mainly produces gas, the reservoir containing capillary water co-produces gas and water, and the reservoir containing free water mainly produces water. They believe that the clarification of the occurrence state of water in the reservoir is of great significant for predicting production performance. Zhu et al., (2014, 2016) concluded that the occurrence state of formation water in tight reservoirs is determined by petrophysical properties, pore structure, and accumulation dynamics. Although they all obtained the occurrence characteristics of water in the reservoir, they were all predicted by analyzing the experimental or simulated curves. These conventional physical and numerical simulation methods cannot intuitively and comprehensively study gas–water two-phase percolation characteristics and formation water occurrence patterns during the accumulation process. In addition, no intensive study on formation water in ultradeep carbonate gas reservoirs exists. However, the occurrence state and percolation mechanism of formation water in this type of gas reservoir are extremely complicated because of their unique reservoir structure and strong heterogeneity. Therefore, three types of microscopic visual

models were used to conduct gas flooding water visualization experiments to simulate the hydrocarbon accumulation process of different types of carbonate reservoirs. The formation process and occurrence state of formation water in different types of carbonate reservoirs were observed. The influence mechanism of different types of residual water on gas percolation in multiple media was analyzed. Furthermore, the water saturation under different pressure differentials and water film thickness in pores of different sizes were quantified by the ImageJ gray analysis method.

3.2.1 Similarity Principles for Microscopic Visualization Experiments

The similarity principle is an important prerequisite for using experimental techniques to simulate fluid flow during the accumulation and production of hydrocarbon reservoirs. The following five aspects of similarities were conduct according to the requirements of the similarity principle in microscopic visualization experiment. (1) Similarity in microscopic pore structure: three types of microscopic visual models with representative microstructures were developed based on the CT scan images of typical core samples of ultradeep carbonate reservoirs. (2) Similarity in wettability: the material used to fabricate the microscopic visual model is float glass with the same wettability and similar contact angle as the lithology of the study area. (3) Similarity in fluid flow patterns: the gas flooding water visualization experiment was conducted to simulate the formation process and occurrence state of formation water during the accumulation process according to the hydrocarbon migration and accumulation theory. The water flooding gas visualization experiment was also conducted to simulate the formation process and distribution characteristics of trapped gas during the water encroachment process according to the edge and bottom water encroachment theory in gas reservoirs. (4) Similarity in reservoir conditions: the microscopic visual model was pressurized and heated by a customized model holder and constant temperature oven. However, none of the existing microscopic visual models can withstand high pressure due to the limitations of material and technical. The maximum stress that the new model can withstand is 10 MPa, which exceeds most of the microscopic visual models at the time. Although the pressure of the visualization experiments are lower than the reservoir conditions, the results and conclusions of the relevant studies are still of great significance. (5) Similarity in fluid properties: the water samples used in the visualization experiment were prepared according to the chemical composition of the formation water in the study area, and the gas samples were collected from a gas well in the study area. These similarity principles are applicable to both water flooding gas and gas flooding water microscopic visualization experiments.

3.2.2 Experimental Apparatus

The apparatus of the microscopic visualization experiments are composed of three systems, namely displacement system, data acquisition system and visualization system. The schematic diagram of the experimental apparatus is shown in Fig. 3.12. The displacement system consists of a syringe pump (260D, Teledyne ISCO, USA) that provides constant microflow and micropressure, a back pressure pump, a natural gas tank, a formation water tank, a fluid storage tank that collects produced fluid, a back pressure valve, and several pressure sensors. The data acquisition system is composed of a high-resolution microscope camera (Infinity 3-6UR, HLOT, USA) to precisely captures local microscopic images, thereby enabling further investigation of the two-phase percolation dynamic and residual water occurrence characteristics in porous media; a digital video (DV) recorder to record the overall percolation process of the visual model, thereby enabling further quantitative characterization of fluid saturation and recovery factor at different times; a backlight and a reflector to improve the quality of images and videos; a data and image collector; a computer; and several pressure sensors and temperature sensors. The visualization system mainly includes a visual model holder, a thermostat and three types of visual models. The microscopic visualization experimental system is shown in Fig. 3.13. The customized visual model holder is an important equipment in addition to the visual model (Fig. 3.14). This holder was designed with four injection/production ports corresponding to the four inlet/outlet ports of the visual model, and the visual model can be fastened on the stainless frame and withstand the confining pressure. Meanwhile, O-rings were added around the four ports to improve the sealing performance of the visual model.

3.2.3 Experimental Fluids

The water sample used in the visualization experiment is standard brine prepared according to the chemical composition of formation water in study area, as shown in Table 3.3. The gas sample used in the visualization experiment is the natural gas collected from an actual gas well in the Deng IV Member reservoir, and its composition and properties are shown in Table 3.4. The configured water sample needs to be dyed blue using Methyl blue reagent to clearly identify the location and morphology of water and gas. The concentration of Methyl blue reagent is 0.1 mL per 1.0 L of solution.

3.2.4 Experimental Procedure

The detailed experimental procedure of gas flooding water microscopic visualization is summarized as follows. (1) The visual model and model holder were cleaned with

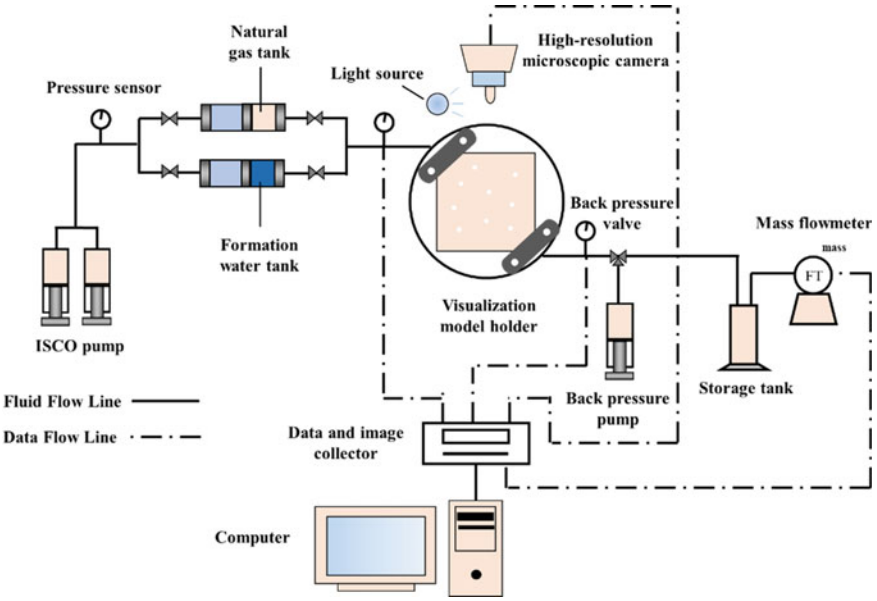

Fig. 3.12 Schematic diagram of the microscopic visualization experimental system

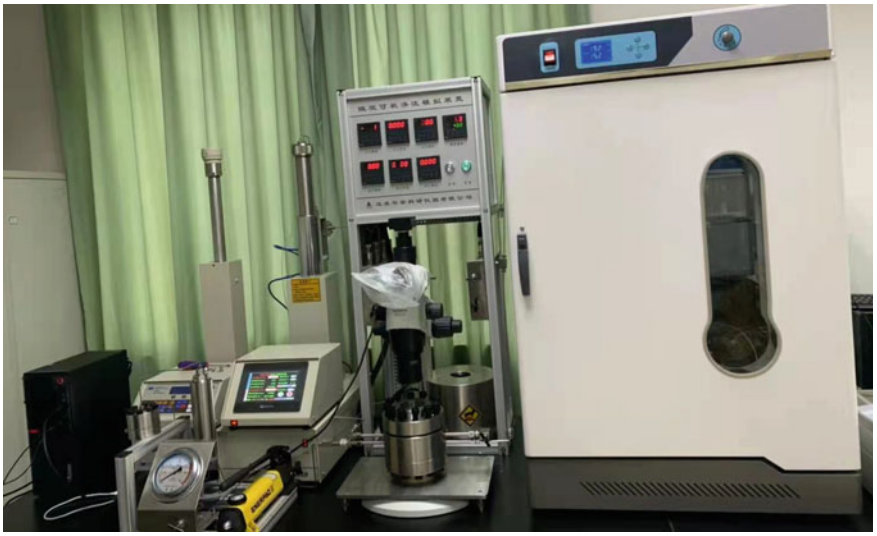

Fig. 3.13 Microscopic visualization experimental apparatus

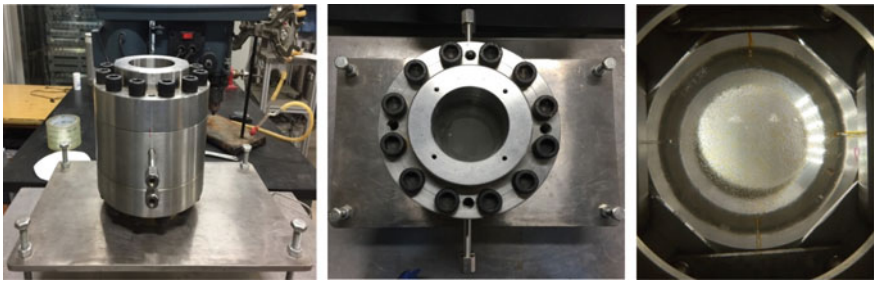

(a) Overall structure (b) Top structure (c) Internal structure

Fig. 3.14 Appearance of the customized visual model holder

Table 3.3 Chemical composition of the water samples used in visualization experiments

Positive ions (mg/L)					Negative ions (mg/L)			Mineralization degree (mg/L)	Water type
K^+	Na^+	Ca^{2+}	Mg^{2+}	Ba^{2+}	HCO_3^-	Cl^-	SO_4^{2-}		
2596	34,527	1762	233	1467	716	63,596	119	106,241	$CaCl_2$

distilled water and then placed in an oven to dry. (2) The visual model was installed in the model holder, and then the experimental devices were connected according to Fig. 3.12. (3) The sealing performance of the entire experimental system was tested by injecting high-purity nitrogen, and then the visual model was evacuated for 40 min. (4) The intermediate vessel and experimental lines were heated and maintained at 80 °C before the experimental fluid was injected into the visual model. (5) The water sample was injected into the model at a constant flow rate of 0.01 mL/min until the saturation pressure of the visual model reached 8 MPa. (6) The gas sample was injected into the model with different displacement pressure differentials (0.05–1.00 MPa) until no water was produced at the outlet. (7) The multiphase percolation process was recorded using a microscopic camera and DV during the visualization experiment. (8) Steps 1–7 were repeated for visualization experiments of other types of visual models. (9) The captured images were processed using Photoshop software and ImageJ software after all visualization experiments were completed.

The visualization experiment can not only capture local microscopic images to analyze the percolation mechanism and occurrence characteristics, but also record the overall percolation process of multiphase fluids in the visual model. The overall gas and water distribution images at different times could be obtained through video edition, which can be quantitatively characterized by the ImageJ gray analysis method.

Table 3.4 Composition and properties of the gas samples used in visualization experiments

Percentage of natural gas component/%							Relative density	Pseudo critical pressure/MPa	Pseudo critical temperature/K
CH_4	C_2H_6	C_3H_8	N_2	CO_2	He	H_2S			
93.13	0.07	0.01	0.73	5.01	0.03	1.02	0.6265	4.82	199.55

Table 3.5 Experimental scheme for microscopic visualization of gas flooding water

Microscopic visual model	Displacement pressure differential/MPa
Fracture type model	0.05, 0.1, 0.15, 0.2, 0.3, 0.4, 0.5, 0.6, 0.7, 0.8, 0.9, 1.0
Cavity type model	0.05, 0.1, 0.15, 0.2, 0.3, 0.4, 0.5, 0.6, 0.7, 0.8, 0.9, 1.0
Fracture-cavity type model	0.05, 0.1, 0.15, 0.2, 0.3, 0.4, 0.5, 0.6, 0.7, 0.8, 0.9, 1.0

3.2.5 Experimental Scheme

The three types of visual models were subjected to gas flooding water visualization experiments under different displacement pressure differentials. The experimental program is shown in Table 3.5.

3.2.6 Formation Mechanism of Residual Water in Different Types of Reservoirs

The gas flooding water visualization experiment is mainly used to simulate the formation process of gas reservoirs. The properties of the gas allow it to enter tiny pore throats to displace formation water. However, it was found that none of the three types of visual models could be fully saturated with water during the experimental preparation stage. This is because the injected water preferentially enters the small pore throats and occupies the large channel walls, and finally completely fills most of the fractures, cavities, pores and throats. However, some dead ends and blind corners can only be partially saturated with water under the limitation of experimental pressure (Figs. 3.15a, 3.16a and 3.17a). The interspace of the original formation should be completely saturated with formation water according to the hydrocarbon migration and accumulation theory (Li & Li, 2011). Therefore, the model space that was not saturated with water should be considered to be occupied by irreducible water.

(1) Fracture type visual model

Fractures are the dominant channels for fluid percolation in the fracture type model. The flow conductivity of fractures is far stronger than that of throats, pores and cavities. Therefore, the injected gas preferentially entered the fractures in the visual model at the beginning of the experiment (Dai et al., 2012), and rapidly displaced the formation water in the middle of the fractures (Fig. 3.15b). Subsequently, the water in some pores, fracture folds and channel intersections was gradually displaced with the increase of displacement pressure differential (Fig. 3.15c). The residual water adhering to the fracture wall was carried away by the continuous gas flow with the continuous injection of gas. As a result, the water film gradually thinned and

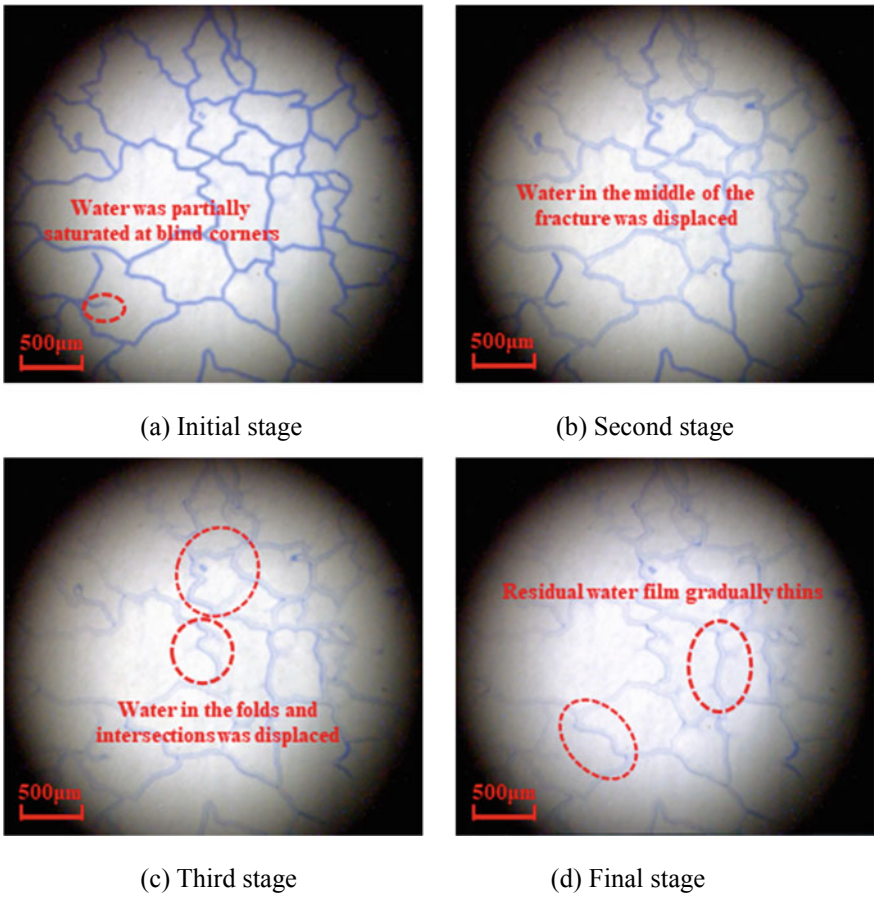

Fig. 3.15 Microscopic visualization of the fracture type model during the gas flooding water process

converged into water droplets at the intersection of the fractures. Finally, a portion of these droplets were carried out of the model by gas flow, only a thin water film was left on the fracture walls (Fig. 3.15d). The residual water film can be further thinned by increasing the displacement pressure differential. Another portion of the droplets was trapped in the fracture folds and necking sits to form irreducible water.

(2) Cavity type visual model

The porous media of the cavity type visual model is composed of small-sized pore throats and large-sized cavities. The percolation capacity of the model is mainly controlled by the size and distribution of the pore throats. The injected gas preferentially advances along the dominant percolation channel. Subsequently, the continuously injected gas gradually occupied most of the storage space and displaced most of the water therein. When the injected gas entered a cavity, a circle of small gas flow

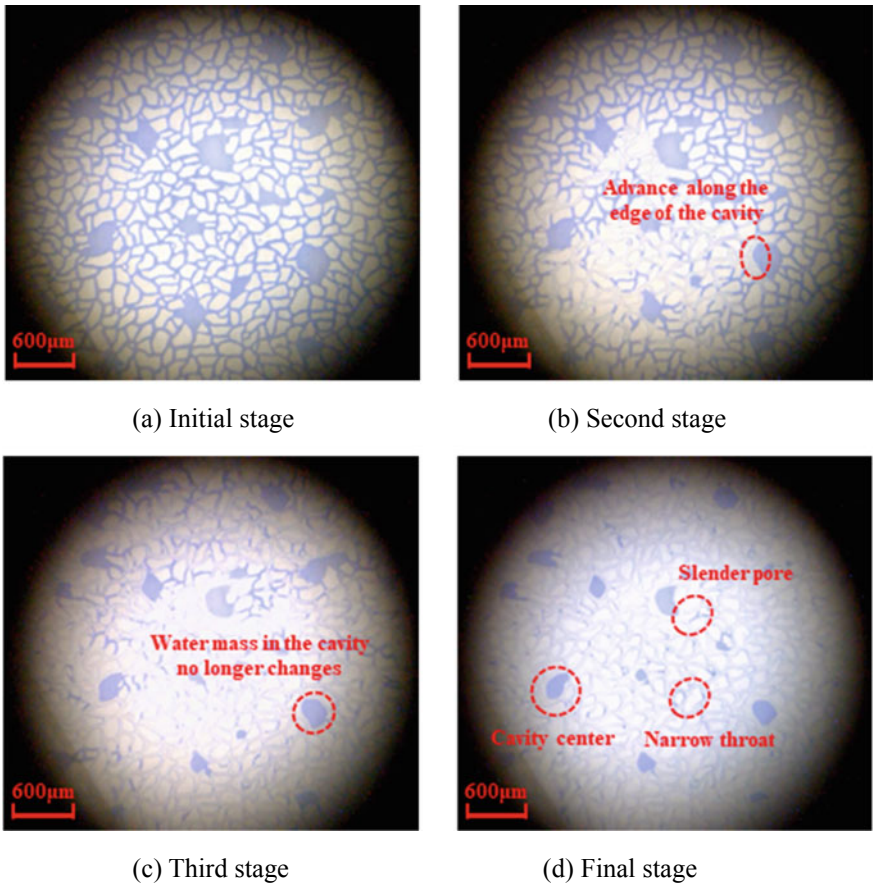

Fig. 3.16 Microscopic visualization of the cavity type model during the gas flooding water process

channels was first formed around the water body of the cavity (Fig. 3.16b). The gas flow channel gradually widened as the gas continues to enter the cavity. Meanwhile, the water at the edge of the water body was continuously carried out of the cavity by the gas flow. Eventually, a relatively rounded water mass formed in the center of the cavity. When the shape of the water mass no longer changes, it means that the injected gas cannot completely displace the residual water mass from the cavity under this displacement pressure differential (Fig. 3.16c). In the later stage of the gas flooding water visualization experiment, the water film on the pore wall aggregated and thickened, and was then partially displaced out when the water film thickness reached a critical value. Finally, residual water formed at the locations of slender pores, narrow throats and bottom of cavities (Fig. 3.16d). The gas–water front in the cavity type visual model advanced uniformly at a relatively slow rate because there are no fractures in the model. However, the residual water mass at the bottom of

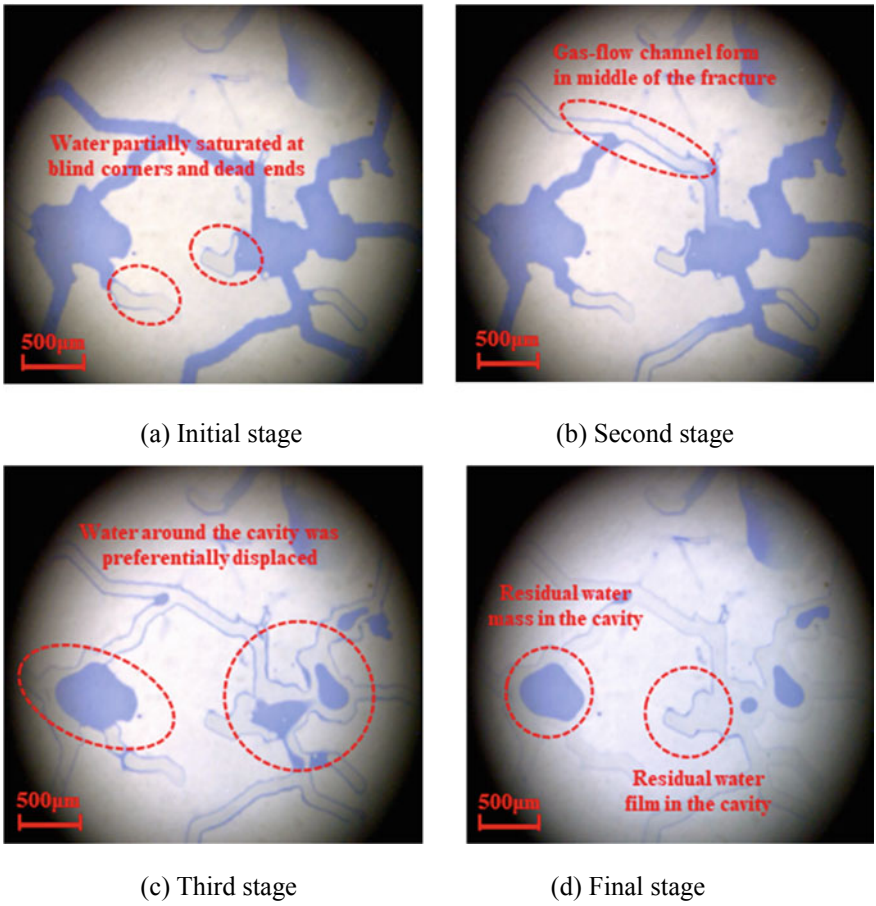

Fig. 3.17 Microscopic visualization of the fracture-cavity type model during the gas flooding water process

the cavity was further reduced, and the water film on the channel wall was further thinned with the continuous increase of the displacement pressure differential.

(3) Fracture-cavity type visual model

The combination structure of fractures and cavities is the unique structure of ultra-deep carbonate gas reservoirs. Neither the blind corners of cavities nor the dead ends of fractures cannot be fully saturated with water (Fig. 3.17a). The injected gas preferentially entered the fracture at the beginning of the experiment, and quickly displaced the formation water in the middle of the fracture (Fig. 3.17b). When the injected gas entered a cavity, the water around the cavity was preferentially displaced to form a gas flow channel (Fig. 3.17c). The water mass in the middle of the cavity was continuously eroded and shrunk as more gas entered the cavity. Accordingly, the

movable water stripped from the water mass converged into water droplets or water columns in the fractures at the cavity outlet, and is then displaced. When the water body in the cavity shrinked to a certain extent and no longer changed, a residual water mass was formed at the bottom of the cavity. In addition, the water bodies in several cavities connected by multiple fractures were almost completely replaced by gas, and only residual thin water films were formed on the cavity walls (Fig. 3.17d). These residual water films or residual water masses will gradually became thinner or smaller with the increase of the displacement pressure differential. In summary, the occurrence location and state of residual water in the reservoir are mainly affected by the pore structure characteristics and accumulation dynamics. The special pore structure and multi-stage gas charging process of ultradeep carbonate gas reservoirs result in complex and diverse occurrence patterns of formation water. Therefore, it is necessary to further study the residual water occurrence patterns and its effect on gas-phase percolation of this type gas reservoir.

3.2.7 Occurrence Patterns of Residual Water and Its Effect on Gas Percolation

The storage space is initially saturated with formation water during the rock deposition process. Then, the original water in the reservoir is displaced by oil or gas during the hydrocarbon migration and accumulation process, thereby forming a coexistence state of oil and water or gas and water (Zhu et al., 2008). The water displaced and migrated at this stage is called primary movable water. When an oil and gas reservoir is formed and discovered, the water in the reservoir space could be called residual water, and the saturation and occurrence characteristics of residual water are related to the accumulation conditions (Zhu et al., 2016). A portion of the residual water in the reservoir may be converted into secondary movable water and then gradually produced under the pressure differential during the hydrocarbon exploitation process. The secondary movable water is retained in the porous media during the hydrocarbon accumulation process because the hydrocarbon charging force is less than the migration resistance. However, the water in the reservoir cannot be completely displaced even if the hydrocarbon accumulation power is sufficient. There is still a certain amount of residual water distributed or trapped in the corners of rock particles, narrow pore throats or adsorbed on the rock matrix surface. Residual water at these locations cannot participate in fluid flow under conventional production conditions and is therefore referred to as irreducible water. The classification results of formation water based on the above analysis are shown in Fig. 3.18.

Fractures are the dominant percolation channels for fracture type and fracture-cavity type reservoirs. The water in the middle of the fracture is initially displaced in the gas flooding water visualization experiment. Capillary force is the resistance to gas-phase flow because the visual model is hydrophilic. Moreover, the magnitude of capillary force is inversely proportional to the size of the percolation channel.

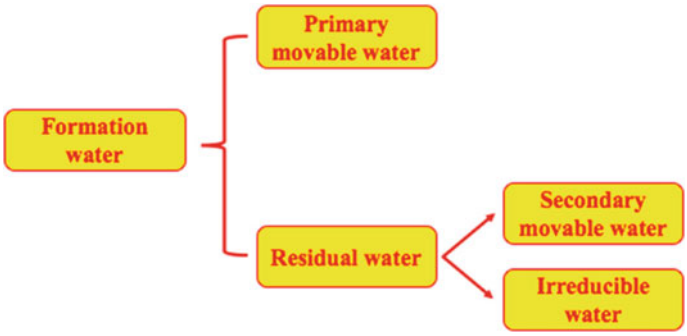

Fig. 3.18 Classification of formation water during hydrocarbon accumulation and development

Therefore, the capillary resistance of gas percolation in fractures is weak. The effect of surface tension makes the residual water to adhere to the wall surfaces of poorly connected fractures in the form of "thin water film" (Fig. 3.19a). The residual water of this occurrence pattern has low saturation and little effect on the gas-phase percolation characteristics and percolation capacity. In contrast, throats with high capillary resistance are the dominant channels for gas percolation in pore type and cavity type reservoirs. Consequently, residual water is present on the particle surface in the form of a "thick water film". The residual water in this occurrence pattern further narrows the originally narrow gas-phase percolation channel and increases the percolation resistance. The relationship between the residual water film thickness and the percolation channel size will be described in detail later. The residual water in the form of water film is difficult to be carried out by the gas flow when the displacement pressure differential is low. However, the water around the water film can be stripped off by the gas flow and become an important part of the secondary movable water when the displacement pressure differential increases to a certain extent and the displacement lasts for a long time.

The residual water mass at the bottom of the cavity is a special occurrence pattern of residual water in cavity type and fracture-cavity type reservoirs. The injected water preferentially break through along the periphery of the water body as it enters the cavity. Then the gas flow channel is formed and gradually widens with the continuous injection of gas. Meanwhile, the water body in the middle of the cavity is continuously eroded and then converges into water droplets at the exit of the cavity. These water droplets are carried out of the cavity by the subsequent gas flow. The size and shape of the water body in the cavity remain unchanged after the dominant gas flow channel is completely formed. This water is eventually trapped at the bottom of the cavity to form a residual "water mass" (Fig. 3.19b). The small-sized residual water mass has little effect on the gas percolation because there is still a wide gas flow channel in the upper part of the cavity. In contrast, the large-sized residual water mass may inhibit gas flow at low displacement pressure differential. The increase of the displacement pressure differential can break the force balance of the water mass, and therefore the external water of the water mass can be converted into secondary movable water.

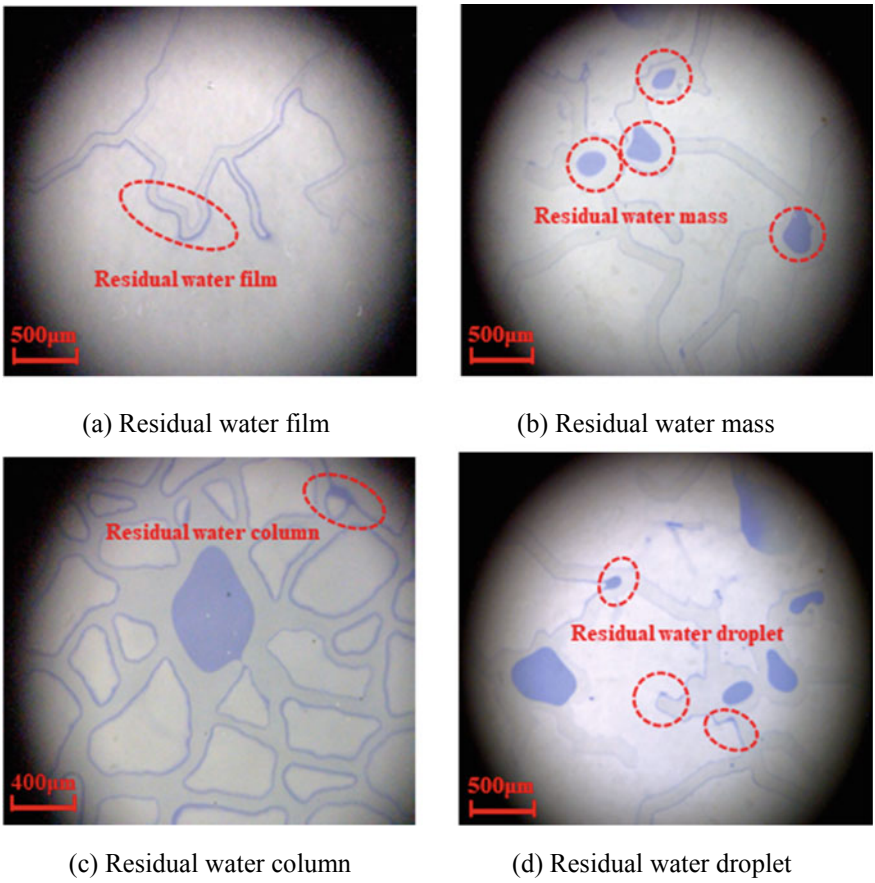

(a) Residual water film (b) Residual water mass

(c) Residual water column (d) Residual water droplet

Fig. 3.19 Several types of residual water occurrence patterns observed in visualization experiments

Capillary force is the resistance for gas-phase percolation in hydrophilic reservoirs. The capillary resistance of the water in the narrow throat is large, and the water cutoff phenomenon occurs when the gas flooding force is insufficient. This residual water is trapped throughout the throat in the form of a "water column" (Fig. 3.19c). The residual water in this occurrence pattern not only blocks the flow channel, but also closes the large pores controlled by the small throat. This is also the main reason why the gas-phase percolation capacity and recovery factor of the reservoir is greatly reduced after water encroachment. It should be noted that the residual "water column" formed by the cutoff phenomenon observed in the visualization experiment cannot flow even at high displacement pressure differentials. Therefore, the residual water of this occurrence pattern is defined as irreducible water. When the injected gas enters multiple channels at the same time, the capillary resistance in the narrow and long channels is greater than that in the wide and short channels. Accordingly, residual water is easily formed in the narrow and long channels, thereby reducing

the effective percolation channel and pore throat coordination number. The residual "water column" at these locations can be displaced at high displacement pressure differentials and is therefore defined as secondary movable water. In addition, some residual water is trapped in the blind corners and dead ends of pores and cavities in the form of "water droplet" because the injected gas cannot effectively sweep these locations (Fig. 3.19d). Residual water in this occurrence pattern is also classified as irreducible water because it is difficult to participate in fluid flow even if the displacement pressure differential increases.

In summary, there are four main types of residual water occurrence patterns in various types of ultradeep carbonate gas reservoirs, namely "water film", "water mass", "water column", "water droplet". The main influencing factors and formation mechanisms of residual water in different occurrence patterns are summarized in Table 3.6.

3.2.8 *Quantitative Characterization of Gas Flooding Water Visualization Experiments*

The images of gas flooding water visualization experiment could only be used for qualitative description and analysis of the residual water distribution. In order to quantify the visualization experimental images under different displacement pressure differentials, the ImageJ gray analysis method was utilized to study the distribution of water saturation and the proportion of residual water film thickness for the three types of visual models.

The water saturation variation curves of the three types of visual models were obtained by quantifying the number of residual water pixels under different displacement pressure differentials. The saturation calculation formula is as follows.

$$S_{\mathrm{rw}} = \frac{A_{\mathrm{w}}}{A_{\mathrm{v}}} = \frac{N_{\mathrm{w}}}{N_{\mathrm{v}}} \tag{3.1}$$

where S_{rw} is the residual water saturation, f; A_{w} is the area occupied by residual water in the visual model, $\mu\mathrm{m}^2$; A_{v} is the area occupied by the voids in the visual model, $\mu\mathrm{m}^2$; N_{w} is the pixel number of residual water in the visual model; N_{v} is the pixel number of voids in the visual model.

The calculation results of water saturation are illustrated in Fig. 3.20. It could be concluded that the movable water and residual water saturations are parameters directly related to petrophysical properties, pore structure and displacement pressure differential. It should be noted that the locations in the visual model that are not saturated with water are also defined as irreducible water. Therefore, the initial water saturation is 100% for all three visual models. The residual water saturations of the three types of visual models decrease with the increase of displacement pressure differential, and the residual water saturation of the model with fractures is higher than that of the model without fractures under the same pressure differential. Therefore,

Table 3.6 Influencing factors and formation mechanisms of residual water in different occurrence patterns

Occurrence pattern	Dominant influence factor	Formation mechanism	Water type
Residual thin water film on the fracture surface	Surface tension	The wider the flow channel, the weaker the capillary resistance, and the thinner the residual water film	Secondary movable water
Residual thick water film on the pore surface	Capillary force	The narrower the flow channel, the greater the capillary resistance, and the thicker the residual water film	Secondary movable water
Residual water mass at the bottom of the cavity	Displacement pressure	Capillary forces for large-sized cavities can be negligible. The higher the displacement pressure differential, the smaller the residual water mass	Secondary movable water
Residual water column in the narrow throat	Jamin effect	The Jamin effect is evident at the narrow throat because of great capillary resistance. The formation water at the narrow throat is trapped by the cutoff phenomenon	Irreducible water
Residual water column in the elongated pore	Capillary force	The capillary resistance of elongated pores is high. When the displacement pressure differential is insufficient, the formation water is retained in the pores	Secondary movable water
Residual water droplet in the blind corner and dead end	Channel connectivity	It is difficult for injected gas to enter blind corners and dead ends with poor connectivity. The residual water at these locations is fully trapped by the surrounding gas	Irreducible water

the worse the reservoir petrophysical properties and the smaller the displacement pressure differential, the higher the residual water saturation. Figure 3.20b shows that the injected gas cannot enter the cavity model to from an effective flow when the displacement pressure differential is low. The fluid in the model begins to flow only when the displacement pressure differential increases enough to overcome the capillary resistance created by the water lock effect. This phenomena is consistent with the threshold pressure effect introduced in Chap. 2. In contrast, the injected gas can enter the visual model with fractures and migrate rapidly at a relatively low displacement pressure differential. Therefore, there is no threshold pressure effect in these visual models, and the decline rate of residual water saturation is relatively fast. The residual water saturations of the three visual models decrease rapidly under low displacement pressure differential. The water displaced out of the visual model at this stage is primary movable water, mainly from fractures and macropores with low capillary resistance and cavities with well connectivity. The decline rate of residual water saturation becomes slower as the displacement pressure differential increases gradually. The water displaced out of the visual model at this stage is secondary movable water, mainly from micropores with great capillary resistance, water films on the walls of fractures and macropores, and the residual water masses at the bottom of cavities. The value of water saturation keeps constant when the displacement pressure differential increases to a certain extent. The final residual water saturation is defined as the irreducible water saturation. The irreducible water saturations of fracture type, cavity type and fracture-cavity type visual models obtained by the gas flooding water visualization experiment are 10.2%, 15.3% and 23.5%, respectively. The reason why the irreducible water saturation of the fracture-cavity type visual model is higher than that of the cavity type visual model is that there is a certain amount of irreducible water at the bottom and blind corners of the large cavity. The formation of this residual water is related to the shape and collocation of the pore-cavity-fracture system (Sayegh & Fisher, 2009). Furthermore, the decline rate of residual water saturation of the fracture-cavity type visual model is slightly slower than that of the fracture type visual model. This is because the flow of the injected gas in the cavity is greatly inhibited by the water body. The injected gas requires a high displacement pressure differential and a long displacement time to pass through the cavity. Therefore, the cavity has the effect of slowing down the flow rate of the displacing phase. This conclusion is consistent with the gas–water two-phase percolation characteristics introduced in Chap. 2.

In addition, the visualization experimental results show that the residual water film thickness on fracture and pore channel walls is not only related to the channel size, but also to the displacement pressure differential. Therefore, fractures and pores with different sizes were selected in visual models for quantitative investigations to clarify the influencing factors of residual water saturation. Then, ImageJ gray analysis was used to quantify the proportion of residual water film thickness in channels of different sizes under different displacement pressure differentials. The saturation calculation formula is as follows.

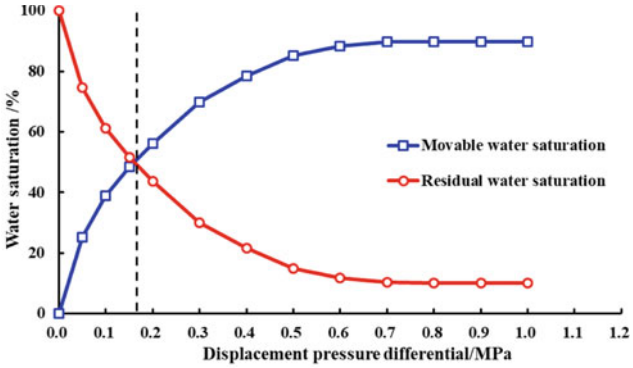

(a) Fracture type visual model

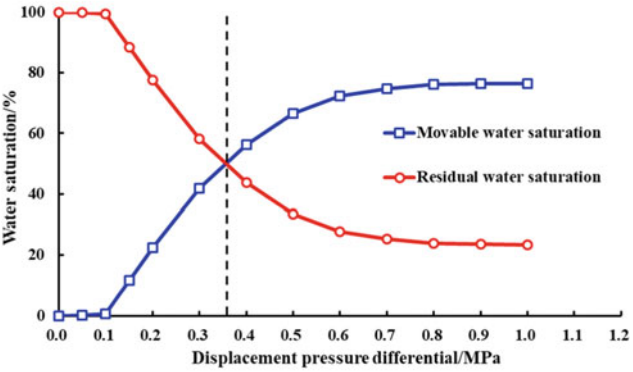

(b) Cavity type visual model

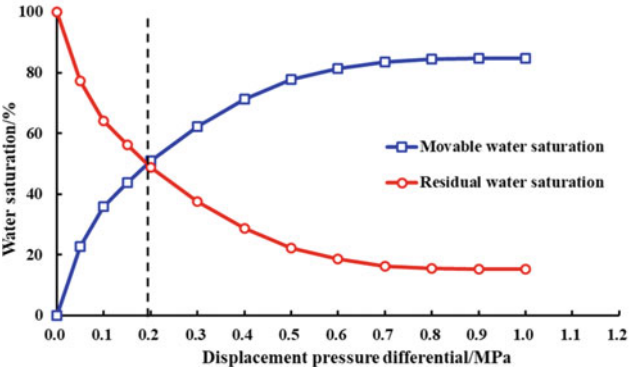

(c) Fracture-cavity type visual model

Fig. 3.20 Quantification results of water saturation based on ImageJ gray analysis method

$$p_w = \frac{T_w}{T_c} = \frac{N_w}{N_v} \tag{3.2}$$

where p_w is the proportion of the residual water film thickness in the channel, f; T_w is the thickness of residual water film, μm; T_c is the size of the fracture or pore channel, μm; N_w is the pixel number of residual water film in the channel; N_v is the pixel number of the fracture or pore channel. The calculation results of the proportions of residual water films of different sizes in the flow channel are shown in Fig. 3.21.

It can be seen from the figure that the smaller the flow channel size, the greater the relative thickness of the water film under the same pressure differential. The effective percolation channel narrows with the increase of the water film thickness, thereby affecting the gas-phase percolation characteristics and percolation capacity. The proportion of the residual water film thickness in the flow channel starts to increase exponentially when the size of the channel is reduced to a certain extent. Therefore, the extremely narrow throat is completely occupied by the water film and forms a "cutoff" type of irreducible water there. In contrast, the proportion of residual water film thickness in wide fractures is low, and therefore the effect of water film on gas-phase percolation in fractures is not obvious. Furthermore, the proportion of water film thickness in flow channels with different sizes decreases with the increase of displacement pressure differential. The smaller the flow channel size, the greater the proportion reduction in water film thickness. However, when the displacement pressure differential increases to a certain extent, the proportion of the water film thickness in the channels of different sizes no longer decreases and eventually forms a "thin film" type of irreducible water. It should be noted that the proportion of water film thickness in fractures of different sizes has little difference under high displacement pressure differential. This proportion is the theoretical minimum value

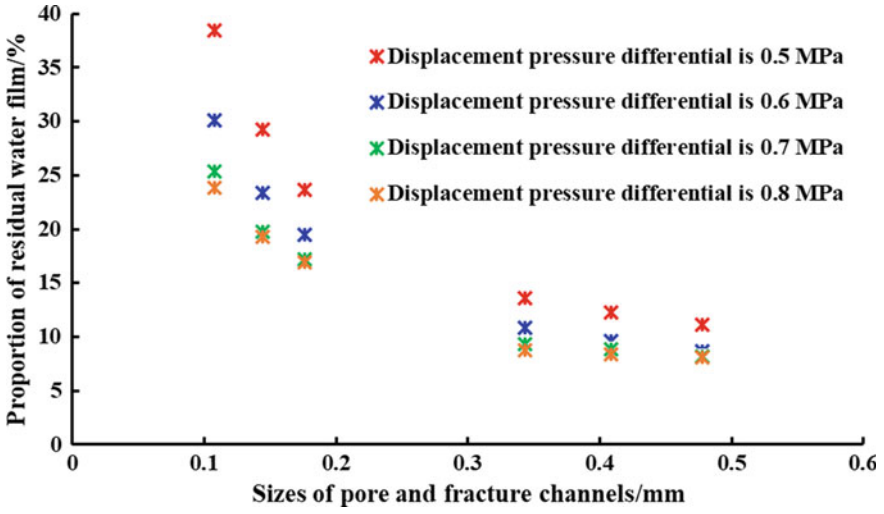

Fig. 3.21 Quantification results of residual water film based on ImageJ gray analysis method

of the residual water film thickness in the flow channel of each size, which is defined as the "relative critical thickness". Therefore, the worse the reservoir petrophysical properties, the smaller the pore throat size, the greater the capillary resistance, and the higher the content of "capillary" type of irreducible water formed. The finer the rock particles, the larger the contact area between the particles and water, and the higher the content of "thin film" type of irreducible water formed (Chen et al., 2014).

The following suggestions can be put forward for the development of different types of ultradeep carbonate gas reservoirs by analyzing the formation mechanism and occurrence characteristics of formation water in different types of visual models. Residual water saturation and irreducible water saturation are relatively high in the pore type and cavity type reservoirs with relatively poor petrophysical properties. The gas production capacity of these reservoirs is weak because of narrow effective flow channels and threshold pressure effects (Wang et al., 2017). Therefore, it is not recommended to exploit pore type and cavity type gas reservoirs in the high production stage in the early stage of development. These types of reservoirs can be exploited in the high pressure differential stable production phase in the later stage of development. In contrast, residual water saturation and irreducible water saturation are relatively high in fracture type and fracture-cavity type reservoirs with relatively high petrophysical properties. The gas percolation capacity of these reservoirs is strong because of the wide effective flow channels and no threshold pressure effects. Therefore, these types of reservoirs can be used as the dominated gas supply reservoirs in the early stage of development, but excessive gas production rate will also aggravate the water encroachment intensity of edge and bottom water. Liquid accumulation gradually forms in the wellbore as the edge and bottom water of these reservoirs advance to the gas well, resulting in liquid retention and capillary imbibition effects in other reservoirs. Eventually, natural gas in the near-wellbore area of other reservoirs is sequestered by these water, thereby inhibiting the overall gas supply capacity of the commingled production.

3.3 Microscopic Visualization of Gas–Water Relationship During Water Encroachment Process

Water encroachment is a serious problem in the development of edge and bottom water reservoirs. Many ultradeep carbonate gas reservoirs in the Sichuan Basin belong to edge and bottom water reservoirs. The diversity and heterogeneity of the reservoir media in this type of gas reservoirs complicates the percolation characteristics of gas–water two-phase and the formation mechanism of trapped gas during the water encroachment process (Rong et al., 2016). Production data indicates that the abundant energy of aquifer exacerbates the formation of water channeling, resulting in relatively high amounts of trapped gas and relatively low gas recovery (Rezaee et al., 2013). Recently, the characteristics of water encroachment and the formation mechanism of trapped gas have attracted much attention as the research focus of

enhancing gas recovery. Suekane et al. (2010) observed two types of trapped gas bubbles in sandstone gas reservoirs by microfocused X-ray computed tomography and analyzed the trapping mechanism of residual gas. Rezaee et al. (2013) revealed the effect of heterogeneity on trapped gas formation mechanism and gas recovery factor through physical simulation experiments. Li et al. (2014) divided the water encroachment into two successive stages, where the initial stage is dominated by capillary, and the pseudo steady stage is affected by pore pressure. Geistlinger and Mohammadian (2015) used X-ray microtomography to study gas trapping during capillary imbibition and then compared the experimental results with those predicted by percolation theory. Su et al. (2017) revealed water encroachment process and CBM gas trapping mechanism based on the measurement of surface tension, contact angle, and gas-phase permeabilities of coal samples. However, no systematic investigation has been reported on the gas–water percolation characteristics and trapped gas formation mechanism of ultradeep carbonate gas reservoirs, especially through visualization experimental techniques. Therefore, three types of microscopic visual models were used to conduct water flooding gas visualization experiments to simulate the water encroachment process of different types of carbonate gas reservoirs. The characteristics of gas–water two-phase percolation in various types of reservoirs during water encroachment process were observed. The formation mechanism and influencing factors of different types of trapped gas were analyzed. Furthermore, various types of trapped gas distribution, gas–water saturation dynamics and recovery factors under different displacement pressure differentials were quantified by ImageJ gray analysis method.

3.3.1 Experimental Procedure

The detailed microscopic visualization experimental procedure of water flooding gas is summarized as follows. (1) The visual model and model holder were cleaned with distilled water and then placed in an oven to dry. (2) The visual model was installed in the model holder, and then the experimental devices were connected according to Fig. 3.12. (3) The sealing performance of the entire experimental system was tested by injecting high-purity nitrogen, and then the visual model was evacuated for 40 min. (4) The intermediate vessel and experimental lines were heated and maintained at 80 °C before the experimental fluid was injected into the visual model. (5) The gas sample was injected into the model at a constant flow rate of 0.01 mL/min until the saturation pressure of the visual model reached 8 MPa. (6) The water sample was injected into the model with different displacement pressure differentials (0.10–0.30 MPa) until no gas was produced at the outlet. (7) The multiphase percolation process was recorded using a microscopic camera and DV during the visualization experiment. (8) Steps 1–7 were repeated for visualization experiments of other types of visual models. (9) The captured images were processed using Photoshop software and ImageJ software after all visualization experiments were completed.

Table 3.7 Experimental scheme for microscopic visualization of water flooding gas

Microscopic visual model	Displacement pressure differential/MPa
Fracture type model	0.10, 0.15, 0.20, 0.25, 0.30
Cavity type model	0.10, 0.15, 0.20, 0.25, 0.30
Fracture-cavity type model	0.10, 0.15, 0.20, 0.25, 0.30

The visualization experiment can not only capture local microscopic images to analyze the water encroachment characteristics of gas–water two-phase and formation mechanism of trapped gas, but also record the overall percolation process of multiphase fluid in the visual model. The overall gas and water distribution images at different times could be obtained through video edition, which can be quantitatively characterized by the ImageJ gray analysis method.

3.3.2 Experimental Scheme

The three types of visual models were subjected to water flooding gas visualization experiments under different displacement pressure differentials. The experimental program is shown in Table 3.7. It should be noted that the focus of the visualization experiment of gas flooding water and water flooding gas is different. The gas flooding water experiment focuses on the occurrence characteristics of residual water under different hydrocarbon charging forces. Therefore, the relationship between the displacement pressure differential and the final water saturation is mainly quantified. It is not necessary to quantify the residual water saturation at different gas injection times. In contrast, the water flooding gas experiment focuses on the two-phase percolation characteristics at different water encroachment times and the recovery factor at different pressure differentials. Therefore, the relationship between water injection time and fluid saturation, as well as the relationship between displacement pressure differential and recovery factor should be quantified.

3.3.3 Characteristics of Gas–Water Two-Phase Percolation During Water Encroachment

(1) Fracture type visual model

The percolation capacity of fluid in fractures is much stronger than that in pores and cavities. Therefore, fractures are the dominant percolation channels in fracture type and fracture-cavity type visual models. The water encroachment process within the fracture type model can be subdivided into three stages. The dominant percolation pattern in the early stage of water encroachment is “gas in water”. When injected

water entered the visual model, water films were first formed along both sides of the fracture due to the hydrophilicity of the model (Fig. 3.22a). The water film gradually thickened and then formed water streams. Water streams flowed along the fracture walls in the form of a continuous phase (Fig. 3.22b), while gas migrated in the middle of the fracture in the form of dispersed bubbles or gas columns (Fig. 3.22c). The injected water gradually displaced most of the gas in the fracture, but a small amount of gas was retained in the fracture folds and necking sites due to the "cutoff" phenomenon (Fig. 3.22d). The second stage of the water encroachment process began when water channeling occurred. The energy of residual gas bubbles or gas columns in the model was continuously replenished by the continuous injection of water. The bubble broke through the preceding water column and continued to flow along the fracture when the accumulated energy could overcome the percolation resistance (Fig. 3.23). Most of the gas in the fracture system had been displaced when the later stage of water encroachment began. A small amount of residual gas bubbles were trapped at the intersection of microfractures because of insufficient displacing energy to overcome the Jamin effect. When the subsequent gas bubble flowed to the intersection, it merged with the trapped gas bubble and transferred energy. The front part of the trapped gas bubble separated and formed a small gas bubble to pass through the intersection when the energy was accumulated to a certain extent. The rear end of the gas bubble was still trapped at the intersection and waiting to gather additional energy from subsequent bubbles before they can pass (Fig. 3.24).

(2) Cavity type visual model

There are both small-sized pore throats and large-sized cavities in the cavity type visual model. Therefore, the percolation capacity of this model is mainly controlled by the throat size and distribution. The capillary resistance and displacement pressure differential of the cavity type model are also larger than those of the fracture type model. When injected water entered the model, water films were first formed along both sides of the pores channel. The water film thickened rapidly to form a water column because the size of pores is far smaller than that of fractures, and then alternately advanced with the gas column (Fig. 3.25a). And meanwhile, the water film fronts in some pore channels converged at the intersection to form water streams, thereby blocking the gas columns in the middle section of the channels to form trapped gas (Fig. 3.25b). When the injected water entered a cavity, the water film first extended to the walls around the cavity. Then the injected water gradually filled the cavity and compressed the gas along both sides of the gas channel. The gas channel in the cavity was completely filled with water after a period of time, and the trapped gas was formed at the necking site of the cavity outlet (Fig. 3.25c). Eventually, most of the space within the cavity was occupied by water, while various types of trapped gas were formed in the pore throat (Fig. 3.25d).

(3) Fracture-cavity type visual model

The combined structure of fractures and cavities is the unique structure of fracture-cavity carbonate gas reservoirs. The particularity of this structure makes the water

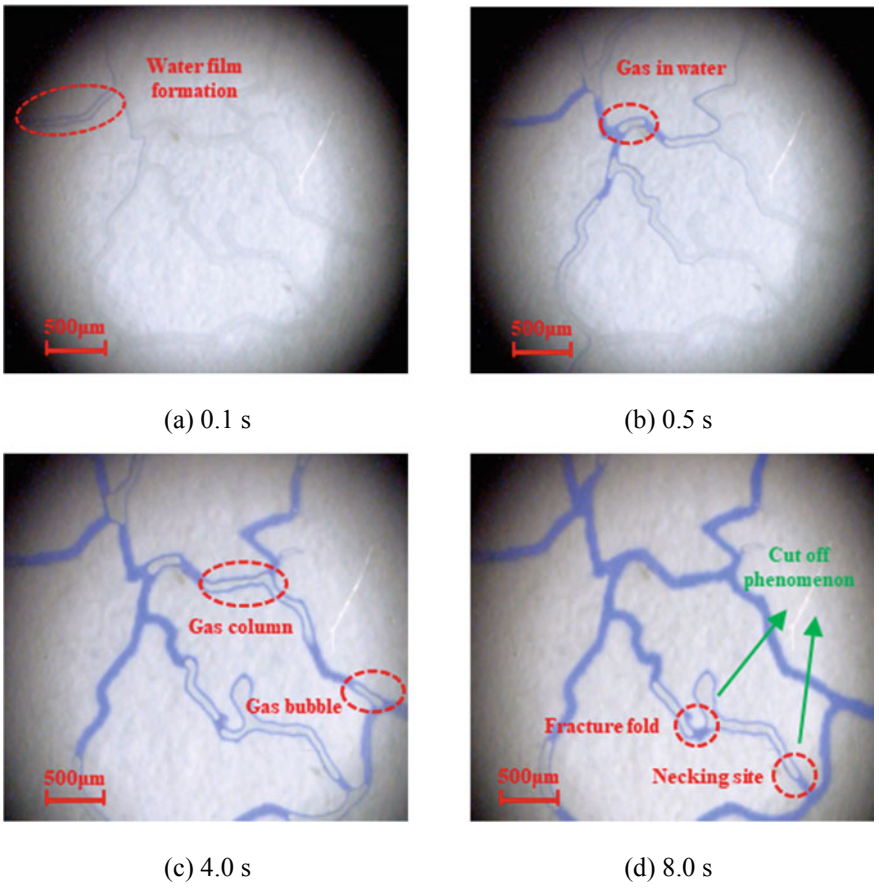

Fig. 3.22 Microscopic visualization of the fracture type model in the early stages of the water encroachment process

encroachment characteristics and trapped gas distribution of fracture-cavity type reservoirs different from those of other types of reservoirs. Water films were first formed along both sides of the fracture, then gradually thickened and formed water streams (Fig. 3.26a). Meanwhile, the gas flowed with water streams in the form of gas core or gas slug (Fig. 3.26b). When the injected water entered the cavity from the fracture, it not only entered the cavity wall in the form of a water film, but also directly enters the middle of the cavity in the form of a water column. This is because the conductivity capacity and channel size of fracture are much stronger and larger than those of pores in the cavity type model. Eventually, the gas in the cavity was gradually displaced by the injected water in a piston-like displacement manner (Fig. 3.26c). When the injected water advanced to the cavity outlet, it preferentially entered the high-permeability fractures on the dominant flow line, and then successively entered other microfractures or low-permeability pore channels (Fig. 3.26d).

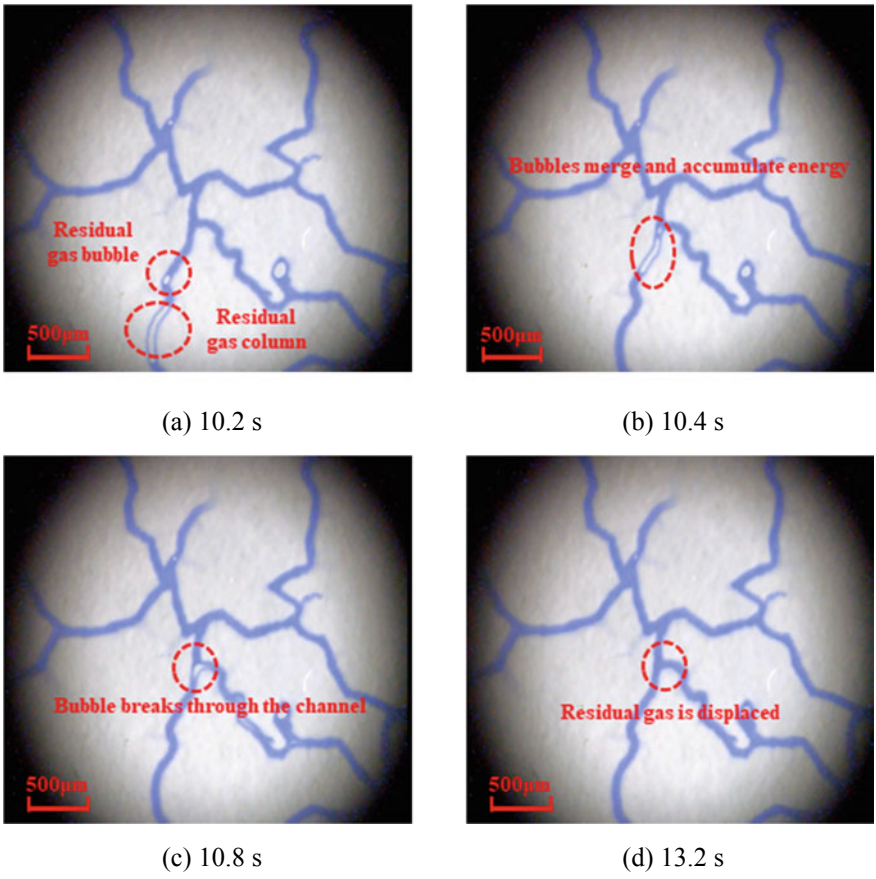

Fig. 3.23 Microscopic visualization of the fracture type model in the second stages of the water encroachment process

3.3.4 Formation Mechanism of Different Types of Trapped Gas

When water flooding gas visualization experiments were completed, various types of trapped gas were formed at different locations of the three types of visual models. Some types of trapped gas could be observed in all three visual models, whereas some special types of trapped gas were only present in specific visual models. The microscopic visualization experiment can be used to intuitively study the formation mechanism and production method of various types of trapped gas, which is of great significance for improving the gas recovery factor of ultradeep carbonate gas reservoirs with edge and bottom water. The trapped gas observed in the three models could be divided into the following six types according to the formation mechanism.

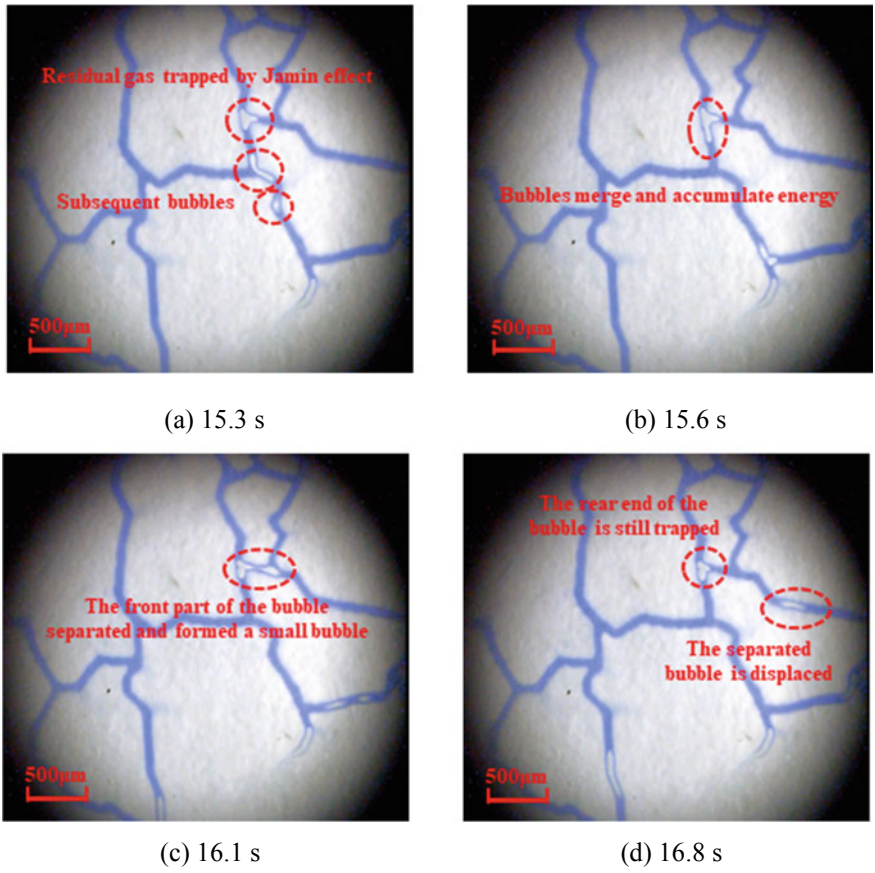

Fig. 3.24 Microscopic visualization of the fracture type model in the later stages of the water encroachment process

(1) Trapped gas formed at dead ends and blind corners

A certain amount of trapped gas can be formed at the dead ends or blind corners of pores, cavities and fractures, and therefore this type of trapped gas is widely distributed in the three visual models (Zhang et al., 2005) (Fig. 3.27). Gas in these locations is difficult to be displaced by water because effective percolation channels cannot be formed despite the hydrophilicity of the visual model. Gas at these locations may be completely trapped when the water flow pressure in the channel is far higher than the trapped gas pressure. The experimental results show that this type of trapped gas can only be partially recovered by reducing the water injection pressure. In order to more intuitively present the occurrence locations and recovery mechanisms of various types of trapped gas, a series of schematic diagrams were drawn with reference to the phenomena observed in the visualization experiments. Figure 3.28 shows the recovery mechanism of trapped gas at dead ends and blind corners. The trapped

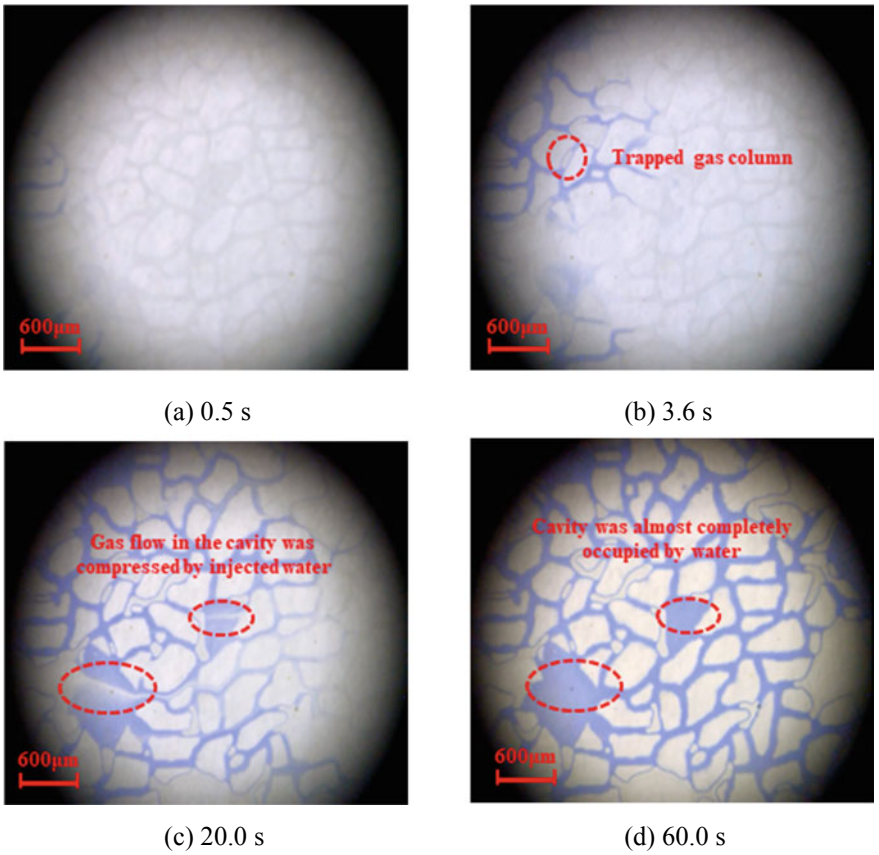

(a) 0.5 s (b) 3.6 s

(c) 20.0 s (d) 60.0 s

Fig. 3.25 Microscopic visualization of the cavity type model during the water encroachment process

gas at these locations expands and reoccupies the effective percolation channel after the external pressure is reduced. Then the expanded gas can be partially displaced by subsequent hydrodynamic forces. Meanwhile, the energy of the gas is gradually consumed, resulting in a continuous decrease in the gas pressure. The gas is trapped again in this location when the gas pressure drops below the external channel pressure. Therefore, this type of trapped gas can only be partially recovered by reducing the reservoir pressure or during the production decline stage. Shut-in operations are commonly used in the field to restore reservoir pressure. However, this operation may completely sequester this type of trapped gas.

(2) Trapped gas formed by circumfluence phenomenon

The trapped gas formed by circumfluence phenomenon is affected by the capillary force and hydrodynamic force, which are closely related to the channel size and displacement pressure differential, respectively. This type of trapped gas could be

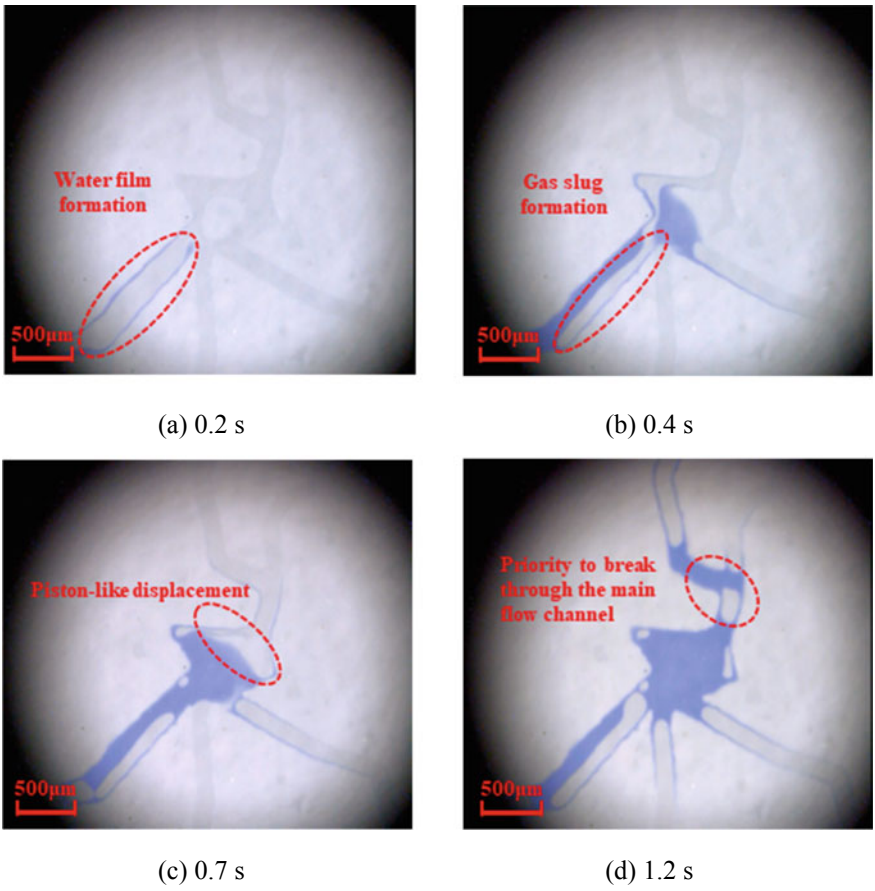

Fig. 3.26 Microscopic visualization of the fracture-cavity type model during the water encroachment process

Fig. 3.27 Trapped gas formed at dead ends or blind corners

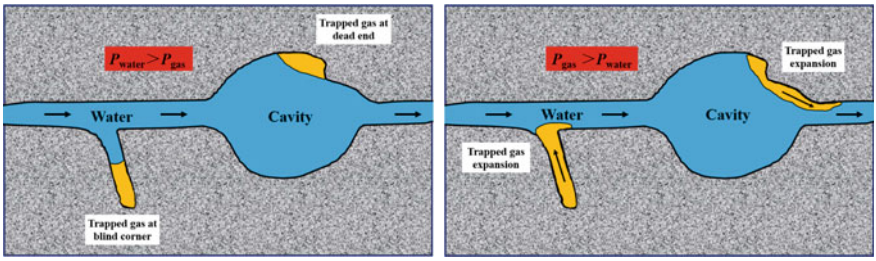

(a) Trapped gas at dead ends and blind corners (b) Trapped gas is partially displaced after expansion

Fig. 3.28 Schematic diagram of the recovery mechanism of the trapped gas at dead ends or blind corners

observed in all three types of visual models (Fig. 3.29), but the formation mechanism is different. The flow channel size of the cavity type model is relatively small and therefore the capillary force is generally large. When the displacement pressure difference is relatively low, the capillary force is the dominant motive power for fluid flow, and the trapped gas is mainly formed by the circumfluence phenomenon. The injected water preferentially enters the relatively small flow channel at a rapid flow rate under the action of capillary force when it arrives at a plurality of flow channels with different diameters (Ren et al., 2003). The water in the small channel migrates to the outlet prior to the water in other large channels because of the small gas volume and fast flow rate in the small channel. Subsequently, the gas in large channels that has not yet been displaced is blocked by the water from the small channel to form trapped gas. On the contrary, when the displacement pressure differential is relatively high, the hydrodynamic force becomes the dominant motive power for fluid flow, and the gas–water two-phase percolation mechanism is opposite to that when capillary force is the dominat motive power. The injected water preferentially enters the relatively large channel at a rapid flow rate under the action of hydrodynamic force because of the weak flow resistance of the large channel. The water in the large channel migrates to the outlet prior to the water in other small channels, and then blocks the gas in the small channels that have not yet been displaced. Figure 3.30 shows the formation mechanism of trapped gas caused by the circumfluence phenomenon. The flow channel size of the fracture type and fracture-cavity type models is relatively large and therefore the capillary force is generally small. Therefore, the injected water preferentially enters the wide fractures and then quickly breaks through the model regardless of the displacement pressure difference. Therefore, the water in the dominant fractures not only traps gas in some pores and microfractures, but also reduces the gas supply capacity of these regions to dominant fractures. This phenomena explains why the gas production rate and recovery factor of gas reservoirs with fractures are greatly reduced after water breakthrough. Therefore, it is suggested to apply the exploitation method of amplifying the production pressure differential step by step for the three types of reservoirs to improve the gas recovery in channels of different sizes and reduce the water encroachment intensity.

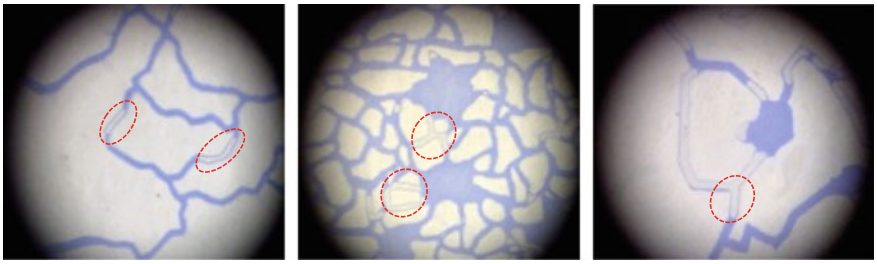

(a) Fracture type model (b) Cavity type model (c) Fracture-cavity type model

Fig. 3.29 Trapped gas formed by circumfluence phenomenon

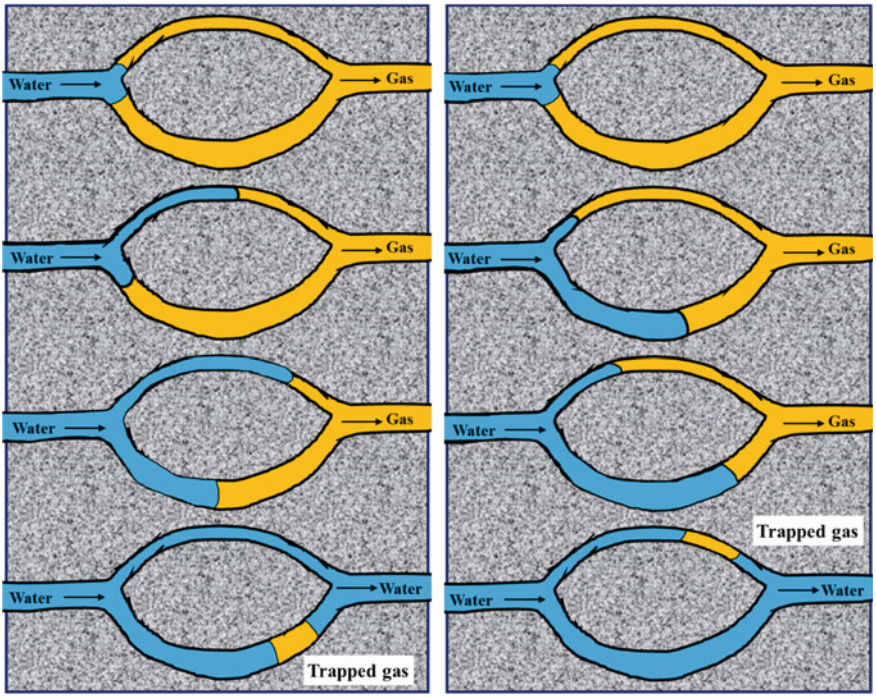

(a) Trapped gas formed at the large channel (b) Trapped gas formed at the small channel

Fig. 3.30 Schematic diagram of the formation mechanism of trapped gas caused by circumfluence phenomenon

(3) Trapped gas formed by cutoff phenomenon

It was observed that the trapped gas formed by cutoff phenomenon was distributed in the center of the pore or fracture channel in the form of discontinuous gas bubbles or gas columns. This type of trapped gas was observed in all three types of visual

models (Fig. 3.31). The Jamin effect, also known as the gas lock effect, is the primary mechanism for the formation of this type of trapped gas (An et al., 2016; Mo et al., 2017). The pore structure of ultradeep carbonate reservoirs is complex and the size of flow channels varies significantly. When a gas bubble or oil droplet flows through a narrow pore throat or fracture fold, the capillary force of the arcs on both sides of the gas bubble or oil droplet acts as flow resistance because of the radii difference between the front and rear of the channel. The gas bubble or oil droplet needs to stretch itself and change its shape to pass through the necking channel. However, this deformation consumes system energy, thereby restricting the transport of gas bubbles or oil droplets and adding additional percolation resistance. This resistance is essentially a microcapillary force effect. The gas-phase flow in the cavity type model experiences additional resistance from the Jamin effect as it enters the narrow pore throats. Furthermore, the water film at the narrow throat thickens and further narrows the gas flow channel due to the hydrophilicity of the model, thereby aggravating the Jiamin effect and increasing the gas-phase percolation resistance. The continuous gas phase can only pass through the narrow throat by shrinking and deforming by consuming its own energy. However, when the original system energy is insufficient, only the front of the gas bubble can be separated to form a small bubble to pass through the narrow throat first. The rest of the gas bubble can only be trapped at the throat until it collides with subsequent bubbles before it can pass again. Figure 3.32 shows the formation mechanism of trapped gas caused by the cutoff phenomenon. Trapped gas bubbles or gas columns caused by cutoff phenomenon can also be observed on rough surfaces or folds of fractures. The experimental results show that this type of trapped gas can be recovered in two ways. One is to increase the hydrodynamic force by increasing the displacement pressure differential to replenish the energy of trapped gas bubbles (Fig. 3.33a). The other is to expand and accumulate the trapped gas by reducing the model pressure, and then the expanded trapped gas can be partially recovered by its own energy (Fig. 3.33b).

(4) Trapped gas formed at H-shaped channels

The trapped gas formed at H-shaped channels is unique to the cavity type visual model, as shown in Fig. 3.34. The formation mechanism of this type of trapped gas

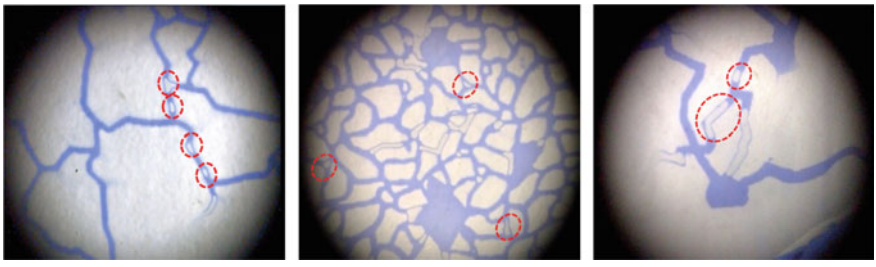

(a) Fracture type model (b) Cavity type model (c) Fracture-cavity type model

Fig. 3.31 Trapped gas formed by cutoff phenomenon

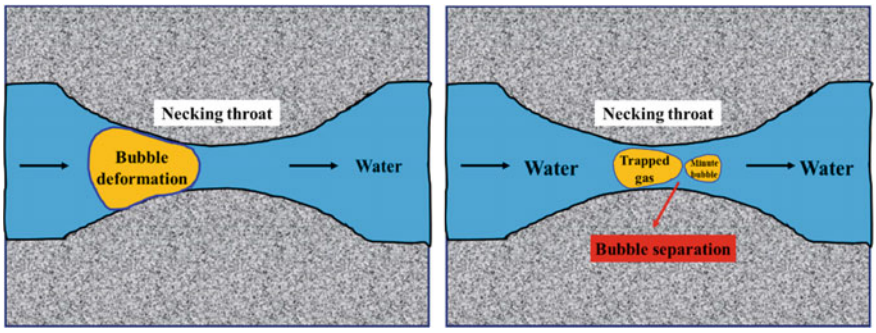

(a) Bubble deform at the necking throat (b) Separation and migration of minute bubble

Fig. 3.32 Schematic diagram of the formation mechanism of trapped gas caused by cutoff phenomenon

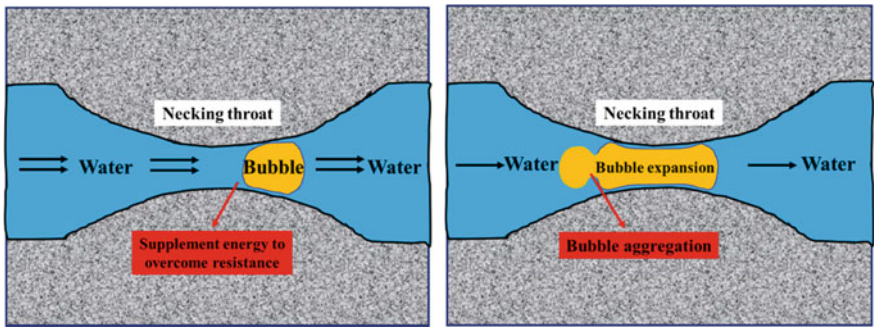

(a) Bubble energy is replenished (b) Expansion and aggregation of bubbles

Fig. 3.33 Schematic diagram of the recovery mechanism of trapped gas caused by cutoff phenomenon

can be explained from the following two aspects. On the one hand, the injected water preferentially advances along the two "sideways" of the H-shaped channel because of the capillary fingering phenomenon, thereby bypassing the "bridge" connecting the two "sideways" (Fig. 3.35a). On the other hand, when the injected gas breaks through the "sideways", the water in the "sideways" slowly enters the "bridge" of the H-shaped channel due to the hydrophilicity of the model, and gradually compresses the gas in the "bridge" to form trapped gas (Fig. 3.35b). The experimental results show that this type of trapped gas can be recovered in two ways. One is to expand the trapped gas in the "bridge" to the "sideways" by reducing the reservoir pressure, and then the expanded gas can be partially displaced by subsequent hydrodynamic forces (Fig. 3.36a). The other is to break the pressure balance between the two "sideways" by changing the displacement pressure differential. The trapped gas in the "bridge" enters the "sideway" where the pressure is relatively low, and is then displaced by

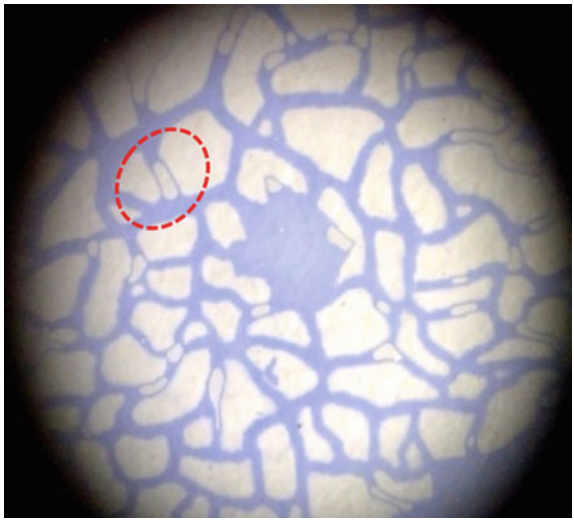

Fig. 3.34 Trapped gas formed at the H-shaped channel observed in the cavity type visual model

subsequent hydrodynamic forces (Fig. 3.36b). The trapped gas formed at H-shaped channels is a special form of the circumfluence phenomenon.

(5) Trapped gas formed at dumbbell-shaped channels

A unique trapped gas formed at dumbbell-shaped channels was observed in the fracture-cavity type visual model, as shown in Fig. 3.37. The formation mechanism of this type of trapped gas is as follows. When the injected water enters the cavity, it preferentially fills the cavity space and displaces the gas out along the fracture at the outlet. However, when there is only one fracture as the outlet channel of the two cavities at the same time, the two parts of gas are compressed at the fracture simultaneously to form trapped gas. Figure 3.38 shows the formation mechanism of trapped gas formed at the dumbbell-shaped channel. The experimental results show that this type of trapped gas is difficult to recover by changing the displacement

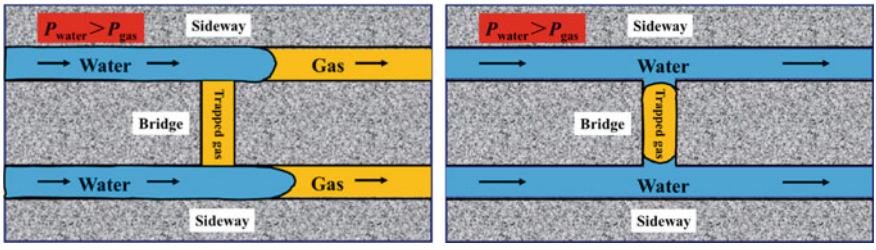

(a) Water bypasses the bridge (b) Water gradually enters the bridge

Fig. 3.35 Schematic diagram of the formation mechanism of trapped gas formed at H-shaped channels

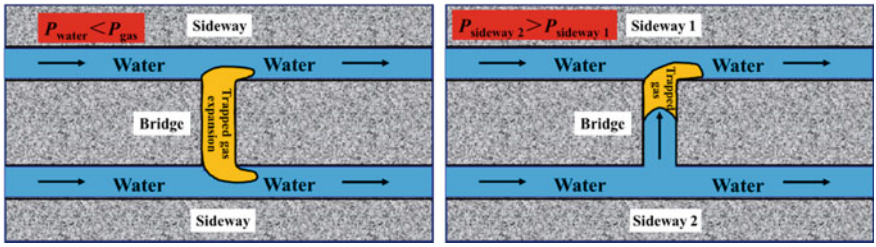

(a) Trapped gas is displaced after expansion (b) Pressure balance of trapped gas is broken

Fig. 3.36 Schematic diagram of the recovery mechanism of trapped gas formed at H-shaped channels

pressure differential because the water body energy in the cavities at both ends of the fracture is large.

(6) Trapped gas formed at the network of microfractures

Some trapped gas columns were observed in the microfracture of the fracture type and fracture-cavity type visual models, as shown in Fig. 3.39. The main reason for the formation of this type of trapped gas is that large fractures have extremely high flow conductivity but extremely low capillary resistance. Therefore, injected water preferentially breaks through the model rapidly along large fractures, and multiple microfracture regions separated by large fractures are blocked by water. As a result, the originally connected region is divided into a plurality of disconnected regions. The pressure system in each region is different, thereby forming some "dead gas regions" in the microfracture network (Cieslinski & Mosdorf, 2005). The experimental results show that this type of trapped gas can be recovered by reducing the reservoir pressure

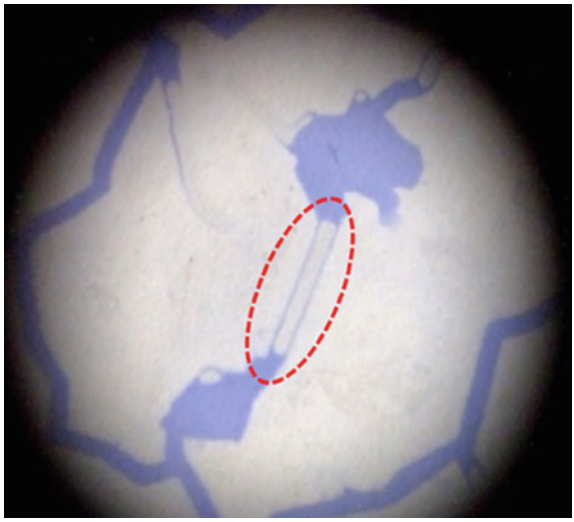

Fig. 3.37 Trapped gas formed at the dumbbell-shaped channel observed in the fracture-cavity type visual model

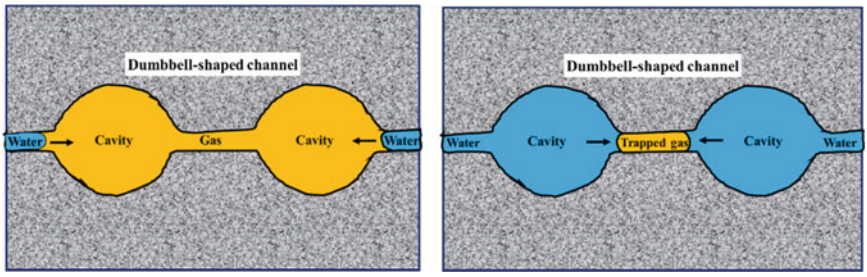

(a) Water enters dumbbell-shaped channel (b) Gas is compressed and trapped in the fracture

Fig. 3.38 Schematic diagram of the formation mechanism of trapped gas formed at dumbbell-shaped channels

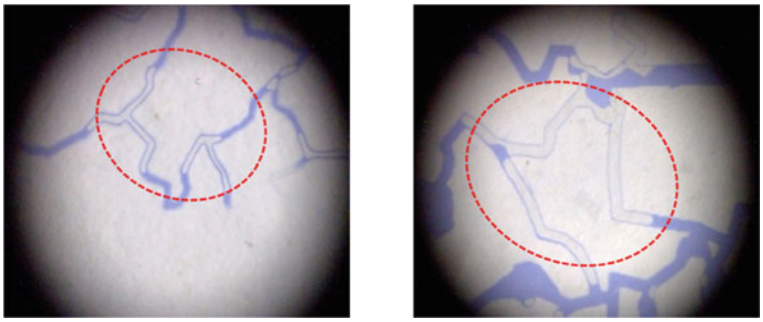

(a) Fracture type model (b) Fracture-cavity type model

Fig. 3.39 Trapped gas formed at the network of microfractures observed in the fracture type and fracture-cavity type visual models

to expand itself into dominant fractures, and then be displaced by the injected water (Fig. 3.40). In summary, the experimental results show that various types of trapped gas can be partially recovered by reducing reservoir pressure. Therefore, these types of trapped gas are dynamically changing during gas reservoir exploitation but cannot be fully recovered. The dominant influencing factors and formation mechanism of the six types of trapped gases are summarized in Table 3.8.

3.3.5 Quantitative Characterization of Different Types of Trapped Gas

The ImageJ gray analysis method was used to quantify the distribution characteristics of different types of trapped gas in the three types of visual models by counting the total number of pixels of each type of trapped gas. It can be seen from Fig. 3.41 that

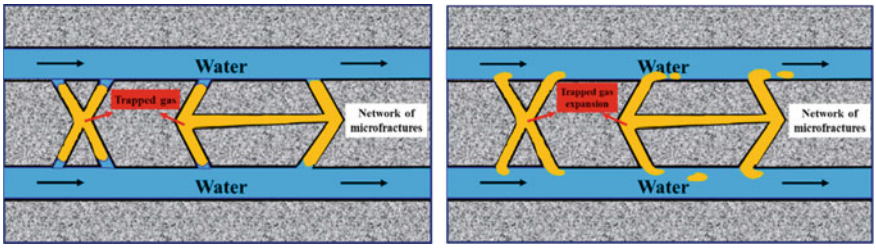

(a) Trapped gas formed at microfracture network (b) Trapped gas is displaced after expansion

Fig. 3.40 Schematic diagram of the recovery mechanism of trapped gas formed at the network of microfractures

the distribution characteristics of various types of trapped gas in different types of visual models are different. The trapped gas in the cavity type model is mainly formed by the phenomena of circumfluence and cutoff because of the complex pore throat structure and strong capillary force of the reservoir. The trapped gas formed at the H-shaped channel, as the unique type observed in cavity type and pore type reservoirs, only accounts for 8.37%. In contrast, most of the trapped gas in the fracture type and fracture-cavity type visual models is formed at the network of microfractures, dead ends and blind corners. The trapped gas formed at the dumbbell-shaped channel, as the unique type observed in fracture-cavity type reservoirs, only accounts for 7.58%. Therefore, it is particularly important to recover the trapped gas formed by the circumfluence and cutoff phenomena to improve the gas recovery factor of the cavity type and pore type reservoirs. Similarity, further recovery of the trapped gas formed at the network of microfractures, dead ends and blind corners is the key to improving the gas recovery factor of fracture type and fracture-cavity type reservoirs.

3.3.6 Quantitative Characterization of Saturation and Recovery Factor

The gas saturation dynamics of the three types of visual models at different water encroachment times obtained by the ImageJ gray analysis method is illustrated in Fig. 3.42. The high-permeability fractures in the fracture type model lead to a rapid drop in gas saturation at the initial stage of water encroachment (Fig. 3.42a). The replenishment of reservoir energy by external water bodies is the dominant reason for the high production in this stage, and the produced gas mainly comes from the dominant fractures and the large pores connected to fractures. However, the water rapidly advances along the dominant fractures and breaks through the model in a short period of time, leading to a small swept area and a short water-free gas recovery period. The experimental results after quantification show that the water-free recovery factor is only 51.3%. The decline rate of gas saturation in the fracture type model rapidly slows down after the water breaks through the model, and the ultimate

Table 3.8 Formation mechanism and influencing factors of different types of trapped gas

Trapped gas type	Dominant influence factor	Formation mechanism	Reservoir type
Trapped gas formed at dead ends and blind corners	Channel connectivity	No effective flow channels are formed at dead ends and blind corners	All types
Trapped gas formed by circumfluence phenomenon	Capillary force, hydrodynamic force	Water in small channels breaks through prior to large channels when capillary force is the dominant motive power Water in large channels breaks through prior to small channels when hydrodynamic force is the dominant motive force	All types
Trapped gas formed by cutoff phenomenon	Jamin effect	Additional capillary resistance at the necking throat due to the Jamin effect. Thick water film at the throat further aggravates the Jamin effect	All types
Trapped gas formed at H-shaped channels	Capillary force	Water preferentially breaks through the two "sideways" and bypasses the "bridge" given the capillary fingering phenomenon	Cavity type
Trapped gas formed at dumbbell-shaped channels	Channel connectivity	When the fracture serves as the outlet channel of the two cavities, the two parts of gas are compressed into the fracture simultaneously to form trapped gas	Fracture-cavity type
Trapped gas formed at the network of microfractures	Capillary force	Water preferentially breaks through large fractures with extremely low capillary resistance, blocking the microfracture regions to form "dead gas regions"	Fracture type and fracture-cavity type

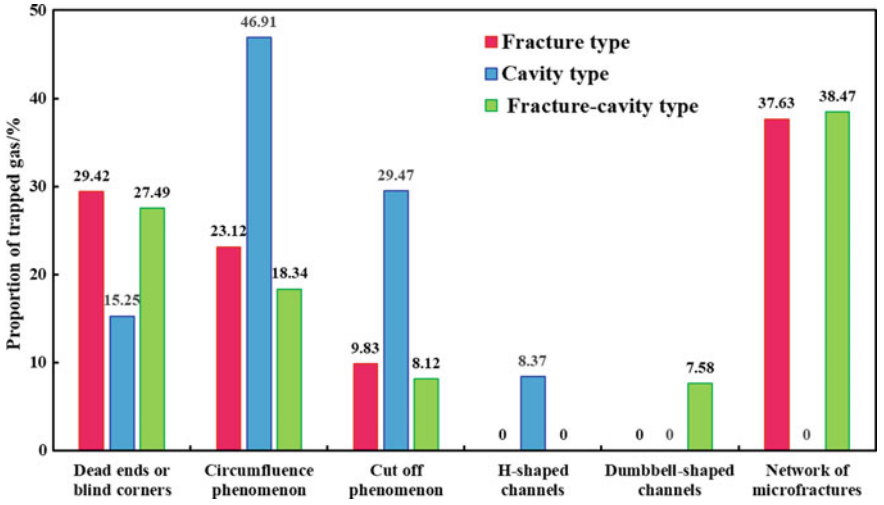

Fig. 3.41 The content proportion of different types of trapped gas in three types of visual models

gas recovery factor is only 63.5%. The natural gas in the low permeability area is blocked by fractures and large pores after water breakthrough, making it difficult to be recovered. Finally, a large amount of gas is trapped at dead ends, blind corners and microfracture network, and only 12.2% of the gas can be recovered during the long-term co-production of gas and water. Therefore, strictly controlling the production pressure differential of gas wells is the key to improving the recovery factor of fracture type reservoirs. A reasonable production pressure differential can not only reduce the water invasion intensity, prolong the water-free production period, but also improve the sweep efficiency. When the water breaks through the gas well, it is recommended to switch to the exploitation method of reducing the production pressure differential step by step. The trapped gas formed at dead ends, blind corners and microfracture network can partially enter the dominant flow channel after expansion, and then be displaced out under the action of subsequent hydrodynamic forces. It should be noted that well shut-in operation commonly used to restore reservoir pressure may completely trap the gas at these locations.

The flow channel of the cavity type model is narrow, and therefore the percolation resistance is large. In addition, it was observed that scattered small-scale cavities mainly affect the intensity and characteristics of water encroachment locally. The overall advancement of the gas–water front in the cavity type model is similar to the uniform advancement of the pore type reservoir. Therefore, the cavity as the main storage space has little effect on the water encroachment of reservoirs without fractures. Figure 3.42b shows that the gas saturation decreases slowly, the water-free production period is long, and the water-free recovery factor is as high as 65.0%. The trapped gas formed after water breakthrough is mainly caused by circumfluence and cutoff phenomena, and the ultimate gas recovery factor is 68.4%. Although the water-free recovery factor of the cavity type model is 13.7% higher than that of

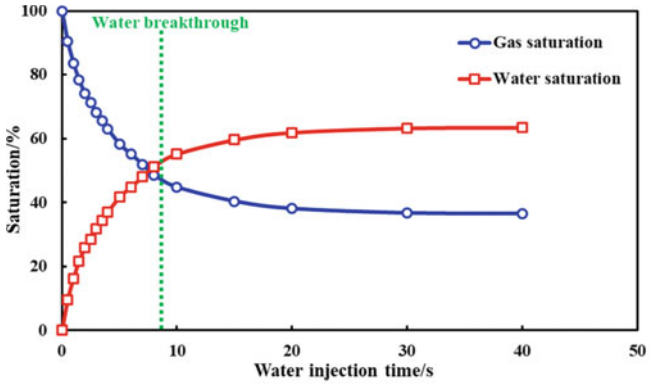

(a) Fracture type visual model

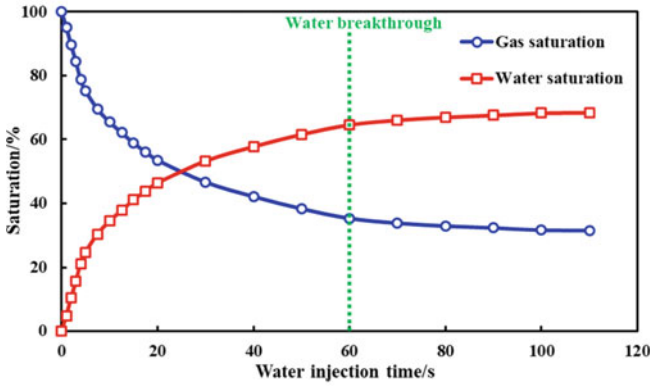

(b) Cavity type visual model

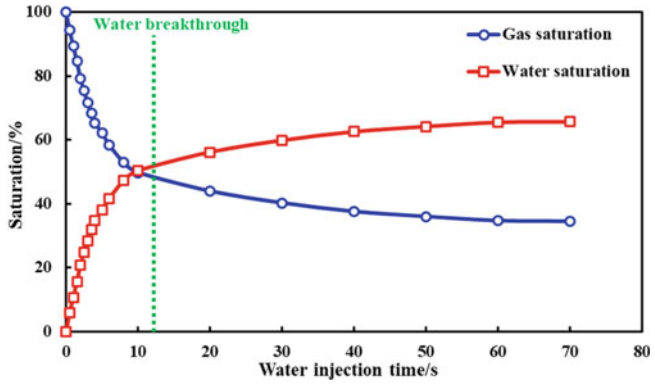

(c) Fracture-cavity type visual model

Fig. 3.42 Gas saturation of three types of visual models at different water encroachment times

the fracture type model, the ultimately recovery factor is only 4.9% different. This is because the trapped gas formed by the circumfluence and cutoff phenomena is difficult to be recovered after water breakthrough. Besides, although fracture type reservoirs can still recover a certain amount of natural gas after water breakthrough, it takes a long time and the production is extremely low. Most of the gas production after water breakthrough is obtained without economic benefits. Accordingly, the effective recovery factor of the fracture type model should be well below 63.5%, but slightly above 51.3%. The exploitation method of increasing the production pressure differential step by step is proposed for the cavity type reservoir to further improve the gas recovery factor. This method can not only use the capillary force to recover the gas in small channels when the pressure differential is low, but also can use the hydrodynamic force to displace the gas trapped in large channels caused by circumfluence phenomenon when the pressure differential is high.

It can be seen from Fig. 3.42c that the variation law of gas–water saturation of the fracture-cavity type model is similar to that of the fracture type model. Furthermore, the type of trapped gas and its recovery method are also the same as those of the fracture type model. However, the large amount of gas stored in the cavity can slow down the encroachment rate of water in the connected fractures, thereby prolonging the water-free production period. Therefore, the water-free recovery factor and ultimate recovery factor of the fracture-cavity type model are 52.1% and 65.6%, respectively, which are both slightly higher than those of the fracture type model.

The ultimate recovery factors of the three types of models under different displacement pressure differentials are illustrated in Fig. 3.43. The comparison results show that the existence of fractures has a great influence on the variation law of recovery factor. The recovery factor of the cavity type model increases from 47.8 to 76.7% as the pressure differential increases from 0.1 to 0.3 MPa. However, the increase rate of recovery factor decreases gradually with the increase of pressure differential. In contrast, the recovery factor of the model with fractures increases first and then decreases with the increase of pressure differential. The recovery factor of the fracture type model increases from 71.2 to 84.4% as the pressure differential increases from 0.1 to 0.15 MPa, which is higher than that of the cavity type model. However, the recovery factor of the fracture type model decreases from 84.4 to 45.6% as the pressure differential continued to increase from 0.15 to 0.30 MPa, which is lower than that of the cavity type model. This is because the high displacement pressure differential will lead to sever water channeling in fractured reservoirs, and it also indicates the necessity of reasonably controlling the production pressure differential during gas reservoir exploitation. The recovery factor variation law of the fracture-cavity type model is similar to that of the fracture type model. However, the recovery factor of the fracture-cavity type model is slightly lower than that of the fracture type model when the pressure differential is lower than 0.2 MPa, indicating that the gas in cavities is difficult to be completely displaced under the low pressure differential. The recovery factor of the fracture-cavity type model is slightly higher than that of the fracture type model when the pressure differential is higher than 0.2 MPa, indicating that the cavity can weaken the water encroachment intensity and improve the sweep efficiency. It should be noted that the recovery factor of the three types of models

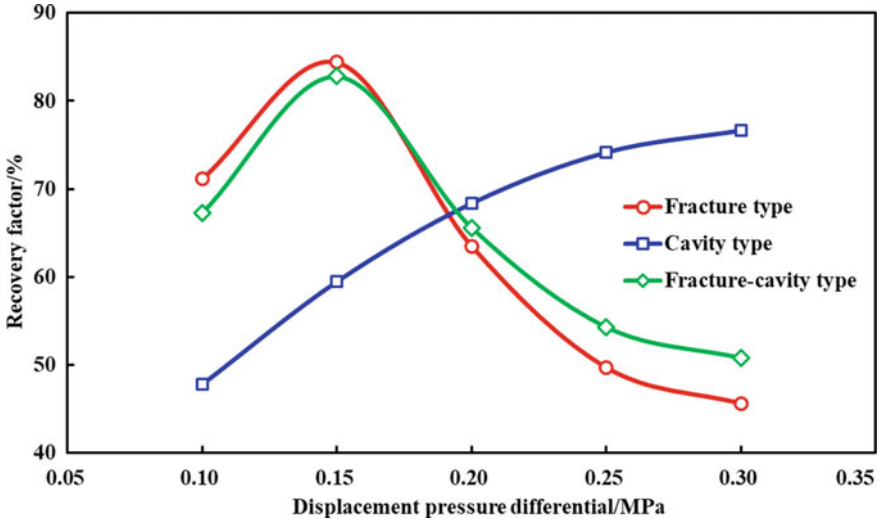

Fig. 3.43 Gas recovery factor of three types of visual models under different displacement pressure differentials

obtained by the microscopic visualization experiment is generally higher than that of the actual reservoir, because the pore structure of the two-dimension visual model is simpler than that of the three-dimensional reservoir. Nevertheless, the quantitative visualization experimental results still have reference value in the investigation of the dynamic laws of saturation and recovery factor.

3.4 Summary

In this chapter, CT scan images of different types of ultradeep carbonate gas reservoirs were selected as the microscopic pore structure patterns of the visual model, and then the fracture type, cavity type and fracture-cavity type visual models were fabricated by microelectronic lithography technique. These visual models enable accurate characterization of microscopic pore structures in ultradeep carbonate gas reservoirs, with excellent sealability and pressure resistance. Subsequently, a microscopic visualization experimental system was established, and the visualization experimental operation procedure was designed. The ImageJ gray analysis method was introduced to quantify the fluid saturation and recovery factor in visual images. Then, a series of gas flooding water visualization experiments were conducted to simulate the formation process and occurrence state of formation water in different types of carbonate reservoirs during hydrocarbon accumulation. The influence mechanism of different types of residual water on gas percolation in multiple media was analyzed. Finally,

a series of water flooding gas visualization experiments were conducted to simulate the water encroachment process and trapped gas formation process of different types of carbonate gas reservoirs. The formation mechanism, influencing factors and recovery methods of different types of trapped gas were analyzed. In addition, the saturation dynamics and recovery factors for the three types of models were also quantified. The important conclusions obtained are summarized as follows.

(1) The formation water of ultradeep carbonate gas reservoirs is composed of primary movable water and residual water. Primary movable water refers to the part of formation water displaced by natural gas in the process of hydrocarbon migration and accumulation. Residual water refers to various types of formation water retained in the reservoir because of insufficient hydrocarbon charging force, and can be subdivided into flowable secondary movable water and immobile irreducible water. There are four main occurrence modes of residual water, namely "water film", "water mass", "water column" and "water droplet". The four types of residual water occur in different locations of different types of reservoirs, and their formation mechanisms and effects on percolation mechanisms are also different. The dominant factors affecting the occurrence characteristics of residual water are capillary force, hydrocarbon charging force and flow channel connectivity.

(2) The residual water saturation decreases rapidly at low displacement pressure differentials. The formation water displaced in this stage is primary movable water, mainly from the fractures and large pores with low percolation resistance and the cavities with well connectivity. The residual water saturation decreases slowly as the displacement pressure differential continues to increase. The formation water displaced in this stage is secondary movable water, mainly from the small pores with strong percolation resistance, the water films on the walls of fractures and large pores, and water masses at the bottom of cavities. When the displacement pressure differential increases to a certain extent, the residual water saturation that no longer decreases is the irreducible water saturation. The irreducible water is mainly distributed in poorly connected blind corners and dead ends, narrow throats and flow channel walls.

(3) Water film is a type of residual water commonly found in hydrophilic reservoirs. The effective percolation channel narrows with the increase of the water film thickness, thereby affecting the gas-phase percolation characteristics and percolation capacity. The space occupied by the water film increases with the decrease of the flow channel size under the same displacement pressure differential. The proportion of the residual water film thickness in the flow channel starts to increase exponentially when the channel size decreases to a certain extent. In addition, the proportion of water film thickness in flow channels of different sizes decreases with the increase of displacement pressure differential. The smaller the size of the flow channel, the greater the decrease in the proportion of water film thickness. When the displacement pressure differential increases to a certain extent, the proportion of the water film thickness tends to be constant, and finally a "thin film" type of irreducible water is formed.

(4) The gas–water two-phase percolation characteristics and trapped gas formation mechanism in the three types of visual models are different during water encroachment because of the difference in pore structure. A total of six types of trapped gas were observed in the water flooding gas visualization experiments. The trapped gas of the cavity type model is mainly formed by the circumfluence and cutoff phenomena, whereas most of the trapped gas in the fracture type and fracture-cavity type visual models is formed at the microfracture network, dead ends and blind corners. Capillary force, hydrodynamic force, Jamin effect and pore throat connectivity are the main factors affecting the formation of various types of trapped gas. Some types of trapped gas can be partially recovered by increasing the displacement pressure differential or reducing the reservoir pressure.

(5) The gas saturation of the fracture type model decreases rapidly before water breakthrough, and decreases slowly for a long time after water beakthrough. Therefore, the water-free production period of fracture type reservoirs is short, and the water-free recovery factor and ultimate recovery factor are both low. The variation law of gas–water saturation of the fracture-cavity type model is similar to that of the fracture type model. However, the recovery factor of the fractured-cavity type is slightly higher than that of the fracture type because the cavity can weaken the intensity of water encroachment. The overall advancement of the gas–water front in the cavity type model is similar to the uniform advancement in the pore type reservoir. The gas saturation of the cavity type model decreases slowly, the water-free production period is long, and the water-free recovery factor and ultimate recovery factor are both high, but the exploitation period is long.

(6) Strictly controlling the production pressure differential of gas wells is the key to improving the recovery factor of fracture type and fracture-cavity type reservoirs. A reasonable production pressure differential can reduce the water encroachment intensity, prolong the water-free production period, and improve the sweep efficiency. When the water breaks through the gas well, it is recommended to switch to the exploitation method of reducing the production pressure differential step by step. The exploitation method of increasing the production pressure differential step by step is suitable for cavity type reservoirs. This method can not only use capillary force to recover the gas in small channels when the pressure differential is low, but also can use the hydrodynamic force to displace the gas trapped in large channels caused by circumfluence phenomenon when the pressure differential is high.

(7) The recovery factor of cavity type reservoirs increases with the increase of displacement pressure differential, but the increase rate gradually decreases. In contrast, the recovery factor of reservoirs with fractures increases first and then decreases with the increase of the pressure differential. Therefore, reasonable control of the production pressure differential is the key to improving the recovery factor of fractured reservoirs. Cavities have little effect on the water encroachment characteristics of reservoirs without fractures. Nevertheless, cavities can effectively weaken the water encroachment intensity of reservoirs with

fractures, and improve sweep efficiency and ultimate recovery factor. However, the recovery factor of the fracture-cavity type is slightly lower than that of the fracture type under the condition of low displacement pressure differential because the gas in the cavity is difficult to be displaced.

References

An, S., Yao, J., Yang, Y. F., Zhang, L., Zhao, J. L., et al. (2016). Influence of pore structure parameters on flow characteristics based on a digital rock and the pore network model. *Journal of Natural Gas Science and Engineering, 31*, 156–163.

Bai, B., Missouri-Rolla, U. O., Liu, Y., Coste, J. P., & Li, L. (2007). Preformed particle gel for conformance control: Transport mechanism through porous media. *SPE Reservoir Evaluation and Engineering, 10*, 176–184.

Bonnet, J., & Lenormand, R. (1977). Constructing micromodels for the study of multiphase flow in porous media. *Oil & Gas Science and Technology—Rev IFP, 42*, 477–480.

Buchgraber, M., Al-Dossary, M., Ross, C. M., & Kovscek, A. R. (2012). Creation of a dualporosity micromodel for pore-level visualization of multiphase flow. *Journal of Petroleum Science and Engineering, 86–87*, 27–38.

Chen, K. G., Wen, Y. N., He, T. H., Sun, W. M., Wang, C., et al. (2014). Irreducible water saturation models of tight sandstone gas reservoirs with low porosity and permeability and its application-taking a block of Shanxi Formation tight sandstone reservoir in Sulige gas field as an example. *Natural Gas Geoscience, 25*(2), 273–277.

Cieslinski, J. T., & Mosdorf, R. (2005). Gas bubble dynamics-experiment and fractal analysis. *International Journal of Heat and Mass Transfer, 48*, 1808–1818.

Dai, J. Y., Li, J. T., Wang, B. G., & Pan, R. (2012). Distribution regularity and formation mechanism of gas and water in the western area of Sulige gas field, NW China. *Petroleum Exploration and Development, 39*, 560–566.

Davis, J. A., & Jones, S. C. (1968). Displacement mechanism of micellar solutions. *Journal of Petroleum Technology, 20*, 1415–1428.

Doryani, H., Malayeri, M. R., & Riazi, M. (2016). Visualization of asphaltene precipitation and deposition in a uniformly patterned glass micromodel. *Fuel, 182*, 613–622.

Fang, F. F., Li, X. Z., Gao, S. S., Xue, H., Zhu, W. Q., et al. (2016). Visual simulation experimental study on water invasion rules of gas reservoir with edge and bottom water. *Natural Gas Geoscience, 27*(12), 2246–2252.

Geistlinger, H., & Mohammadian, S. (2015). Capillary trapping mechanism in strongly water wet systems: Comparison between experiment and percolation theory. *Advances in Water Resources, 79*, 35–50.

George, D. S., Hayat, O., & Kovscek, A. R. (2005). A microvisual study of solution-gas-drive mechanism in viscous oils. *Journal of Petroleum Science and Engineering, 46*, 101–119.

Han, X., Tan, X., Li, X., Pang, Y., & Zhang, L. (2022). Water invasion performance of complex fracture-vuggy gas reservoirs based on classification modeling. *Advances in Geo-Energy Research, 5*(2), 222–232.

Hatiboglu, C. U., & Babadagli, T. (2010). Experimental and visual analysis of Co- and countercurrent spontaneous imbibition for different viscosity ratios, interfacial tensions, and wettabilities. *Journal of Petroleum Science and Engineering, 70*, 214–228.

Hu, Y., Shao, Y., Lu, J. L., & Zhang, Y. F. (2011). Experimental study on occurrence models of water in pores and the influencing to the development of tight gas reservoir. *Natural Gas Geoscience, 22*(1), 176–181.

Li, M. C., & Li, J. (2011). "Dynamic trap": A main action of hydrocarbon charging to form accumulations in low permeability-tight reservoir. *Acta Petrolei Sinica, 31*, 718–722.

Li, G., Ren, W. X., Meng, Y. F., Wang, C. L., & Wei, N. (2014). Micro-flow kinetics research on water invasion in tight sandstone reservoirs. *Journal of Natural Gas Science and Engineering, 20*, 184–191.

Li, X. Z., Guo, Z. H., Wan, Y. J., Liu, X. H., Zhang, M. L., et al. (2017). Geological characteristics and development strategies for Cambrian Longwangmiao Formation gas reservoir in Anyue gas field, Sichuan Basin, SW China. *Petroleum Exploration and Development, 44*(3), 398–406.

Liu, H. X., Ren, D., Gao, S. S., Hu, Z. M., Ye, L. Y., et al. (2015). Water influx mechanism and development strategy of gas reservoirs with edge and bottom water. *Natural Gas Industry, 35*(2), 47–53.

Mahers, E. G., Wright, R. J., & Dawe, R. A. (1981). Visualization of the behavior of EOR reagents in displacements in porous media. *Experimental Techniques, 13*, 511–525.

Mattax, C. C., & Kyte, J. R. (1961). Ever see a waterflood? *Oil & Gas Journal, 59*, 115–128.

Mo, F., Du, Z. M., Peng, X. L., Tang, Y., & Sun, H. S. (2017). Pore-scale analysis of flow resistance in tight sandstones and its relationship with permeability jail. *Journal of Natural Gas Science and Engineering, 44*, 314–327.

Mohammadi, S., Ghazanfari, M. H., & Masihi, M. (2013a). A pore-level screening study on miscible/immiscible displacements in heterogeneous models. *Journal of Petroleum Science and Engineering, 110*, 40–54.

Mohammadi, S., Maghzi, A., Ghazanfari, M. H., Masihi, M., Mohebbi, A., et al. (2013b). On the control of glass micro-model characteristics developed by laser technology. *Energy Sources, Part A, 35*, 193–201.

Mosavat, N., & Torabi, F. (2016). Micro-optical analysis of carbonated water injection in irregular and heterogeneous pore geometry. *Fuel, 175*, 191–201.

Ren, D. M., Zhang, L. H., & Zhu, S. Q. (2003). Study on transportation numerical simulation of coalbed methane reservoir. *Journal of Hydrodynamics (Ser. B), 15*, 63–67.

Rezaee, M., Rostami, B., & Pourafshary, P. (2013). Heterogeneity effect on non-wetting phase trapping in strong water drive gas reservoirs. *Journal of Natural Gas Science and Engineering, 14*, 185–191.

Romero-Zeron, L. B., & Kantzas, A. (2007). The effect of wettability and pore geometry on foamed-gel-blockage performance. *SPE Reservoir Evaluation and Engineering, 10*, 150–163.

Rong, Y. S., Pu, W. F., Zhao, J. Z., Li, K. X., Li, X. H., et al. (2016). Experimental research of the tracer characteristic curves for fracture cave structures in a carbonate. *Journal of Natural Gas Science and Engineering, 31*, 417–427.

Sayegh, S. G., & Fisher, D. B. (2009). Enhanced oil recovery by CO_2 flooding in homogeneous and heterogeneous 2D micromodels. *Journal of Canadian Petroleum Technology, 48*(8), 30–36.

Schneider, M., Osselin, F., Andrews, B., Rezgui, F., & Tabeling, P. (2011). Wettability determination of core samples through visual rock and fluid imaging during fluid injection. *Journal of Petroleum Science and Engineering, 78*, 476–485.

Smith, J. D., Chatzis, I., & Ioannidis, M. A. (2005). A new technique to measure the breakthrough capillary pressure. *Journal of Canadian Petroleum Technology, 44*, 25–31.

Sohrabi, M., Kechut, N. I., Riazi, M., Jamiolahmady, M., Ireland, S., et al. (2012). Coreflooding studies to investigate the potential of carbonated water injection as an injection strategy for improved oil recovery and CO_2 storage. *Transport in Porous Media, 91*, 101–121.

Su, X. B., Wang, Q., Song, J. X., Chen, P. H., Yao, S., et al. (2017). Experimental study of water blocking damage on coal. *Journal of Petroleum Science and Engineering, 156*, 654–661.

Suekane, T., Zhou, N., Hosokawa, T., & Matsumoto, T. (2010). Direct observation of trapped gas bubbles by capillarity in sandy porous media. *Transport in Porous Media, 82*, 111–122.

Wan, J., Tokunaga, T. K., Tsang, C., & Bodvarsson, G. S. (1996). Improved glass micromodel methods for studies of flow and transport in fractured porous media. *Water Resources Research, 32*, 1955–1964.

Wang, X. M., Zhao, J. Z., & Liu, X. S. (2012). Occurrence state and production mechanism of formation water in tight sandstone reservoirs of Sulige area, Ordos Basin. *Petroleum Geology & Experiment, 34*, 400–405.

Wang, Y., Liu, H., Pang, Z., & Gao, M. (2016). Visualization study on plugging characteristics of temperature-resistant gel during steam flooding. *Energy & Fuels, 30*, 6968–6976.

Wang, L., Yang, S. L., Liu, Y. C., Xu, W., Deng, H., et al. (2017). Experimental investigation on gas supply capability of commingled production in a fracture-cavity carbonate gas reservoir. *Petroleum Exploration and Development, 44*(5), 824–833.

Wang, L., Yang, S. L., Peng, X., Deng, H., Meng, Z., et al. (2018a). An improved visual investigation on gas–water flow characteristics and trapped gas formation mechanism of fracture–cavity carbonate gas reservoir. *Journal of Natural Gas Science and Engineering, 49*, 213–226.

Wang, L., Yang, S. L., Peng, X., Liao, Y., Liu, Y. C., et al. (2018b). Visual investigation of the occurrence characteristics of multi-type formation water in a fracture–cavity carbonate gas reservoir. *Energies, 11*, 661.

Wang, L., He, Y. M., Wang, Q., Liu, M. M., Jin, X., et al. (2020). Multiphase flow characteristics and EOR mechanism of immiscible CO_2 water-alternating-gas injection after continuous CO_2 injection: A micro-scale visual investigation. *Fuel, 282*, 118689.

Wang, J., Dong, M., & Asghari, K. (2006). Effect of oil viscosity on heavy oilwater relative permeability curves. In: *15th SPE-DOE improved oil recovery symposium*, Tulsa, OK.

Wu, Z. B., Liu, H. Q., Pang, Z. X., Wu, Y. L., & Wang, X. (2016). A visual investigation of enhanced heavy oil recovery by foam flooding after hot water injection. *Journal of Petroleum Science and Engineering, 147*, 361–370.

Wu, Z. B., Wang, L., Xie, C. J., & Yang, W. B. (2019). Experimental investigation on improved heavy oil recovery by air assisted steam injection with 2D visualized models. *Fuel, 252*, 109–115.

Yun, W., & Kovscek, A. R. (2015). Microvisual investigation of polymer retention on the homogeneous pore network of a micromodel. *Journal of Petroleum Science and Engineering, 128*, 115–127.

Zhang, L. H., Feng, G. Q., Li, X. P., & Li, Y. (2005). Water breakthrough simulation in naturally fractured gas reservoirs with water drive. *Journal of Hydrodynamics (Ser. B), 17*, 466–472.

Zhao, J. Z., Cao, Q., Bai, Y. B., Er, C., Li, J., et al. (2016). Petroleum accumulation from continuous to discontinuous: Concept, classification and distribution. *Acta Petrolei Sinica, 37*, 145–159.

Zhu, R., Lou, Z. H., Niu, S. F., Ma, X. J., Jin, A. M., et al. (2008). Occurrence of formation water and measures for water control of Ordovician reservoirs in Tahe oilfield. *Journal of Zhejiang University (Engineering Science), 42*, 1843–1848.

Zhu, H. Y., Xu, X., Gao, Y., Hu, Y., An, L. Z., et al. (2014). Occurrence characteristics of tight sandstone pore water and its influence on gas seepage: A case study from the Denglouku gas reservoir in the Changling Gas Field, Southern Songliao Basin. *Natural Gas Industry, 34*, 54–58.

Zhu, H. Y., Xu, X., An, L. Z., Guo, C. M., & Xiao, J. R. (2016). An experimental on occurrence and mobility of pore water in tight gas reservoirs. *Acta Petrolei Sinica, 37*, 230–236.

Zou, C. N., Du, J. H., Xu, C. C., Wang, Z. C., Zhang, B. M., et al. (2014). Formation, distribution, resource potential, and discovery of Sinian-Cambrian giant gas field, Sichuan Basin, SW China. *Petroleum Exploration and Development, 41*, 306–325.

Chapter 4
Sensitivity Characteristics of the Ultradeep Carbonate Gas Reservoir

Reservoir sensitivity is a key factor that cannot be ignored in the development of oil and gas reservoirs, because it is directly related to formation damage and affects oil and gas production and recovery factor. Precipitation, swelling, or migration of clay particles occurs in the pore throats when the external fluid is incompatible with the reservoir minerals, thereby blocking pore throat channels and causing formation damage (Mcglade et al., 2013; Yang et al., 2008). Therefore, reservoir sensitivity is defined as the sensitivity degree of oil and gas reservoirs to various types of formation damage, including velocity sensitivity, water sensitivity, salinity sensitivity, alkali sensitivity and acid sensitivity (Bazin et al., 2010; Kang et al., 2014; Wang et al., 2018a, 2018b; Wu et al., 2017; Yuan & Wood, 2018). These five conventional sensitivities and stress sensitivity are the main factors causing formation damage during the exploration and exploitation. The degree of different reservoir sensitivities is usually obtained in laboratory by measuring changes in core permeability during different types of fluid injection experiments (Liao et al., 2012). Formation damage will inevitably lead to changes in reservoir pore structure and fluid percolation characteristics, thereby indirectly affecting the production capacity and recovery factor of oil and gas reservoirs. Systematic evaluation and analysis of reservoir sensitivity characteristics are the basis for revealing reservoir damage mechanism and influencing factors. Developing appropriate reservoir protection and damage prevention measures is the key to maintaining efficient development of oil and gas reservoirs (Ma et al., 2016). In recent years, many scholars have extensively conducted laboratory injection experiments of different types of reservoirs, summarized the sensitivity characteristics, and analyzed the dominant factors causing formation damage accordingly (Liu et al., 2020, 2021; Tan et al., 2021b; Tao et al., 2017; Wang et al., 2019; Zhao et al., 2019).

Formation damage is one of the main obstacles affecting the efficient development of ultradeep carbonate gas reservoirs (Tan et al., 2021b). The diversity of reservoir sensitivity characteristics caused by multiple media and strong heterogeneity increases the difficulty of sensitivity research (Rashid et al., 2017; Wang et al., 2020). At present, there is a lack of systematic and comprehensive understanding of the

© The Author(s), under exclusive license to Springer Nature Singapore Pte Ltd. 2023

L. Wang, *Ultradeep Carbonate Gas Reservoirs*,
https://doi.org/10.1007/978-981-19-9708-2_4

reservoir sensitivity characteristics and formation damage mechanism of ultradeep carbonate gas reservoirs, which hinders the effective implementation of formation damage prevention and treatment measures. Therefore, core samples from different types of ultradeep carbonate gas reservoirs in the Sichuan Basin were selected, and a series of injection experiments were conducted under different fluid flow rates, salinity, alkalinity and acidity. Subsequently, internal factors (pore structure characteristics, mineral composition and content) for different types of sensitivity characteristics, and external factors (pH, displacement pressure differential) that lead to changes in pore structure or original fluid state were revealed. In addition, the permeability and porosity stress sensitivity characteristics of different types of reservoirs were studied, and the relevant factors (reservoir type, initial petrophysical properties, temperature and pressure conditions) affecting the stress sensitivity characteristics of ultradeep carbonate gas reservoirs were analyzed. In contrast to other conventional reservoir sensitivities, the production capacity reduction caused by stress sensitivity is common and inevitable during gas reservoir exploitation. More importantly, the fractures and cavities of ultradeep carbonate rocks are more developed and heterogeneous than those of conventional clastic rocks. The research in this chapter reveals the sensitivity characteristics and damage mechanism of ultradeep carbonate gas reservoirs, and provides a theoretical basis for the design and implementation of gas reservoir acidification, stimulation, production allocation and gas recovery improvement operations.

4.1 Conventional Reservoir Sensitivity Characteristics

The reservoir may interact physically or chemically with external fluids such as drilling fluids, fracturing fluids, acidizing fluids, edge and bottom water during the drilling, production, hydraulic fracturing and workover stages of oil and gas reservoirs (Bennion, 2002; Xu et al., 2016; Zhang et al., 2020). The type and extent of this interaction depends on the sensitivity of the reservoir petrophysical properties to the flow rate, salinity, acidity and alkalinity of the external fluid. Therefore, conventional reservoir sensitivity is usually divided into velocity sensitivity, water sensitivity, salinity sensitivity, alkali sensitivity and acid sensitivity according to previous studies. The formation damage caused by sensitivity is the result of the combined action of its internal potential damage factors and external induced damage conditions. Potential damage factors mainly refer to the inherent properties of the reservoir, including lithology, pore structure, sensitive minerals and fluid properties. External induced conditions refer to various factors that cause changes in reservoir pore structure and petrophysical properties during various field operations. Different types of sensitive minerals in reservoir rocks are the basis and prerequisite for formation damage. Sensitive minerals are a class of minerals that are prone to physical or chemical reactions in contact with fluids, resulting in a decrease or increase in petrophysical properties. It can be observed by scanning electron microscopy (SEM) that sensitive minerals are mainly distributed in the pore surfaces or throat channels that

Table 4.1 Common sensitive minerals and their reservoir damage types

Sensitivity type		Sensitive mineral type	Formation damage type
Velocity sensitivity		Kaolinite, illite, microcrystalline quartz, microcrystalline muscovite, degraded illite and microcrystalline feldspar	Particle dispersion Particle migration
Acid sensitivity	HCl	Prochlorite, chamosite, chlorite-smectite, glauconite, hydrobiotite, ferrocalcite, ferrodolomite, hematite, pyrite and magnesioferrite	Chemical precipitation $Fe(OH)_3\downarrow$ $SiO_2\downarrow$ Particle migration
	HF	Calcite, dolomite, anorthite, zeolites and various clay minerals	Chemical precipitation $CaF_2\downarrow$ $SiO_2\downarrow$
Alkali sensitivity		Potassium feldspar, albite, microcrystalline quartz, chalcedony, plagioclase and various clay minerals	Silicate precipitation Silicone gel
Water sensitivity		Chlorite-smectite, illite–smectite, smectite, degraded illite, degraded chlorite and hydromuscovite	Lattice expansion Dispersion and migration
Salinity sensitivity		Gypsum, barite, pyrite, calcite, hematite, celestite, anhydrite, siderite, magnetite	Salt precipitation

are in preferential contact with external fluids. Common sensitive minerals can also be subdivided into acid-sensitive minerals, alkali-sensitive minerals, salt-sensitive minerals, water-sensitive minerals and velocity-sensitive minerals. Various types of sensitive minerals and their damage types to the reservoir are summarized in Table 4.1 (Zhang, 1993). It should be noted that the same mineral may have several different sensitivities, and formation damage is also the result of the combined effect of various sensitivities.

Investigation of formation damage caused by mineral sensitivities date back to the 1940s. Johnston and Beeson (1945) conducted water-sensitive damage experiments on a large number of core samples and demonstrated that the injection of low-salinity water can reduce the permeability of clay-bearing reservoirs. Then, Khilar and Fogler (1984) revealed the critical salinity of Berea sandstone sensitivity through a series of water injection experiments. Eleri and Ursin (1992) studied the physical and mechanical aspects of formation damage caused by particle migration at high fluid velocities. Ge et al. (2006) evaluated formation damage caused by alkali sensitivity during alkali/surfactant/polymer injection. Wang et al. (2019) revealed the damage mechanisms of water sensitivity and salinity sensitivity for a lignite reservoir based on the steady-state core flow method. At present, the fluid injection experiment is still a direct and effective method to study the reservoir sensitivity characteristics, which can reflect the damage degree of various sensitivities to reservoir permeability from a macro perspective. In addition, mercury intrusion

porosimetry (Kang et al., 2003), CT scanning (Wang et al., 2021), SEM (Rahman et al., 1995), X-ray diffraction (Amorim et al. 2007) or X-ray fluorescence (Elraies & Basbar, 2015), nuclear magnetic resonance (Guo et al., 2018; Zhang et al., 2019), and pressure-transmission tests (Zhang et al., 2020) are also commonly used to assist in the investigation of damage mechanism at the microscopic level. Therefore, the possible formation damage mechanism caused by carbonate reservoir minerals was briefly introduced based on previous studies. Then, the characteristics of five types of sensitivities of ultradeep carbonate gas reservoirs were studied based on the results of classical fluid injection experiments and reservoir characteristics analysis. In addition, some development suggestions and protective operations were proposed for the main sensitivity characteristics affecting ultradeep carbonate gas reservoirs.

4.1.1 Formation Damage Types and Mechanisms of Carbonate Reservoirs

Formation damage in conventional homogeneous reservoirs is mainly affected by sensitive minerals. In contrast, formation damage in carbonate reservoirs is not only related to mineral type and content, but also affected by multiscale pore structure characteristics. It is well known that mineral-induced formation damage manifests as fluid sensitivity and reservoir deformation, corresponding to five conventional sensitivities and stress sensitivity, respectively. Four common types of formation damage were summarized as follows based on previous studies.

(1) Dissolution and precipitation

Significant mineral dissolution occurs when certain minerals have high solubility in the external working fluid. For example, carbonate minerals are highly soluble in acidifying fluids. Mineral dissolution is a double-edged sword that changes the pore structure of reservoirs. It not only enlarges the original pores or forms secondary pores to improve porosity and permeability, but also releases some movable fine particles and loosens the rock matrix structure, thereby increasing the risk of formation damage and collapse. In contrast, particle precipitation mainly comes from the chemical reaction between minerals of calcium, iron and aluminum ions in the reservoir and certain components in the external working fluid, especially in reservoir acidizing operations. Acid-sensitive minerals such as dolomite are preferentially dissolved upon contact with acidifying solution and then converted into new precipitates. In addition, changes in reservoir pressure and temperature around the wellbore caused by fluid injection or hydrocarbon production can lead to changes in critical saturation conditions for high-salinity formation water. Consequently, part of the salt originally dissolved in the formation water is released to form a physical precipitation (Tang et al., 2015). The effect of particle precipitation on the pore throat structure is negative because it not only fills large pores but also blocks small throats. Previous

experimental results showed that the porosity and permeability of sandstone reservoirs decreased by 12.5% and 76.8% at 80 °C and 20 MPa respectively due to salt precipitation.

(2) Swelling and dispersion

Mineral swelling is one of the common formation damage mechanisms. Wilson et al. (2014) proposed that mineral swelling can reduce reservoir permeability and fracture conductivity to varying degrees, because swelling minerals may expand to several times their original volume under certain conditions, thereby significantly narrowing or even closing some percolation channels. The swelling mechanism of rock minerals comes from their strong sensitivity to water and salt, and the degree of swelling depends on the type and distribution of swelling minerals, as well as the salinity of fluid. The minimum salt concentration that causes significant mineral swelling is defined as the critical salt concentration, which decreases as the pH of the fluid increases. Therefore, acidic conditions can significantly inhibit the mineral swelling mechanism. Low salinity fluids not only cause mineral swelling, but also induce dispersion of some clay minerals (e.g. kaolinite and illite). The mechanism of mineral dispersion is that the electrostatic repulsion between the surfaces of mineral particles greatly exceeds the Van der Waals attraction. The magnitude of Van der Waals attraction is closely related to the salinity and pH of the fluid (Gupta et al., 2011). The lower the ion concentration, the higher the pH, the greater the repulsive force relative to the Van der Waals attraction, and the easier the minerals dispersion. Mineral dispersion can reduce pore size or even block throats to reduce reservoir permeability, and the degree of permeability reduction is proportional to the content of easily dispersible minerals. Although both mineral swelling and dispersion are caused by the sensitivity of the related minerals to water and salt, the mechanisms of formation damage are different. Therefore, the decrease in reservoir permeability caused by mineral swelling is reversible, whereas the formation damage caused by mineral dispersion is permanent.

(3) Detachment and migration

Mineral detachment from rock matrix could be induced by the high shear stress of the high-speed flowing fluid, as well as the dissolution of certain minerals tightly cementing the rock matrix and insoluble minerals, which is mainly controlled by mechanical stress acting on the particles (Bedrikovetsky et al., 2011). The probability of particle detachment is generally proportional to the difference between the current fluid flow velocity and the critical velocity (Bedrikovetsky et al., 2012). Once the particles are detached from the rock matrix, they migrate with fluid into percolation channels and potentially deposit in tortuous pores or block narrow throats. The fine particle migration of uncemented or weakly cemented minerals and strong brittle minerals is one of the important forms of formation damage. The effect of particle migration is controlled by various factors of reservoir wettability, pore throat size distribution, flow velocity and fluid properties. Typically, fine particles are more likely to migrate and become trapped in narrow throats at high pH and low salinity environments. The damage mechanisms of fine particle migration mainly include fine

surface deposition and/or attachment, bridging in pore throats (Yuan et al., 2016). Previous studies have demonstrated that formation damage caused by fine particle migration is particularly pronounced in reservoirs with high clay mineral content.

(4) Deformation and creep

The reservoir space is gradually closed as the effective stress increases. Mineral deformation usually occurs after the reservoir space is closed, resulting in reservoir stress sensitivity and variation in petrophysical properties (Xu et al., 2018a). Elastic deformation and plastic deformation are two forms of reservoir mineral deformation. Plastic deformation of minerals is an irreversible process that causes destructive deformation of minerals and permanent changes in reservoir petrophysical properties. In contrast, the elastic deformation of minerals is a reversible process and therefore the mineral morphology and reservoir properties can be restored to the initial state to a certain extent after stress unloading. The hardness of a mineral determines its ability to resist and recover from deformation. Clay minerals are the dominant deformation minerals after the reservoir space is closed because of their extremely high elastic deformation and low elastic modulus. Therefore, the clay mineral content in the reservoir can be used as one of the important parameters to judge the stress sensitivity degree of tight reservoirs. In addition, minerals such as salts and clays may exhibit creep behavior under long-term high effective stress because they are greatly affected by ambient temperature, stress and action time (Rahimi & Hosseini, 2015). The creep behavior is a plastic deformation process that not only results in loss of fracture conductivity, but also permanent damage to rock permeability. Previous studies have shown that long-term creep behavior further enhances formation damage from stress-sensitive effects.

In summary, fluid sensitivity is the dominant formation damage mechanism of various types of hydrocarbon reservoirs, and is mainly affected by the sensitive mineral composition and fluid properties (Zhao et al., 2019). Velocity sensitivity, water sensitivity, salinity sensitivity, alkali sensitivity and acid sensitivity caused by physical or chemical reactions between external fluids and reservoir minerals are all fluid sensitivity. Different types of storage spaces and percolation channels in ultradeep carbonate gas reservoirs lead to complex and diverse sensitivity characteristics. Five conventional sensitivity characteristics of ultradeep carbonate gas reservoirs were introduced by combining the results of classical fluid injection experiments and reservoir characteristics analysis. The classical fluid injection experiment process refers to the Industry Standard SY/T 5358-2010 of the P.R. of China. The damage degree of different types of fluids to the formation can be expressed by the relative variation ratio of permeability, which is calculated by Eq. (4.1).

$$D = \frac{K_0 - K_\mathrm{i}}{K_0} \times 100\% \tag{4.1}$$

where D is the relative variation ratio of permeability, mD; K_0 and K_i are the core permeability before and after the fluid injection experiment, respectively. The positive

and negative values of D represent the negative and positive effects of injected fluid on reservoir permeability, respectively.

4.1.2 Velocity Sensitivity Evaluation

Velocity sensitivity refers to the phenomenon that the detachment and migration of formation particles caused by the change of fluid velocity in the reservoir lead to the blocking of pore throats and fractures. Particle detachment and migration caused by velocity sensitivity may occur in various operation processes (e.g. drilling, completion, acidizing, test and production) because the injection velocity of the working fluid is significantly greater than the fluid migration velocity of hydrocarbon accumulation. Excessive flow velocity or pressure fluctuations can induce and promote particle detachment and migration.

The fracture-cavity type, cavity type and pore type core samples of the Deng IV Member gas reservoir were selected for velocity sensitivity experiments to compare the velocity sensitivity characteristics of different types of reservoirs. The temperature and pressure conditions required by the Industry Standard SY/T 5358-2010 are far lower than the reservoir conditions of ultradeep carbonate gas reservoirs. However, the effect of actual reservoir temperature and pressure conditions on the physical and chemical reactions caused by fluid sensitivity cannot be ignored. Therefore, the temperature, overburden pressure and pore pressure of the actual reservoir were simulated during the experiment. The prepared water samples were injected into the core sample at different injection velocities, and then the core permeability was measured at different flow velocities. The water samples were prepared according to the analysis of formation water components to avoid the influence of pH and salinity sensitivity on the experimental results.

The variation trend of dimensionless permeability of various carbonate cores with the increase of simulated formation water flow velocity is shown in Fig. 4.1. It should be noted that the sensitivity experimental results of each type of reservoir are obtained by averaging the experimental data of multiple core samples. The final permeability loss rates of fracture-cavity type, cavity type and pore type samples caused by velocity sensitivity are 2.55%, 14.81% and 21.84%, respectively. The velocity sensitivity of pore type reservoirs is relatively strong because of small pore throat size and poor connectivity. The velocity sensitivity of cavity type reservoirs is relatively weak because the pore throat size is larger than that of pore type reservoirs. Moreover, the large storage space of the cavity can capture a certain amount of free fine particles, thereby reducing the blockage of the flow channel by fine particles. However, large pores and cavities can also be blocked by bridging or accumulation when the number of particles is high. The reason for the increased permeability loss in the cavity type sample at high flow velocities is the generation of more movable particles at high impact forces. In contrast, the effect of velocity sensitivity on fracture-cavity type reservoirs is extremely weak, because the developed fractures increase the percolation channel size and improve the reservoir space connectivity. The permeability of the

fracture-cavity type sample was even improved at low flow velocities because the original free fine particles were carried out of the core by the injected fluid. Large percolation channel size increases the difficulty of blocking pore throats by fine particle, and the high pore throat coordination number weakens the effect of partial percolation channel blockage on the overall percolation capacity. Table 4.2 shows the evaluation standard for the degree of velocity sensitivity. Therefore, the velocity sensitivity of various types of reservoirs in the Deng IV Member is weak or none, reflecting that the formation damage caused by the high injection velocity of working fluid or the high production rate of natural gas is not significant.

Formation particles mainly come from the following sources: (1) original free mineral particles and easily movable clay particles in the reservoir; (2) detached particles caused by the impact force of fast fluid flow in the percolation channel; (3) movable particles formed by the physical or chemical reaction of clay minerals and water in the reservoir. Therefore, the velocity sensitivity is related to the clay mineral content and the consolidation degree in addition to the external fluid properties. Previous studies have also confirmed that some minerals such as booklet kaolinite, hair-like illite, microcrystalline quartz and muscovite, are easily detached and migrated under high shear rates of fluid flow (Tan et al., 2021b). Among them,

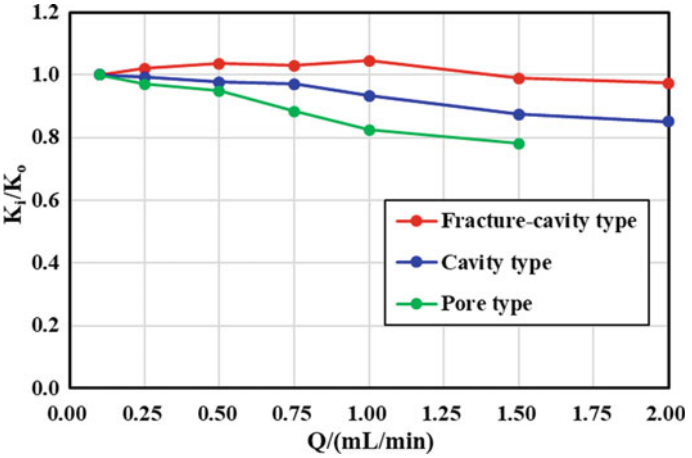

Fig. 4.1 Velocity sensitivity characteristics of different types of ultradeep carbonate gas reservoirs

Table 4.2 Evaluation standard for velocity sensitivity (SY/T 5358-2010)

Permeability loss rate/%	Velocity-sensitive degree
$D \leq 5$	None
$5 < D \leq 30$	Weak
$30 < D \leq 50$	Moderately weak
$50 < D \leq 70$	Moderately strong
$D > 70$	Strong

booklet kaolinite is considered to be the most velocity-sensitive mineral, which is one of the important reasons for fine particle migration during fluid flow (Wilson et al., 2014). According to the mineral composition and pore structure characteristics of the ultradeep carbonate gas reservoirs in the Deng IV Member, although clay minerals were found in all samples, the content percentage is low, only ranging from 1.07% to 3.94%, with an average of 1.43%. Additionally, carbonate reservoir rocks have good consolidation and cementation. Therefore, there are few original free particles in the reservoirs, and the reservoir rock can withstand the strong impact force from the high-velocity fluid. These are the two main reasons for the weak velocity sensitivity of ultradeep carbonate gas reservoirs.

The determination of velocity sensitivity characteristics of gas reservoirs has the following three purposes: (1) evaluate the velocity sensitivity degree of the study area, and calculate the critical flow velocity that causes significant reservoir damage; (2) determine a reasonable fluid injection velocity for subsequent other sensitivity experiments; (3) predict the critical gas production velocity and working fluid injection velocity free from velocity-sensitive damage. The maximum flow velocity corresponding to the permeability loss rate of 20% is usually taken as the critical flow velocity, and 80% of the critical flow velocity is usually used as the injection velocity for other sensitivity experiments. However, the permeability loss rate of both fracture-cavity type and cavity type samples in the Deng IV Member gas reservoir is lower than 20%, and the critical flow velocity can only be determined according to the velocity sensitivity of pore type samples. The calculated critical flow velocity of pore type samples is approximately 1.25 mL/min, which is also the fluid injection velocity for other sensitivity experiments. There is no need to deliberately limit the injection and production velocities of actual gas wells because most of the production wells in ultradeep carbonate gas reservoirs are deployed in fracture-cavity type and cavity type reservoirs.

4.1.3 Water Sensitivity Evaluation

Water sensitivity refers to the phenomenon that clay minerals swell, disperse, detach and migrate after the external low-salinity fluid enters the reservoir, which narrows or even blocks the percolation channel, thereby reducing the reservoir petrophysical properties. Different clay minerals have different swelling properties. Dissolution and swelling properties of common clay minerals are illustrated in Table 4.3. The swellability of clay mineral is mainly related to the capacity of cation exchange. The types and concentrations of cations in the aqueous solution are different, and therefore the capacity of cation exchange, as well as the degree of swelling, dispersion and permeability reduction caused by exchange are also different.

There are two main mechanisms by which water sensitivity causes reservoir damage. One is that swelling clay minerals such as smectite swell to several times their original size when they come into contact with low-salinity fluids, thereby occupying more storage space and compressing percolation channels. The dispersion of

Table 4.3 Dissolution and swelling properties of common clay minerals in formation

Clay mineral type	Cation exchange capacity mg/100 g	Swelling capacity	Specific surface m^2/cm^3	Relative solubility	
				HCl	HF
Kaolinite	3–15	None	8.8	Low	Low
Illite	10–40	Extremely Weak	39.6	Low	Moderately low
Smectite	76–150	Strong	34.9	Low	Moderate
Chlorite	0–40	Weak	14	High	High
Illite/smectite	/	Moderately strong	34.9–39.6	Varying	Varying

tiny particles occurs when the additional pressure caused by clay minerals swelling increases to a certain extent. The other is that non-swelling clay minerals such as kaolinite can be transformed into particles for dispersion and migration due to the abrupt change in ion concentration when they come into contact with low-salinity fluids. Therefore, the purpose of water sensitivity experiments is to evaluate the degree of reservoir permeability loss caused by clay swelling or particle migration.

The evaluation method of the water sensitivity experiment consists of the following three steps: (1) measure the initial permeability of the sample by using the simulated formation water; (2) measure the intermediate permeability of the sample at the same fluid injection velocity by using an intermediate fluid with half the salinity of the formation water; (3) measure the sample permeability in the same way using distilled water. It should be noted that a total of 10–15 pore volume (PV) of intermediate fluid and distilled water needs to be injected into the sample, and at least 12 h are required for the low-salinity fluid to fully contact and react with rock minerals.

The variation trend of dimensionless permeability of various carbonate core samples with the increase of distilled water injection is shown in Fig. 4.2. The permeability of the sample decreases slowly as the injection volume of distilled water increases. The sample permeability basically no longer changes when the injection volume reaches a certain amount. It means that the water-sensitive reaction caused by a small amount of clay minerals in the carbonate core has been basically completed, and the time required for stabilization is related to the characteristics of clay minerals. The final permeability loss rates of fracture-cavity type, cavity type and pore type cores caused by water sensitivity are 4.45%, 10.43% and 15.58%, respectively. The formation damage caused by water sensitivity mainly includes percolation channel shrinkage cause by clay swelling and percolation channel blockage caused by particle detachment and migration. The smaller the percolation channel size, the worse the pore throat connectivity, and the more significant the effect of clay swelling on the percolation channel size and the effect of particle blockage on the pore throat connectivity. Therefore, the damage degree of water sensitivity to fracture-cavity type reservoirs is weaker than that of the other two types of reservoirs. Table 4.4

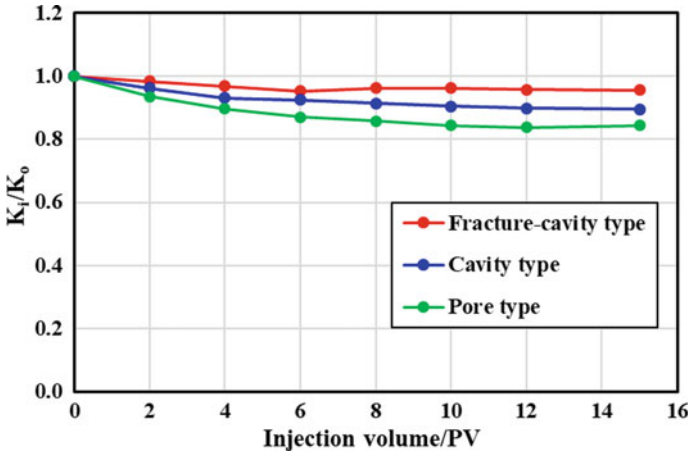

Fig. 4.2 Water sensitivity characteristics of different types of ultradeep carbonate gas reservoirs

Table 4.4 Evaluation standard for water and salinity sensitivity (SY/T 5358-2010)

Permeability loss rate/%	Water-sensitive degree
$D \leq 5$	None
$5 < D \leq 30$	Weak
$30 < D \leq 50$	Moderately weak
$50 < D \leq 70$	Moderately strong
$70 < D \leq 90$	Strong
$D > 90$	Extremely strong

shows the evaluation standard for the degree of water sensitivity. The water sensitivity of various reservoirs in the Deng IV Member gas reservoir is evaluated as weak or none, but weaker than the effect of velocity sensitivity. This is because the characteristics of water sensitivity are mainly related to the type, content and distribution of clay minerals. However, the content of clay minerals in the Deng IV Member gas reservoir is low and scattered. In addition, the relatively low content of smectite in clay minerals results in weak hydration swelling, while the relatively high content of kaolinite but good cementation results in weak particle dispersion and migration. Therefore, the formation damage of water sensitivity to ultradeep carbonate gas reservoirs can usually be ignored.

4.1.4 Salinity Sensitivity Evaluation

Salinity sensitivity refers to the phenomenon that a series of low-salinity external fluids enter the reservoir and then induce clay swelling, detachment, dispersion and

migration, thereby changing the pore structure and reducing the reservoir petrophysical properties. The fundamental reason for salinity sensitivity is that clay minerals in the reservoir are sensitive to the ion type and ion concentration of external water, and therefore the formation damage mechanism of salinity sensitivity is similar to that of water sensitivity (Gardner & Arias, 2000). For example, smectite swells when in contact with low-salinity fluids, and kaolinite disperses and migrates when ion concentrations are abruptly changed. Previous studies have shown that low-salinity fluids should be used with caution when selecting working fluids for moderate or strong water-sensitive reservoirs. However, there are also cases where working fluids with higher salinity than formation water lead to a decrease in reservoir permeability. This is because high-salinity fluids compress the diffused double electron layer thickness of clay particles, causing particle destabilization and detachment, increasing the risk of pore throat blockage. The purpose of the salinity sensitivity evaluation experiment is to reveal the variation law of reservoir permeability when exposed to fluids with different salinities, and to provide a theoretical basis for selecting working fluids with appropriate salinity.

The operation process of the salinity sensitivity experiment can be divided into two types of the salinity gradually increases and the salinity gradually decreases. The experimental process of increasing salinity is only applicable to salinity sensitivity experiments where the salinity of external fluids is higher than that of the formation fluids or has special requirements. However, the formation water salinity of the Deng IV Member gas reservoir is high, mostly between 50 and 100 g/L, which is generally higher than that of conventional working fluids. It should be noted that the cores used for the salinity sensitivity experiments were taken from several wells in the same area to ensure that the initial formation water salinity of these cores was similar. The initial fluid salinity of the salinity sensitivity experiment was set to 85 g/L, and the experiment process of gradually decreasing salinity was adopted. The initial permeability of the sample was measured by injecting a fluid with initial salinity. Then, fluid with salinities of 115, 100, 85, 70, 55, 40, 25, 10 and 0 g/L were injected to measure sample permeability. The measurement method of sample permeability under different salinity fluids can refer to the water sensitivity experiment. The purpose of setting the salinity of 100 and 115 g/L is to study the effect of injection of working fluid with higher salinity than that of formation water in special circumstances or encroachment of formation water with high salinity in other layers on reservoir permeability.

The variation trend of dimensionless permeability of various carbonate cores with the decrease of fluid salinity is shown in Fig. 4.3. The permeability of the three types of carbonate samples remains basically unchanged when the fluid salinity is higher than that of the formation water. This is because the clay minerals are well cemented with the rock framework and can resist the effect of a certain degree of high-salinity fluid on clay minerals. Conversely, the permeability of the three types of carbonate samples decreases first at a extremely slow rate and then at a relatively fast rate when the fluid salinity is lower than that of the formation water. This is because the clay swelling process could be divided into the hydration swelling of the outer surface caused by the surface hydration energy and of the inner surface caused by the repulsion of the

electric double layer. The hydration swelling of the outer surface means that water is adsorbed around the clay mineral particles under the osmotic effect to form a water film, which makes the clay mineral slightly swell. The hydration swelling of the inner surface becomes the dominant effect of clay swelling when the fluid salinity decreases below the critical salinity. The hydration swelling volume of the inner surface is far larger than that of the outer surface and therefore the magnitude of the decrease in permeability increases when the fluid salinity is below a certain value. It should be noted that the hydration swelling of the outer surface is reversible, whereas the hydration swelling of the inner surface is irreversible. The final permeability loss rates of fracture-cavity type, cavity type and pore type samples caused by salinity sensitivity are 6.55%, 11.97% and 15.46%, respectively. The experimental results of salinity sensitivity are similar to those of water sensitivity because the mechanism of formation damage caused by salinity sensitivity is the same as that of water sensitivity. The evaluation standard for the degree of salinity sensitivity are also the same as that for the degree of water sensitivity (Table 4.4). Therefore, the salinity sensitivity of ultradeep carbonate gas reservoirs is evaluated as weak, and the reason for the low degree of formation damage caused by salinity sensitivity is similar to that of water sensitivity. The fluid salinity corresponding to the reservoir permeability loss rate of 20% is generally regarded as the critical salinity of a reasonable working fluid. The critical salinity cannot be determined in ultradeep carbonate gas reservoirs, which means that the formation damage caused by salinity can be ignored when preparing working fluids.

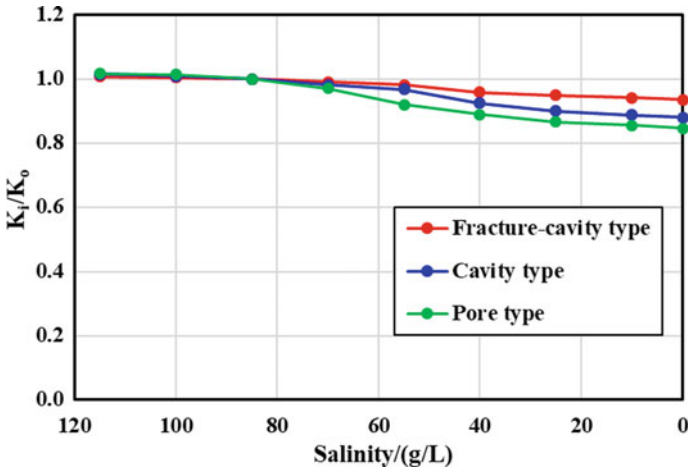

Fig. 4.3 Salinity sensitivity characteristics of different types of ultradeep carbonate gas reservoirs

4.1.5 Alkali Sensitivity Evaluation

Alkali sensitivity refers to the phenomenon that the alkaline external fluid enters the reservoir and then physically and chemically reacts with alkali-sensitive minerals to generate solid precipitation or colloidal substances, which leads to changes in pore structure and decrease in reservoir petrophysical properties. The pH value of the original formation fluid in the reservoir is generally distributed between 4 and 9. A pH value of the external working fluid higher than the initial pH value of the reservoir may result in a mismatch between the reservoir minerals and the fluid. The purpose of studying the reservoir alkali sensitivity is to determine whether the alkalin working fluids (e.g. drilling fluid, fracturing fluid) injected into the well causes damage to the reservoir and to evaluate the degree of alkali damage. The degree of reaction between the alkaline working fluid and the reservoir rock is much weaker than that between acidic working fluid and reservoir rock. Nevertheless, the formation damage caused by alkaline working fluid is considerable because of the long contact time with the reservoir rock.

The fracture-cavity type, cavity type and pore type cores of the Deng IV Member gas reservoir were selected for alkali sensitivity experiments to compare the alkali sensitivity characteristics of different types of reservoirs. The actual reservoir temperature, overburden pressure and pore pressure were simulated during the experiment. Previous studies have shown that the dissolved amounts of clay minerals in different types of alkaline solutions are in the order of NaOH > KOH > Na_2CO_3 > $NaHCO_3$. Among them, the reactions of CO_3^{2-} and HCO_{3-} with rock mineral are complex and affected by many factors. However, alkali sensitivity experiments are only used to study the effect of pH on reservoir permeability. Therefore, sodium hydroxide or potassium hydroxide is usually used to change the pH of the experimental fluid. In this experiment, sodium hydroxide was used to prepare alkaline solutions with pH values of 7.0, 8.5, 10.0, 11.5 and 13.0 for fluid injection experiments, and then the core permeability was measured at a fluid injection velocity of 1.25 mL/min. A total of 10–15 PV of alkaline solution need to be injected, and at least 12 h are required for the alkaline solution to fully contact and react with rock minerals. Finally, the permeability of the sample was measured by using the alkaline solution at this pH value.

The variation trend of dimensionless permeability of various carbonate core samples with the increase of pH value of alkaline solution is shown in Fig. 4.4. Core permeability decreases significantly as the pH of the injected fluid increases. The final permeability loss rates of fracture-cavity type, cavity type and pore type cores caused by alkali sensitivity are 25.07%, 32.55% and 38.82%, respectively. The formation damage caused by alkali sensitivity is mainly precipitation and blockage, supplemented by hydration swelling. The smaller the percolation channel size, the worse the pore throat connectivity, and the more significant the effect of precipitation on the percolation channel size and the effect of particles on the pore throat connectivity. Therefore, the damage degree of alkali sensitivity to fracture-cavity type reservoirs is weaker than that of the other two types of reservoirs. In addition, the small

amount of alkali scale and dispersed particles formed at relatively low pH value have little effect on fracture-cavity type and cavity type reservoirs, and the permeability of fracture-cavity type reservoir decreased significantly only at relatively high pH value. Table 4.5 shows the evaluation standard for the formation damage caused by alkali sensitivity. Therefore, the alkali sensitivity of fracture-cavity type reservoirs is evaluated as weak, whereas the cavity type and pore type reservoirs are evaluated as moderately weak. During drilling operations, it is necessary to always pay attention and adjust the pH value of the drilling fluid in time to reduce the formation damage caused by alkali sensitivity to ultradeep carbonate gas reservoirs. If the pH value corresponding to the permeability loss rate of 20% is taken as the critical pH value of the alkaline working fluid, then the pH value of the alkaline working fluid for fracture-cavity type, cavity type and pore type reservoirs should be controlled below 11.5, 10 and 9.5, respectively.

The mechanism of formation damage caused by alkali sensitivity has three aspects. (1) Clay minerals become easily hydrated and swellable sodium-type clays through ion exchange with alkaline fluids, thereby indirectly exacerbating the damage of water-sensitive swelling to reservoirs. (2) The high pH environment increases the repulsion of the electric double layer on the mineral surface, and some particles that

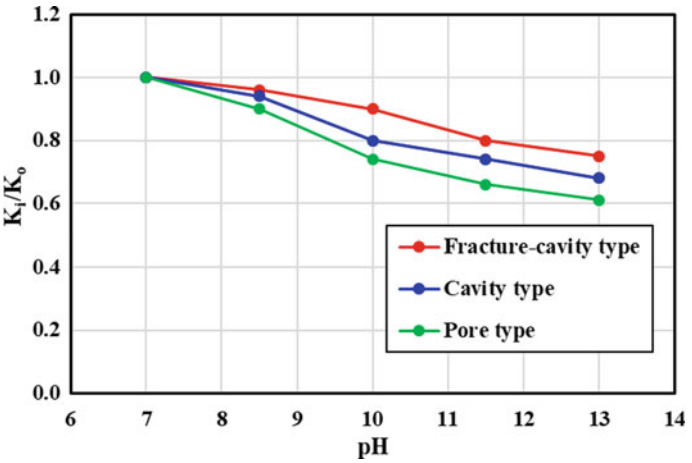

Fig. 4.4 Alkali sensitivity characteristics of different types of ultradeep carbonate gas reservoirs

Table 4.5 Evaluation standard for alkali sensitivity (SY/T 5358-2010)

Permeability loss rate/%	Alkali-sensitive degree
$D \leq 5$	None
$5 < D \leq 30$	Weak
$30 < D \leq 50$	Moderately weak
$50 < D \leq 70$	Moderately strong
$D > 70$	Strong

are not well cemented with the rock matrix migrate with the alkaline working fluid and then form blockages in some locations. (3) Alkaline fluid can have different degrees of chemical reactions with different reservoir minerals, and the reactivity is kaolinite, gypsum, smectite, illite, dolomite and zeolite in descending order. Feldspar, chlorite and quartz have moderate reactivity with alkaline fluids. The chemical reaction of alkalis with rock minerals not only results in the exchange of cations, but also the generation of new minerals or alkali scales. These new minerals and alkali scales are dispersed, migrated, precipitated and blocked in the reservoir with the alkaline fluid, thereby causing different degrees of damage to the reservoir. The minerals in the Deng IV Member ultradeep carbonate reservoirs are dominated by dolomite, followed by quartz and organic matter, and minor amounts of clay minerals and pyrite. Dolomite will generate precipitates of calcium carbonate and sodium hydroxide in an alkaline environment according to Eq. (4.2), but less reactive than clay minerals (Mohnot et al., 1987). In addition, quartz will also convert to water-soluble or water-insoluble silicates in alkaline environments with high pH according to Eqs. (4.3) and (4.4). Hydration swelling and particle dispersion contribute little to reservoir damage because the clay mineral content is extremely low. Therefore, these alkali scale and silicate precipitation are the dominant mechanism of alkali-sensitive formation damage to ultradeep carbonate gas reservoirs. However, the alkali sensitivity of ultradeep carbonate gas reservoirs is weak or moderately weak because of the reactivity of dolomite and quartz in an alkaline environment is not significant.

$$CaMg(CO_3)_2 + OH^- \rightarrow CaCO_3 \downarrow + Mg(OH)_2 \downarrow + CO_3^{2-} \tag{4.2}$$

$$SiO_2 + NaOH \rightarrow Na_2SiO_3 + H_2O \tag{4.3}$$

$$NaSiO_3 + Ca_2^+ \rightarrow CaSiO_3 \downarrow + Na^+ \tag{4.4}$$

4.1.6 Acid Sensitivity Evaluation

Reservoir acidification is one of the main operations to improve hydrocarbon production during the oil and gas reservoir exploitation. The purpose of acidification is to increase the permeability of the reservoir near the wellbore by dissolving certain minerals in the rock. However, a large amount of precipitation material may be generated at the same time as the dissolution of rock minerals. Reservoir permeability increases and hydrocarbon production are both improved when the amount of dissolved minerals in the acidification operation is greater than the amount of generated precipitation. Otherwise, acidification will cause irreversible damage to the reservoir.

Acid sensitivity refers to the phenomenon that the acid working fluid enters the reservoir and then physically and chemically reacts with acid-sensitive minerals and

formation fluid to generate precipitation and gel or release fine particles, resulting in changes in pore structure and reservoir petrophysical properties. The acid sensitivity characteristics is the comprehensive result of the interaction between acid and rock, acid and formation fluid, acid and reaction product, and reaction product and reaction product. There are two main forms of formation damage caused by acid sensitivity. One is the chemical precipitation or gel generated by the physical and chemical reactions between acid fluids and reservoir rock minerals. The other is the velocity sensitivity caused or exacerbated by the direct destruction of the original pore structure by the acid fluid. There are three potential factors leading to acid sensitivity of reservoirs. (1) The iron minerals in the reservoir are prone to form iron hydroxide precipitation, thereby blocking the percolation channel and reducing the acidification effect. (2) Fluoride ions in mud acid can react with calcium ions and magnesium ions to form insoluble calcium fluoride and magnesium fluoride, and quartz can also react with hydrofluoric acid to form fluorosilicate and hydrated silica gel. (3) The dispersion and migration of clay particles released by acidification can also reduce the acidification effect. The purpose of evaluating the acid sensitivity of the reservoir is to determine whether the acid fluid causes formation damage and the damage degree, and to provide a theoretical basis for the optimization of the acid fluid formulation and the development of acidification scheme. Different acid fluid formulations should be prepared or selected according to the mineral composition and fluid properties of the reservoir. Inappropriate formulations or unreasonable operations not only fail to improve reservoir permeability, but also cause reservoir damage and affect production capacity.

Sandstone reservoirs are generally acidified with mud acid (a mixture of 12 wt% HCl and 3 wt% HF), while carbonate reservoirs are usually acidified with hydrochloric acid or a mixture of hydrochloric acid and organic acids. Therefore, 15 wt% HCl solution was selected as the test fluid for acid sensitivity experiments of carbonate reservoirs. The core permeability prior to acid fluid treatment was first measured by simulated formation water. Subsequently, a total amount of 1.0–1.5 PV acid solution was reversely injected into the core, and the carbonate core needs to react with the acid solution for more than 30 min. Finally, simulated formation water was used again to measure the core permeability after acid fluid treatment.

The permeability comparison of three types of cores in ultradeep carbonate gas reservoirs before and after acid treatment is illustrated in Fig. 4.5. The sample permeability values under different injected PVs cannot be measured because of the small volume of injected acid fluid. The permeability of the three types of cores were improved to varying degrees after reacting with 15% hydrochloric acid for 30 min. The final permeability loss rates of fracture-cavity type, cavity type and pore type cores caused by acid sensitivity are −21.14%, −26.97% and −36.03%, respectively. The acid-sensitive minerals that react with hydrochloric acid in ultradeep carbonate gas reservoirs are mainly pyrite, silicoide and dolomite. Fe^{2+}, Mg^{2+} and Si^{4+} can be released from pyrite, dolomite and silicoide respectively under the acidic condition of hydrochloric acid. Fe^{2+} is greatly susceptible to be oxidized to Fe^{3+} (Tan et al., 2021b). The concentration of H^+ in solution decreases as the chemical reaction proceeds. When the pH value of the solution is higher than a certain value, the new

precipitation of $Fe(OH)_3$ and $Mg(OH)_2$ and the gel of SiO_4 will be generated, which will block the percolation channel. Nevertheless, the permeability of the three types of carbonate cores was finally improved, indicating that the improvement effect of hydrochloric acid on ultradeep carbonate gas reservoirs is significantly better than the damage effect. This is because the content of iron-bearing minerals and silicoide minerals in the Deng IV Member reservoir is low, and the reaction rate of dolomite with dilute hydrochloric acid is slow. The lower the initial reservoir permeability, the better the acidification improvement effect. Therefore, hydrochloric acid can be selected as the working fluid for acidification of various types of reservoirs in ultradeep carbonate gas reservoirs. Table 4.6 shows the evaluation standard for the formation damage caused by acid sensitivity.

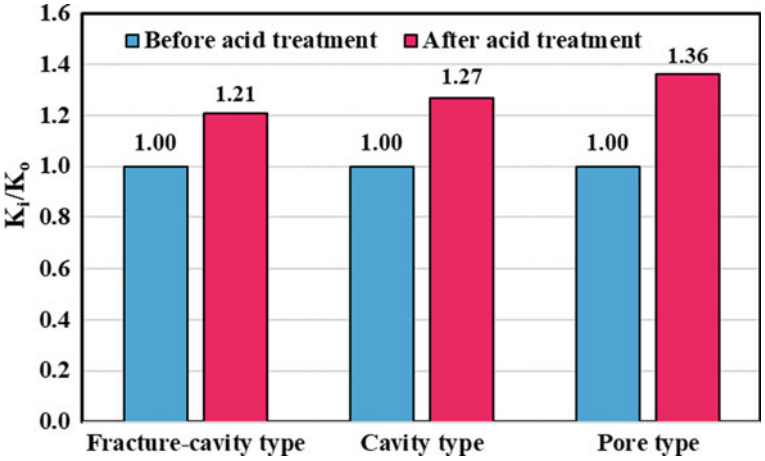

Fig. 4.5 Acid sensitivity characteristics of different types of ultradeep carbonate gas reservoirs

Table 4.6 Evaluation standard for acid sensitivity (SY/T 5358-2010)

Permeability loss rate/%	Acid-sensitive degree
$D \leq 5$	None
$5 < D \leq 30$	Weak
$30 < D \leq 50$	Moderately weak
$50 < D \leq 70$	Moderately strong
$D > 70$	Strong

4.1.7 Summary of Conventional Reservoir Sensitivity Characteristics

The sensitivity degrees of different types of reservoirs in ultradeep carbonate gas reservoirs obtained by evaluating the five sensitivities are summarized in Table 4.7. Fracture-cavity type reservoirs have no velocity sensitivity, water sensitivity and acid sensitivity, and only alkali sensitivity causes a slight decrease in reservoir permeability. The sensitivity characteristics of cavity type reservoirs and pore type reservoirs are consistent. Velocity sensitivity, water sensitivity, and salinity sensitivity all slightly reduce the permeability of the two types of reservoirs. In contrast, alkali sensitivity causes the most significant formation damage to ultradeep carbonate gas reservoirs, and is a sensitivity that requires high attention in various operation. The formation damage caused by acid sensitivity is less than the reservoir improvement caused by acidification, Therefore, HCl acidification can be used for plug removal and stimulation of ultradeep carbonate gas reservoirs.

4.2 Reservoir Stress Sensitivity Characteristics

The effective stress of the reservoir is the difference between the overburden pressure and the pore pressure in the reservoir space. Oil and gas reservoirs may experience multiple effective stress drops and rises during development. Reservoir pressure and effective stress decrease when external fluid replenishment cannot offset reservoir fluid production. Reservoir pressure and effective stress can be recovered during shut-in stage because of continued fluid replenishment from other connected areas. Reservoir sensitivity refers to the phenomenon that the mineral deformation and creep caused by changes in effective stress, resulting in the compression and release of pores and cavities, as well as the opening and closing of fractures and throats, thereby affecting the reservoir storage and percolation capacities. The stress sensitivity characteristics of reservoirs are the result of the interaction between rock mineral deformation and fluid percolation, reflecting the response of reservoir pore throat geometry and fracture wall morphology to effective stress variation (Ru et al., 2019). The deformation of rock minerals can be divided into elastic deformation

Table 4.7 Degrees of five sensitives of different types of ultradeep carbonate gas reservoirs

Sensitivity type	Pore type	Cavity type	Fracture-cavity type
Velocity sensitivity	Weak	Weak	None
Water sensitivity	Weak	Weak	None
Salinity sensitivity	Weak	Weak	Weak
Alkali sensitivity	Moderately weak	Moderately weak	Weak
Acid sensitivity	None	None	None

and plastic deformation. The decrease is permeability and porosity caused by elastic deformation is recoverable, while that caused by plastic deformation is permanent. Overall, formation damage caused by stress sensitivity is common but unavoidable in almost all oil and gas reservoirs. Clarifying the stress sensitivity behavior of reservoirs is of great significance to the development of hydrocarbon reservoirs (Tan et al., 2021a).

The purpose of the stress sensitivity experiment is to reveal the deformation process of the pore throat structure and fracture channel of the reservoir caused by the effective stress variation, evaluate the relationship between the degree of permeability and porosity loss and the effective stress, thereby providing a theoretical basis for the formulation of a reasonable production scheme. The stress sensitivity coefficient of permeability obtained from the experiment can not only be used to evaluate the degree of the reservoir stress sensitivity, but also an indispensable parameter in the reservoir numerical simulation and productivity prediction model. The stress sensitivity coefficient of porosity can be used to adjust the porosity value when estimating the residual reserves of the reservoir at different development stages. In addition, revealing reservoir stress sensitivity behavior can help control formation damage and leakage (Kang et al., 2015). These damages and leakages are essentially caused by deformation and closure of reservoir spaces and percolation channels (Zheng et al., 2015). The stress sensitivity of reservoirs was first proposed by Fatt and Davis (1952), and they found that rock permeability rapidly decreased by 11–41% with the increase of effective stress. Subsequently, scholars have conducted extensive investigations on the generation mechanism, formation damage degree and influencing factors of reservoir stress sensitivity through various techniques (Alam et al., 2014; Xiao et al., 2016). Xiao et al. (2016) developed binomial, exponential, power and logarithmic models to characterize the stress sensitivity characteristics of different types of reservoirs. Dou et al. (2016) indicated that there are several problems in the application of the current stress sensitivity testing methods, evaluation methods and judgement standards in tight reservoirs, and proposed revisions to the test standards from five aspects. Jia et al. (2017) measured permeability and porosity in stress sensitivity experiments by steady-state pulses and transient pulses, and concluded that permeability is affected by porosity and pore structure. Xu et al., (2018a, 2018b) indicated that the petrophysical properties of the reservoir rock change significantly when the effective stress increases, which successively affects the fluid production behavior of fractures and pore throats in the reservoir. Zhang et al. (2018) reveal the effects of pore throat and fracture structures, mineral types, and rock properties on the stress sensitivity of fractured tight reservoirs. The results of previous studies have shown that the stress sensitivity characteristics of different types of reservoirs are quite different. The main factors affecting reservoir stress sensitivity are summarized in Table 4.8. Sandstone gas reservoirs have relatively uniform stress sensitivity characteristics because of their relatively homogeneous reservoir. In contrast, ultradeep carbonate gas reservoirs have diverse stress-sensitivity characteristics because their heterogeneous reservoirs are classified into pore type, cavity type and fracture-cavity type according to the combination of reservoir media. Fractures and throats are the main percolation channels in ultradeep carbonate gas reservoirs, and their

closure and opening will directly affect the percolation capacity of fluids. Cavities and pores are the main storage spaces of ultradeep carbonate gas reservoirs, and their compression and release also affect the storage capacity of the reservoir to a certain extent. Furthermore, the extremely high temperature and pressure conditions and complex percolation mechanism of ultradeep carbonate gas reservoirs further increase the difficulty of studying the stress sensitivity characteristics. However, existing stress sensitivity studies mainly focus on sandstone reservoirs and conventional carbonate reservoirs. The reported stress sensitivity under high temperature and pressure conditions is usually inferred from the stress sensitivity experimental results under relatively low pressure conditions. The results obtained by this inference cannot truly reflect the stress sensitivity characteristics under actual ultradeep reservoir conditions. Therefore, it is of great significance to fully simulate the high temperature and pressure conditions of the reservoir to reveal the stress sensitivity characteristics of different types of ultradeep carbonate gas reservoirs.

In this section, an experimental method for measuring core sample stress sensitivity under high temperature and pressure conditions was developed, and corresponding improvement measures were also introduced. Subsequently, a series of stress sensitivity experiments were conducted on full-diameter and plunger core samples of different types of ultradeep carbonate reservoirs. Then, the permeability and porosity stress sensitivity characteristics of various types of reservoirs were evaluated according to the experimental results, and the formation damage degree and stress sensitivity mechanism of different types of reservoirs were also analyzed. Finally, the effects of temperature and pressure conditions, reservoir types and petrophysical properties on the stress sensitivity characteristics of ultradeep carbonate gas reservoirs were discussed.

Table 4.8 Main factors affecting reservoir stress sensitivity

Influencing factors	Effect of influencing factors
Reservoir permeability	The smaller the initial permeability, the smaller the percolation channel size, the worse the pore throat connectivity, and the stronger the stress sensitivity
Reservoir rock type	The greater the hardness of the rock particles, the stronger the compression resistance of the reservoir, and the weaker the stress sensitivity
Type and degree of cementation	The better the cementation between the rock particles, the stronger the stiffness of the reservoir, and the weaker the effect of stress sensitivity
Water saturation	The non-flowable liquid layer attached to the surface of the percolation channel exacerbate the effect of stress sensitivity on reservoir permeability. The higher the initial water saturation, the stronger the effect of stress sensitivity
Shale and impurity content	Shale and impurity particles are more prone to deformation and blockage than rock particles. The higher the shale and impurity content, the stronger the reservoir stress sensitivity

4.2.1 Experimental Samples and Conditions

Six full-diameter cores and a large number of plunger cores from the DengIV Member of Sinian System in the Sichuan Basin were selected for stress sensitivity experiments under conventional and reservoir conditions. These cores were divided into pore type, cavity type and fracture-cavity type according to the development of cavities and fractures. The end faces of these core samples were cut and polished using a diamond wire cutting machine. The petrophysical parameters of the full-diameter cores are shown in Table 4.9. These full-diameter cores were used to further study the stress sensitivity characteristics of different types of reservoirs under different temperature and pressure conditions because they can better reflect the reservoir heterogeneity of ultradeep carbonate gas reservoirs than plunger cores. However, the acquisition of full-diameter core samples is difficult and the experiment period is long, and therefore they cannot be used for large-scale stress sensitivity experiments. Therefore, a large number of plunger cores were also selected for experiments to investigate the influencing factors of stress sensitivity of ultradeep carbonate gas reservoirs.

The temperature and pressure of the stress sensitivity experiment were designed according to the ultra-high temperature and pressure conditions of the Deng IV Member reservoir. The experimental temperature is 150 °C, the confining pressure is 138 MPa, the initial pore pressure is 56 MPa, and the abandonment pressure is 10 MPa. Therefore, the initial effective stress and the maximum effective stress of the experiment is 82 MPa and 128 MPa, respectively. The experimental temperature, confining pressure and pore pressure of conventional conditions are 80 °C, 60 MPa and 35 MPa, respectively. The temperature and pressure of the conventional conditions were set to be half of the reservoir conditions because the confining pressure of 60 MPa is the highest pressure that can be achieved by conventional stress sensitivity experiments. High-purity nitrogen was used as the experimental gas to simulate natural gas because the use of natural gas for ultra-high temperature and pressure experiments can easily cause powerful combustion and explosions. The experimental

Table 4.9 Petrophysical parameters of full-diameter core samples used for stress sensitivity experiments

Core number	Core type	Length/mm	Diameter/mm	Permeability/mD	Porosity/%
DF4	Pore type	101.1	65.4	0.013	2.24
DF2	Pore type	105.1	69.3	0.108	3.69
DF10	Cavity type	81.3	66.8	0.074	4.96
DF5	Cavity type	100.5	6.94	0.121	6.09
DF3	Fracture-cavity type	73.9	66.3	0.606	6.19
DF7	Fracture-cavity type	103.4	69.2	0.713	6.21

Table 4.10 Chemical composition of formation water in Deng IV Member

Positive ions (mg/L)					Negative ions (mg/L)			Mineralization degree (mg/L)	Water type
K^+	Na^+	Ca^{2+}	Mg^{2+}	Ba^{2+}	HCO_3^-	Cl^-	$SO4_2^-$		
2596	34,527	1762	233	1467	716	63,596	119	106,241	$CaCl_2$

water was prepared in the laboratory based on the chemical composition of the formation water in the Deng IV Member, as shown in Table 4.10. It should be noted that the experimental water preparation was performed in the reactor rather than in the glass container. The temperature and pressure of the reactor should be maintained continuously after water sample preparation to prevent salt precipitation from water. The prepared experimental water sample was used to establish irreducible water saturation for different types of cores because the irreducible water film has different degrees of negative effects on the stress sensitivity of different types of reservoirs.

4.2.2 Experimental Apparatus

The stress sensitivity experiments of ultradeep carbonate gas reservoirs under formation conditions were conducted on the ultra-high temperature and pressure physical simulation experiment system. The experimental system can be divided into four subsystems, namely the injection system, the pressurization system, the core system and the data collection system (Fig. 4.6). The detailed introduction of the experimental system can be found in Chap. 2. Compared with the conventional experimental system, the newly developed experimental system has the following advantages in performing stress sensitivity experiments. (1) Previous studies have confirmed that pressure and temperature conditions are external conditions that affect the reservoir stress sensitivity characteristics. The new experimental system can fully simulate the high temperature and pressure conditions of ultradeep reservoirs. Therefore, the stress sensitivity characteristics obtained by laboratory experiments are closer to those of the actual reservoir. (2) The increase of reservoir effective stress is a continuous and slow process during the reservoir exploitation, while the effective stress of the sample changed many times in a short period of time during the stress sensitivity experiment. Abrupt changes in effective stress may cause more severe or even irreversible damage to the pore structure. The slow pressure drop process can be simulated by the constant-speed depressurization mode of the back-pressure pump in the new experimental system. The minimum pressure drop rate is 0.005 MPa/min. The pressure tracking mode of the syringe pump can keep the displacement pressure constant with the increase of the effective pressure. Therefore, the continuous and slow increase of the effective stress simulated by this stress sensitivity experiment is more consistent with the actual situation. (3) The effective stress needs to be adjusted many times during the stress sensitivity experiment, and therefore the permeability under different effective stresses needs to be measured at steady state. The

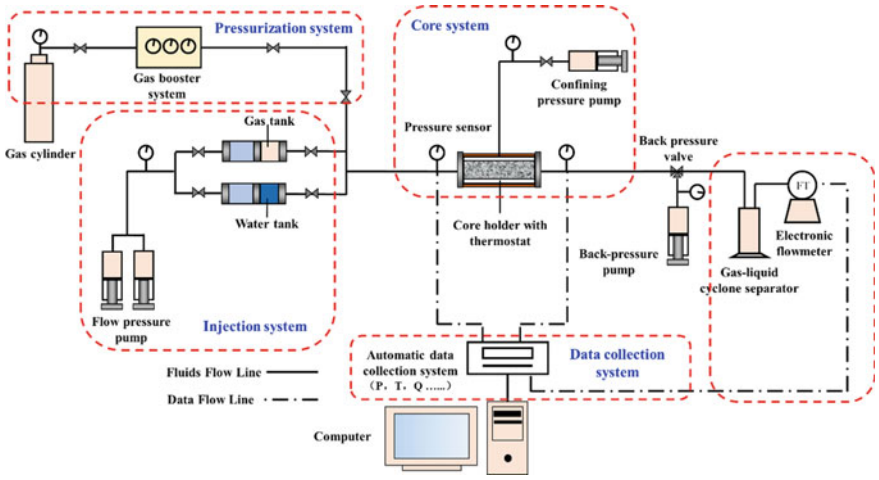

Fig. 4.6 Schematic diagram of ultra-high temperature and pressure physical simulation experiment system

data collection system can monitor the gas flow rate in real time and automatically calculate the instantaneous permeability of the core. Therefore, the instantaneous permeability that remains constant for a long time is the exact permeability under this effective stress. The experimental system can not only calculate permeability according to Darcy's law from the collected pressure and flow rate data, but also calculate porosity according to Boyle's law from pressure and volume data. Automatic data collection and calculation functions reduce personal errors and improve experimental efficiency.

4.2.3 Experimental Scheme

The goal of this study is to reveal the influence of the stress sensitivity characteristics of ultradeep carbonate gas reservoirs. In order to compare the stress sensitivity characteristics of different types of ultradeep carbonate reservoirs under conventional and reservoir conditions, the allocation of experimental samples is shown in Table 4.11. Then the effects of pore structure and experimental conditions on the stress sensitivity characteristics were analyze. In addition, a large number of plunger core samples were used to study the relationship between initial petrophysical properties and stress sensitivity. The permeability and porosity measurement of the stress sensitivity experiment takes the initial effective stress (82 MPa) as the starting point, and slowly reduces the flow pressure according to the designed effective stress values until it drops to the abandonment pressure (10 MPa). The permeability and porosity of full-diameter core samples at 8–10 effective stress points need to be measured to reveal the variation law of stress sensitivity. In contrast, it is only necessary to

Table 4.11 Experimental scheme of reservoir stress sensitivity

Core number	Core size	Core type	Reservoir type	Temperature and pressure condition	Petrophysical properties
DF4	Full-diameter core	Pore type	√	√	
DF2		Pore type	√		
DF10		Cavity type	√	√	
DF5		Cavity type	√		
DF3		Fracture-cavity type	√	√	
DF7		Fracture-cavity type	√		
/	Plunger core	Pore type Cavity type Fracture-cavity type	√		√

measure the porosity and permeability of the plunger core at the initial and final effective stress to obtain factors related to the stress sensitivity degree.

4.2.4 Experimental Method

There are two ways to change the effective stress in the stress sensitivity experiment, one is that the confining pressure is constant and the flow pressure is changed, and the other is that the flow pressure is constant and the confining pressure is changed. The first way can better reflect the actual decline process of reservoir pressure than the second way (Liu et al., 2014). The effective stress (σ_e) equation established by Terzaghi (Eq. (4.5)) was used to calculate the difference between the confining pressure (σ) around the core and the flow pressure (p_i) exerted at the core axis. The Terzaghi effective stress equation reflects the relationship between rock framework stress and reservoir pore pressure, describes the stress variation characteristics of tight reservoirs, and reveals the stress sensitivity degree to pressure variation (Dou et al., 2016). Core permeability under different effective stress was calculated by Darcy's law of gas phase (Eq. (4.6)). The length (L) and diameter (A) of the sample were measured with vernier calipers. Stabilized displacement pressure differential ($p_1 - p_2$) and fluid flow rate (Q) were obtain from the data collection system. The calculation formula of the permeability loss rate under different effective stress can be referred to Eq. (4.1). In addition, the fluid pressure is gradually increased after the effective stress reaches a maximum value to simulate the process of reservoir pressure recovery caused by well shut-in operation or external fluid replenishment. However, the petrophysical properties (e.g. permeability, porosity and pore size distribution) of the reservoir cannot be fully restored to their original state. The phenomenon

of irreversible formation damage caused by stress sensitivity is called the stress sensitivity hysteresis effect (Cao & Lei, 2019). The stress sensitivity hysteresis effect is particularly obvious in tight reservoirs and is the dominant reason for the permanent formation damage caused by the stress sensitivity. The irreversible permeability loss rate (D') can be used to reflect the degree of stress sensitivity hysteresis effect, and its calculation formula is Eq. (4.7). K_0 and K_0' represent the initial permeability and the permeability when the effective stress returns to the initial value, respectively. The permeability hysteresis effect is often used to judge the effectiveness of pressure recovery operations.

$$\sigma_e = \sigma - p_i \tag{4.5}$$

$$K_g = \frac{2Qp_0\mu L}{A(p_1^2 - p_2^2)} \tag{4.6}$$

$$D' = \frac{K_0 - K_0'}{K_0} \times 100\% \tag{4.7}$$

The stress sensitivity degree of tight reservoir is usually quantified by the stress sensitivity coefficient calculated by Eq. (4.8). This formula was first proposed by Jones (1975), and it expresses the relationship between permeability and effective stress of natural fractured reservoirs. The evaluation standard for the stress sensitivity based on the stress sensitivity coefficient are shown in Table 4.12.

$$S_s = \frac{1 - (K_i/K_0)^{1/3}}{\lg(\sigma_i/\sigma_0)} \tag{4.8}$$

where S_s is the stress sensitivity coefficient, dimensionless; σ_0 is the initial effective stress, MPa; σ_i is the effective stress at different test points, MPa; K_0 is the core permeability under initial effective stress, mD; K_i is the core permeability under different effective stress, mD.

Table 4.12 Stress sensitivity evaluation standard based on stress sensitivity coefficient

Stress sensitivity coefficient	Stress sensitivity degree
$S_S \leq 0.05$	None
$0.05 < S_S \leq 0.30$	Weak
$0.30 < S_S \leq 0.50$	Moderately weak
$0.50 < S_S \leq 0.70$	Moderately strong
$0.70 < S_S \leq 1.00$	Strong
$S_S > 1.00$	Extremely strong

4.2.5 Experimental Procedure

The detailed experimental procedure of the stress sensitivity experiment under ultra-high temperature and pressure conditions is as follows. (1) The gas in the intermediate container was pressurized to 50 MPa through the gas booster system, and then connected to the experimental system. (2) The experimental core was placed in the core holder after being cleaned and dried and saturated with irreducible water, and then the experimental system was connected according to Fig. 4.6. (3) The confining pressure of the core system was increased to 5 MPa by the confining pressure pump. (4) The temperature of the core system was increased to 150 °C through the electric heating jacket, and the confining pressure was automatically increased with the increase of the pore pressure during the heating process through the pressure tracking function during the heating process. (5) The valve of the intermediate container was slowly opened to allow the gas to enter the core system when the temperature stabilizes at 150 °C. The pore pressure of the core system was gradually increased to 50 MPa, and the confining pressure was also increased to 55 MPa with the increase of pore pressure. (6) The pore pressure and confining pressure were gradually increased to 56 and 138 MPa by the flow pressure pump and the confining pressure pump. The initial temperature and pressure conditions of the reservoir were finally established when the upstream and downstream pressures of the core system stabilized. This pressure and temperature increase process can effectively reduce the irreversible damage to the pore throat structure of the core sample caused by excessive initial effective stress and rapid increase of effective stress. (7) The upstream pressure was maintained at 56 MPa, and the downstream pressure was set at 54 MPa by the back-pressure pump. The sample permeability and porosity under the initial effective stress were calculated from the gas flow rate under a constant pressure differential. The reason for using the constant pressure mode to conduct the stress sensitivity experiment of the heterogeneous reservoir is to avoid excessive differences in the pressure gradients of samples with different permeability in the constant velocity mode. The reason for setting the displacement pressure differential to 2 MPa is to ensure that the gas flow in different core samples follows Darcy's law. (8) The effective stress of the sample was increased by simultaneously reducing the upstream and downstream pressures, and the stable permeability and porosity under different effective stresses were measured. The effective stress drop interval is 5 MPa, and the effective stress drop rate is 0.005 MPa/min. The effective stress loading process ended when the downstream pressure dropped below 10 MPa. (9) The effective stress of the sample was decreased by simultaneously increasing the upstream and downstream pressures, and the stable permeability and porosity under different effective stresses were measured again. The effective stress rise interval is 5 MPa, and the effective stress rise rate is 0.005 MPa/min. The effective stress unloading process ended when the downstream pressure returned to 54 MPa. (10) The stress sensitivity characteristic curve of the stress loading and unloading process was drawn by taking the effective stress as the abscissa and the dimensionless permeability under different effective stresses as the ordinate. The stress sensitivity experimental process under

conventional conditions can directly refer to the oil and gas industry standard SY/T 5358-2010 or related references.

4.2.6 Improvements in Stress Sensitive Experiments

Dou et al. (2016) proposed that the current stress sensitivity evaluation standard have some problems when applied to different types of tight reservoirs. Therefore, the stress sensitivity experimental method should be adjusted according to the reservoir characteristics. The improvements of the stress sensitivity experiments for ultradeep carbonate gas reservoirs are as follows.

(1) Ultradeep carbonate gas reservoirs have strong reservoir heterogeneity and diverse reservoir media. Therefore, full-diameter core samples of different types of reservoirs should be selected as far as possible for stress sensitivity experiments.
(2) There are a certain number of cavities and microfractures developed in ultradeep carbonate gas reservoirs. The pressure should be loaded and unloaded slowly when conducting stress sensitivity experiments to avoid the irreversible damage to the initial reservoir structure of samples caused by the rapid increase in effective stress.
(3) The temperature and pressure conditions of ultradeep carbonate gas reservoirs are extremely high, and the irreducible water saturation of different types of reservoirs varies greatly. Temperature, pressure, and irreducible water are all key factors that affect the stress sensitivity characteristics of reservoirs. Therefore, the temperature, pressure and water conditions of the actual reservoir should be completely simulated when performing stress sensitivity experiments.
(4) The initial formation pressure of ultradeep carbonate gas reservoirs is high, and therefore 8–10 permeability tests should be conducted under different effective stresses to obtain accurate and complete stress sensitive characteristics.
(5) The tightness of pore type and cavity type reservoirs in ultradeep carbonate gas reservoirs leads to a long flow rate stabilization time. Therefore, the stabilization time of 30 min required in the standard needs to be extended to 1–2 h. In addition, the displacement pressure differential of the stress sensitivity experiment should be set according to the Darcy flow stage obtained from the gas-phase percolation experiment to avoid errors caused by non-Darcy flow on the calculation results.

4.2.7 Permeability Stress Sensitivity of Different Types of Carbonate Reservoirs

(1) Fracture-cavity type sample

The permeability stress sensitivity experiment results of fracture-cavity type samples are illustrated in Fig. 4.7. The stress sensitivity characteristics and key parameters

of the two full-diameter core samples are similar. The permeability stress sensitivity characteristics of fracture-cavity type samples can be divided into three stages according to the relationship between dimensionless permeability and effective stress (Wang et al., 2018a, 2018b). The total permeability loss rate of the DF3 sample during the stress loading process is 67.58%, and the permeability loss rates of the three stages are 50.21%, 15.69% and 1.68%, respectively. The total permeability loss rate of the DF7 sample during the stress loading process is 66.74%, and the permeability loss rates of the three stages are 53.64%, 11.74% and 1.36%, respectively. The first stage is the rapid decline stage of permeability dominated by microfractures. Fractures are the dominant percolation channels in fracture-cavity type reservoirs, and they are preferentially closed when the effective stress gradually increases. The greater the effective stress, the more obvious the fracture closure and the greater the decrease in permeability. The permeability of the fracture-cavity type sample is close to that of the cavity type sample when the fractures are closed to a certain extent. The second stage is the slow decline stage of permeability dominated by cavities and macroscopic pore throats. The percolation capacity of the samples at this stage is mainly contributed by cavities and macroscopic pore throats. The relative change of pore throat radius has little effect on the absolute percolation capacity of macroscopic pore throats and cavities as the effective stress continues to increase (Gao et al., 2015). Therefore, the permeability loss rate of the second stage is far lower than that of the first stage. The third stage is the extremely slow decline stage of permeability dominated by rock minerals. The stress sensitivity of the third stage mainly comes from the mineral deformation and creep caused by the compression of the rock framework. Deformation and creep under extremely high effective stress generally exhibit the characteristics of plastic deformation. However, the main mineral components of ultradeep carbonate gas reservoirs are dolomite with high hardness, while the content of clay minerals is extremely low. Consequently, the permeability loss rate at this stage is extremely low and difficult to recover. The reason that the effective stress required for sample DF7 to enter the second stage is higher than that of sample DF3 may be that the fracture of sample DF7 is more developed. Therefore, the critical effective stress of different samples at each stage is not constant. The specific values of these effective stresses mainly depend on the properties of fractures, cavities and pore throats in the sample.

The recovery process of sample permeability during effective stress unloading process is also illustrated in Fig. 4.7. The sample permeability recovered slowly with the increase of effective stress, but the re-opening of partial fractures under low effective stress can rapidly increase the permeability recovery rate. The permeability of the two fracture-cavity type samples eventually recovered to only about 50% of the initial permeability. The irreversible loss rate of permeability under different effective stresses can be divided into two stages, as shown in Fig. 4.8. The irreversible loss rate of the first stage increases slowly and is generally less than 15%, reflecting that the compressed cavities and macroscopic pore throats could be greatly recovered during the stress unloading process. The irreversible loss rate in the second stage increases rapidly and is generally higher than 20%, reflecting that although the reopened fractures can increase the permeability recovery rate, the complete

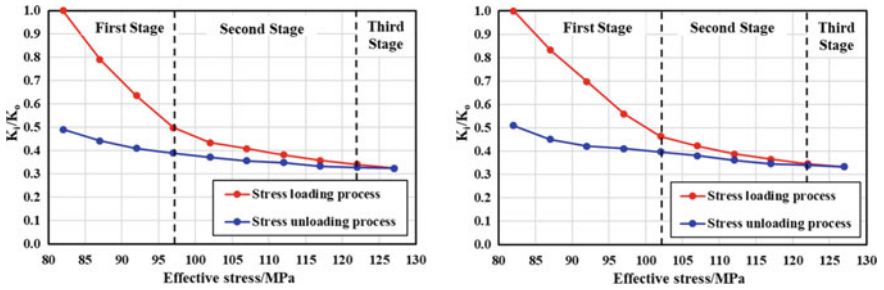

(a) Sample DF3 (b)Sample DF7

Fig. 4.7 Permeability stress sensitivity characteristic curves of fracture-cavity type samples under reservoir conditions

closure of most fractures greatly increases the irreversible permeability of fracture-cavity type samples. Therefore, fracture-cavity type reservoirs have excellent percolation capacity, but are not suitable for exploitation with high production pressure differential. This is because a high production pressure differential not only greatly reduces the permeability of the reservoir near the wellbore, but also permanently closes the fractures developed in the reservoir. The method of restoring reservoir pressure through shut-in operation to increase permeability is also less effective for fracture-cavity type reservoirs. In addition, amplifying the production pressure differential will also cause high-velocity non-Darcy flow of gas phase and intense water encroachment of edge and bottom water in fracture-cavity type reservoirs, which is not conducive to improve gas production and recovery factor.

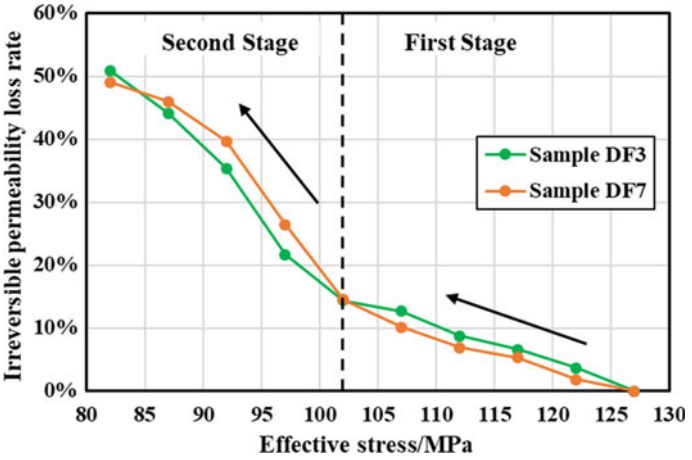

Fig. 4.8 Relationship between irreversible permeability loss rate and effective stress of fracture-cavity type samples

(2) Cavity type sample

The permeability stress sensitivity experiment results of cavity type samples are illustrated in Fig. 4.9. The stress sensitivity characteristics of the two full-diameter core samples are similar, but the key parameters are different. The permeability stress sensitivity characteristics of cavity type samples can be divided into two stages according to the relationship between dimensionless permeability and effective stress. The total permeability loss rate of DF5 sample during the stress loading process is 40.94%, and the permeability loss rates in the two stages are 37.83% and 3.11%. The total permeability loss rate of the DF10 sample during the stress loading process is 46.66%, and the permeability loss rates of the three stages are 42.05% and 4.61%. The first stage is a slow decline stage of permeability dominated by cavities and macroscopic pore throats. Bedding cavities and macroscopic pore throats are the dominant percolation channels in cavity type reservoirs, and they are preferentially compressed when the effective stress gradually increases. Cavities and macroscopic pore throats are difficult to be compressed with the increase of effective stress, and therefore the permeability decline rate is slowed down. The second stage begins when cavities and macroscopic pore throats cannot be compressed further. The second stage is the extremely slow decline stage of permeability dominated by rock minerals. The stress sensitivity of the second stage mainly comes from the mineral deformation and creep caused by the compression of the rock framework. In contrast, the effective stress corresponding to the compression of the rock framework of the cavity type reservoir is significantly lower than that of the fractured-cavity type reservoir. Moreover, the permeability loss rate of the cavity type samples caused by the rock framework compression is only slightly increased. This is because the ultra-deep carbonate reservoirs dominated by dolomite are highly resistant to compression. It is difficult to cause a significant drop in permeability at this stage unless the rock is fractured or broken. The reason why the permeability loss rate of sample DF10 is significantly higher than that of sample DF5 is that the initial permeability and porosity of the former are significantly lower than those of the latter. The relative changes in the radii of the relative large cavities and pore throats have relatively little effect on the absolute percolation capacity under the same effective stress.

The recovery process of sample permeability during effective stress unloading process is also illustrated in Fig. 4.9. Different form the permeability recovery curves of fracture-cavity type samples, the dimensionless permeability of the cavity type sample did not increase rapidly at low effective stress. The permeability of the two cavity type samples eventually recovered to about 70% of the initial permeability. The irreversible loss rate of permeability under different effective stresses can also be divided into two stages, as shown in Fig. 4.10. The irreversible loss rate of the first stage increases slowly and is generally less than 5%, reflecting that although the mineral deformation and creep caused by the rock framework compression belong to plastic deformation, it causes little irreversible permeability loss to the sample. The increase rate of irreversible permeability loss in the second stage is slightly increased, generally higher than 5%, reflecting that the compressed cavities and macroscopic pore throats can be greatly recovered during the stress unloading process. Therefore,

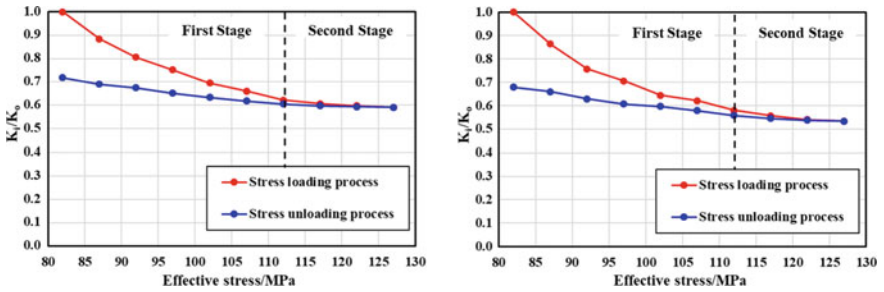

(a) Sample DF5 (b) Sample DF10

Fig. 4.9 Permeability stress sensitivity characteristic curves of cavity type samples under reservoir conditions

cavity type reservoir have strong storage capacity and weak stress sensitivity, and can be exploited under a relative high production pressure differential. Higher production pressure differentials can increase the gas production of cavity type reservoirs without causing a significant decrease in permeability. In addition, the method of restoring reservoir pressure through shut-in operation to increase permeability is also effective for cavity type reservoirs.

(3) Pore type sample

The permeability stress sensitivity experiment results of pore type samples are illustrated in Fig. 4.11. The stress sensitivity characteristics of the two full-diameter core samples are similar, but the key parameters are different. The permeability stress sensitivity characteristics of pore type samples can be divided into two stages

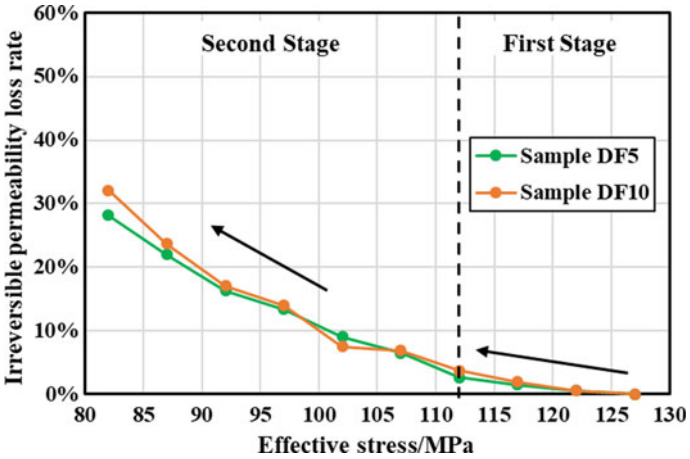

Fig. 4.10 Relationship between irreversible permeability loss rate and effective stress of cavity type samples

according to the relationship between dimensionless permeability and effective stress. The total permeability loss rate of the DF2 sample during the stress loading process is 60.72%, and the permeability loss rates of the two stages are 56.05% and 4.67%. The total permeability loss rate of the DF4 sample during the stress loading process is 64.25%, and the permeability loss rates of the three stages are 59.18% and 5.07%. The first stage is the moderate decline stage of permeability dominated by microscopic pore throats. Microscopic pore throats are the dominant percolation channels in pore type reservoirs, and they are preferentially compressed when the effective stress gradually increases. Although the microscopic pore throats are also difficult to be compressed, the permeability decline rate of the pore type samples in the first stage is significantly higher than that of the cavity samples. This is because the radius of microscopic pore throats is smaller than that of cavitie and macroscopic pore throats, and the relative change of the pore throat radius has a great effect on the absolute percolation capacity of the microscopic pore throat. More importantly, pore type reservoirs have poor pore throat connectivity and low pore throat coordination number. The closure of key percolation channels has a great negative impact on the overall percolation capacity. The second stage begins when the microscopic pore throats cannot be compressed further. The second stage is the extremely slow decline stage of permeability dominated by rock minerals. The stress sensitivity of the second stage mainly comes from the mineral deformation and creep caused by the compression of the rock framework. In contrast, the effective stress corresponding to the compression of the rock framework of the pore type sample is similar to that of the cavity type sample, but the permeability loss rate of the pore type sample caused by compression is slightly higher. The permeability of the pore type sample DF2 is higher than that of the cavity type sample DF10, but the stress sensitivity of the former is stronger than that of the latter. It reflects that cavities can weaken the reservoir stress sensitivity to a certain extent. The reason why the permeability loss rate of sample DF4 is significantly higher than that of sample DF2 is that the initial permeability and porosity of the former are obviously lower than those of the latter.

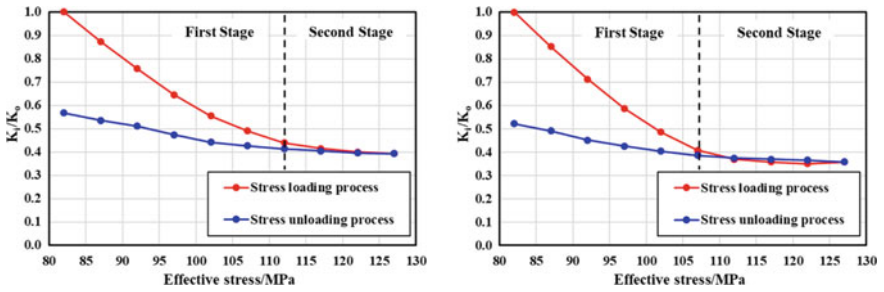

(a) Sample DF2 (b) Sample DF4

Fig. 4.11 Permeability stress sensitivity characteristic curves of pore type samples under reservoir conditions

The recovery process of sample permeability during effective stress unloading process is also illustrated in Fig. 4.11. The permeability of the two pore type cores eventually recovered to about 55% of the initial permeability. The irreversible loss rate of permeability under different effective stresses can also be divided into two stages, as shown in Fig. 4.12. The permeability recovery curve characteristics of the pore type sample DF2 are similar to the two stages of the cavity type samples, but the irreversible permeability loss rate of the sample DF2 is always higher. It should be noted that the irreversible permeability loss rate of the sample DF4 is negative at the initial stage of effective stress unloading. The reason why the sample permeability is slightly improved is that the rock framework can be broken or fractured to form new percolation channels when the effective stress on the sample exceeds the critical fracture pressure. However, the closure and narrowing of the percolation channel caused by plastic deformation as the effective stress decreases will offset this part of the permeability improvement effect. In addition, fine particles from rock broken may block microscopic pore throats, thereby exacerbating irreversible permeability loss. Therefore, the stress sensitivity of pore type reservoirs varies greatly. The stress sensitivity characteristics of pore type reservoirs with relatively high permeability are similar to those of cavity type reservoirs, but the stress sensitivity degree of pore type reservoirs with relatively low permeability is close to that of fracture-cavity type reservoirs. The poor percolation capacity, low gas saturation and strong stress sensitivity of low-permeability pore type reservoirs make them unsuitable as the dominant reservoirs for the development of ultradeep carbonate gas reservoirs. High-permeability pore type reservoirs can be used as the periphery supply area of fracture-cavity type and cavity type reservoirs to supply gas stably in the middle or late stages of gas reservoir development. Pore type reservoirs located in the peripheral area can effectively avoid the dramatic decrease of reservoir permeability caused by the rapid increase of effective stress in the area around the wellbore.

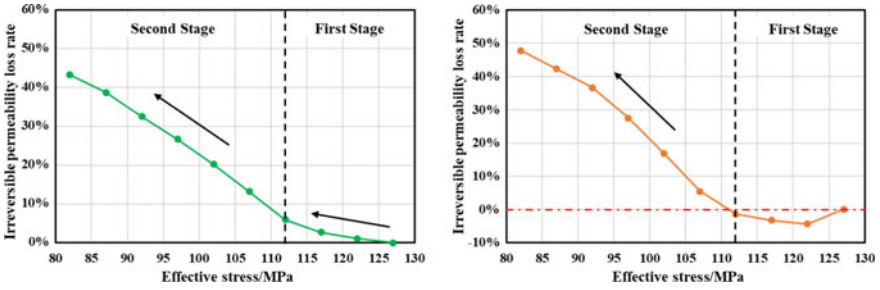

(a) Sample DF2 (b) Sample DF4

Fig. 4.12 Relationship between irreversible permeability loss rate and effective stress of pore type samples

4.2.8 Porosity Stress Sensitivity of Different Types of Carbonate Reservoirs

(1) Fracture-cavity type sample

The porosity stress sensitivity experiment results of fracture-cavity type samples are illustrated in Fig. 4.13. The stress sensitivity characteristics and key parameters of the two full-diameter core samples are similar. The porosity stress sensitivity characteristics of fracture-cavity type samples can also be divided into three stages corresponding to the permeability stress sensitivity. The total porosity loss rate of the DF3 sample during the stress loading process is 18.74%, and the porosity loss rates of the three stages are 15.19%, 3.39% and 0.16%, respectively. The total porosity loss rate of the DF7 sample during the stress loading process is 19.88%, and the porosity loss rates of the three stages are 17.27%, 2.43% and 0.18%, respectively. It can be concluded that the stress sensitivity of porosity in fracture-cavity type samples is obviously weaker than that of permeability by comparing the loss rates of the two parameters. The first stage is the rapid decline stage of porosity dominated by microfractures. The CT scanning results of fracture-cavity type samples show that the developed microfractures are not only the dominant percolation channels, but also occupy about 15% of the storage space. Therefore, compression and closure of fractures can simultaneously lead to a rapid decrease in permeability and porosity. The greater the effective stress, the more obvious fracture closure, and the greater the decrease in permeability and porosity. The porosity of fracture-cavity type samples is close to that of cavity type samples when the fractures are closed to a certain extent. The second stage is the slow decline stage of porosity dominated by cavities and macroscopic pore throats. Cavities and macroscopic pores are difficult to be compressed and the porosity loss rate caused by deformation is low. The third stage is the extremely slow decline stage of porosity dominated by rock minerals. Compression and closure of tiny throats caused by mineral deformation and creep have little effect on porosity. Therefore, the effect of rock framework compression on porosity is significantly weaker than that of permeability. It is also possible that the extremely low porosity loss rate at this stage was caused by measurement errors. The reason that the effective stress required for the sample DF7 to enter the second stage is higher than that of the sample DF3 may be that the fractures of the sample DF7 are more developed.

The recovery process of sample porosity during effective stress unloading process is also illustrated in Fig. 4.13. The sample porosity slowly recovers as the effective stress decreases. The re-opening of microfractures also leads to a rapid increase in porosity recovery at low effective stress. The porosity of the two fracture-cavity type cores eventually recovered to about 85% of the initial porosity. This reflects that the irreversible loss of stress sensitivity to porosity is far lower than that to permeability. The irreversible loss rate of porosity under different effective stresses can be divided into three stages, as shown in Fig. 4.14. The irreversible loss rate of the first stage is almost zero because the effective stress in this stage does not cause porosity loss to the fracture-cavity type sample. The irreversible loss rate of

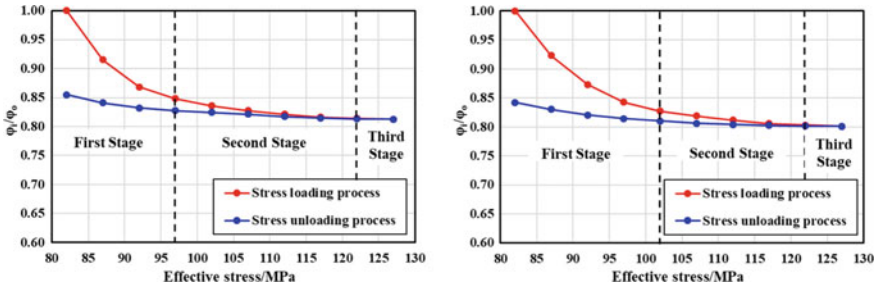

(a) Sample DF3 (b) Sample DF7

Fig. 4.13 Porosity stress sensitivity characteristic curves of fracture-cavity type samples under reservoir conditions

the second stage increases slowly and is generally less than 4%, reflecting that the compressed cavities and microscopic pore throats can be greatly recovered during the stress unloading process. The irreversible loss rate in the third stage increases rapidly and is generally higher than 4%, reflecting that although the reopened fractures can increase the porosity recovery rate, the complete closure of most of the fractures also increases the irreversible porosity of fracture-cavity samples. The phenomenon of rapid variation of porosity with effective stress will not occur if the fraction of storage space occupied by fractures in the reservoir is low. The method of restoring reservoir pressure to increase porosity through shut-in operation is also less effective for fracture-cavity type reservoirs, because the porosity loss rate only recovers from about 80% to about 85% during the stress unloading process. Therefore, the porosity of fracture-cavity type reservoirs should be corrected frequently during the production process, especially when the fractures are compressed in the early stage of exploitation. Otherwise, the calculation and simulation related to reserves and recover factors using initial porosity will inevitably lead to certain errors.

(2) Cavity type sample

The porosity stress sensitivity experiment results of cavity type samples are illustrated in Fig. 4.15. The stress sensitivity characteristics and key parameters of the two full-diameter cores are similar. The porosity stress sensitivity characteristics of cavity type samples can be divided into two stages corresponding to the permeability stress sensitivity. The total porosity loss rate of the DF5 sample during the stress loading process is 13.34%, and the porosity loss rates of the two stages are 12.52% and 0.82%. The total porosity loss rate of the DF10 sample during the stress loading process is 14.73%, and the porosity loss rates of the two stages are 14.25% and 0.48%. It can be concluded that the stress sensitivity of porosity in cavity type samples is significantly weaker than that of permeability by comparing the loss rates of the two parameters. The first stage is the slow decline stage of porosity dominated by cavities and macroscopic pore throats. The variation of porosity with effective stress in the first stage of the cavity type sample is similar to that of the second stage of the fracture-cavity type sample. The CT scanning results of cavity type samples

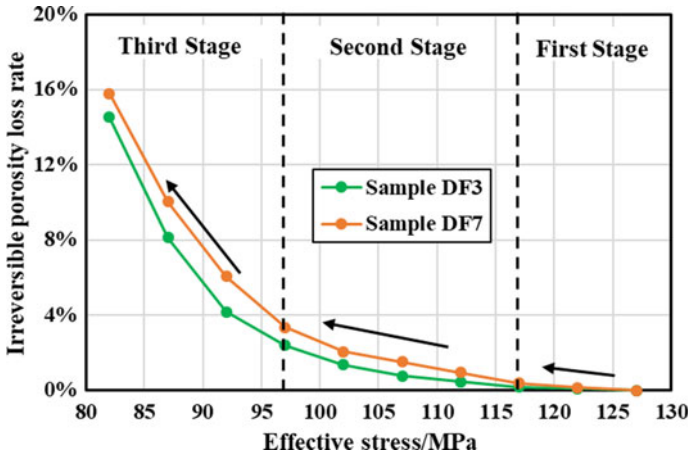

Fig. 4.14 Relationship between irreversible porosity loss rate and effective stress of fracture-cavity type samples

show that the scattered small-scale cavities occupy about 39% of the storage space. Cavities are the most difficult to compress and deform compared to pores, fractures and throats. The second stage begins when the cavities and macroscopic pore throats cannot be compressed further. The second stage is the extremely slow decline stage of porosity dominated by rock minerals. The porosity loss rate of cavity type samples at this stage is still extremely low but slightly higher than that of fracture-cavity type samples. This is because the significant increase in effective stress at this stage causes more and more tiny spaces to be closed due to mineral deformation. It is also not excluded that part of the porosity loss rate is caused by measurement errors.

The recovery process of sample porosity during effective stress unloading process is also illustrated in Fig. 4.15. The sample porosity initially recovers slowly, but the recovery rate gradually increases as the effective stress decreases. The porosity

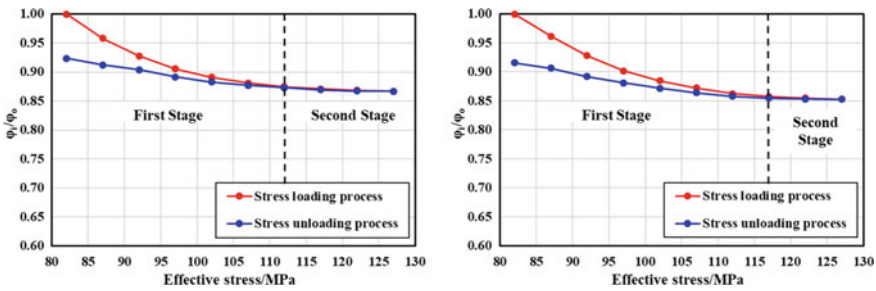

(a) Sample DF5 (b) Sample DF10

Fig. 4.15 Porosity stress sensitivity characteristic curves of cavity type samples under reservoir conditions

of the two cavity type cores eventually recovered to more than 90% of the initial porosity. This reflects that the porosity irreversible loss of cavity type reservoirs caused by stress sensitivity is extremely low. The irreversible loss rate of porosity under different effective stresses can be divided into two stages, as shown in Fig. 4.16. The irreversible loss rate of the first stage is also extremely low, which means that the porosity irreversible loss of the cavity type sample caused by stress sensitivity at this stage can be ignored. The irreversible loss rate of the second stage increases slowly and is generally less than 8%, reflecting that the compressed cavities and microscopic pore throats are greatly recovered during the stress unloading process. The method of restoring reservoir pressure to increase porosity through shut-in operations is relatively effective for cavity type reservoirs because the porosity loss rate recovers from about 85% to about 92% during the stress unloading process. In conclusion, the porosity value of the cavity type reservoir is relatively stable during the exploitation process. The initial porosity can always be used for calculations and simulations related to reserves and recovery factors without apparent errors.

(3) Pore type sample

The porosity stress sensitivity experiment results of pore type samples are illustrated in Fig. 4.17. The stress sensitivity characteristics of the two full-diameter cores are similar, but the key parameters are different. The porosity stress sensitivity characteristics of pore type samples can be divided into two stages corresponding to the permeability stress sensitivity. The total porosity loss rate of the DF2 sample during the stress loading process is 15.54%, and the porosity loss rates of the two stages are 14.80% and 0.74%. The total porosity loss rate of the DF4 sample during the stress loading process is 17.47%, and the porosity loss rates of the two stages were 15.69% and 1.78%. It can also be concluded that the stress sensitivity of porosity in pore

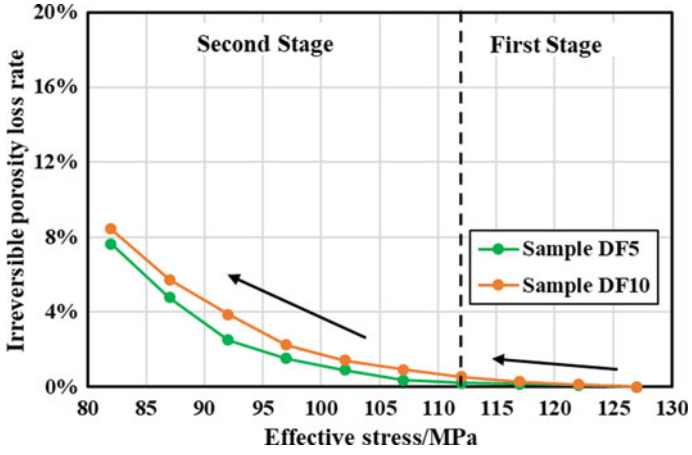

Fig. 4.16 Relationship between irreversible porosity loss rate and effective stress of cavity type samples

type samples is significantly weaker than that of permeability by comparing the loss rates of the two parameters. The first stage is the moderate decline stage of porosity dominated by microscopic pore throats. Although the microscopic pore throats are also difficult to be compressed, the porosity decline rate in the first stage of the pore type samples is slightly higher than that of the cavity samples. This is because the relative change of pore volume has a greater effect on the absolute storage capacity of microscopic pores than that of macroscopic pores and cavities. In addition, pore type reservoirs have poor pore throat connectivity and low pore throat coordination number. The closure of key percolation channels can block some pores with low coordination numbers, thereby forming ineffective pores. The second stage begins when the microscopic pore throats cannot be compressed further. The second stage is the extremely slow decline stage of permeability dominated by rock minerals. The porosity loss rate of the pore type sample DF2 at this stage is still extremely low, whereas the porosity loss rate of the pore type sample DF4 is obviously higher than that of other samples. A significant decrease in dimensionless porosity can be observed when the effective pressure is increased to 122 MPa. Therefore, the additional porosity loss rate may come from the tiny pores that are blocked by the destruction and fracture of the rock framework.

The recovery process of sample porosity during effective stress unloading process is also illustrated in Fig. 4.17. The sample porosity initially recovers slowly, but the recovery rate gradually increases as the effective stress decreases. The porosity of the two pore type cores eventually recovered to 87–90% of the initial porosity. This reflects that the irreversible loss of stress sensitivity to porosity is far lower than that to permeability. The irreversible loss rate of porosity under different effective stresses can also be divided into two stages, as shown in Fig. 4.18. The irreversible loss rate of the first stage is also extremely low for pore type samples. The porosity recovery curve characteristics of the pore type sample DF2 are similar to the two stages of the cavity type sample, but the irreversible porosity loss rate of the sample DF2 is always higher. The irreversible porosity loss rate of the sample DF4 is negative at the initial stage of effective stress unloading because the rock framework is broken or fractured.

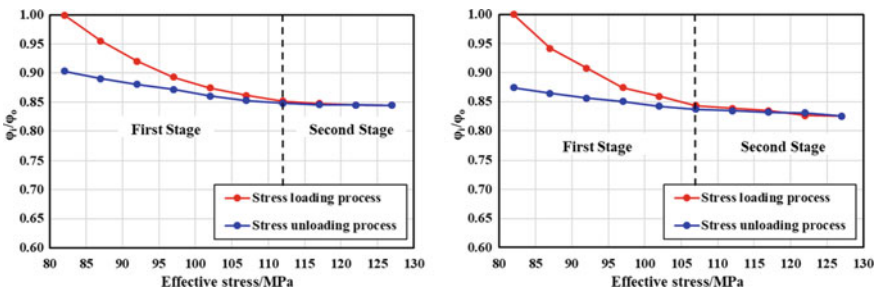

(a) Sample DF2 (b) Sample DF4

Fig. 4.17 Porosity stress sensitivity characteristic curves of pore type samples under reservoir conditions

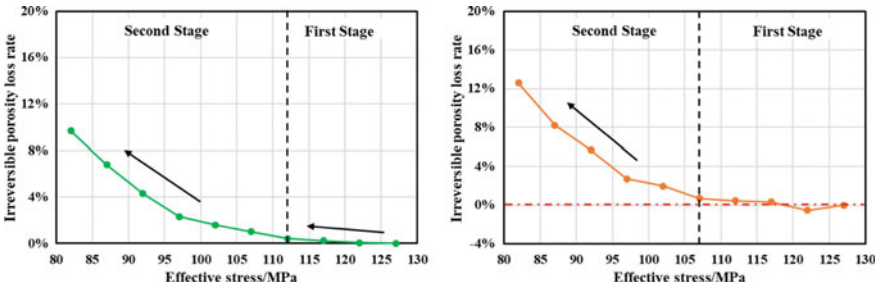

(a) Sample DF2 (b) Sample DF4

Fig. 4.18 Relationship between irreversible porosity loss rate and effective stress of pore type samples

However, the improvement effect of rock framework destruction on porosity is not as obvious as that of permeability. The irreversible loss rate of the second stage is generally less than 12%, reflecting that the recovery degree of microscopic pores is considerable but lower than that of macroscopic pores and cavities. The stress sensitivity characteristics of pore type reservoirs with relatively high porosity are similar to those of cavity type reservoirs, but the stress sensitivity degree of pore type reservoirs with relatively low porosity is close to that of fracture-cavity type reservoirs. Therefore, the porosity value of the pore type reservoir with high porosity is relatively stable with the variation of effective stress, whereas the porosity value of the pore type reservoir with low porosity varies relatively obvious.

The above experimental results show that the effect of permeability stress sensitivity on ultradeep carbonate gas reservoirs is significantly greater than that of porosity stress sensitivity. Moreover, the permeability stress sensitivity characteristic is more widely used both in theoretical research and oilfield development. Therefore, further investigations on the factors affecting the permeability stress sensitivity of ultradeep carbonate gas reservoirs are discussed in the following sections.

4.2.9 Effect of Reservoir Type on Permeability Stress Sensitivity

The stress sensitivity curves of the same type of samples are similar, but the stress sensitivity characteristics and degrees of different types of carbonate samples are obviously different. The stress sensitivity characteristic parameters of different types of reservoirs are indispensable data for the production performance prediction and development scheme formulation of ultradeep carbonate gas reservoirs. Therefore, the stress sensitivity characteristic parameters and evaluation results of the 6 samples are summarized in Table 4.13. It should be noted that the stress sensitivity coefficient

model (Eq. (4.8)) commonly used to evaluate the stress sensitivity degree of fractured tight reservoirs is not suitable for ultradeep carbonate gas reservoirs. This is because the stress sensitivity coefficients of the six samples under different effective stresses are generally greater than 1. The stress sensitivity of all samples will be judged as extremely strong if referring to the stress sensitivity evaluation standard in Table 4.12, because the initial effective stress of ultradeep carbonate reservoirs is far higher than that of conventional reservoirs. Xiao et al. (2016) proposed four relational expressions between permeability and effective stress, namely exponential model, logarithmic model, binomial model and power model. All four models have corresponding parameters to reflect the stress sensitivity degree. It was found that the power model (Eq. (4.9)) had the highest correlation with the stress sensitivity data for the 6 carbonate samples by comparing the fitting results of the four models. Therefore, the stress sensitivity index (α) was used as a parameter to compare the stress sensitivity degree of different samples.

The power function fitting results of stress sensitivity data for different types of samples under reservoir conditions are illustrated in Figs. 4.19, 4.20 and 4.21. The larger the stress sensitivity index, the greater the stress sensitivity degree. The stress sensitivity indices for the six cores are also summarized in Table 4.13. In addition, a large number of plug core samples from different types of carbonate reservoirs were also used for stress sensitivity experiments. The power function fitting results show that the stress sensitivity indices of fracture-cavity type, cavity type and pore type samples are distributed in 2.46–2.68, 1.23–1.84 and 2.04–2.49, respectively. In general, the stress sensitivities degree of pore type samples is slightly weaker than that of fracture-cavity type samples, but both are stronger than those of cavity type samples.

Table 4.13 Permeability stress sensitivity characteristic parameters of three types of samples under reservoir conditions

Core number	Core type	Permeability loss rate (%)	Stress sensitivity degree	Permeability retention rate (%)	Stress sensitivity recovery degree	Stress sensitivity index
DF3	Fracture-cavity type	67.58	Moderately strong	49.11	Moderately weak	2.513
DF7	Fracture-cavity type	66.74	Moderately strong	50.92	Moderately strong	2.598
DF5	Cavity type	40.94	Moderately weak	71.86	Strong	1.208
DF10	Cavity type	46.66	Moderately weak	67.87	Moderately strong	1.410
DF2	Pore type	60.72	Moderately strong	56.74	Moderately strong	2.295
DF4	Pore type	64.25	Moderately strong	52.24	Moderately strong	2.602

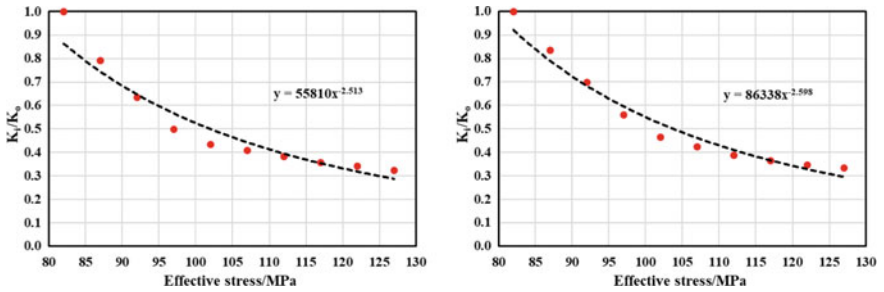

(a) Sample DF3 (b) Sample DF7

Fig. 4.19 Power function fitting results of stress sensitivity data of fracture-cavity type samples under reservoir conditions

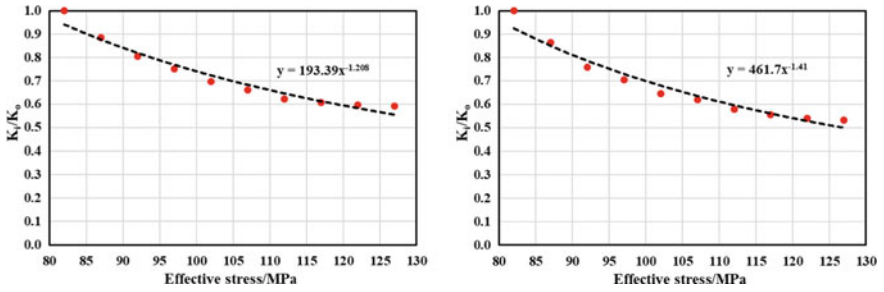

(a) Sample DF5 (b) Sample DF10

Fig. 4.20 Power function fitting results of stress sensitivity data of cavity type samples under reservoir conditions

$$\frac{K_{\mathrm{i}}}{K_0} = C\left(\sigma - p_{\mathrm{p}}\right)^{-\alpha} \tag{4.9}$$

However, the stress sensitivity index can only be used to compare the strength of stress sensitivity among different samples, and cannot be used as a basis for evaluating stress sensitivity degree. Therefore, the permeability loss rate and retention rate are used as parameters to evaluate the damage degree and recovery degree of stress sensitivity, respectively. Permeability loss rate refers to the percentage of permeability reduction caused by stress sensitivity when reservoir pressure drops to abandonment pressure. Permeability retention rate refers to the percentage of finial permeability to initial permeability when reservoir pressure recovers to initial pressure. The evaluation standard of permeability stress sensitivity degree are shown in Table 4.14. The evaluation results show that the stress sensitivity degree of fracture-cavity type and pore type samples is moderately strong, whereas the stress sensitivity degree of cavity type samples is moderately weak. Therefore, the production pressure differential should be reasonably controlled to avoid damage to reservoir permeability caused by stress sensitivity during the exploitation of fracture-cavity type

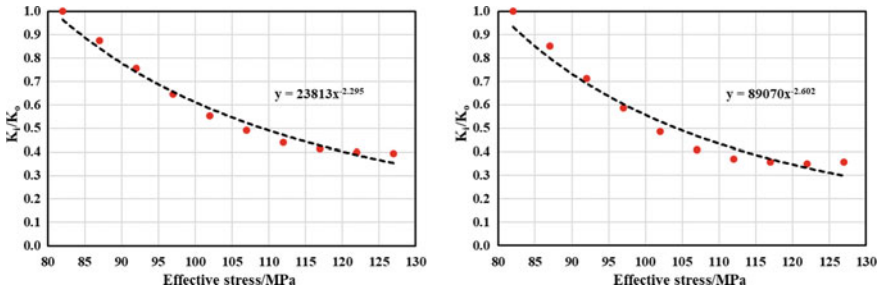

(a) Sample DF2 (b) Sample DF4

Fig. 4.21 Power function fitting results of stress sensitivity data of pore type samples under reservoir conditions

Table 4.14 Evaluation standard for permeability stress sensitivity

Permeability loss rate/%	Stress sensitivity degree	Permeability retention rate/%	Stress sensitivity recovery degree
$D \leq 5$	None	$R > 70$	Strong
$5 < D \leq 30$	Weak	$70 \geq R > 50$	Moderately strong
$30 < D \leq 50$	Moderately weak	$50 \geq R > 30$	Moderately weak
$50 < D \leq 70$	Moderately strong	$30 \geq R > 5$	Weak
$D > 70$	Strong	$R < 5$	None

carbonate gas reservoirs. The stress sensitivity recovery degrees of fracture-cavity type, cavity type and pore type samples are moderately weak to moderately strong, moderately strong to strong, and moderately strong, respectively. It reflects that the stress sensitivity hysteresis effect of the three types of reservoirs is fracture-cavity type, pore type and cavity type in order from strong to weak. Therefore, the method of restoring reservoir pressure through shut-in operations to increase permeability is effective for cavity type reservoirs. Pore type reservoirs are usually used as peripheral replenishment reservoirs for fracture-cavity type and cavity type reservoirs, and their stress sensitivity degree is not as significant as that of reservoirs around the wellbore. In conclusion, the stress sensitivity characteristics of different types of ultradeep carbonate gas reservoirs are significantly different. It is necessary to conduct stress sensitivity research on core samples of various types of reservoirs to fully reveal the stress sensitivity characteristics of this type of gas reservoirs.

4.2.9.1 Effect of Temperature and Pressure Conditions on Permeability Stress Sensitivity

Stress sensitivity experiments under reservoir conditions cannot be conducted in the early stage of ultradeep carbonate gas reservoir exploration and exploitation owing to

the limitation of experimental equipment and technology. The stress sensitivity characteristics under reservoir conditions can only be predicted by stress sensitivity experimental results under conventional temperature and pressure conditions. However, the application effect of stress sensitivity prediction in ultradeep carbonate gas reservoirs is not satisfactory. This is because the stress sensitivity characteristics are not only affected by the effect stress, but also the pressure and temperature conditions of the formation, the fluid phase state and the fluid properties can also have different degrees of influence on the percolation characteristics. Therefore, three types of full-diameter core samples were subjected to stress sensitivity experiments under conventional and reservoir conditions to reveal the effects of high temperature and pressure conditions on the stress sensitivity characteristics of ultradeep carbonate gas reservoirs.

The stress sensitivity characteristic curves of three types of full-diameter cores under conventional conditions are shown in Fig. 4.22. The stress sensitivity curves under reservoir conditions and conventional conditions cannot be compared on one axis because the initial effective stress under the two conditions is quite different. It can be seen from the Fig. 4.22 that the permeability loss rates of the three types of samples under conventional conditions are all higher than those under reservoir conditions during the effective stress loading process. This is because the initial effective stress under conventional conditions is lower than the actual situation, and therefore the compression degree of fractures, cavities, pores, throats and minerals in the samples is significantly reduced under initial conditions. In addition, the permeability recovery rates of the three types of samples under conventional conditions during the effective stress unloading process are also higher than those under reservoir conditions. However, these phenomena cannot indicate whether the stress sensitivity under conventional conditions is stronger or weaker than that under reservoir conditions because the initial effective stress is different in the two conditions. Figure 4.23 shows the power function fitting results for stress sensitivity data points. Therefore, the strength of stress sensitivity was judged by comparing the stress sensitivity indices under the two conditions. The stress sensitivity characteristic parameters of the two experimental conditions are summarized in Table 4.15. The comparison results of stress sensitivity index show that the stress sensitivity of the three types of samples under conventional conditions is weaker than that under reservoir conditions, especially the fracture-cavity type sample.

In addition, the permeability loss rate under reservoir conditions was predicted by stress sensitivity experimental results under conventional conditions, and then the predicted results were compared with the actual results under reservoir conditions. The prediction formula of dimensionless permeability under different effective stress can refer to Eq. (4.10). The permeability loss rate under different effective stress can be predicted by substituting the stress sensitivity index of conventional conditions and the initial pressure data of actual reservoir conditions into Eq. (4.10). The comparison of the predicted and the actual permeability loss rates of the three types of samples when the reservoir pressure drops to the abandonment pressure is shown in Table 4.13. Although the predicted stress sensitivity degrees are consistent with those obtained under reservoir conditions, the predicted permeability loss rates

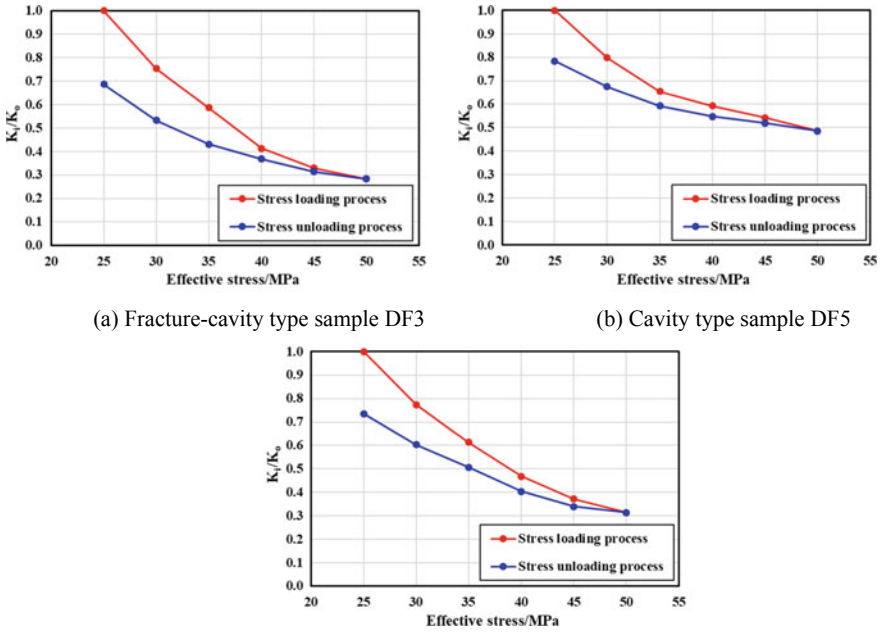

(a) Fracture-cavity type sample DF3

(b) Cavity type sample DF5

(c) Pore type sample DF2

Fig. 4.22 Permeability stress sensitivity characteristic curves of three types of samples under conventional conditions

of fracture-cavity type, cavity type and pore type samples are 16.64%, 12.21% and 13.29% lower than those obtained under reservoir conditions, respectively. It can be concluded that the stress sensitivity under reservoir conditions predicted according to the experimental results under conventional conditions is generally low. Therefore, it is necessary to conduct stress sensitivity experiments of ultradeep carbonate gas reservoirs under reservoir conditions to provide accurate stress sensitivity parameters for the investigations of percolation characteristics and production performance.

$$\frac{K_{\mathrm{i}}}{K_0} = \left(\frac{\sigma - p_{\mathrm{i}}}{\sigma - p_0}\right)^{-\alpha} \tag{4.10}$$

4.2.9.2 Effect of Initial Reservoir Permeability on Permeability Stress Sensitivity

The stress sensitivity of conventional sandstone gas reservoirs generally has a good correlation with petrophysical properties, and decreases with the increase of reservoir permeability. Therefore, the stress sensitivity characteristics and degrees of reservoirs with different petrophysical properties can be predicted by establishing the fitting

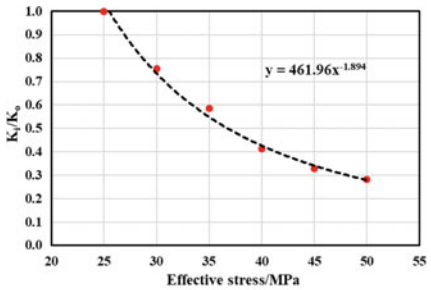

(a) Fracture-cavity type sample DF3

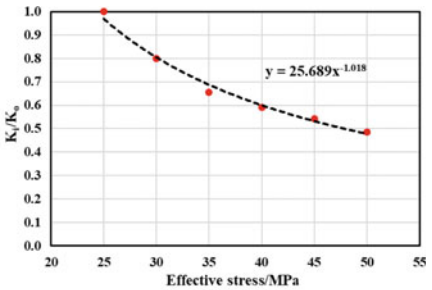

(b) Cavity type sample DF5

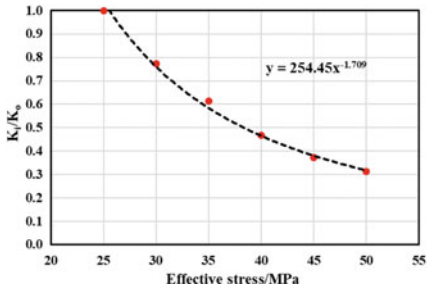

(c) Pore type sample DF2

Fig. 4.23 Power function fitting results for stress sensitivity data of three types of samples under conventional conditions

Table 4.15 Stress sensitivity characteristic parameters of three types of samples under two experimental conditions

Parameters	Conditions	Fracture-cavity type	Cavity type	Pore type
Stress sensitivity index	Conventional conditions	−1.894	−1.018	−1.709
	Reservoir conditions	−2.513	−1.208	−2.295
Permeability loss rate	Conventional conditions	56.98%	36.45%	53.28%
	Reservoir conditions	67.58%	40.94%	60.72%
Stress sensitivity degree	Conventional conditions	Moderately strong	Moderately weak	Moderately strong
	Reservoir conditions	Moderately strong	Moderately weak	Moderately strong

formula of stress sensitivity characteristic parameters and reservoir permeability. However, ultradeep carbonate gas reservoirs have diverse reservoir types and developed fractures and cavities. The correlation between stress sensitivity and initial permeability of different types of reservoirs requires further investigation. Therefore, a large number of plunger core samples from three types of reservoirs were selected for stress sensitivity experiments under reservoir conditions because of the difficulty of drilling full-diameter core samples and the long experimental period. Subsequently, the stress sensitivity index was obtained by fitting the experimental data of each sample with a power function.

The relationship between permeability and stress sensitivity index of fracture-cavity type samples is illustrated in Fig. 4.24a. The distribution range of stress sensitivity index of fracture-cavity type samples is relatively concentrated, mainly distributed between 2.46 and 2.68, with an average value of 2.53. The overall stress sensitivity degree of the 23 samples is evaluated as moderately strong. The correlation between stress sensitivity index and initial permeability of fracture-cavity type samples is poor, and the fitting formula cannot be obtained. However, the stress sensitivity degree increases gradually with the increase of the initial permeability. This is because the percolation capacity of fracture-cavity type reservoirs is mainly contributed by the high-permeability flow channels and high pore thraot connectivity provided by mcirofractures. The compression resistance of microfractures is far weaker than that of cavities, pores and throats, and therefore they are the media that are preferentially compressed or even closed at the initial stage of effective stress loading. The more fractures are developed in the reservoir, the higher the initial permeability, the higher the percentage of permeability contributed by fractures, and the greater the permeability loss due to stress sensitivity effects. When the fractures are compressed to a certain extent, the fracture-cavity type reservoir is infinitely close to the cavity type reservoir, and its subsequent stress sensitivity characteristics and degree are similar to those of the cavity type reservoir. However, the stress sensitivity degree of cavity type reservoirs is relatively weak. Therefore, the overall stress sensitivity of fracture-cavity type reservoirs is mainly affected by the compression process of fractures in the first stage. Fracture-cavity type reservoirs with high initial permeability need to pay more attention to the damage of stress sensitivity to reservoir permeability during the reservoir exploitation process. The average value of the existing stress sensitivity indices can be applied to the reservoir without additional stress sensitivity experimental data, because the stress sensitivity index distribution of fracture-cavity type reservoir is concentrated.

The relationship between permeability and stress sensitivity index of cavity type samples is illustrated in Fig. 4.24b. The distribution range of stress sensitivity index of cavity type samples is relatively wide, mainly distributed between 1.23 and 1.84, with an average value of 1.54. The overall stress sensitivity degree of 28 samples is evaluated as moderately weak. The stress sensitivity of cavity type reservoirs decreases gradually with the increase of initial permeability. Moreover, the correlation between the stress sensitivity index and initial permeability is good, and the fitting formula of the two can be obtained. This is because the percolation capacity of cavity type reservoirs is mainly contributed by bedding cavities and macroscopic pore throats.

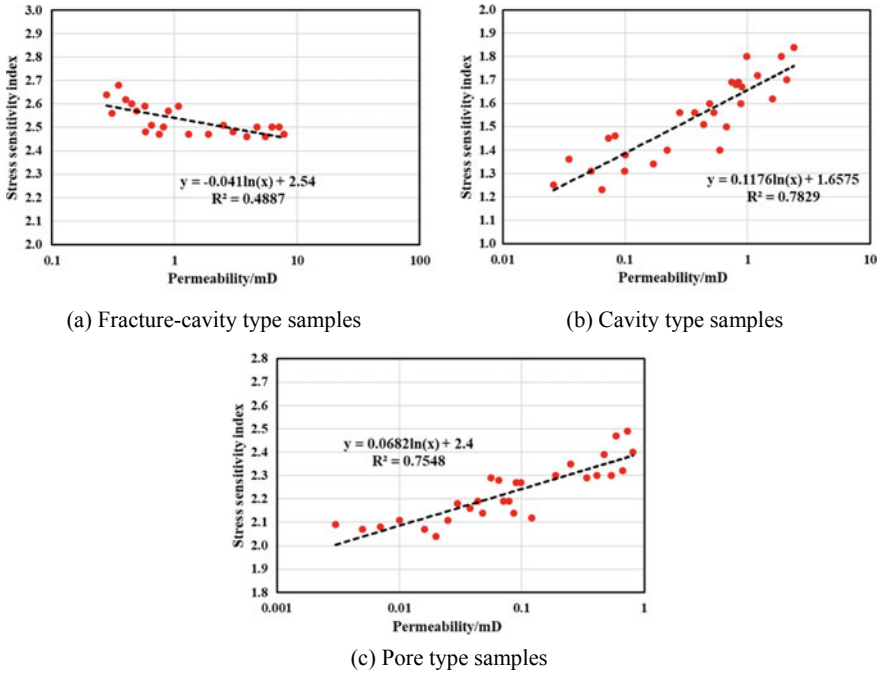

(a) Fracture-cavity type samples

(b) Cavity type samples

(c) Pore type samples

Fig. 4.24 Relationship between permeability and stress sensitivity index of different types of carbonate samples

The compression resistance of cavities and macroscopic pore throats is strong, and the relative change of pore throat radius has little effect on the absolute percolation capacity of macroscopic pore throats and cavities. The higher the permeability of the cavity type reservoir, the more developed bedding cavities and macroscopic pore throats, and the smaller the permeability loss due to stress sensitivity effects. Therefore, high-permeability cavity type reservoirs can be exploited with high production pressure differentials to make up for their low gas production capacity.

The relationship between permeability and stress sensitivity index of pore type samples is illustrated in Fig. 4.24c. The distribution range of stress sensitivity index of pore type samples is relatively wide, mainly distributed between 2.04 and 2.49, with an average value of 2.23. The overall stress sensitivity degree of the 29 samples is between moderately strong and moderately weak. The stress sensitivity of pore type reservoirs decreases gradually with the increase of initial permeability. Furthermore, the correlation between stress sensitivity index and initial permeability is good, and the fitting formula of the two can be obtained. This is because the percolation capacity of pore type reservoirs is mainly contributed by microscopic pore throats. The macroscopic pore throat number and pore throat coordination number gradually increases with the increase of initial permeability, thereby weakening the effect of stress sensitivity on reservoir permeability. However, the compression resistance of

macroscopic pore throats is still weaker than that of cavities, and the number of macroscopic pore throats in pore type reservoirs is limited. Therefore, the value and variation range of the stress sensitivity index of the pore type reservoir are smaller than those of the cavity type reservoir. Pore type reservoirs with relatively high permeability can be used as the peripheral replenishment reservoirs for fracture-cavity type and cavity type reservoirs, whereas pore type reservoirs with extremely low permeability are usually abandoned as unprofitable reservoirs. In addition, the stress sensitivity characteristics of cavity type and pore type reservoirs in different regions can be predicted by the fitting formula.

4.3 Summary

In this chapter, the possible formation damage mechanism caused by carbonate reservoir minerals was briefly introduced. The velocity sensitivity, water sensitivity, salinity sensitivity, alkali sensitivity and acid sensitivity characteristics of three types of ultradeep carbonate gas reservoirs were studied based on the results of classical fluid injection experiments and reservoir characteristics analysis. Then, an experimental method for measuring core stress sensitivity under high temperature and pressure conditions was developed, and corresponding improvement measures were introduced. Subsequently, a series of stress sensitivity experiments were conducted on full-diameter and plunger core samples of different types of ultradeep carbonate reservoirs. In addition, the permeability and porosity stress sensitivity characteristics of various types of reservoirs were evaluated, and the formation damage degree and stress sensitivity mechanism of different types of reservoirs were also analyzed. Finally, the effects of temperature and pressure conditions, reservoir type and initial reservoir permeability on the stress sensitivity of ultradeep carbonate gas reservoirs were discussed. Some development suggestions and protective operations were proposed according to the sensitivity characteristics affecting ultradeep carbonate gas reservoirs. The important conclusions obtained are summarized as follows.

(1) The final permeability loss rates of fracture-cavity type, cavity type and pore type samples caused by velocity sensitivity are 2.55%, 14.81% and 21.84%, respectively. The velocity sensitivity of pore type reservoirs is relatively strong because of small pore throat size and poor connectivity. The large storage space of the cavity type reservoir can capture a certain amount of free fine particles, thereby reducing the blockage of the flow channel by fine particles. The effect of velocity sensitivity on fracture-cavity type reservoirs is extremely weak, because large percolation channel size increases the difficulty of fine particle blocking, and high pore throat coordination number weakens the effect of partial percolation channel blockage on the overall percolation capacity. The velocity sensitivity of various reservoirs in the Deng IV Member is weak or none, reflecting that the formation damage caused by the high injection velocity of working fluid or the high production rate of natural gas is not significant.

The two main reasons for the weak velocity sensitivity are the low content of water-sensitive minerals and good consolidation and cementation.

(2) The final permeability loss rates of fracture-cavity type, cavity type and pore type samples caused by water sensitivity are 4.45%, 10.43% and 15.58%, respectively. The formation damage caused by water sensitivity mainly includes percolation channel shrinkage cause by clay swelling and percolation channel blockage caused by particle detachment and migration. The smaller the percolation channel size, the worse the pore throat connectivity, and the more significant the effect of clay swelling on the percolation channel size and the particle blockage on the pore throat connectivity. The water sensitivity of various reservoirs in the Deng IV Member is weak or none, because the clay mineral in the reservoirs are low in content and dispersed in distribution. In addition, the low content of smectite in clay minerals results in weak hydration swelling, and the high content of kaolinite but good cementation results in weak particle dispersion and migration. The formation damage of water sensitivity to ultradeep carbonate gas reservoirs is usually ignored.

(3) The final permeability loss rates of fracture-cavity type, cavity type and pore type samples caused by salinity sensitivity are 6.55%, 11.97% and 15.46%, respectively. The permeability of the three types of cores first decreased at a extremely low rate and then decreased at a relatively high rate as the fluid salinity decreased. This is because the clay swelling process can be divided into the hydration swelling of the outer surface caused by the surface hydration energy and of the inner surface caused by the repulsion of the electric double layer. The hydration swelling volume of the outer surface is extremely small, but the hydration swelling volume of the inner surface is far larger than that of the outer surface. The salinity sensitivity of the Deng IV Member reservoir is weak. The reason for the low degree of formation damage caused by salinity sensitivity is similar to that of water sensitivity. The formation damage caused by salinity can be ignored when preparing working fluids.

(4) The final permeability loss rates of fracture-cavity type, cavity type and pore type cores caused by alkali sensitivity are 25.07%, 32.55% and 38.82%, respectively. The formation damage caused by alkali sensitivity is mainly precipitation and blockage, supplemented by hydration swelling. The smaller the percolation channel size, the worse the pore throat connectivity, and the more significant the effect of precipitation on the percolation channel size and the effect of particles on the pore throat connectivity. Alkali scale and silicate precipitation are the dominant mechanisms of formation damage caused by alkali sensitivity to ultradeep carbonate gas reservoirs. However, a small amount of alkali scale and dispersed particles formed at a relatively low pH value have little effect on fracture-cavity type and cavity type reservoirs, and the permeability of fracture-cavity type reservoirs decreases significantly only at a relatively high pH value. The alkali sensitivity of fracture-cavity type reservoirs is weak, and of cavity type and pore type reservoirs is moderately weak. It is necessary to adjust the pH of drilling fluid in time during drilling operations to reduce

the formation damage caused by alkali sensitivity to ultradeep carbonate gas reservoirs.

(5) The final permeability loss rates of fracture-cavity type, cavity type and pore type samples caused by acid sensitivity are −21.14%, −26.97% and −36.03%, respectively. Fe^{2+}, Mg^{2+} and Si^{4+} can be released from pyrite, dolomite and silicide in ultradeep carbonate gas reservoirs under an acidic environment, and then the new precipitation of $Fe(OH)_3$ and $Mg(OH)_2$ and the gel of SiO_4 are generated. Nevertheless, the improvement effect of hydrochloric acid on reservoirs is significantly better than the damage effect, because the content of iron-bearing minerals and silicoide minerals in the Deng IV Member reservoir is low, and the reaction rate of dolomite with dilute hydrochloric acid is slow. Therefore, hydrochloric acid can be selected as the working fluid for acidification of ultradeep carbonate gas reservoirs.

(6) The permeability stress sensitivity characteristics of fracture-cavity type reservoirs can be divided into three stages. The first stage is the rapid decline stage of permeability dominated by microfractures. The preferential closure of fractures will lead to a significant reduction in reservoir permeability. The second stage is the slow decline stage of permeability dominated by cavities and macroscopic pore throats. The relative change of pore throat radius has little effect on the absolute percolation capacity of macroscopic pore throats and cavities. The third stage is the extremely slow decline stage of permeability dominated by rock minerals. The ultradeep carbonate reservoirs dominated by dolomite are highly resistant to compression, and it is difficult to cause a significant decrease in permeability unless the rock is fractured or broken. The permeability stress sensitivity characteristics of cavity type reservoirs correspond to the latter two stages of fracture-cavity type reservoirs. The first stage of the permeability stress sensitivity characteristic of pore type reservoirs is the moderate decline stage of permeability dominated by microscopic pore throats. This is because the relative change of the pore throat radius has a great effect on the absolute percolation capacity of the microscopic pore throat. Moreover, the closure of key percolation channels has a great negative impact on the overall percolation capacity because of the poor pore throat connectivity of pore type reservoirs.

(7) The irreversible permeability loss rates of the three types of reservoirs during stress unloading can be divided into a slow increasing stage and a relatively rapid increasing stage. The permeability recovery characteristics of fracture-cavity type samples reflect that reopened fractures can increase the permeability recovery rate, but the complete closure of most fractures greatly increases the irreversible permeability. The permeability recovery characteristics of cavity type samples reflect that the irreversible permeability loss caused by the rock framework compression is extremely small, and the compressed cavities and macroscopic pore throats can be greatly recovered during the stress unloading process. The stress sensitivity characteristics of pore type reservoirs with relatively high permeability are similar to those of cavity type reservoirs,

but the stress sensitivity degree of pore type reservoirs with extremely low permeability is close to that of fracture-cavity type reservoirs.

(8) The porosity stress sensitivity characteristics of three types of reservoirs can be divided into the same stages as the permeability sensitivity characteristics because the action mechanism and relative variation degree of porosity stress sensitivity at each stage are similar to those of permeability. However, the loss degree of porosity during the stress loading process is obviously weaker than that of permeability, whereas the recovery degree of porosity during the stress unloading process is generally greater than that of permeability.

(9) The stress sensitivity degrees of fracture-cavity type, cavity type and pore type reservoirs are moderately strong, moderately weak to weak, and moderately strong to moderately weak, respectively. Therefore, fracture-cavity type reservoirs should be exploited under a relatively low production pressure differential to avoid rapid closure of microfractures. However, relatively high production pressure differentials can increase gas production of cavity type reservoirs without causing a significant decrease in permeability. Pore type reservoirs can be used as peripheral replenishment reservoirs to avoid a dramatic decrease in permeability caused by a rapid increase in effective stress. The stress sensitivity recovery degrees of fracture-cavity type, cavity type and pore type samples are moderately weak to moderately strong, moderately strong to strong, and moderately strong, respectively. Therefore, the method of restoring reservoir pressure through shut-in operation to increase permeability is only suitable for cavity type reservoirs. Additionally, the porosity of fracture-cavity type and low-permeability pore type reservoirs should be corrected frequently during gas reservoir development, especially in the early stage of exploitation.

(10) The power function model has the highest correlation with the stress sensitivity data of ultradeep carbonate gas reservoirs, and the stress sensitivity index can be used as a parameter to compare the stress sensitivity degree of different reservoirs. The comparison results of stress sensitivity index show that the stress sensitivity of the three types of samples under conventional conditions is weaker than that under reservoir conditions, especially the fracture-cavity type samples. Besides, the permeability loss rates of fracture-cavity type, cavity type and pore type samples predicted by the stress sensitivity formula under conventional conditions are 16.64%, 12.21% and 13.29% lower than those under actual reservoir conditions, respectively. Therefore, it is necessary to conduct stress sensitivity experiments of ultradeep carbonate gas reservoirs under reservoir conditions to provide accurate stress sensitivity parameters.

(11) The distribution range of the stress sensitivity indices of fracture-cavity type samples is relatively concentrated, and the correlation between the index and the initial permeability is poor. The average value of existing stress sensitivity indices can be applied to reservoirs without stress sensitivity data. The more developed the fracture, the higher the initial permeability, the greater the permeability contributed by the fracture, and the greater the permeability loss due to stress sensitivity. The distribution ranges of the stress sensitivity indices of cavity type and pore type samples are both relatively wide and have

a good correlation with the initial permeability. The higher the permeability of the cavity type reservoir, the more developed bedding cavities and macroscopic pore throats, and the smaller the permeability loss due to the stress sensitivity effect. The macroscopic pore throat number and pore throat coordination number gradually increase with the increase of the initial permeability of pore type reservoirs, thereby weakening the effect of stress sensitivity on permeability. Nevertheless, the value and variation range of the stress sensitivity index of the pore type reservoir are smaller than those of the cavity type reservoir. The stress sensitivity characteristics of cavity type and pore type reservoirs in different regions can be predicted by the fitting formula.

References

Alam, A. K. M. B., Niioka, M., Fujii, Y., Fukuda, D., & Kodama, J. I. (2014). Effects of confining pressure on the permeability of three rock types under compression. *International Journal of Rock Mechanics and Mining Sciences, 65*(1), 49–61.

Amorim, C. L. G., Lopes, R. T., Barroso, R. C., Queiroz, J. C., Alves, D. B., et al. (2007). Effect of clay–water interactions on clay swelling by X-ray diffraction. *Nuclear Instruments and Methods in Physics Research A, 580*(1), 768–770.

Bazin, B., Bekri, S., Vizika, O., Herzhaft, B., & Aubry, E. (2010). Fracturing in tight gas reservoirs: Application of special-core-analysis methods to investigate formation-damage mechanisms. *SPE Journal, 15*(4), 969–976.

Bedrikovetsky, P., Siqueira, F. D., Furtado, C. A., & Souza, A. L. S. (2011). Modified particle detachment model for colloidal transport in porous media. *Transport in Porous Media, 86*(2), 353–383.

Bedrikovetsky, P., Zeinijahromi, A., Siqueira, F. D., Furtado, C. A., & de Souza, A. L. S. (2012). Particle detachment under velocity alternation during suspension transport in porous media. *Transport in Porous Media, 91*(1), 173–197.

Bennion, D. B. (2002). An overview of formation damage mechanisms causing a reduction in the productivity and injectivity of oil and gas producing formations. *Journal of Canadian Petroleum Technology, 41*(11), 29–36.

Cao, N., & Lei, G. (2019). Stress sensitivity of tight reservoirs during pressure loading and unloading process. *Petroleum Exploration and Development, 46*(1), 138–144.

Dou, H. E., Zhang, H. J., Yao, S. L., Zhu, D., Sun, T., et al. (2016). Measurement and evaluation of the stress sensitivity in tight reservoirs. *Petroleum Exploration and Development, 43*(6), 1116–1123.

Eleri, O. O., & Ursin, J. R. (1992). Physical aspects of formation damage in linear flooding experiments. SPE-23784-MS

Elraies, K. A., & Basbar, A. E. (2015). The effect of water salinity on silica dissolution rate and subsequent formation damage during chemical EOR process. *Journal of Petroleum & Environmental Biotechnology, 2015, 6*(2), 1000209.

Fatt, I., & Davis, D. (1952). Reduction in permeability with overburden pressure. *Journal of Petroleum Technology., 4*(12), 16.

Gao, S. S., Liu, H. X., Ren, D., Hu, Z. M., & Ye, L. Y. (2015). Deliverability equation of fracture-cave carbonate reservoirs and its influential factors. *Natural Gas Industry, 35*(9), 48–54.

Gardner, K. H., & Arias, M. S. (2000). Clay swelling and formation permeability reductions induced by a nonionic surfactant. *Environmental Science & Technology, 34*(1), 160–166.

Ge, Z. X., Liu, W. D., & Huang, Y. Z. (2006). A study on formation damage caused by alkali in ASP flooding system. *Oilfield Chemistry, 23*, 362–364.

Guo, T. K., Gong, F. C., Lin, X., Lin, Q., & Wang, X. Z. (2018). Experimental investigation on damage mechanism of guar gum fracturing fluid to low-permeability reservoir based on nuclear magnetic resonance. *Journal of Energy Resources Technology, 140*(7), 072906.

Gupta, V., Hampton, M. A., Stokes, J. R., Nguyen, A. V., & Miller, J. D. (2011). Particle interactions in kaolinite suspensions and corresponding aggregate structures. *Journal of Colloid and Interface Science, 359*(1), 95–103.

Jia, C. J., Xu, W. Y., Wang, H. L., Wang, R. B., Jun, Y., et al. (2017). Stress dependent permeability and porosity of low-permeability rock. *Journal of Central South University, 24*(10), 2396–2405.

Johnston, N., & Beeson, C. M. (1945). Water permeability of reservoir sands. *Transactions of the AIME, 160*(1), 43–55.

Jones, F. O. (1975). A laboratory study of the effects of confining pressure on fracture flow and storage capacity in carbonate rocks. *International Journal of Rock Mechanics and Mining Sciences & Geomechanics Abstracts, 12*(4). 55–0148906275900273. https://doi.org/10.1016/0148-9062(75)90027-3

Kang, Y. L., Xu, C. Y., You, L. J., Yu, H. F., & Zhang, B. J. (2014). Comprehensive evaluation of formation damage induced by working fluid loss in fractured tight gas reservoir. *Journal of Natural Gas Science and Engineering, 18*, 353–359.

Kang, Y. L., Xu, C. L., You, L. J., Tang, L., & Lian, Z. (2015). Comprehensive prediction of dynamic fracture width for formation damage control in fractured tight gas reservoir. *International Journal of Oil Gas and Coal Technology, 9*(3), 296–310.

Kang, M. S., Watabe, Y., & Tsuchida, T. (2003). Effect of drying process on the evaluation of microstructure of clays using scanning electron microscope (SEM) and mercury intrusion porosimetry (MIP). ISOPE-I-03-138

Khilar, K. C., & Fogler, H. S. (1984). The existence of a critical salt concentration for particle release. *Journal of Colloid and Interface Science, 101*(1), 214–224.

Liao, J., Tang, H., Zhu, X., Ren, M., Zhen, S., et al. (2012). Water sensitivity experiment and damage mechanism of sandstone reservoirs with ultra-low permeability: A case study of the eighth oil layer in the Yanchang Formation of Xifeng oilfield, Ordos Basin. *Oil & Gas Geology, 33*(2), 321–328.

Liu, H. X., Ren, D., Hu, Z. M., & An, W. G. (2014). Establishment and application of seepage mathematical model of Longwangmiao Fm gas reservoirs in the Sichuan Basin. *Natural Gas Industry, 34*(3), 110–114.

Liu, Z. S., Liu, D. M., Cai, Y. D., & Qiu, Y. K. (2020). Permeability, mineral and pore characteristics of coals response to acid treatment by NMR and QEMSCAN: Insights into acid sensitivity mechanism. *Journal of Petroleum Science and Engineering, 198*, 108205.

Liu, Z. Q., Shi, B. B., Ge, T. C., Sui, F. G., Wang, Y., et al. (2021). Tight sandstone reservoir sensitivity and damage mechanism analysis: a case study from Ordos Basin, China and implications for reservoir damage prevention. *Energy Geoscience*, B4.

Ma, K., Jiang, H. Q., Li, J. J., & Zhao, L. (2016). Experimental study on the micro alkali sensitivity damage mechanism in low-permeability reservoirs using QEMSCAN. *Journal of Natural Gas Science and Engineering, 36*, 1004–1017.

Mcglade, C., Speirs, J., & Sorrell, S. (2013). Unconventional gas—a review of regional and global resource estimate. *Energy, 55*, 571–584.

Mohnot, S. M., Bae, J. H., & Foley, W. L. (1987). A study of mineral/alkali reactions. *SPE Reservoir Engineering, 2*(4), 653–663.

Rahimi, S., & Hosseini, M. (2015). Laboratory studies of creep behavior on thick-walled hollow cylindrical salt rock specimens. *Arabian Journal of Geosciences, 8*(8), 5949–5957.

Rahman, S. S., Rahman, M. M., & Khan, F. A. (1995). Response of low-permeability, illitic sandstone to drilling and completion fluids. *Journal of Petroleum Science and Engineering, 12*, 309–322.

Rashid, F., Glover, P. W. J., Lorinczi, P., Hussein, D., & Lawrence, J. A. (2017). Microstructural controls on reservoir quality in tight oil carbonate reservoir rocks. *Journal of Petroleum Science and Engineering, 156*, 814–826.

Ru, Z., An, K., & Hu, J. (2019). The impact of sulfur precipitation in developing a sour gas reservoir with pressure-sensitive effects. *Advances in Geo-Energy Research, 3*(3), 268–276.

Tan, Q. G., Kang, Y. L., You, L. J., Xu, C. Y., Zhang, X. W., et al. (2021a). Stress-sensitivity mechanisms and its controlling factors of saline-lacustrine fractured tight carbonate reservoir. *Journal of Natural Gas Science and Engineering, 88*, 103864.

Tan, Q. G., You, L. J., Kang, Y. L., & Xu, C. Y. (2021b). Formation damage mechanisms in tight carbonate reservoirs: The typical illustrations in Qaidam Basin and Sichuan Basin, China. *Journal of Natural Gas Science and Engineering, 95*, 104193.

Tang, Y., Yang, R., Du, Z., & Zeng, F. (2015). Experimental study of formation damage caused by complete water vaporization and salt precipitation in sandstone reservoirs. *Transport in Porous Media, 107*(1), 205–218.

Tao, S., Tang, D. Z., Xu, H., Li, S., Geng, Y. G., et al. (2017). Fluid velocity sensitivity of coal reservoir and its effect on coalbed methane well productivity: A case of Baode Block, northeastern Ordos Basin, China. *Journal of Petroleum Science and Engineering, 152*, 229–237.

Wang, B. Y., Qin, Y., Shen, J., Wang, G., & Zhang, Q. S. (2018a). Influence of stress and formation water properties on velocity sensitivity of lignite reservoir using simulation experiment. *Fuel, 224*, 579–590.

Wang, L., Yang, S. L., Meng, Z., Chen, Y. Z., Qian, K., et al. (2018b). Time-dependent shape factors for fractured reservoir simulation: Effect of stress sensitivity in matrix system. *Journal of Petroleum Science and Engineering, 163*, 556–569.

Wang, B. Y., Qin, Y., Shen, J., Wang, G., Zhang, Q. S., et al. (2019). Experimental study on water sensitivity and salt sensitivity of lignite reservoir under different pH. *Journal of Petroleum Science and Engineering, 172*, 1202–1214.

Wang, L., He, Y. M., Peng, X., Deng, H., Liu, Y. C., et al. (2020). Pore structure characteristics of an ultradeep carbonate gas reservoir and their effects on gas storage and percolation capacities in the Deng IV member, Gaoshiti-Moxi Area, Sichuan Basin, SW China. *Marine and Petroleum Geology, 111*, 44–65.

Wang, Z. Y., Li, H. X., Lan, X. M., Wang, K., Yang, Y. F., et al. (2021). Formation damage mechanism of a sandstone reservoir based on micro-computed tomography. *Advances in Geo-Energy Research, 5*(1), 25–38.

Wilson, M. J., Wilson, L., & Patey, I. (2014). The influence of individual clay minerals on formation damage of reservoir sandstones: A critical review with some new insights. *Clay Minerals, 49*(2), 147–164.

Wu, X. H., Pu, H., Zhu, K. L., & Lu, S. Q. (2017). Formation damage mechanisms and protection technology for Nanpu nearshore tight gas reservoir. *Journal of Petroleum Science and Engineering, 158*, 509–515.

Xiao, W. L., Li, T., Li, M., Zhao, J. Z., Zheng, L. L., et al. (2016). Evaluation of the stress sensitivity in tight reservoirs. *Petroleum Exploration and Development, 43*(1), 115–123.

Xu, C. Y., Kang, Y. L., You, Z. J., Chen, M. J., et al. (2016). Review on formation damage mechanisms and processes in shale gas reservoir: Known and to be known. *Journal of Natural Gas Science and Engineering, 36*, 1208–1219.

Xu, C., Lin, C., Kang, Y., & You, L. (2018a). An experimental study on porosity and permeability stress-sensitive behavior of sandstone under hydrostatic compression: Characteristics, mechanisms and controlling factors. *Rock Mechanics and Rock Engineering, 51*(8), 2321–2338.

Xu, C., You, Z., Kang, Y., & You, L. (2018b). Stochastic modelling of particulate suspension transport for formation damage prediction in fractured tight reservoir. *Fuel, 221*, 476–490.

Yang, S., Sheng, Z., Liu, Z., Song, Z., Wu, M., et al. (2008). Evaluation and prevention of formation damage in offshore sandstone reservoirs in China. *Petroleum Science, 5*(4), 340–347.

Yuan, B., & Wood, D. A. (2018). A comprehensive review of formation damage during enhanced oil recovery. *Journal of Petroleum Science and Engineering, 167*, 287–299.

Yuan, B., Moghanloo, R. G., & Zheng, D. (2016). Analytical solution of nanoparticles utilization to reduce fines migration in porous medium. *SPE Journal, 21*(6), 2317–2332.

Zhang, S. H. (1993). *Reservoir protection technology*. Petroleum Industry Press.

Zhang, W. T., Wang, Q., Ning, Z. F., Zhang, R., Huang, L., et al. (2018). Relationship between the stress sensitivity and pore structure of shale. *Journal of Natural Gas Science and Engineering, 59*, 440–451.

Zhang, L. F., Zhou, F. J., Zhang, S. C., Li, Z., Wang, J., et al. (2019). Evaluation of permeability damage caused by drilling and fracturing fluids in tight low permeability sandstone reservoirs. *Journal of Petroleum Science and Engineering, 175*, 1122–1135.

Zhang, L. F., Zhou, F. J., Pournik, M., Liang, T. B., Wang, J., et al. (2020). An integrated method to evaluate formation damage resulting from water and alkali sensitivity in dongping bedrock reservoir. *SPE Reservoir Evaluation & Engineering, 23*(1), 187–199.

Zhao, X., Qiu, Z. S., Sun, B. J., Liu, S. J., Xing, X. J., et al. (2019). Formation damage mechanisms associated with drilling and completion fluids for deep-water reservoirs. *Journal of Petroleum Science and Engineering, 173*, 112–121.

Zheng, J., Zheng, L., Liu, H., & Ju, Y. (2015). Relationships between permeability, porosity and effective stress for low-permeability sedimentary rock. *International Journal of Rock Mechanics and Mining Sciences, 78*, 304–318.

Chapter 5
Gas Production Characteristics of the Heterogeneous Ultradeep Carbonate Gas Reservoir

Multilayer commingled production is an important development method for most hydrocarbon reservoirs because there are multiple profitable production layers vertically. Commingled production method can not only reduce drilling cost, but also improve hydrocarbon reservoir recovery. The investigation of gas production characteristics of multilayer commingled production in gas reservoirs can not only reflect the effect of interlayer heterogeneity on the percolation law, but also reveals the reserves mobility and gas production capacity of different gas layers. However, the differences in petrophysical properties, temperature and pressure conditions, gas saturation, effective thickness and geometric parameters of different gas layers make the gas production characteristics of each layer complicated during multilayer commingled production.

According to previous studies, the investigation methods of commingled production mainly include well testing analysis, numerical simulation and physical simulation experiment. Arevalo-Villagran et al. (2000) established a mathematical model of gas flow for commingled production reservoirs based on well test theory and single-layer testing data. Yang et al. (2012) analyzed the gas production capacity of a single layer and evaluated the effect of commingled production through a single-well numerical model established by the reservoir description results and well testing data. Peng et al. (2014) determined the factors affecting the commingled production performance of CBM wells through correlation analysis, and evaluated the influence degree of these factors through grey correlation analysis. Zhao and Wang (2019) conducted numerical simulations for two-seam commingled production of CBM using the gray lattice Boltzmann model, and then reveal the effect of interlayer heterogeneity on the commingled production. However, both well testing analysis and numerical simulation methods require several assumptions and simplifications in modeling and calculations because the percolation mechanism during commingled production is extremely complex (Wang et al., 2021). Therefore, it is difficult to fully simulate the actual commingled production process only by numerical simulation and well test analysis. In contrast, the physical simulation experimental results based on the similarity principle are more consistent with the actual situation because typical

© The Author(s), under exclusive license to Springer Nature Singapore Pte Ltd. 2023

L. Wang, *Ultradeep Carbonate Gas Reservoirs*,
https://doi.org/10.1007/978-981-19-9708-2_5

rock and fluid samples and fully need to be selected to fully simulate reservoir and production conditions. You et al. (2012) studied the characteristics and influencing factors of commingled production in tight sandstone gas reservoirs by establishing a physical simulation model of commingled production. Xu et al. (2018) developed a apparatus for commingled production of multilayer superposed CBM system, and then investigate the gas production characteristics and recovery factor of each single coal layer. Tan et al. (2019) conducted a series of experiments to reveal the wellbore inflow characteristics and influencing factors of sulfur gas reservoirs under commingled production conditions. Liu et al. (2020) developed an experimental technique to evaluate the commingled production performance of tight sandstone gas reservoirs with interlayer interference. Therefore, previous studies on physical simulation of multilayer commingled production mainly focus on tight sandstone gas reservoirs and CBM reservoirs. The complex connection of pores, cavities and fractures and the ultra-high temperature and pressure conditions further increase the difficulty of studying the gas production characteristics of multilayer commingled production in ultradeep carbonate gas reservoirs (Wang et al., 2017). The purpose of this chapter is to reveal the gas production characteristics and influencing factors of different types of reservoirs during multilayer commingled production by conducting a series of physical simulation experiments.

In addition, the heterogeneity of ultradeep carbonate gas reservoir is reflected not only between multiple gas layers in the vertical direction, but also between multiple regions in the horizontal direction. However, previous studies on the effect of horizontal heterogeneity on reservoir production characteristics mainly focused on the petrophysical property difference in different regions (Guo et al., 2021; Hu et al., 2022; Li et al., 2020; Ma et al., 2018; Naderi et al., 2015; Tian et al., 2019). The multiscale pore throats, cavities and fractures of ultradeep carbonate gas reservoirs are unevenly distributed in the horizontal direction of a single gas layer. Therefore, there may be various types of reservoir arrangements and combinations in the gas well control zone. Simply studying the permeability difference cannot truly reflect the horizontal heterogeneity of this type of gas reservoir. Fracture-cavity type reservoirs have excellent storage and percolation capacities, and are the preferred choice for well location in ultradeep carbonate gas reservoirs. However, the pore type and cavity type reservoirs may be distributed in the periphery of the fracture-cavity type reservoir, resulting in complex and variable gas production mechanisms in horizontal heterogeneous gas reservoirs. The purpose of this chapter is also to study the effect of the horizontal heterogeneity and relevant factors on gas production characteristics and gas production capacity of different types of reservoirs in ultradeep carbonate gas reservoirs. Finally, some suggestions for exploration and development to improve the gas production capacity and ultimate recovery factor of heterogeneous carbonate gas reservoirs were put forward based on the physical simulation experimental results.

5.1 Gas Production Characteristics of Interlayer Heterogeneous Gas Reservoirs

5.1.1 Experimental Objective

Six representative core samples were selected from pore type, cavity type and fracture-cavity type carbonate reservoirs, and a physical simulation model of multilayer commingled production under ultra-high temperature and pressure conditions was established based on the similarity principle. Subsequently, an experimental program for multilayer commingled production was designed based on the actual reservoir characteristics and exploitation project of the Deng IV Member gas reservoir. The physical simulation experiment can not only simulate the exploitation process of actual reservoirs, but also study the influence of multiple factors on the simulation results to obtain production dynamic parameters, including instantaneous gas production, cumulative gas production, gas layer pressure, recovery factor, and gas production contribution ratio, etc. (Xu et al., 2018). Therefore, the gas production characteristics and gas supply capacity of three types of carbonate core samples during multilayer commingled production were revealed by processing and analyzing these parameters. Then, the effects of interlayer heterogeneity, permeability difference, depletion pressure differential, initial water saturation and water encroachment on the gas production characteristics of multilayer commingled production were also analyzed. Finally, a radial numerical model of multilayer commingled production was established by Eclipse software to verify the applicability of the experimental results at the gas reservoir scale. The relevant research results can provide a theoretical basis for the formulation of multilayer commingled production scheme and production capacity evaluation of ultradeep carbonate gas reservoirs.

5.1.2 Similarity Principle

The similarity principle is the premise of using the physical simulation experiment technique to study the fluid dynamics characteristics during the actual production process of hydrocarbon reservoirs (Wang et al., 2021). Therefore, four aspects of similarities were designed according to the requirement of similarity principle in the multilayer commingled production simulation experiment.

(1) Similarity in rock and fluid properties: representative natural cores of ultradeep carbonate gas reservoirs were selected according to the petrophysical properties of different types of reservoirs, and the experimental water with the same composition as the formation water was also prepared.
(2) Similarity in multilayer commingled production mode: natural carbonate cores of three different types of reservoirs were in parallel connection in the experiment to simulate the multilayer commingled production mode of a gas well,

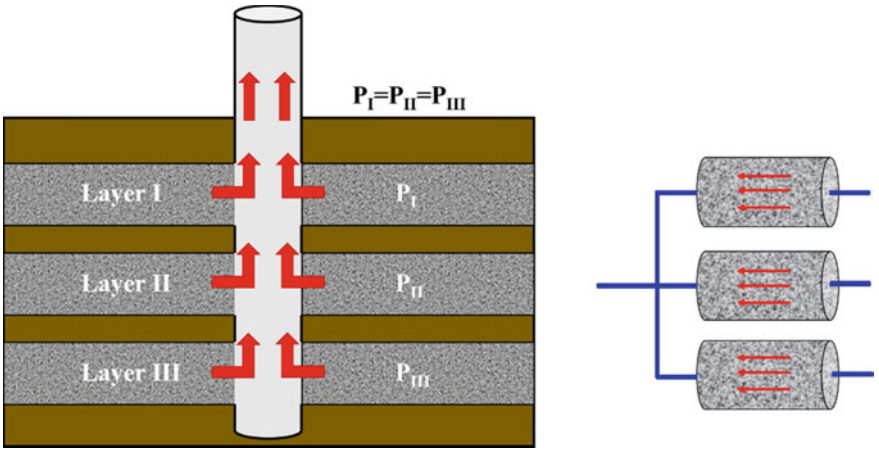

Fig. 5.1 Schematic diagram of multilayer commingled production process and cores connection

as shown in Fig. 5.1. The experiment was conducted in the constant volume depletion mode according to the actual exploitation project of the gas reservoir.

(3) Similarity in the initial conditions: a set of ultra-high temperature and pressure physical simulation experiment system was designed and assembled to simulate the initial reservoir conditions of the ultradeep carbonate gas reservoir.

(4) Similarity in production conditions: the experimental pressure differential was designed according to the pressure differential converted from the production pressure differential by similarity.

5.1.3 Experimental Samples and Conditions

The plunger cores used in the multilayer commingled production experiment were taken from the Deng IV Member of the Sinian System in the Sichuan Basin. Two cores were selected from pore type, cavity type and fracture-cavity type reservoirs respectively according to the reservoir type and heterogeneity characteristics. In addition, each type of core was classified into Class I and Class II according to the relative magnitude of permeability. The end faces of these cores were cut and polished using a diamond wire cutting machine. The petrophysical parameters of these plunger cores are summarized in Table 5.1. It has been introduced in Chap. 1 that each gas layer in the Deng IV Member belongs to a set of temperature and pressure system. Therefore, the temperature and pressure of the multilayer commingled production experiment were designed according to the ultra-high temperature and pressure conditions of the Deng IV Member reservoir. The experimental temperature is 150 °C, the confining pressure is 138 MPa, and the initial pore pressure is 56 MPa. High-purity nitrogen was used as the experimental gas to simulate natural gas because the use of natural gas for ultra-high temperature and pressure experiments can easily cause powerful

Table 5.1 Petrophysical parameters of core samples used in multilayer commingled production experiments

Core number	Length/cm	Diameter/cm	Porosity/%	Permeability/mD	Core type	Core class
G23	3.93	2.528	4.05	0.038	Pore type	Class I
M35	4.48	2.494	3.73	0.010	Pore type	Class II
G39	4.05	2.518	6.55	0.376	Cavity type	Class I
G28	4.04	2.510	5.83	0.101	Cavity type	Class II
G40	4.37	2.510	3.35	8.681	Fracture-cavity type	Class I
M17	3.23	2.500	5.04	2.451	Fracture-cavity type	Class II

Table 5.2 Chemical composition of formation water in Deng IV Member

Positive ions (mg/L)					Negative ions (mg/L)			Mineralization degree (mg/L)	Water type
K^+	Na^+	Ca^{2+}	Mg^{2+}	Ba^{2+}	HCO_3^-	Cl^-	$SO4_2^-$		
2596	34,527	1762	233	1467	716	63,596	119	106,241	$CaCl_2$

combustion and explosions. The experimental water was prepared in lab based on the chemical composition of the formation water in the Deng IV Member, as shown in Table 5.2. It should be noted that the experimental water preparation was performed in the reactor rather than in the glass container. The temperature and pressure of the reactor should be maintained continuously after water sample preparation to prevent salt precipitation from water. The prepared experimental water sample was used to establish different initial water saturation for core samples. The gas Mass Flow Controller (MFC) is generally used to simulate the exploitation mode of constant volume and constant production, but only suitable for conventional temperature and pressure conditions. The ultra-high temperature and pressure conditions of ultra-deep carbonate gas reservoirs exceed the withstand range of the MFC. Therefore, the constant volume and constant pressure exploitation mode was selected for the experiment. This exploitation mode can also prevent gas wells from producing water by controlling the production pressure differential.

5.1.4 Experimental Apparatus

The multilayer commingled production experiments of ultradeep carbonate gas reservoirs under formation conditions were conducted on the ultra-high temperature and

pressure physical simulation experiment system. The experimental system can be divided into four subsystems, namely injection system, pressurization system, core system and data collection system (Fig. 5.2a). Except for the core system, the apparatus of the other three systems are the same as those introduced in Chap. 2. The core system consists of three core holders connected in parallel by pipelines and valves, and each core holder was surrounded by a heating jacket (Fig. 5.2b). In addition, the inlet and outlet ends of each core holder were equipped with pressure sensors to measure and record the pressure variations of different core samples.

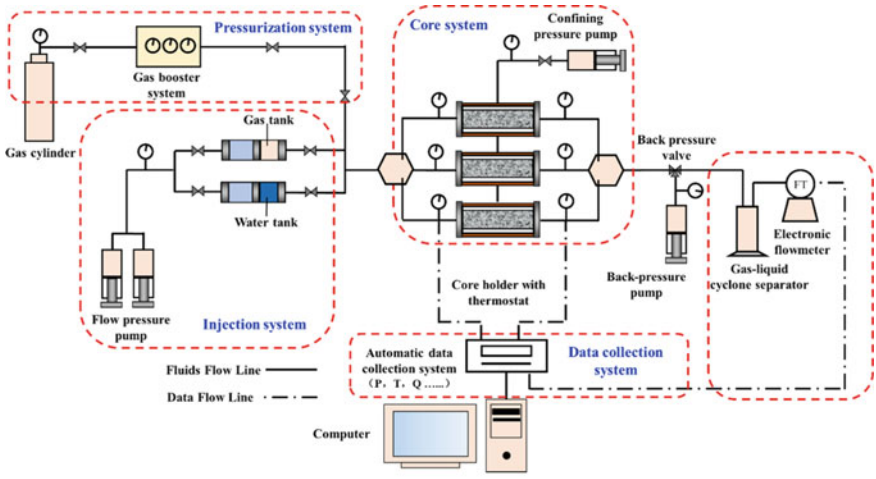

(a) Flow chart of physical simulation experiment system of multilayer commingled production

(b) Photograph of three core holders connected in parallel

Fig. 5.2 Schematic diagram of the physical simulation experiment system of multilayer commingled production

5.1.5 Experimental Scheme

The physical simulation experiment program of multilayer commingled production consists of five sets of experiments. (1) Class I core samples of pore type, cavity type and fracture-cavity type were placed in core holders for "parallel connection" experiments to study the gas production characteristics of different types of reservoirs during multilayer commingled production. (2) Class I core samples of pore type, cavity type and fracture-cavity type were replaced with the corresponding Class II core samples one by one for comparative experiments to study the effect of interlayer heterogeneity on the gas production characteristics of multilayer commingled production. (3) The effect of different depletion pressure differentials (1, 3 and 5 MPa) on the gas production characteristics were studied by changing the back pressure. (4) The effect of different initial water saturations on gas production characteristics was studied by using capillary imbibition to establish water saturations (10, 30, 50 and 80%) in three types of cores (You et al., 2005). (5) The effect of water encroachment on the gas production characteristics of multilayer commingled production was studied by the method of constant pressure water flooding at the inlet end. The parameters of experimental program are shown in Table 5.3.

The measured irreducible water saturations of fracture-cavity type, cavity type and pore type core samples are 13%–18%, 19%–23% and 22%–30%, respectively. The initial water saturation of the three types of cores was set below the irreducible water

Table 5.3 Experimental scheme of physical simulation of multilayer commingled production

Experiment type	Core type	Depletion pressure differential/MPa	Initial water saturation/%
Effect of interlayer heterogeneity on gas production characteristics	①, ②, ③	3	10
	④, ②, ③		
	①, ⑤, ③		
	①, ②, ⑥		
Effect of depletion pressure differential on gas production characteristics	①, ②, ③	1	10
		3	
		5	
Effect of initial water saturation on gas production characteristics	①, ②, ③	3	10
			30
			50
			80
Effect of water encroachment on gas production characteristics	①, ②, ③	3	10

Notes ① represents the pore type core of Class I; ② represents the cavity type core of Class I; ③ represents the fracture-cavity type core of Class I; ④ represents the pore type core of Class II; ⑤ represents the cavity type core of Class II; ⑥ represents the fracture-cavity type core of Class II

saturation when studying the effects of interlayer heterogeneity, depletion pressure differential and water encroachment on the gas production characteristics of multilayer commingled production. The reason for this setting is to ensure the uniqueness of variables and avoid the effect of the initial gas–water two-phase percolation on the experimental results. The well log interpretation data show that the water saturation in the study area is mainly distributed between 9 and 75%, so the initial water saturation of all experimental cores is set at about 10%.

5.1.6 Experimental Procedure

The detailed experimental procedure of the multilayer commingled production experiment under ultra-high temperature and pressure conditions is as follows. (1) The gas in the intermediate container was pressurized to 50 MPa through the gas booster system, and then connected to the experimental system. (2) The cleaned and dried cores were saturated with simulated formation water by to the set value by capillary imbibition method, and then the cores were placed in the core holders and the experimental system was connected according to Fig. 5.2a. (3) The confining pressure of the core system was increased to 5 MPa by the confining pressure pump. (4) The temperature of the core system is increased to 150 °C by the electric heating jacket, and the confining pressure automatically increased with the increase of pore pressure during the heating process through the pressure tracking function. (5) The valve of the intermediate container was opened slowly to let the gas enter the core system when the temperature was stabilizes at 150°C. The pore pressure of the core system gradually increased to 50 MPa, and the confining pressure also increased to 55 MPa with the increase of pore pressure. (6) The pore pressure and confining pressure were gradually increased to 56 and 138 MPa by the flow pressure pump and the confining pressure pump. The initial temperature and pressure conditions of the reservoir were finally established when the upstream and downstream pressures of the core system stabilized. (7) The inlet valve of the core system was closed, and the outlet pressures (55, 53 and 51 MPa) were set through the back-pressure pump and back-pressure valve to simulate different depletion pressure differentials (1, 3 and 5 MPa). The instantaneous gas production and cumulative gas production at the outlet were measured by an electronic flowmeter and a high-precision balance, respectively. (8) The gas production contribution ratio is defined as the proportion of the total gas production produced by a single core sample to the total gas production of commingled production at a certain time (Liu et al., 2010). The sum of the gas production contribution ratios of the three cores is always 100%.

5.1.7 *Effect of Interlayer Heterogeneity on Gas Production Characteristics*

The multilayer commingled production simulation experimental results of the three types of core samples under the depletion pressure differential of 3 MPa are shown in Fig. 5.3. The experimental results show that the variation patterns and characteristics of the pressure and production contribution ratio of pore type, cavity type and fracture-cavity type samples are different during different stages of multilayer commingled production. The multilayer commingled produced process can be divided into three stages according to the gas production contribution ratio of different types of samples in different time periods. In the first stage of multilayer commingled production (0–50 s), the pressure of the fracture-cavity type sample decreases sharply, whereas the pressure variations of the pore type and cavity type samples lag behind that of the fracture-cavity type sample (Fig. 5.3a). It can be seen from the cumulative gas production curves that more than 85% of the gas in the fracture-cavity type sample was produced in the first stage, although the duration of this stage is short (Fig. 5.3b). Therefore, the fracture-cavity type is the dominant gas supply sample with a gas production contribution ratio of 40–60% (Fig. 5.3c). However, the gas production contribution ratios of the fracture-cavity type sample and the cavity type sample decreases rapidly and increases rapidly, respectively. The second stage of multilayer commingled production lasted for a relatively long time (50–230 s). The pressure drop of the fracture-cavity type sample is slowed down, while the pressure decrease rates of the cavity type and pore type samples were relatively high because of the influence of pressure drop hysteresis (Fig. 5.3a). The cumulative gas production curves show that the gas production capacity of the three types of samples is gradually weakened, especially the fracture-cavity type sample (Fig. 5.3b). Therefore, the production contribution ratio of the fracture-cavity type sample continues to decrease, whereas those of the cavity type and pore type samples gradually increase (Fig. 5.3c). Pore type and cavity type reservoirs with relatively low petrophysical properties become the dominant gas supply layers in the second stage. The third stage of multilayer commingled production lasted for a very long time (230–770 s). The upstream pressure of fracture-cavity type and cavity type samples is infinitely close to the downstream pressure, while the upstream pressure of the pore type sample is still higher than the downstream pressure (Fig. 5.3a). The cumulative gas production curves show that the gas produced in this stage is all supplied by the pore type sample with the lowest petrophysical properties, but the extremely low gas production and extremely long production time make the exploitation in this stage unprofitable (Fig. 5.3b). The production contribution ratio of the pore type sample increases slowly but not significantly, because the gas production provided by this stage is extremely small (Fig. 5.3c). It should be noted that the multilayer commingled production process is not affected by gas backflow because the initial pore pressure of the three cores is the same (Wang et al., 2021). Eventually, the contribution ratio of commingled gas production is fracture-cavity type, cavity type and pore type in order from high to low.

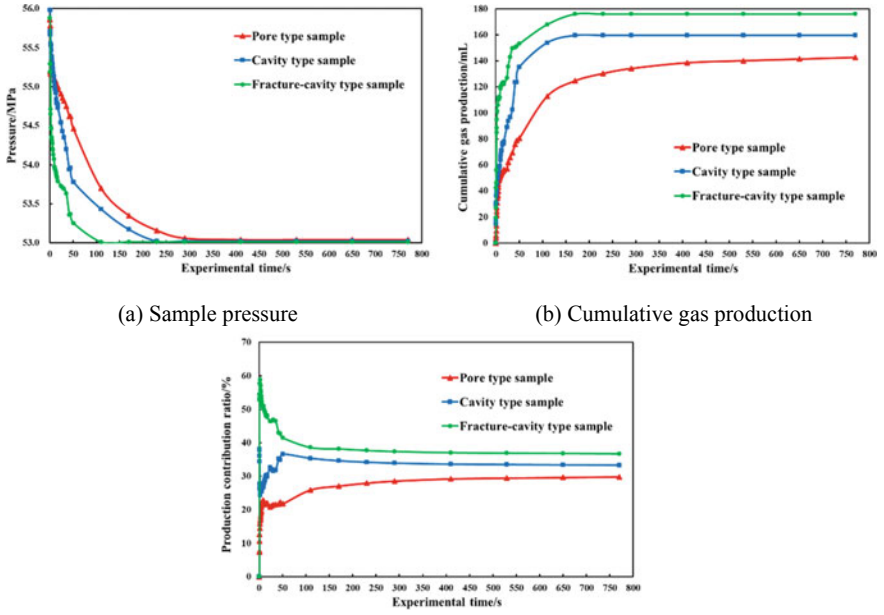

(a) Sample pressure

(b) Cumulative gas production

(c) Gas production contribution ratio

Fig. 5.3 Multilayer commingled production simulation experimental results of Class I samples under the depletion pressure differential of 3 MPa and initial water saturation of 10%

In summary, the production contribution ratio of the fracture-cavity type sample firstly decreases rapidly and then decreases slowly, that of the cavity type sample firstly increases rapidly and then decreases slowly, and that of the pore type sample continuously increase slowly. The proportion of cumulative gas production in different commingled production stages to total commingled gas production is shown in Fig. 5.4a. The gas production of the first, second and third stages of multilayer commingled production accounts for 69.79%, 24.43% and 5.78% of the total gas production, representing the high production, stable production and low production stages of gas wells, respectively. Therefore, the first stage of multilayer commingled production is the key to the development effect of interlayer heterogeneous reservoirs. The proportion of gas production in the first stage should be increased as much as possible while improving the ultimate commingled recovery factor. The gas production contribution ratios of different types of samples in different commingled production stages are illustrated in Fig. 5.4b. The fracture-cavity type, as the dominant gas supply sample in the first stage, provided 49.19% of the commingled gas production. In contrast, the pore type sample provided only 19.24% of the commingled gas production. The cavity type and pore type are the main gas supply samples in the second stage, providing 42.85% and 53.83% of the commingled gas production, respectively. Almost all of the commingled gas production in the third stage comes from the pore type sample. These data clearly shows the cooperative and alternate

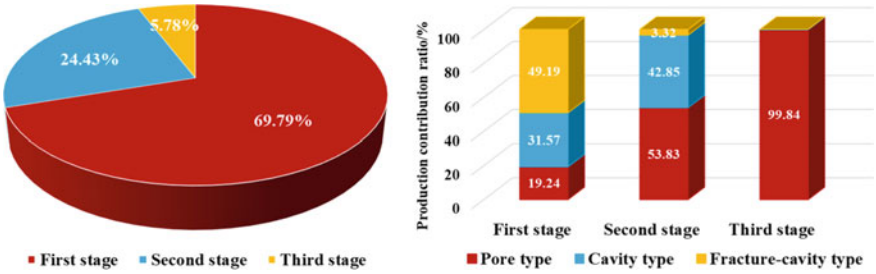

(a) Gas production proportion (b) Production contribution ratio

Fig. 5.4 Proportion and contribution ratio of gas production in different stages of multilayer commingled production

gas production characteristics of three different types of reservoirs in different stages of multilayer commingled production.

5.1.8 Effect of Permeability Differences on Gas Production Characteristics

Three types of core samples with different permeability were selected in turn for comparative experiments to reveal the effect of the permeability differences of the three types of reservoirs on the gas production capacity of multilayer commingled production. It should be noted that the permeability of Class II cores is lower than that of Class I cores in the same type of reservoir. The experimental results show that the variation laws of pressure, cumulative gas production and production contribution ratio of different core combinations are similar to those in Fig. 5.3. However, the values of single-layer recovery factor, production contribution ratio and commingled production recovery factor are different for different core combinations (Table 5.4). Both the production contribution ratio and the commingled production recovery factor of the pore type and cavity type samples decreased when the Class I sample was replaced by the Class II sample (④②③ and ①⑤③). Although the permeability reduction of the fracture-cavity type sample also reduced its production contribution ratio, it improved the commingled production recovery factor (①②⑥). The permeability of fracture-cavity type reservoirs is generally higher than that of cavity type and pore type reservoirs. Therefore, the permeability reduction of the fracture-cavity type sample means a decrease in the permeability difference between layers, while the permeability reduction of the other two types of samples means an increase in the permeability difference between layers. It can be concluded that the absolute value of the sample permeability affects its own production contribution ratio, and the greater the permeability, the greater the production contribution ratio. The relative value of the sample permeability affects the total recovery factor of commingled production,

and the smaller the permeability difference, the higher the commingle production recovery factor. In addition, the variation of permeability has little effect on the recovery factor of fracture-cavity type reservoirs, but has a great impact on pore type and cavity type reservoirs. Therefore, the stronger the interlayer heterogeneity of the ultradeep carbonate gas reservoir, the weaker the gas production capacity of each gas layer, and the lower the recovery factor of multilayer commingled production.

5.1.9 Effect of Depletion Pressure Differential on Gas Production Characteristics

The multilayer commingled production simulation experimental results of the three types of core samples under the depletion pressure differential of 5 and 1 MPa are illustrated in Figs. 5.5 and 5.6, respectively. The pressure drop rates of the three types of samples under the three depletion pressure differentials are always the highest in the fracture-cavity type and the lowest in the pore type by comparing the pressure variation curves. It reflects that the pressure drop rate of the gas layer during the multilayer commingled production process is related to its petrophysical properties (Fig. 5.5a). The better the petrophysical properties of the gas layer, the faster the pressure drop. However, this pressure variation difference between gas layers decreases as the depletion pressure differential decreases (Fig. 5.6a). It also reflects from the side that the relatively high depletion pressure differential will aggravate the effect of the interlayer pressure difference on gas production capacity of each gas layer during multilayer commingled production. When the initial depletion pressure differential is lower than a certain value, the pressure of the pore type and cavity type samples does not decrease until a period of time after the start of commingled production (Fig. 5.6a). This phenomenon can be explained by the presence of the threshold pressure effect in the ultradeep carbonate reservoirs with low permeability. Difference in pressure variations between different types of samples will inevitably lead to differences in gas production characteristics.

When the initial depletion pressure differential is relatively low (1 MPa), the superior gas production capacity of the fracture-cavity type sample cannot be fully exerted, and the gas production hysteresis phenomenon also occurs in the pore type and cavity type samples (Fig. 5.6b). Therefore, the instantaneous gas production and cumulative gas production of each sample are relatively low, and the cooperative gas supply capacity of multiple gas layers during commingled production is limited by the low pressure differential, which cannot effectively exert the efficient production capacity of gas wells. When the initial depletion pressure differential is relatively high (5 MPa), most of the gas in the fracture-cavity type sample is rapidly produced in a short time (Fig. 5.5b). Although the pore type and cavity type sample can maintain continuous gas supply, the gas supply capacity is limited. Therefore, the alternate gas supply capacity of multiple gas layers in commingled production is restricted by the high pressure differential, and it is difficult for gas wells to maintain

Table 5.4 Multilayer commingled production experimental results of core combinations with different permeability

Core combination type	Pore type		Cavity type		Fracture-cavity type		Recovery factor of commingled production/%
	Recovery factor%	Contribution ratio/%	Recovery factor%	Contribution ratio/%	Recovery factor%	Contribution ratio/%	
①②③	3.29	29.84	3.41	33.36	3.85	36.80	3.52
④②③	2.54	25.45	2.74	31.53	3.83	43.02	3.05
①⑤③	2.86	28.65	3.01	30.78	3.84	40.57	3.31
①②⑥	3.42	30.12	3.56	33.81	4.07	36.07	3.74

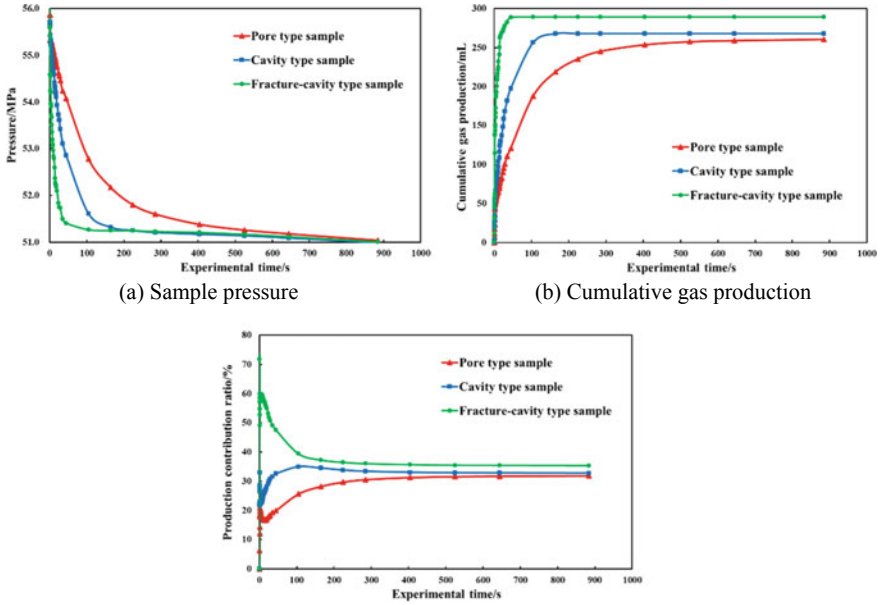

(a) Sample pressure

(b) Cumulative gas production

(c) Gas production contribution ratio

Fig. 5.5 Multilayer commingled production simulation experimental results of Class I samples under the depletion pressure differential of 5 MPa and initial water saturation of 10%

high gas production for a long time. When the initial depletion pressure is reasonable (3 MPa), the gas production contribution ratio of different types of reservoirs can quickly reach a stable level (Figs. 5.3c, 5.5c and 5.6c), and the cumulative gas production can maintain rapid growth for a relatively long period of time. Therefore, a reasonable production pressure difference can give full play to the cooperative gas production capacity and alternate gas production capacity of multiple gas layers during multilayer commingled production, and achieve the state of "dynamic replenishment balance". In other words, efficient and stable gas supply can be achieved between different types of reservoirs under a reasonable production pressure differential. This dynamic balance state will be disrupted if the initial pressure differential is too high or too low, thereby affecting the gas production capacity of each gas layer. In conclusion, the production pressure differential of multilayer commingled production in ultradeep carbonate gas reservoirs should be reasonably controlled, which can be determined by combining the results of physical simulation experiments and gas reservoir numerical simulations.

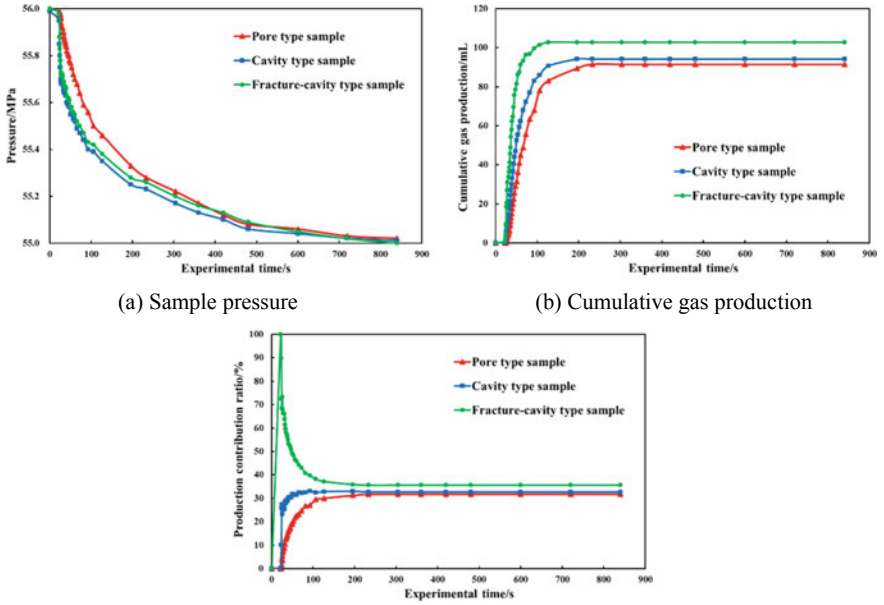

(a) Sample pressure

(b) Cumulative gas production

(c) Gas production contribution ratio

Fig. 5.6 Multilayer commingled production simulation experimental results of Class I samples under the depletion pressure differential of 1 MPa and initial water saturation of 10%

5.1.9.1 Effect of Initial Water Saturation on Gas Production Characteristics

The gas production curves of different initial water saturations show that both the instantaneous gas production and cumulative gas production of the three types of samples decrease significantly with the increase of initial water saturation, and the lower the sample petrophysical properties, the greater the decline in gas production capacity. When the initial water saturation is higher than the irreducible water saturation, the gas in the pore type and cavity type samples needs to overcome a certain viscous resistance to flow, while a small amount of formation water is produced at the outlet end of the fracture-cavity type sample. The multilayer commingled production simulation experimental results of the three types of core samples under different initial water saturations are illustrated in Fig. 5.7. The production contribution ratio of the fracture-cavity type sample increases rapidly with the increase of initial water saturation, whereas those of pore type and cavity type samples decrease. The higher the initial water saturation, the greater the variation of the production contribution ratios of the three types of samples. 80% of the commingled gas production is supplied by the fracture-cavity type sample when the initial water saturation reaches 80%, while the pore type sample only provides 4.5% of the total gas production.

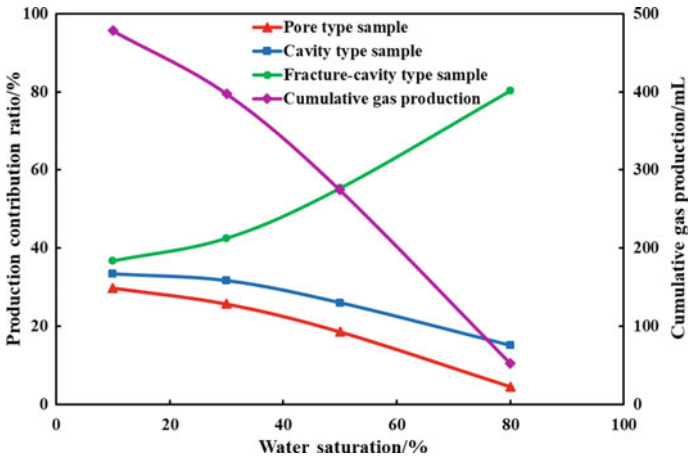

Fig. 5.7 Experimental results of multilayer commingled production of Class I core samples under different initial water saturation

This phenomenon can be explained from the two aspects of interlayer permeability difference and wellbore liquid accumulation both caused by high water saturation. In the first aspect, formation water tends to form a water film on the pore wall or a water wedge at the throat (You et al., 2006), thereby reducing the radius of the percolation channel or the connectivity between the pore and the throat. Pore type and cavity type samples have relatively small pore throat radius and relatively low coordination number, and the throat is the dominant channel for fluid percolation in the two types of samples. It has been introduced in Chap. 2 that the effect of movable water on the gas phase percolation capacity of pore type and cavity type reservoirs is much greater than that of fracture-cavity type reservoirs. Therefore, the gas-phase relative permeability of pore type and cavity type reservoirs decreases more than that of fracture-cavity type reservoirs at the same water saturation, thereby further exacerbating the interlayer permeability difference. The increase of interlayer permeability difference will lead to the reduction of the recovery factor of multilayer commingled production and the production contribution ratio of low-permeability gas layers. In the second aspect, the movable water in the fracture-cavity type reservoir flows rapidly to the well bottom along the dominant fractures, and gradually forms liquid accumulation in the wellbore and nearby areas. The accumulated water in the wellbore enters other gas layers with relatively low petrophysical properties through capillary imbibition, causing liquid phase retention in the area near the wellbore (Liang et al., 2021). As a results, the gas production capacity of these reservoirs is further inhibited because some of the percolation channels at the outlet end are blocked by water from the fracture-cavity type reservoir. Therefore, the commingled gas production under high water saturation is extremely low and mainly comes from fracture-cavity type reservoirs.

5.1.9.2 Effect of Water Encroachment on Gas Production Characteristics

The water encroachment process during multilayer commingled production was simulated by conducting water injection operation with constant pressure differential at the inlet end of the core system. Figure 5.8 shows the experimental results of multilayer commingled production simulation under the effect of water encroachment process. The differences in cumulative gas production and production contribution ratio of the three types of samples under the influence of water encroachment are more obvious than those under depletion production. The cumulative gas production and production contribution ratios of depletion production and water encroachment simulation experiments are summarized in Table 5.5. The cumulative gas production of pore type, cavity type and fracture-cavity type samples decreased by 56.72, 28.76 and 5.21% under the influence of water encroachment. Furthermore, the gas production contribution ratio of the pore type sample decreases, while that of the fracture-cavity type sample increases. Therefore, the effect of water encroachment on pore type reservoirs with relatively low petrophysical properties is most serious in both single-layer production and multilayer commingled production.

The first 50 s of the cumulative gas production curves obtained from the depletion production and water encroachment simulation experiments were enlarged to compare and analyze the effect of water encroachment on the gas production capacity of the three types of samples in the initial stage of multilayer commingled production (Fig. 5.9). The gas production capacity of the fracture-cavity type and cavity type samples was improved temporarily at the beginning because of the energy supplement from water injection. In contrast, the gas production capacity of the pore type sample was basically unchanged at the beginning because it is difficult for injected water to enter the tight porous media in a short time. The injected water advances rapidly along the dominant fractures of the fracture-cavity type sample, and imbibes

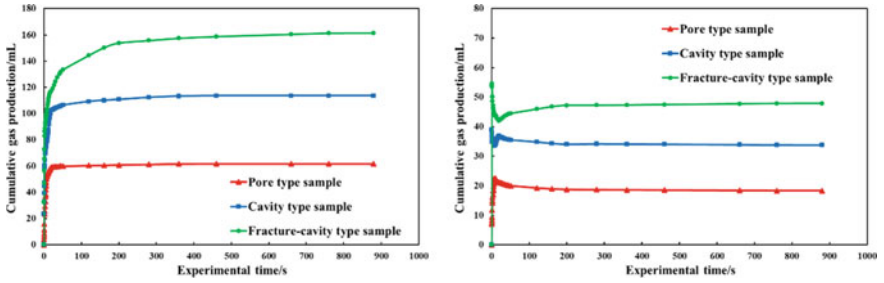

(a) Cumulative gas production (b) Gas production contribution ratio

Fig. 5.8 Multilayer commingled production simulation experimental results of Class I samples during water encroachment

Table 5.5 Comparison of experimental results of depletion production and water encroachment simulation

Sample type	Experiment type	Depletion production	Water encroachment
Fracture-cavity type	Cumulative gas production/mL	170.21	161.33
	Production contribution ratio/%	36.80	47.90
Cavity type	Cumulative gas production/mL	159.58	113.69
	Production contribution ratio/%	33.37	33.76
Pore type	Cumulative gas production/mL	142.69	61.75
	Production contribution ratio/%	29.83	18.34

into the matrix in contact with the fractures under the combined action of capillary force and rock wettability. The gas in the matrix surrounded by fractures will be trapped by the imbibed water after the injected water breaks through the core sample. Accordingly, both the gas production capacity and the recovery factor of the fracture-cavity type sample are inhibited after water breakthrough. The inhibition mechanisms of water encroachment on the gas production capacity and production contribution ratio of pore type and cavity type samples is consistent with those of high initial water saturation, but the effect of water encroachment on core samples is later but stronger. It can also be seen from Fig. 5.9 that the cumulative gas production curves of the pore type and cavity type samples almost no longer rise after 50 s. Even if the multilayer commingled production process continues for a long time, only a small amount of gas can be produced after the injected water breaks through the core system, and the gas production is mainly provided by the fracture-cavity type sample. Therefore, water encroachment has serious effects on all types of reservoirs during multilayer commingled production, especially on gas layers with relatively low petrophysical properties.

The pore type sample was taken out immediately and the core surface was carefully observed after the water encroachment simulation experiment. It can be seen from Fig. 5.10 that both the inlet and outlet ends of the core were wetted by water, whereas the central area is relatively dry. This phenomenon fully confirms that the water produced by the fracture-cavity type reservoir can form liquid accumulation in the wellbore and nearby areas, and inhibit the gas production capacity of other reservoirs with relatively low petrophysical properties. The water at the inlet end of the sample was caused by water encroachment, whereas the water at the outlet end came from capillary imbibition and liquid phase retention processes. The gas in the middle of

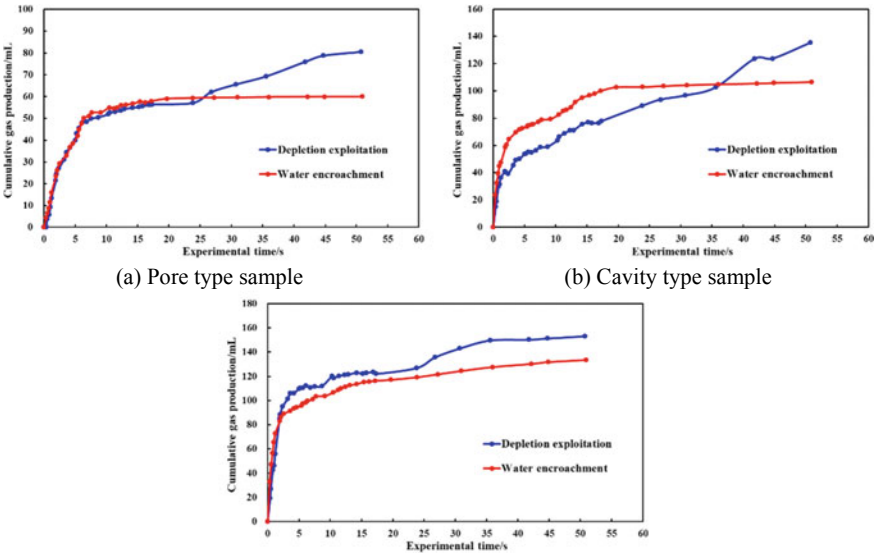

(a) Pore type sample (b) Cavity type sample

(c) Fracture-cavity type sample

Fig. 5.9 Comparison results of cumulative gas production in the initial stage of depletion exploitation and water encroachment

the sample was trapped by the water at the outlet end before the water at the inlet end reached the wellbore. Therefore, there is no trace of any external water entering the middle of the sample.

Fig. 5.10 Photograph of the pore type sample after water encroachment experiment

5.1.9.3 Numerical Simulation Results of Interlayer Heterogeneous Gas Reservoirs

The size of the plunger core sample used in the physical simulation experiment of multilayer commingled production is small. Whether the gas production characteristics and influence mechanisms of multilayer commingled production obtained from the experiment are applicable to the actual ultradeep carbonate gas reservoir needs further verification. The ultradeep carbonate gas reservoir in the Deng IV Member is still in the initial stage of exploration and development, with few production wells, short production time, and lack of corresponding field production data. Therefore, a single-well radial numerical model was established using the Eclipse software based on the well test model of GS1 well in the Deng IV Member gas reservoir. The numerical model is subdivided into three layers vertically, representing fracture-cavity type, cavity type, and pore type reservoirs, respectively. The basic rock physical property parameters, high-pressure fluid physical property parameters, and gas–water relative permeability curves of each layer are set according to logging data and physical simulation experimental results. The parameters of the same layer take the same value. The initial reservoir pressure of the numerical model is 56 MPa, the initial reservoir temperature is 150°C, the initial water saturation is 10%, the radius of the well control zone is 500 m, and the geological reserves in the well control zone are 1.62×10^8 m^3. The gas well is depleted under constant bottom hole pressure, the depletion pressure differential is 5 MPa, and the expected exploitation life is 30 years.

The numerical simulation results of the pressure, cumulative gas production and production contribution ratio of the three types of reservoirs are shown in Fig. 5.11. It could be found that the variation trends of the three types of curves obtained from physical simulation experiment results (Fig. 5.3) and single-well numerical simulation results (Fig. 5.12) are basically the same. The comparison results demonstrate the applicability of the core-scale physical simulation experimental results at the gas reservoir scale, but the variation range of the curves obtained at the core scale is larger than that obtained at the gas reservoir scale. This is because the length of the plunger core is short, and the pressure drop funnel can quickly transfer to the boundary. In addition, the curves obtained from the experiments are irregular because the pore structure and fluid distribution of the core sample are far more complicated than those of the numerical model. The geological and production data that can be obtained in the initial stage of gas reservoir development are relatively scarce. The rationality of the multilayer commingled production performance of ultradeep carbonate gas reservoirs obtained by numerical simulation, well testing and other methods depends on the accuracy of the data used. In contrast, the results obtained from physical simulation experiments based on similarity principles and actual reservoir cores are more in line with the fluid flow characteristics under reservoir conditions. Moreover, some physical simulation experimental results are indispensable parameters for numerical

simulation and mathematical modeling of gas reservoirs. Therefore, physical simulation experiment is an indispensable method to study the dynamic characteristics of multilayer commingled production.

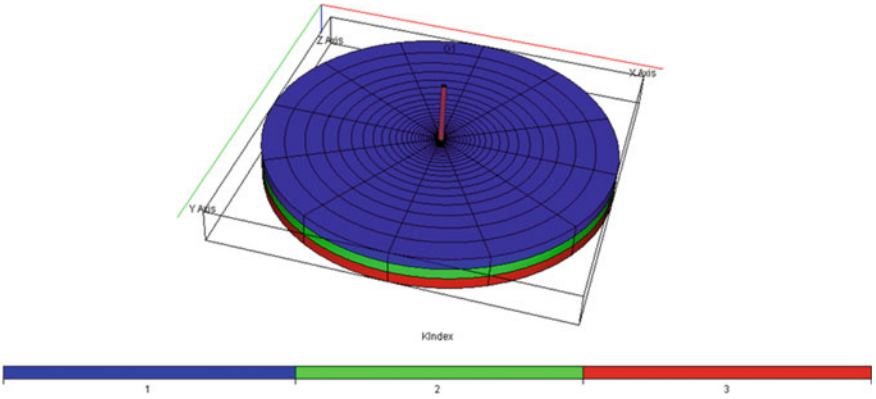

Fig. 5.11 Radial numerical model of multilayer commingled production in well GS1

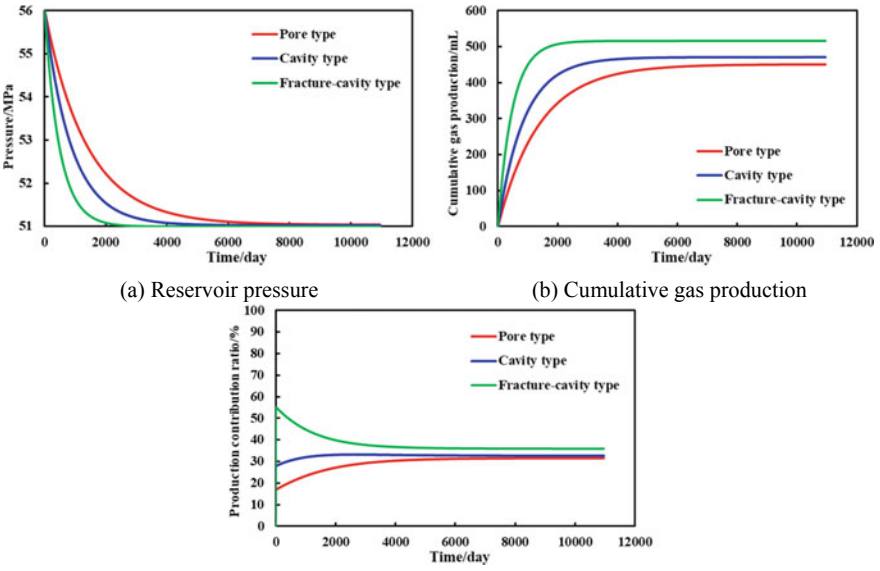

(a) Reservoir pressure

(b) Cumulative gas production

(c) Gas production contribution ratio

Fig. 5.12 Numerical simulation results of multilayer commingled production

5.2 Gas Production Characteristics of Horizontal Heterogeneous Gas Reservoirs

5.2.1 Experimental Objective

Six representative core samples were selected from pore type, cavity type and fracture-cavity type carbonate reservoirs, and a physical simulation model of horizontal heterogeneous reservoir production under ultra-high temperature and pressure conditions was established based on the similarity principle. Subsequently, an experimental program for horizontal heterogeneous reservoir production was designed based on the actual reservoir characteristics and exploitation project of the Deng IV Member gas reservoir. The gas production characteristics and gas supply capacity of three types of carbonate core samples during horizontal heterogeneous reservoir production were revealed by processing and analyzing the parameters of pore pressure, cumulative gas production, instantaneous gas production, production contribution ratio and recovery factor. Then, the effects of horizontal heterogeneity, permeability difference, depletion pressure differential, initial water saturation and water encroachment on the gas production characteristics of horizontal heterogeneous reservoir production were also analyzed. Finally, some suggestions were put forward to improve the gas production capacity and recovery factor of heterogeneous reservoirs in ultradeep carbonate gas reservoirs. The relevant research results can provide a theoretical basis for well location deployment, production scheme formulation and production capacity evaluation of ultradeep carbonate gas reservoirs.

5.2.2 Similarity Principle

The similarity principle of rock and fluid properties, initial conditions and production conditions in the simulation experiment of horizontal heterogeneous reservoir production is similar to that in the simulation experiment of multilayer commingled production, only the production modes of the two are different. Natural carbonate core samples from different types of reservoirs were connected in series to simulate the production of horizontal heterogeneous reservoirs, as shown in Fig. 5.13. The arrangement and combination of different types of cores can simulate the horizontal heterogeneity in the gas well control zone (Ma et al., 2018).

5.2.3 Experimental Samples, Conditions and Apparatus

The three types of plunger core samples used in the simulation experiment of horizontal heterogeneous reservoir production are the same as those used in the simulation

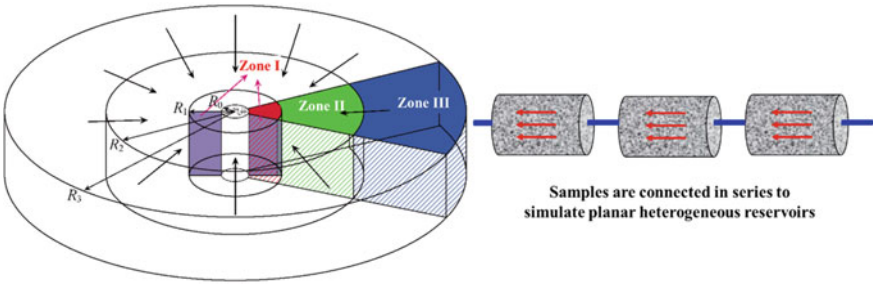

Fig. 5.13 Schematic diagram of horizontal heterogeneous reservoir and cores connection

experiment of multilayer commingled production. Each type of core was also classified into Class I and Class II according to the relatively magnitude of permeability. The petrophysical parameters of the plunger cores are summarized in Table 5.1. The experimental temperature is 150 °C, the confining pressure is 138 MPa, and the initial pore pressure is 56 MPa. High-purity nitrogen was used as the experimental gas to simulate natural gas. The experimental water was prepared in lab based on the chemical composition of the formation water in the Deng IV Member, as shown in Table 5.2. The prepared experimental water sample was used to establish different initial water saturation for core samples. The constant volume and constant pressure exploitation mode was also used for this experiment. The simulation experiment of horizontal heterogeneous reservoir production of ultradeep carbonate gas reservoirs under formation conditions were conducted on the ultra-high temperature and pressure physical simulation experiment system. The experimental system can be divided into four subsystems, namely injection system, pressurization system, core system and data collection system (Fig. 5.14a). Except for the core system, the apparatus of the other three systems are the same as those of the multilayer commingled production simulation experiment. The core system consists of three core holders connected in series by pipelines and valves, and each core holder was surrounded by a heating jacket (Fig. 5.14b). In addition, the inlet and outlet ends of each core holder were equipped with pressure sensors to measure and record the pressure variations of different core samples in the horizontal direction.

5.2.4 Experimental Scheme

The physical simulation experiment program of horizontal heterogeneous reservoir production consists of five sets of experiments. (1) Class I core samples of pore type, cavity type and fracture-cavity type were placed in core holders for "series connection" experiment to study the gas production characteristics of different types of reservoirs during horizontal heterogeneous reservoir production. Three core combinations were designed to simulate the situation that the reservoir near the wellbore is

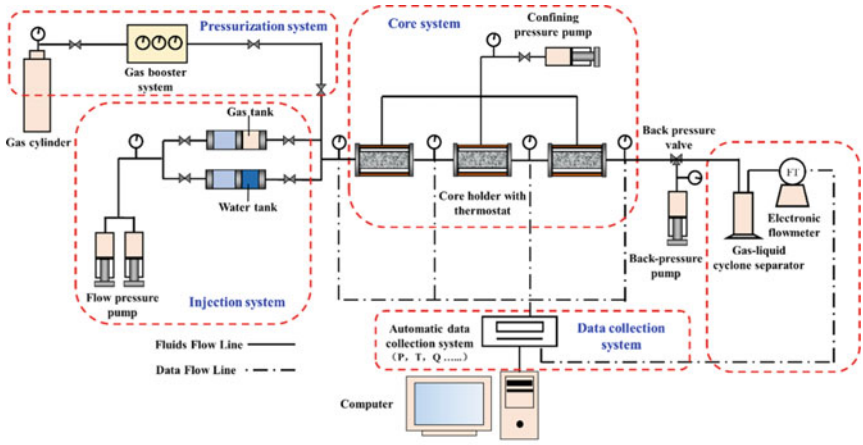

(a) Flow chart of physical simulation experiment system of horizontal heterogeneous reservoir production

(b) Photograph of three core holders connected in series

Fig. 5.14 Schematic diagram of the physical simulation experiment system of horizontal heterogeneous reservoir production

of fracture-cavity type, cavity type and pore type, respectively (Table 5.6). (2) Class I core samples of pore type, cavity type and fracture-cavity type were replaced by the corresponding Class II core samples one by one for comparative experiments to study the effect of horizontal heterogeneity on the gas production characteristics. (3) The effect of different depletion pressure differentials (3, 5 and 7 MPa) on the gas production characteristics were studied by changing the back pressure. (4) The effect of different initial water saturations on gas production characteristics was studied by

Table 5.6 Experimental scheme of physical simulation of horizontal heterogeneous reservoir production

Experiment type	Core combination type	Depletion pressure differential/MPa	Initial water saturation/%
Effect of interlayer heterogeneity on gas production characteristics	Inlet → ① → ② → ③ → Outlet	5	10
	Inlet → ① → ③ → ② → Outlet		
	Inlet → ② → ③ → ① → Outlet		
Effect of permeability differences on gas production characteristics	Inlet → ① → ② → ③ → Outlet	5	10
	Inlet → ④ → ② → ③ → Outlet		
	Inlet → ① → ⑤ → ③ → Outlet		
	Inlet → ① → ② → ⑥ → Outlet		
Effect of pressure differential on gas production characteristics	Inlet → ① → ② → ③ → Outlet	3	10
		5	
		7	
Effect of initial water saturation on gas production characteristics	Inlet → ① → ② → ③ → Outlet	5	10
			30
			50
			70
Effect of water encroachment on gas production characteristics	Inlet → ① → ② → ③ → Outlet	5	10

establishing the initial water saturations (10, 30, 50 and 80%) in three types of cores. (5) The effect of water encroachment on the gas production characteristics of horizontal heterogeneous reservoir production was studied by the method of constant pressure water flooding at the inlet end. The parameters of experimental program are shown in Table 5.6. The initial water saturation of the three types of cores was also set below the irreducible water saturation when studying the effects of interlayer heterogeneity, depletion pressure differential and water encroachment on the gas production characteristics of horizontal heterogeneous reservoir production.

5.2.5 Experimental Procedure

The pressurization process of the horizontal heterogeneous reservoir production simulation experiment under ultra-high temperature and pressure conditions is consistent with that of the multilayer commingled production simulation experiment. The initial temperature and pressure conditions of the reservoir were finally established when the upstream and downstream pressures of the core system stabilized. Then, the inlet valve of the core system was closed, and the outlet pressure (53,

51 and 49 MPa) was set through the back-pressure pump and back-pressure valve to simulate different depletion pressure differentials (3, 5 and 7 MPa). The reason for increasing the depletion pressure differential is that the increase in core sample length after the series treatment leads to a decrease in the pressure gradient under the same pressure differential. The simulation experiment results of horizontal heterogeneous reservoir production under the depletion pressure differential of 1 MPa are not significant. It should be noted that only the gas production of the sample near the outlet end could be measured, and the gas produced by other samples can only enter the samples connected to it. The actual amount of gas contributed by each sample cannot be directly measured. Therefore, the gas production contribute ratio of the sample was obtained by allocating the total gas production according to the pore pressure variation of each sample. The premise of adopting this method is to ignore the effect of porosity stress sensitivity on the volume of storage space. The porosity stress sensitivity of the three types of ultradeep carbonate reservoirs introduced in Chap. 4 is relatively weak. Therefore, there is no obvious error in calculating the production contribution ratio of the three types of samples by this method. The sum of the gas production contribution ratio of the three cores is always 100%.

5.2.6 *Effect of Horizontal Heterogeneous on Gas Production Characteristics*

The production simulation experimental results of the horizontal heterogeneous reservoirs simulated by different core sample combinations under the depletion pressure differential of 5 MPa are shown in Figs. 5.15, 5.16 and 5.17. Different core sample combinations represent that gas wells are drilled in different types of reservoirs. It could be concluded that the horizontal heterogeneity of the reservoir and the well location have a significant impact on the gas production characteristics by comparing the experimental results of the three sample combinations. In addition, the experimental results also show that the variation patterns and characteristics of the pressure and production contribution ratio of the pore type, cavity type and fracture-cavity type samples are different in different production stages of horizontal heterogeneous reservoirs. The production stage division standards of the three types of sample combinations were unified based on the instantaneous gas production. The magnitude of instantaneous gas production can reflect the high production, stable production and low production stages of a gas well. Therefore, the instantaneous gas production corresponding to the high production stage, stable production stage and low production stage are > 1.0, 0.5–1.0, and < 0.5 mL/s according to the conversion formula between the experimental gas production and the gas well production.

Figure 5.15 shows the production characteristics of gas wells located in fracture-cavity type reservoirs, with good petrophysical properties in the near-well region and gradually worsening in the far-well region. In the high production stage (0–74 s), the pressure of the fracture-cavity type sample decreases sharply, whereas

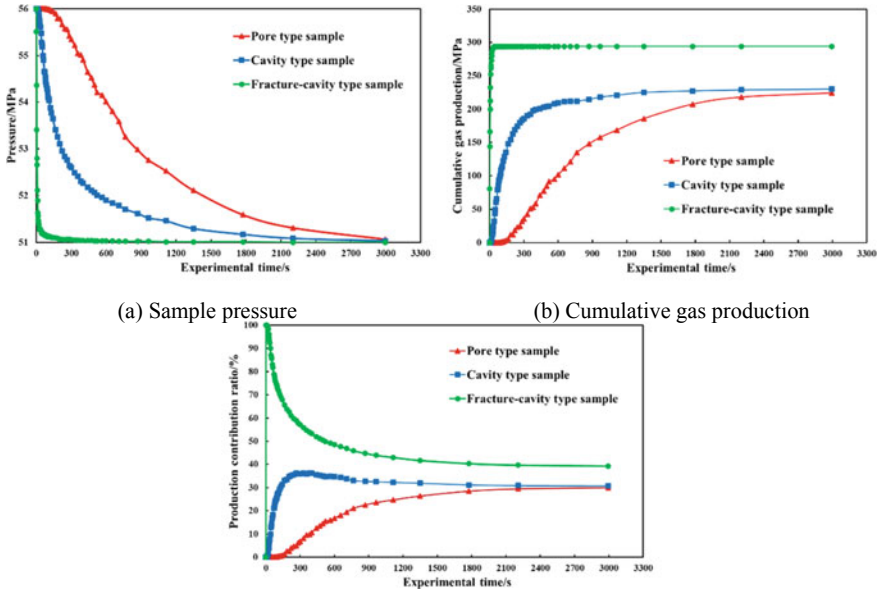

(a) Sample pressure (b) Cumulative gas production

(c) Gas production contribution ratio

Fig. 5.15 Horizontal heterogeneous reservoir production simulation experimental results of Class I samples under the depletion pressure differential of 5 MPa and initial water saturation of 10% (Inlet → ① → ② → ③ → Outlet)

the pressure variations of the cavity type and pore type samples lag behind that of the fracture-cavity type sample (Fig. 5.15a). It reflects that the fracture-cavity type sample preferentially produces gas, followed by the cavity type sample, while the pore type sample begins to produce gas after a period of time. The reason for the pressure drop hysteresis of the pore type sample is that the transfer rate of the pressure drop funnel in the fracture-cavity type sample is much faster than that in the cavity type sample. It can be seen form cumulative gas production curves that almost all the natural gas in the fracture-cavity type sample was produced in the high production stage although the duration of this stage was relatively short (Fig. 5.15b). Therefore, the fracture-cavity type is the dominant gas supply sample with a gas production contribution ratio of 78.61–100%. However, the gas production contribution ratios of the fracture-cavity type sample and the cavity type sample decreases rapidly and increases rapidly, respectively (Fig. 5.15c). It should be noted that the production contribution ratio of the pore type sample is 0 in the high produced stage.

The stable production stage lasted for a relatively long time (74–184 s). The upstream pressure of the fracture-cavity type sample is infinitely close to the downstream pressure, while the pressure decline rates of the cavity type and pore type samples were still relatively high because of the effect of pressure drop hysteresis (Fig. 5.15a). Figure 5.15b shows that the cumulative gas production of the pore type sample begins to increase gradually, that of the cavity type sample continues

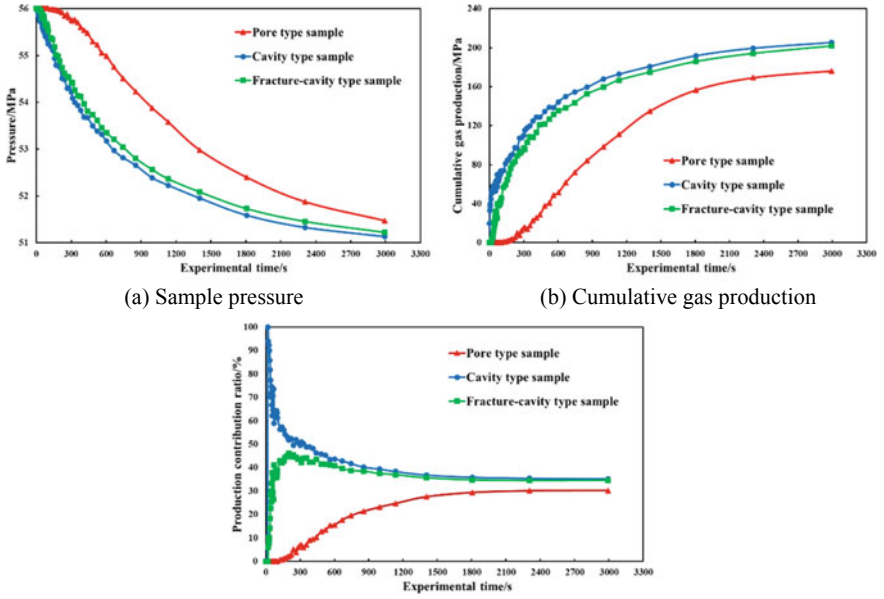

(a) Sample pressure

(b) Cumulative gas production

(c) Gas production contribution ratio

Fig. 5.16 Horizontal heterogeneous reservoir production simulation experimental results of Class I samples under the depletion pressure differential of 5 MPa and initial water saturation of 10% (Inlet → ① → ③ → ② → Outlet)

to increase rapidly, while that of the fracture-cavity type sample basically stops increasing. Therefore, the production contribution ratio of the fracture-cavity type sample continues to decrease, whereas those of the cavity type and pore type samples gradually increase (Fig. 5.15c). The cavity type becomes the dominant gas supply sample in the stable production stage, and the outermost pore type sample also begins to produce gas in this stage.

The low production stage lasted for a very long time (184–2996 s). The pressure drop of the cavity type sample slows down, while that of the pore type sample is still fast (Fig. 5.15a). The cumulative gas production curves show that the gas produced in this stage is mainly supplied by the pore type sample, but the extremely low gas production and extremely long production time make the exploitation in this stage unprofitable (Fig. 5.15b). The gas production contribution ratio of the pore type sample increases slowly but lasts for a long time. Eventually, the production contribution ratio of the pore type sample is similar to that of the cavity type sample (Fig. 5.15c). However, gas wells are generally abandoned when actual production falls below beneficial production. Therefore, the production contribution ratio of cavity type reservoirs is usually higher than that of pore type reservoirs. The production contribution ratio of the fracture-cavity type sample is always higher than that of the other two samples.

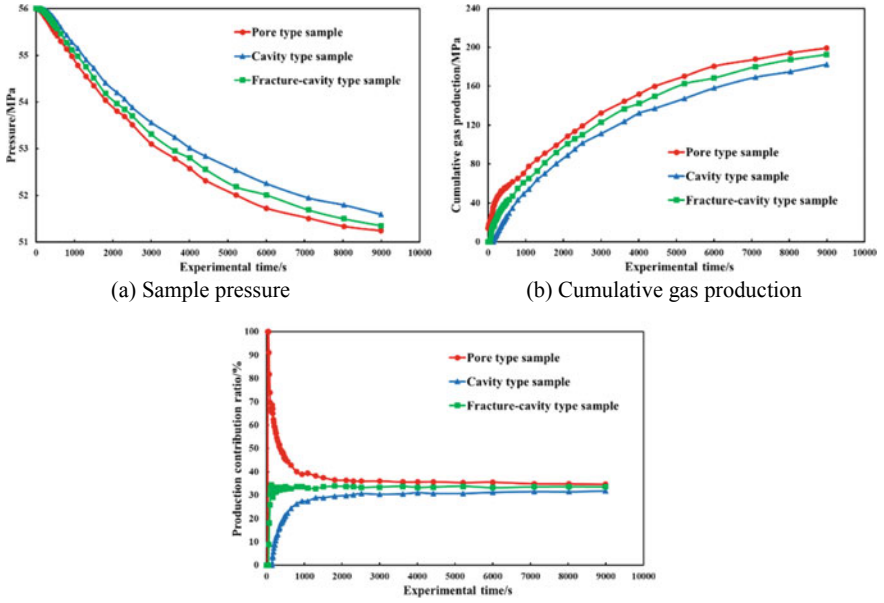

(a) Sample pressure

(b) Cumulative gas production

(c) Gas production contribution ratio

Fig. 5.17 Horizontal heterogeneous reservoir production simulation experimental results of Class I samples under the depletion pressure differential of 5 MPa and initial water saturation of 10% (Inlet → ② → ③ → ① → Outlet)

Figure 5.16 shows the production characteristics of gas wells located in cavity type reservoirs. The periphery of the cavity types reservoir is followed by the fracture-cavity type reservoir and the pore type reservoir. In the high production stage (0–24 s), the pressure of the cavity type sample decreases firstly at a relatively fast rate, but the decline rate is significantly slower than that of the fracture-cavity type sample in Fig. 5.15a. The pressure variation law and degree of the fracture-cavity type sample are basically the same as those of the cavity type sample, but slightly lag behind that of the cavity type sample (Fig. 5.16a). In contrast, the pressure variation of the pore type sample lags significantly behind the other two samples. It reflects that drilling wells in the cavity type reservoir will inhibit the gas production capacity of the peripheral fracture-cavity type reservoir, but has little effect on the production characteristics of the outermost pore type reservoir. Therefore, the duration and cumulative gas production of the high production stage of this sample combination were significantly reduced (Fig. 5.16b). The cavity type is the dominant gas supply sample with a gas production contribution ratio of 89.90–100%. However, the gas production contribution ratio of the cavity type sample and the fracture-cavity type sample decreases rapidly and increases rapidly, respectively (Fig. 5.16c). It should still be noted that the production contribution ratio of the pore type sample in this stage is 0.

The stable production stage lasted for a relatively long time (26–222 s). The pressure drop rate of the cavity type and fracture-cavity type samples gradually slows down, and the pressure of the pore type sample begins to decrease (Fig. 5.16a). Figure 5.16b shows that the cumulative gas production of the cavity type sample and the fracture-cavity type sample increases simultaneously, while that of the pore type sample is just beginning to increase gradually. Therefore, the production contribution ratio of the cavity type sample continues to decrease, whereas that of the cavity type and pore type samples gradually increases (Fig. 5.16c). Both cavity type and fracture-cavity type are the main gas supply samples in the stable production stage, and the outermost pore type sample also begins to produce gas.

The low production stage lasted for a very long time (222–2994 s). The pressure drop rates of the cavity type and fracture-cavity type samples continues to slow down, while that of the pore type sample is still fast (Fig. 5.16a). It should be noted that the experimental duration of this sample combination is longer than that of the first sample combination, because the pressure of the three samples did not completely drop to 51 MPa at the end of the experiment. It indicates that the production period of gas wells in cavity type reservoirs was longer than that in fracture-cavity type reservoirs. The cumulative gas production curves show that the cavity type and fracture-cavity type samples still produce a large amount of gas in the low production stage (Fig. 5.16b). Although the cumulative gas production in the low production stage is large, the instantaneous gas production is lower than the effective production capacity. Therefore, a large amount of gas in the cavity type and fracture-cavity type samples becomes unprofitable compared to the first sample combination. Nevertheless, the porosity type is still the dominant gas supply sample in the low production stage. Therefore, the gas production contribution ratio of the pore type sample increases slowly but lasts for a long time (Fig. 5.16b). Eventually, the production contribution ratio of the cavity type sample is similar to that of the fracture-cavity type sample, but slightly higher than that of the pore type sample. However, gas wells are generally abandoned when actual production falls below beneficial production. Therefore, the production contribution ratio of pore type reservoirs is usually much lower than that of the other two types of reservoirs. In conclusion, the production characteristics of the fracture-cavity type sample are similar to those of the cavity type sample, reflecting that the gas production capacity of the peripheral high-quality reservoirs is inhibited by the reservoirs with relatively low petrophysical properties near the wellbore.

Figure 5.17 shows the production characteristics of gas wells located in pore type reservoirs. The periphery of the pore type reservoir is followed by the fracture-cavity type reservoir and the cavity type reservoir. The experimental results show that the instantaneous gas production of this sample combination is always lower than 1.0 mL/s, reflecting that there is no high production stage in the entire gas production process. Therefore, drilling wells in pore type reservoirs with extremely low petrophysical properties will seriously weaken the gas production of the peripheral high-quality reservoirs. In the stable production stage (0–120 s), the pressure of the pore type sample decreased firstly at a slow and constant rate, and the decline rate is significantly slower than that of the cavity type sample in Fig. 5.16a. The pressure

variation law and degree of the fracture-cavity type and cavity type samples are basically the same as those of the pore type sample, but lag behind that of the pore type sample (Fig. 5.17a). The fracture-cavity type and cavity type samples lag behind the pore type sample by 57 s and 147 s, respectively. It reflects that drilling wells in pore type reservoirs will inhibit the gas production capacity of all the peripheral reservoirs with relatively high petrophysical properties. Therefore, the duration and cumulative gas production of the stable production stage of this sample combination were significantly reduced (Fig. 5.17b). The pore type is the dominant gas supply sample with a gas production contribution ratio of 66.60–100%. However, the gas production contribution ratios of the pore type sample and the fracture-cavity type sample decreases rapidly and increases rapidly, respectively (Fig. 5.17c).

The low production stage lasted for a very long time (177–8991 s). The pressure drop rate of the pore type and fracture-cavity type samples first remained constant and then gradually slowed down, and the pressure of the cavity type sample begins to decrease (Fig. 5.17a). The pressure of the three samples did not completely drop to 51 MPa when the experiment was conducted for 8991 s, indicating that the production period of this sample combination is much longer than that of the other two sample combinations. Figure 5.17b shows that the cumulative gas production of the three types of samples increased simultaneously at a similar rate during this stage. Both the cavity type and fracture-cavity type samples still produced a large amount of gas in the low production stage. As a result, most of the gas produced by the fracture-cavity type sample and all the gas produced by the cavity type sample become unprofitable gas production. Therefore, the production contribution ratio of the pore type sample continued to decrease, whereas that of the fracture-cavity type and cavity type samples gradually increased (Fig. 5.17c). Eventually, the production contribution ratios of the three types of samples stabilized for a long time. However, gas wells are generally abandoned when actual production falls below beneficial production. Therefore, the production contribution ratio of pore type reservoirs is usually far higher than that of the other two types of reservoirs. In conclusion, the production characteristics of the fracture-cavity type and cavity type samples are similar to those of the pore type sample, reflecting that the low-quality reservoirs in the near-wellbore region will force the gas production characteristics of the peripheral high-quality reservoirs to be consistent with them. In other words, the excellent gas production capacity of reservoirs with high petrophysical properties cannot be exerted under the obstruction of reservoirs with low petrophysical properties.

In summary, the production contribution ratio of reservoirs located in the near-wellbore region gradually decreases, whereas that of the reservoirs located in the far-wellbore regions sequentially and gradually increases. The proportions of cumulative gas production in different production stages to the total horizontal heterogeneous reservoir production under the three sample combinations are shown in Figs. 5.18a, 5.19a and 5.20a. It can be concluded that drilling wells in fracture-cavity type reservoirs can not only give full play to the gas production capacity of high-quality reservoirs in the near-wellbore region, but also effectively develop peripheral reservoirs with relatively low petrophysical properties. Consequently, most of the gas in the heterogeneous reservoir can be recovered during the high production and

stable production stages. In contrast, drilling wells in cavity type reservoirs not only reduces the instantaneous gas production of the reservoir near the wellbore, but also inhibits the gas production capacity of peripheral reservoirs with relatively high petrophysical properties to a certain extent. Although the stable production stage of heterogeneous reservoirs can be extended, the high production stage is greatly shortened. As a result, most of the gas in the heterogeneous reservoir is recovered in the low production and stable production stages. By comparison, drilling wells in pore type reservoirs inhibits the gas production capacity of high-quality reservoirs in the entire heterogeneous reservoir, resulting in the absence of high production stage. Accordingly, most of the gas in heterogeneous reservoirs can only be produced during the low production stage.

The gas production contribution ratio of different types of samples in different production stages for the three sample combinations are shown in Figs. 5.18b, 5.19b and 5.20b. In the first type of sample combination, fracture-cavity type, cavity type and pore type are the dominant gas supply samples in the high production stage, stable production stage and low production stage, respectively. All the gas in the

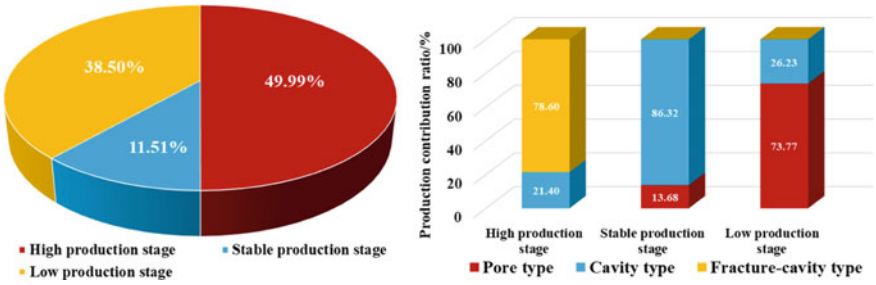

(a) Gas production proportion (b) Production contribution ratio

Fig. 5.18 Proportion and contribution ratio of gas production in different stages of horizontal heterogeneous reservoir production (Inlet → ① → ② → ③ → Outlet)

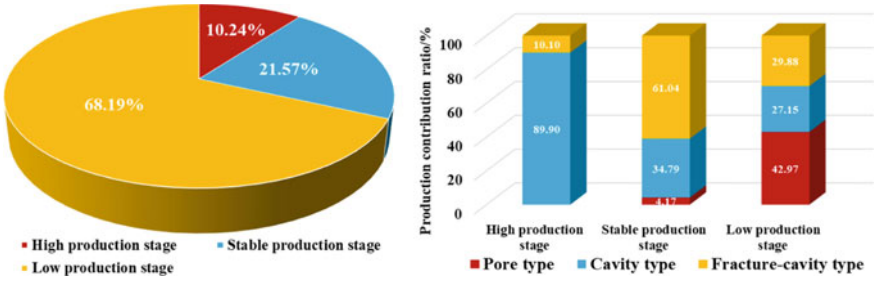

(a) Gas production proportion (b) Production contribution ratio

Fig. 5.19 Proportion and contribution ratio of gas production in different stages of horizontal heterogeneous reservoir production (Inlet → ① → ③ → ② → Outlet)

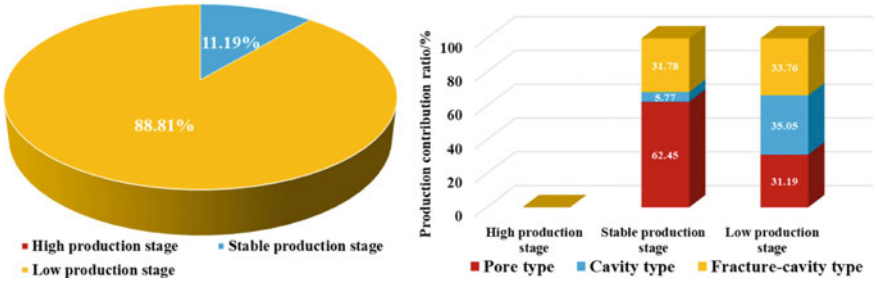

(a) Gas production proportion (b) Production contribution ratio

Fig. 5.20 Proportion and contribution ratio of gas production in different stages of horizontal heterogeneous reservoir production (Inlet → ② → ③ → ① → Outlet)

fracture-cavity type sample and a part of the gas in the cavity type sample were recovered during the high production stage, and most of the gas in the cavity type sample and a part of the gas in the pore type sample were recovered during the stable production stage. The distribution pattern of petrophysical properties gradually decreases from inside to outside can realize the cooperative and alternate gas production characteristics of the three types of reservoirs in different production stages of heterogeneous reservoirs. In the second type of sample combination, cavity type and fracture-cavity type are the dominant gas supply samples in the high production stage and stable production stage, respectively. However, the difference of production contribution ratio of the three samples in the low production stage is small. The cavity type reservoir near the wellbore cannot maintain the high production stage for a long time because of its limited gas production capacity. The peripheral fracture-cavity type reservoir cannot exert its excellent gas production capacity due to the inhibition of the cavity type reservoir. Although the duration of stable production stage is extended, a part of the gas in the fracture-cavity type reservoir can only be produced in the low production stage. Therefore, the development effect of the distribution pattern of petrophysical properties increase first and then decrease from inside to outside is worse than that of petrophysical properties gradually decreases from inside to outside. In the third type of sample combination, the pore type is the dominant gas supply sample in the stable production stage, while the three types of samples have similar production contribution ratios in the low production stage. The instantaneous gas production of the pore type reservoir near the wellbore is always lower than the requirement of the high production stage because its gas production capacity is extremely low. The gas from the peripheral fracture-cavity type reservoir can replenish the pore type reservoir, but the effect is not significant. As a result, a considerable part of natural gas in the fracture-cavity type and cavity type reservoirs can only be produced in the low production stage. In contrast, the development effect of the distribution pattern of petrophysical properties gradually increases from inside to outside is the worst.

Therefore, fracture-cavity type reservoirs should be preferentially selected for the exploitation of ultradeep carbonate gas reservoirs, and drilling production wells in pore type reservoirs must be avoid. In order to improve the experimental efficiency and highlight the research focus, only the first commonly used sample combination was subject to physical simulation experiments to study the effects of permeability difference, depletion pressure differential, initial water saturation and water encroachment on the gas production characteristics of horizontal heterogeneous reservoirs.

5.2.7 Effect of Permeability Differences on Gas Production Characteristics

Three types of core samples with different permeability were selected one by one for comparative experiments to reveal the effect of the permeability differences of three types of reservoirs on the gas production capacity of horizontal heterogeneous reservoirs. It should be noted that the permeability of Class II cores is lower than that of Class I cores in the same type of reservoir. The experimental results show that the variation laws of pressure, cumulative gas production and production contribution ratio of different sample combinations are similar to those in Fig. 5.15. However, the values of recovery factor, production contribution ratio and commingled production recovery factor are different for different core combinations (Table 5.7). The permeability reduction of the outermost pore type sample greatly reduces its recovery factor, and also slightly reduces the recovery factor of the cavity type sample, but has little effect on the recovery factor of the fracture-cavity type sample near the wellbore. Consequently, the production contribution ratio of the fracture-cavity type and cavity type samples increased, but the total recovery factors of horizontal heterogeneous reservoir decreased. The permeability reduction of the cavity type sample located in the middle not only greatly reduces the recovery factor of the cavity type and pore type samples, but also slightly reduces that of the fracture-cavity type sample. Therefore, the production contribution ratio of the fracture-cavity type sample increased but the total recovery factors decreased. The permeability reduction of the fracture-cavity type sample near the wellbore slightly reduced its recovery factor, but greatly increased the recovery factor of the cavity type and pore type samples. As a result, the production contribution ratio of the fracture-cavity type sample decreased but the total recovery factors increased. The permeability reduction of the fracture-cavity type sample means the decrease of the permeability difference between reservoirs in different regions, whereas the permeability reduction of the other two types of samples means the increase of the permeability difference between reservoirs in different regions. The absolute value of reservoir permeability affects its own recovery factor and production contribution ratio. The greater the permeability value, the higher the recovery factor and production contribution ratio. The relative value of reservoir permeability affects the total recovery factor and the

production contribution ratio difference. The smaller the permeability difference, the higher the total recovery factor, and the smaller the difference in production contribution ratio. In addition, the variation of permeability has little effect on the recovery factor of fracture-cavity type reservoirs, but has a great impact on pore type and cavity type reservoirs. Therefore, the weaker the horizontal heterogeneity of the ultradeep carbonate gas reservoir, the stronger the gas production capacity of the peripheral reservoirs with relatively low petrophysical properties, and the higher the total recovery factor of the reservoir.

5.2.8 Effect of Depletion Pressure Differential on Gas Production Characteristics

The first sample combination was selected to conduct the horizontal heterogeneous reservoir production simulation experiment under different depletion pressure differentials. The experimental results show that the production characteristics of horizontal heterogeneous reservoirs under three depletion pressure differentials are similar, but the production performance parameters are significantly different. The proportion of cumulative gas production in high production, stable production and low production stages under different depletion pressure differentials is illustrated in Fig. 5.21. There are two reasons why the proportion of cumulative gas production in the high production stage under the initial depletion pressure differential of 3 MPa is lower than that under the initial pressure differential of 5 MPa. The first is that the overall reduction of instantaneous gas production under low depletion pressure differential makes the production process transition to the stable production stage in advance. The second is that the continuous gas supply of the peripheral cavity type and pore type samples under low pressure differential prolongs the stable production stage. Consequently, although the reduction of depletion pressure differential weakened the gas production capacity of the high production stage to a certain extend, it greatly increased the duration of the stable production stage and reduced the proportion of cumulative gas production in the low production stage. However, the proportion of cumulative gas production in the high production stage under the initial pressure differential of 7 MPa is also lower than that under the initial pressure differential of 5 MPa. This is because the gas in the fracture-cavity type sample is rapidly recovered under high pressure differential, and a deficit is formed near the wellbore, while the replenishment capacity of the peripheral pore type and cavity type samples to the fracture-cavity type sample is limited in the short term. However, it is difficult for the cavity type and pore type sample to maintain high production stage and stable production stages for a long time by their own gas production capacity. Therefore, although the growth of depletion pressure differential improves the instantaneous gas production of the high production stage, it greatly shortens the duration of the high production stage and increases the proportion of cumulative gas production in the low production stage.

Table 5.7 Experimental results of the first type of sample combination under different permeability differences

Types of core combinations	Pore type		Cavity type		Fracture-cavity type		Total recovery factor/%
	Recovery factor/%	Contribution ratio/%	Recovery factor/%	Contribution ratio/%	Recovery factor/%	Contribution ratio/%	
① → ② → ③	4.84	29.98	4.91	30.73	6.43	39.30	5.39
④ → ② → ③	3.90	25.99	4.75	31.95	6.40	42.05	5.01
① → ⑤ → ③	3.98	28.07	4.03	28.68	6.22	43.25	4.73
① → ② → →⑥	5.21	31.31	5.33	32.32	6.14	36.37	5.56

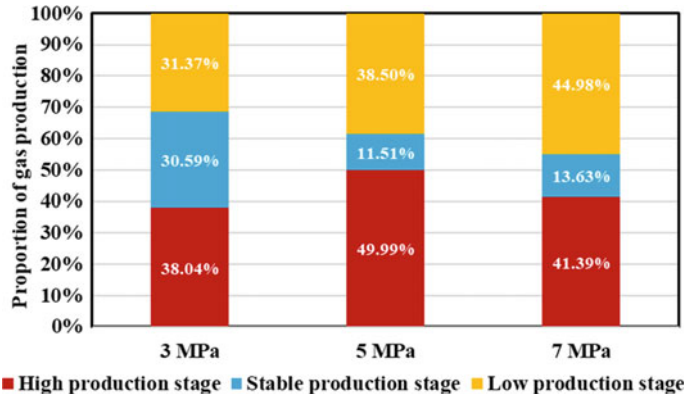

Fig. 5.21 Proportion of cumulative gas production in each production stage under different depletion pressure differential

The gas production contribution ratios of different types of samples in different production stages under the initial depletion pressure differentials of 3 and 7 MPa are shown in Figs. 5.22 and 5.23. The production contribution ratio of the cavity type sample in the high production stage decreases with the increase of depletion pressure differential. This is because a part of the gas in the fracture-cavity type sample can only be recovered in the stable production stage because of the reduction of depletion pressure differential, and the gas in the cavity type sample can effectively replenish the fracture-cavity type sample in the high production stage. In contrast, the replenishment time of the cavity type sample to the fracture-cavity type sample is greatly shortened under the high depletion pressure differential, thereby reducing the production contribution ratio of the cavity type sample in the high production stage. Therefore, it is necessary to increase the production contribution ratio of cavity type and pore type reservoirs in the high production and stable production stages respectively to realize the dynamic replenishment between different types of reservoirs in the horizontal direction. This dynamic replenishment can effectively increase the duration and cumulative gas production proportion of the profitable production stage (high production and stable production stages).

The ultimate recovery factor and production contribution ratio of different types of samples under different depletion pressure differentials are illustrated in Fig. 5.24. The production contribution ratios of the three types of samples are similar under relatively low depletion pressure differential, reflecting the effective utilization of the gas in the three types of samples. However, the growth of depletion pressure differential increases the production contribution ratio of the fracture-cavity type sample, but decreases that of the pore type and cavity type samples. It indicates that the gas production of horizontal heterogeneous reservoirs under relatively high depletion pressure differential is mainly supplied by fracture-cavity type reservoirs, while the gas in the peripheral reservoirs with relatively low petrophysical properties cannot be effectively utilized. Therefore, the difference in recovery factor of

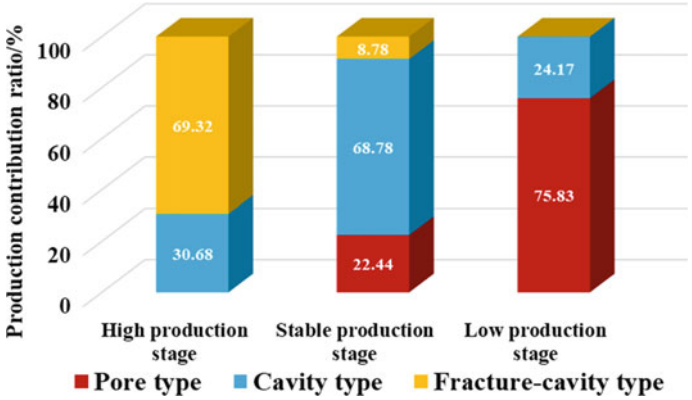

Fig. 5.22 Production contribution ratio in different production stages of horizontal heterogeneous reservoir under depletion pressure differential of 3 MPa

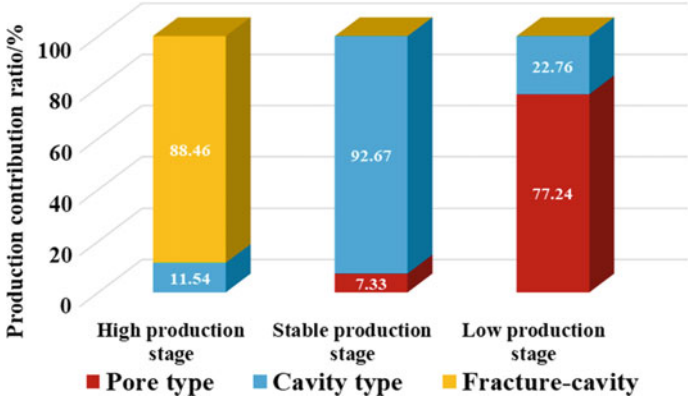

Fig. 5.23 Production contribution ratio in different production stages of horizontal heterogeneous reservoir under depletion pressure differential of 7 MPa

the three types of samples is small under relatively low depletion pressure differential, but it expands rapidly with the increase of depletion pressure differential. It reflects that the growth of depletion pressure differential has a stronger inhibitory effect on the recovery factor improvement of the pore type and cavity type samples than that of the fracture-cavity type sample. As a result, the increase rate of the total recovery factor of horizontal heterogeneous reservoir decreases with the increase of initial depletion pressure differential. Therefore, a relatively low production pressure differential can give full play to the cooperative gas production and alternate gas production capacities of horizontal heterogeneous reservoirs, thereby improving the ability of peripheral reservoirs with relatively low petrophysical properties to dynamically replenish reservoirs with relatively high petrophysical properties. In

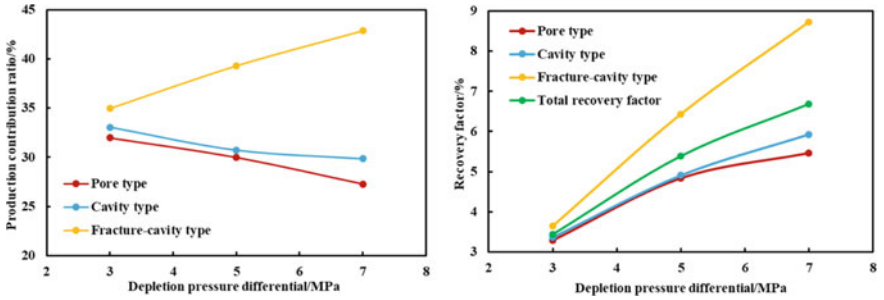

(a) Production contribution ratio (b) Ultimate recovery factor

Fig. 5.24 Ultimate recovery factors and production contribution ratios of different types of samples under different depletion pressure differentials

other words, effective and stable gas supply can be achieved between different types of reservoirs under relatively low production pressure differentials. This dynamic replenish state can be broken if the initial pressure differential is too high, thereby affecting the gas production capacity of peripheral reservoirs with relatively low petrophysical properties. In conclusion, the initial production pressure differential of horizontal heterogeneous reservoirs should be appropriately reduced to prolong the duration of the profitable production stage, increase the proportion of cumulative gas production in the profitable production stage, and improve the recovery factor of peripheral reservoirs with relatively low petrophysical properties. It should be noted that the production pressure differential should not be too low to limit the excellent gas production capacity of the fracture-cavity type reservoir in the near-wellbore region. The reasonable production pressure differential can be determined by combining physical simulation experiments with reservoir numerical simulations.

5.2.9 Effect of Initial Water Saturation on Gas Production Characteristics

The gas production curves of different initial water saturations show that both the instantaneous gas production and cumulative gas production of horizontal heterogeneous reservoirs decrease to varying degrees with the increase of initial water saturation. The higher the initial water saturation, the greater the decline of gas production capacity. When the initial water saturation is higher than the irreducible water saturation, the gas in the peripheral pore type and cavity type samples need to overcome a certain viscous resistance to flow, and a small amount of formation water is produced at the outlet end of the fracture-cavity type sample near the wellbore.

The horizontal heterogeneous reservoir production simulation experimental results of the three types of core samples under different initial water saturations

are illustrated in Fig. 5.25. The production contribution ratios of the fracture-cavity type and pore type samples increases and decreases respectively with the increase of initial water saturation, whereas that of the cavity type sample first increases and then decreases. The higher the initial water saturation, the greater the variation in the production contribution ratios of the three types of samples. Threshold pressure effect, gas–water two-phase flow and wellbore liquid accumulation are the main reasons for the large difference in production contribution ratio and low recovery factor under high initial water saturation. The irreducible water saturation of fracture-cavity type and cavity type reservoirs is generally below 30%, while that of the pore type reservoirs is above 30%. There is a small amount of movable water in the fracture-cavity type and cavity type samples when the initial water saturation is 30%, but the decrease in ultimate recovery factor is not obvious. This is because the liquid carrying capacity of horizontal heterogeneous reservoirs is greater than the liquid supply capacity under this initial water saturation, and a small amount of movable water near the wellbore can be carried out by gas flow to avoid the effect of wellbore accumulation. However, the increase of water saturation has a greater inhibitory effect on the percolation capacity of pore type reservoirs than that of the other two types of reservoirs. As a result, the production contribution ratio of the pore type sample decreased significantly, while that of the fracture-cavity type and cavity type samples increased. The movable water content in horizontal heterogeneous reservoirs increases greatly when the initial water saturation increases to 50%. The gas flow rate can be significantly reduced under the effect of gas–water two-phase percolation, resulting in the liquid carrying capacity of the gas flow being lower than the liquid supplying capacity of the reservoir. Consequently, more and more formation water accumulates near the wellbore to form liquid accumulations, and the gas in the peripheral reservoir is blocked by the accumulated liquid before being recovered, thereby greatly reducing the ultimate recovery of horizontal heterogeneous reservoirs. This is also the reason why the production contribution ratio of the cavity type begins to decline under the relatively high water saturation. When the initial water saturation of horizontal heterogeneous reservoirs is extremely high, sever wellbore liquid accumulation shortens the duration of the gas production stage. The duration and efficiency of replenishing gas to fracture-cavity type reservoirs from cavity type reservoirs are also greatly reduced by the effect of two-phase percolation and fluid accumulation. In addition, the production contribution ratio of the pore type sample is 0 because the threshold pressure effect cannot be overcome. Eventually, the gas production of horizontal heterogeneous reservoirs with high initial water saturation mainly comes from reservoirs with relatively high petrophysical properties near the wellbore, whereas a large amount of gas in the peripheral reservoirs with relatively low petrophysical properties is trapped by formation water.

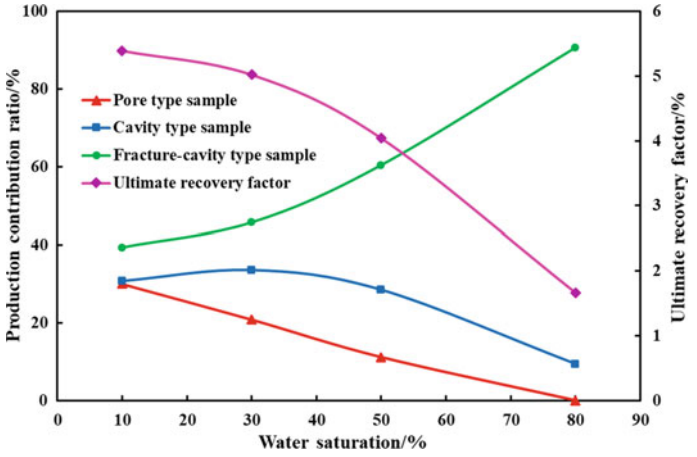

Fig. 5.25 Experimental results of horizontal heterogeneous reservoir production under different initial water saturations

5.2.9.1 Effect of Water Encroachment on Gas Production Characteristics

The water encroachment process during horizontal heterogeneous reservoir production was simulated by conducting water injection operation with constant pressure differential at the inlet end of the core system. The gas recovery factor and production contribution ratio of each production stage under the influence of depletion production and water encroachment are summarized in Figs. 5.26 and 5.27, respectively. Although the ultimately recovery factor of the heterogeneous core combination under the influence of water encroachment was reduced by 1.30%, the recovery factor in the profitable production stage was slightly improved, especially in the stable production stage. In contrast, the recovery factor in the low production stage decreased significantly. Therefore, the proportion of gas production in the high production stage and stable production stage was greatly increased. This result can be explained by comparing the cumulative gas production curves of depletion exploitation and water encroachment processes, as shown in Fig. 5.28. In the early stage of the water encroachment, the external water advances slowly in the pore type sample, and it takes a period of time for the pressure drop funnel to transfer to the gas–water interface of the pore sample. The gas production characteristics of the high production stage during water encroachment process are similar to those during depletion production, because the displacement system has not yet formed in the heterogeneous reservoir (Fig. 5.28). However, the cumulative gas production in the stable production stage of the water encroachment process is slightly higher than that of the depletion production process when the displacement system is formed. The energy supplementation of external water to heterogeneous reservoirs can improve the gas production capacity to a certain extent. This is the main reason for the significant increase of gas recovery factor and production proportion in the stable production stage. When the external

water enters the fracture-cavity type sample through the cavity type sample, it will rapidly advance to the well bottom along the dominant fracture under the effect of high pressure differential, and then gradually form wellbore fluid accumulation. The instantaneous gas production of horizontal heterogeneous reservoirs decreases rapidly and the water production gradually increase. Consequently, the duration of the low production stage dominated by the pore type sample was greatly shortened under the influence of water encroachment, and a large amount of gas in the pore type sample was trapped by external water. Therefore, the cumulative gas production curve of water encroachment process tends to be stable, while that of depletion production process continues to rise slowly. It can be concluded that the influence of water encroachment on this type of horizontal heterogeneous reservoir is mainly reflected in the stable production and low production stages. The outermost pore type reservoir with extremely low petrophysical properties can effectively slow down the water encroachment intensity, so that the high production stage dominated by the fracture-cavity type sample can avoid the influence of water encroachment. Moreover, the gas production capacity of the stable production stage dominated by the cavity type sample was slightly improved under the negative influence of gas–water two-phase percolation and the positive influence of energy supplement. For homogeneous fracture-cavity type reservoirs, the external water will rapidly advance to the well bottom along the dominant fractures in the high production stage, thereby forming serious fluid accumulation. As a result, the duration of the high production stage is drastically shortened, and a large amount of natural gas in the matrix region near the fracture is trapped by external water.

In conclusion, the negative effect of water encroachment on the gas production capacity of horizontal heterogeneous reservoirs with good petrophysical properties in the near-well region and gradually worsening in the far-well region is obviously weaker than that of homogeneous reservoirs and interlayer heterogeneous reservoirs. Therefore, this type of heterogeneous reservoir is superior to other types of

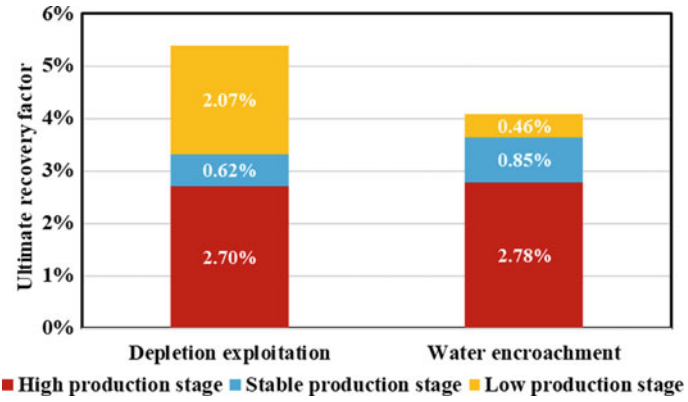

Fig. 5.26 Comparison of recovery factors in different production stages under depletion exploitation and water encroachment

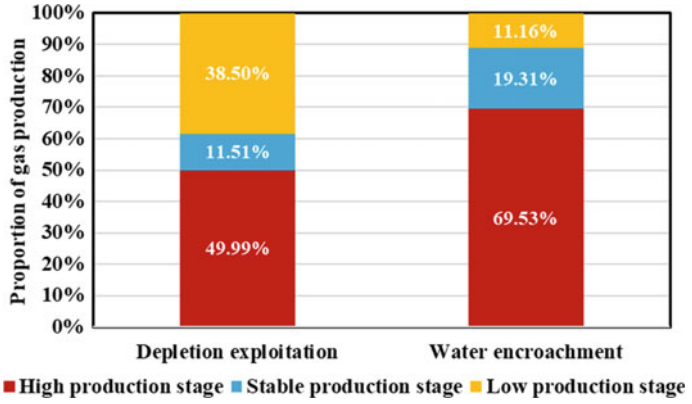

Fig. 5.27 Cumulative gas production proportion in different production stages under depletion exploitation and water encroachment

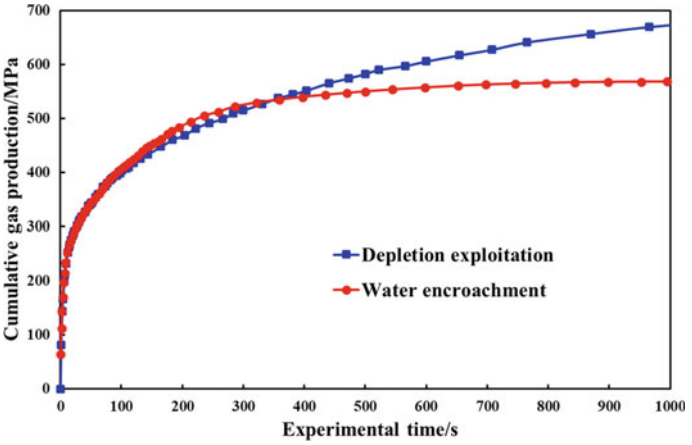

Fig. 5.28 Comparison of cumulative gas production under depletion exploitation and water encroachment

heterogeneous reservoirs in terms of gas production capacity and water encroachment prevention, and is the key area for well deployment of ultradeep carbonate gas reservoirs.

5.3 Suggestions for the Exploration and Development of Ultradeep Carbonate Gas Reservoirs

The complex relationship of pores, cavities and fractures in ultradeep carbonate gas reservoirs leads to the interlayer heterogeneity and horizontal heterogeneity of this type of gas reservoirs being significantly stronger than that of other types of gas reservoirs. The gas production characteristics of heterogeneous reservoirs in ultradeep carbonate gas reservoirs were obtained and the influencing factors were analyzed through a series of physical simulation experiments. In order to improve the gas production capacity and ultimate recovery factor of heterogeneous carbonate gas reservoirs in the benefit stage, the following suggestions for gas reservoir exploration and development are put forward based on the results of physical simulation experiments.

(1) The optimal selection of gas well locations is crucial for the efficient development of both interlayer and horizontal heterogeneous reservoirs. Fracture-cavity type reservoirs have strong gas storage capacity and gas production capacity. Therefore, the location where fracture-cavity type reservoirs are developed should be selected as far as possible for well deployment on the premise of satisfying other well location optimization factors. Gas layers with small petrophysical property differences should be selected as far as possible to reduce the effect of interlayer heterogeneity on commingled production capacity. In addition, the reservoir combination with good petrophysical properties in the near-well region and gradually worsening in the far-well region should be selected to exert the gas production capacity of the near-wellbore reservoirs and the gas replenishment capacity of the peripheral reservoirs.

(2) It is necessary to improve the identification accuracy between gas and water layers under ultradeep conditions. The multiple reservoir media and strong heterogeneity of ultradeep carbonate gas reservoirs make the logging response relationship extremely complex, thereby increasing the quantitative evaluation difficulty of reservoir gas saturation. The coexistence of high- and low-resistivity gas layers and high-resistivity water layers further increases the difficulty of distinguishing gas layers and water layers though well logging. Therefore, the premise of realizing high and stable production of gas wells is to prevent co-production of high-quality gas reservoirs and high water saturation reservoirs by improving the logging interpretation accuracy.

(3) The production pressure differential of heterogeneous reservoirs should be reasonable, because it directly affects the gas production capacity and ultimate recovery factor of each production stage. The reasonable production pressure differential of heterogeneous reservoirs can be determined by combing the research results of physical simulation experiments and reservoir numerical simulations. It is necessary to prevent too low production pressure differential from inhibiting the gas supply capacity of reservoirs with high petrophysical properties, and to prevent too high production pressure differential from

breaking the dynamic replenishment state of reservoirs with low petrophysical properties to reservoirs with high petrophysical properties.

(4) The optimal timing of multilayer commingled production and the combination of different types of reservoirs in the horizontal direction should be selected for heterogeneous reservoirs under the influence of edge and bottom water encroachment. The optimal timing of multilayer commingled production for gas wells without or far from edge and bottom water is the early production stage. The fracture-cavity type reservoir should not be developed prematurely during multilayer commingled production if the gas well is close to the edge and bottom water. This type of reservoir can be reperforated in the later stage of commingled production. The combination of fracture-cavity type reservoirs in the near-wellbore area and pore type reservoirs in the peripheral area can not only give full paly to the excellent production capacity of the fracture-cavity type reservoir, but also effectively slow down the migration rate of external water through the pore type reservoir.

5.4 Summary

In this chapter, both the physical simulation models of multilayer commingled production and horizontal heterogeneous reservoir production under ultra-high temperature and high pressure conditions were established respectively based on the similarity principle. Subsequently, the experimental scheme for multilayer commingled production and horizontal heterogeneous reservoir production were designed respectively. The gas production characteristics and gas supply capacity of three types of carbonate core samples under two heterogeneous conditions were revealed by processing and analyzing the parameters of pore pressure, cumulative gas production, production contribution ratio and recovery factor. Then, the effect of reservoir heterogeneity, permeability difference, depletion pressure differential, initial water saturation and water encroachment on the gas production characteristics of the two types of heterogeneous reservoirs were also analyzed. Finally, some suggestions were put forward to improve the gas production capacity and recovery factor of heterogeneous reservoirs in ultradeep carbonate gas reservoirs. The important conclusions obtained are summarized as follows.

(1) The effect of interlayer heterogeneity on gas production characteristics of multilayer commingled production was revealed. The multilayer commingled production process can be divided into three stages. The first stage lasts for a short period of time. The pressure variation of pore type and cavity type reservoirs lags behind that of fracture-cavity type reservoirs, and the fracture-cavity type is the dominant gas supply reservoir. The second stage lasts for a relatively long time. The production contribution ratio of the cavity type and pore type reservoirs gradually increases, and the two types of reservoirs become the dominant gas supply layers. The third stage lasts for a very long time. The gas produced in this stage is all supplied by pore type reservoirs. However, the

extremely small gas production and long production time make the exploitation in this stage unprofitable. The absolute value of reservoir permeability affects its own production contribution ratio. The greater the permeability, the greater the production contribution ratio. The relative value of reservoir permeability affects the total recovery factor of commingled production. The smaller the permeability difference, the higher the recovery factor of commingle production.

(2) The effect of depletion pressure differential on gas production characteristics of multilayer commingled production is revealed. The pressure drop rate of gas layer during multilayer commingled production is related to its petrophysical properties. However, this pressure variation difference between gas layers decreases as the depletion pressure differential decreases. When the initial depletion pressure differential is relatively low, the cooperative gas supply capacity of multiple gas reservoirs in multilayer commingled production is limited by the low pressure differential, and the efficient production capacity of gas wells cannot be effectively exerted. When the initial depletion pressure differential is relatively high, the alternate gas supply capacity of multiple gas reservoirs in multilayer commingled production is limited by the high pressure differential, and it is difficult for gas wells to maintain the high production rate for a long time. A reasonable production pressure difference can give full play to the cooperative and alternate gas production capacities of multiple gas reservoirs during multilayer commingled production to achieve the "dynamic replenishment balance" state.

(3) The effect of initial water saturation on gas production characteristics of multilayer commingled production was revealed. The instantaneous and cumulative gas productions of three types of reservoirs decrease significantly with the increase of initial water saturation. The lower the petrophysical properties of the reservoir, the greater the decline in gas production capacity. Therefore, the production contribution ratio of fracture-cavity type reservoirs increases rapidly with the increase of water saturation. This is because the effect of movable water on the gas phase percolation capacity of pore type and cavity type reservoirs is much greater than that of fracture-cavity type reservoirs, thereby further exacerbating the interlayer permeability difference. Furthermore, the liquid accumulation in the wellbore caused by the water production of fracture-cavity type reservoirs will enter other reservoirs with relatively low petrophysical properties through capillary imbibition. Consequently, the gas production capacity of these reservoirs is further inhibited because some percolation channels at the outlet end are blocked.

(4) The effect of water encroachment on gas production characteristics of multilayer commingled production was revealed. The cumulative gas production of pore type, cavity type and fracture-cavity type samples decreased by 56.72%, 28.76% and 5.21% under the effect of water encroachment. The gas production contribution ratio of pore type reservoirs decreases while that of fracture-cavity type reservoirs increases. Only a small amount of gas can be recovered from the fracture-cavity type reservoir after the external water breaks through the multilayer commingled production system. Therefore, water encroachment

has serious effect on various types of reservoirs during multilayer commingled production, especially gas layers with low petrophysical properties. The inhibition mechanism of water encroachment on the gas production capacity and production contribution ratio of pore type and cavity type reservoirs is consistent with that of high initial water saturation, but the effect of water encroachment on reservoirs is later but stronger.

(5) The effect of horizontal heterogeneity on gas production characteristics of different reservoir combinations was revealed. The distribution pattern of petrophysical properties gradually decreases from inside to outside can realize the cooperative and alternate gas production characteristics of three types of reservoirs in different production stages of heterogeneous reservoirs. In the second reservoir combination, the cavity type reservoir near the wellbore cannot maintain the high production stage for a long time, and the peripheral fracture-cavity type reservoir cannot exert its excellent gas production capacity. In the third reservoir combination, the instantaneous gas production of the pore type reservoir near the wellbore is extremely low. The peripheral fracture-cavity type reservoir can replenish the pore type reservoir, but the effect is not obvious. Therefore, drilling wells in fracture-cavity type reservoirs can not only give full play to the gas production capacity of high-quality reservoirs in the near-wellbore region, but also effectively develop peripheral reservoirs with relatively low petrophysical properties. The absolute value of reservoir permeability affects its own recovery factor and production contribution ratio. The greater the permeability value, the higher the recovery factor and production contribution ratio. The relative value of reservoir permeability affects the total recovery factor and production contribution ratio difference. The smaller the permeability difference, the higher the total recovery factor, and the smaller the difference in production contribution ratio.

(6) The effect of depletion pressure differential on gas production characteristics of the first type of heterogeneous reservoir combination was revealed. Although the reduction of depletion pressure differential weakens the gas production capacity of the high production stage to a certain extend, it greatly prolongs the duration of the stable production stage and reduces the proportion of cumulative gas production in the low production stage. Although the growth of depletion pressure differential improves the instantaneous gas production of the high production stage, it greatly shortens the duration of the high production stage and increased the proportion of cumulative gas production in the low production stage. A relatively low production pressure differential can give full play to the cooperative and alternate gas production capacities of horizontal heterogeneous reservoirs, thereby improving the ability of peripheral reservoirs to dynamically replenish reservoirs near wellbore. Therefore, the initial production pressure differential of horizontal heterogeneous reservoirs should be appropriately reduced to increase the duration and cumulative gas production of the profitable production stage, and improves the recovery factor of peripheral reservoirs.

(7) The effect of initial water saturation on gas production characteristics of the first type of heterogeneous reservoir combination was revealed. Both the instantaneous and cumulative gas productions decrease to varying degrees with the increase of initial water saturation. The production contribution ratio of the fracture-cavity type and pore type reservoirs increases and decreases respectively with the increase of initial water saturation, whereas that of the cavity type reservoir first increases and then decreases. The gas flow rate is significantly reduced with the increase of water saturation, resulting in the liquid carrying capacity of the gas flow being lower than the liquid supplying capacity of the heterogeneous reservoir. Formation water accumulates near the wellbore to form liquid accumulations, and the gas in the peripheral reservoir is blocked by the accumulated liquid before being recovered, thereby greatly reducing the recovery factor of horizontal heterogeneous reservoirs. Threshold pressure effect, gas–water two-phase flow and wellbore liquid accumulation are the main reasons for the large difference of production contribution ratio and low recovery factor under high initial water saturation.

(8) The effect of water encroachment on gas production characteristics of the first type of heterogeneous reservoir combination was revealed. Although the total recovery factor of the heterogeneous reservoir decreases under the effect of water encroachment, the recovery factor in the profitable production stage is slightly improved, especially in the stable production stage. The outermost pore type reservoir can effectively slow down the water encroachment intensity, so that the high production stage dominated by the fracture-cavity type reservoir can avoid the effect of water encroachment. Moreover, the gas production capacity in the stable production stage dominated by the cavity type reservoir is slightly improved under the negative influence of gas–water two-phase percolation and the positive influence of energy supplementation. Therefore, the negative effect of water encroachment on the gas production capacity of horizontal heterogeneous reservoirs with good petrophysical properties in the near-well region and gradually worsening in the far-well region is weak.

References

Arevalo-Villagran, J. A., Wattenbarger, R. A., El-Banbi, A. H. (2000). Production analysis of commingled gas reservoirscase histories. *SPE* 58985.

Guo, P., Dong, C., Wang, Z. H., Yang, Z. X., Liu, X., et al. (2021). Experimental study on areal flowing during depletion of a high-pressure heterogeneous gas reservoir. *Chemistry and Technology of Fuels and Oils, 57*, 406–414.

Hu, Y., Jia, Y. Z., He, D. B., Wang, J. P., Li, Z. C., et al. (2022). Characterization method of gas reservoir heterogeneity and physical simulation experiment of production. *Natural Gas Geoscience, 33*(2), 297–302.

Li, Q. Y., Yue, X. A., Zhang, L. J., & Maen, H. (2020). Production performance by polymer conformance control in ultra-low permeability heterogeneous sandstone reservoirs produced under their natural energy. *Journal of Petroleum Science and Engineering, 193*, 107348.

Liang, Y. S., Lai, F. P., Dai, Y. T., Shi, H., & Shi, G. S. (2021). An experimental study of imbibition process and fluid distribution in tight oil reservoir under different pressures and temperatures. *Capillarity, 4*(4), 66–75.

Liu, G. F., Meng, Z., Luo, D. Y., Wang, J. N., Gu, D. H., et al. (2020). Experimental evaluation of interlayer interference during commingled production in a tight sandstone gas reservoir with multi-pressure systems. *Fuel, 262*, 116557.

Liu, Q. G., Wang, H., Wang, R. C., & Li, X. C. (2010). A computing method for layered production contribution and affecting factors analyzing in commingled gas reservoirs. *Journal of Southwest Petroleum University (science & Technology Edition), 32*(1), 80–84.

Ma, H. Y., Gao, S. S., Ye, L. Y., Liu, H. X., Xiong, W., et al. (2018). Change of water saturation in tight sandstone gas reservoirs near wellbores. *Natural Gas Industry, 38*(5), 77–86.

Naderi, M., Rostami, B., & Khosravi, M. (2015). Effect of heterogeneity on the productivity of vertical, deviated and horizontal wells in water drive gas reservoirs. *Journal of Natural Gas Science and Engineering, 23*, 481–491.

Peng, L. S., Qiao, L., Gong, M., & Lv, Y. M. (2014). Factors affecting the production performance of coalbed methane wells with multiple-zone. *Journal of China Coal Society, 39*, 2060–2067.

Tan, Y. S., Li, H. T., Zhou, X., Wang, K., Jiang, B., et al. (2019). Inflow characteristics of horizontal wells in sulfur gas reservoirs: A comprehensive experimental investigation. *Fuel, 238*, 267–274.

Tian, F., Wang, X. D., & Xu, W. L. (2019). A semi-analytical model for multiple-fractured horizontal wells in heterogeneous gas reservoirs. *Journal of Petroleum Science and Engineering, 183*, 106369.

Wang, L., He, Y. M., Wang, Q., Liu, M. M., & Jin, X. (2021). Improving tight gas recovery from multi-pressure system during commingled production: An experimental investigation. *Natural Resources Research, 30*(5), 3673–3694.

Wang, L., Yang, S. L., Liu, Y. C., Xu, W., Deng, H., et al. (2017). Experimental investigation on gas supply capability of commingled production in a fracture-cavity carbonate gas reservoir. *Petroleum Exploration and Development, 44*(5), 824–833.

Xu, J., Zhang, C. L., Peng, S. J., Jia, L., Guo, S. C., et al. (2018). Multiple layers superposed CBM system commingled drainage schedule and its optimization. *Journal of China Coal Society, 43*(6), 1677–1686.

Yang, X. F., Liu, Y. C., Li, J., Wang, Y., & Deng, H. (2012). Effect of separate layer recovery or multilayer commingled production and the optimal selection of development methods for two-layer gas reservoirs. *Natural Gas Industry, 32*, 57–60.

You, L. J., Kang, Y. L., Chen, Y. J., Cheng, Q. J., & You, H. Z. (2006). Stress sensitivity of fractured tight gas sands in consideration of fractures and water saturation. *Journal of China University of Petroleum (edition of Natural Science), 30*(2), 59–63.

You, L. J., Kang, Y. L., & Chen, Y. J. (2005). New method of water saturation of tight gas-spontaneous imbibition. *Journal of Southwest Petroleum Institute, 27*(1), 28–31.

You, L. J., Li, L., Kang, Y. L., Shi, Y. J., Zhang, H. T., et al. (2012). Gas supply capacity of tight sandstone in considering effective stress and water saturation. *Natural Gas Geoscience, 23*, 764–769.

Zhao, Y. L., & Wang, Z. M. (2019). Effect of interlayer heterogeneity on multi-seam coalbed methane production: A numerical study using a gray lattice Boltzmann model. *Journal of Petroleum Science and Engineering, 174*, 940–947.